BULK AND INTERFACIAL EFFECTS ON DENSITY IN POLYMER NANOCOMPOSITES

Laxmi Kumari Sahu, M.Tech.

Dissertation Prepared for the Degree of

DOCTOR OF PHILOSOPHY

UNIVERSITY OF NORTH TEXAS

May 2007

APPROVED:

Nandika A. D'Souza, Major Professor
Witold Brostow, Committee Member
Mohamed El Bouanani, Committee Member
Tae-Youl Choi, Committee Member
Michael Kaufman, Chair of the Department of Materials Science and Engineering
Oscar Garcia, Dean of the College of Engineering
Sandra L. Terrell, Dean of the Robert B. Toulouse School of Graduate Studies

Sahu, Laxmi Kumari, *Bulk and interfacial effects on density in polymer nanocomposites.* Doctor of Philosophy (Materials Science and Engineering), May 2007, 227 pp., 57 tables, 128 illustrations, chapter references.

The barrier properties of polymers are a significant factor in determining the shelf or device lifetime in polymer packaging. Nanocomposites developed from the dispersion of nanometer thick platelets into a host polymer matrix have shown much promise. The magnitude of the benefit on permeability has been different depending on the polymer investigated or the degree of dispersion of the platelet in the polymer. In this dissertation, the effect of density changes in the bulk and at the polymer-platelet interface on permeability of polymer nanocomposites is investigated. Nanocomposites of nylon, PET, and PEN were processed by extrusion. Montmorillonite layered silicate (MLS) in a range of concentrations from 1 to 5% was blended with all three resins. Dispersion of the MLS in the matrix was investigated by using one or a combination of X-ray diffraction (XRD), scanning electron microscopy (SEM) and transmission electron microscopy (TEM). Variation in bulk density via crystallization was analyzed using differential scanning calorimetry (DSC) and polarized optical microscopy. Interfacial densification was investigated using force modulation atomic force microscopy (AFM) and ellipsometry. Mechanical properties are reported. Permeability of all films was measured in an in-house built permeability measurement system. The effect of polymer orientation and induced defects on permeability was investigated using biaxially stretched, small and large cycle fatigue samples of PET and nylon nanocomposites. The effect of annealing in nylon and nanocomposites was also investigated. The measured permeability was compared to predicted permeability by considering the MLS as an ideal dispersion and the matrix as a system with concentration dependent crystallinity.

ACKNOWLEDGEMENTS

A journey is easier when you travel together. Interdependence is certainly more valuable than independence. This thesis is the result of three and half years of work whereby I have been accompanied and supported by many people. It is a pleasant opportunity to express my gratitude for all of them.

The first person I would like to extend my deepest gratitude is my advisor Dr. Nandika D'Souza, both professional and personally for her incessant motivation, invaluable guidance and great patience. Her overly enthusiastic and integral view on research and her mission for providing "high-quality work and not less" has made a deep impression on me. I owe her a lot of gratitude for having me shown this way of research. I also thank her for the outstanding inputs for my dissertation. I am really glad to be her student under this amazing personality.

I sincerely thank Dr. Mohamed El Bouanani for his teaching and constant help in the permeability system and his advice when I needed it. I gratefully acknowledge the precious opportunity of getting a chance to work with him. My technical discussions with him tremendously improved my ability to solve problems practically in UHV systems, especially in the permeability system. This keen insight and compassion for the knowledge motivated me to probe further and further into research. I am grateful to Dr. Witold Brostow for his teaching on the subject of polymers and thermodynamics which helped me in my research work. I have lined up to the standards of his teaching and the many important lessons I learnt in his class.

I thank Dr. Rick Reidy for always being pleasantly willing in letting me use his spin caster; Dr. Brian Gorman for his teaching in microscopy courses and laboratory and my training under him helped me a lot in my experiments.

Thanks to my colleagues Ali Shaito, Ajit Ranade, Siddhi Pendse, Divya Kosuri and others for their help and making a homely atmosphere in the laboratory; David Garrett who helped me with TEM sample preparation and imaging, and to John Sawyer, and Craig Collins, for their technical and logistic help; to Alberta Caswell, Joan Jolly, Wendy Agnes, and Alaina Bailey for their help and assistance and making an friendly atmosphere in the Materials Science and Engineering Department each semester. I would like to thank Dr. Bruce Gnade, University of Texas at Dallas for helping me to access UTD clean. He was one of my inspiration sources during PhD and now. I sincerely thank Dr Amit Dharia, Transmit Technology, for helping me in processing the polymer films.

I am very grateful to my husband, Radhakanta Samantara for his love, support and patience during these years of my studies. I would like to thank my family for their support during my student life, and for their patience and encouragement while have been away for many years. Without my family it would have been impossible to do my PhD. Finally, my gratitude also goes to Subhransu Mishra and family, and my friends who helped me at every moment.

TABLE OF CONTENTS

Page

LIST OF TABLES

LIST OF FIGURES

Page

CHAPTER 1

INTRODUCTION

Polymers are used in a wide range of applications ranging from food packaging to flat panel displays because of their flexibility, light weight, low cost, solvent resistance, transparency, physical strength, printability, and process ability. Improving the barrier properties is a key need for packaging applications. Traditional barrier materials such as metals, glass, and paper exhibit low permeability. However, they lack required flexibility. On the other hand, one of the major limitations in shelf life for packaging and device lifetimes is the permeability of the packaging material to gas and moisture.

Flexible displays for instance are an area of much interest. These flexible displays have the potential to replace newspapers, books, rigid flat screens. These devices will be highly beneficial as it has advantages such as being foldable, over conventional display.[1] Both the electro luminescent (EL) organic and the cathode materials such as Ca, Mg, Li in organic light emitting diode (OLED) device are very susceptible to oxidation and degradation.[2, 3] For the LED device, a lifetime of 10,000 hr requires a maximum permeability rate of 5×10^{-6} g/m^2/day for water vapor. This required value is four to five orders of magnitude less than the actual value in polymers.[4] Most plastics have water vapor permeation rate of 10^{-1}–10^{-2} g/m^2/day at 25 °C, which adversely affects the lifetime of OLED device. For oxygen gas, a lifetime of 10,000 hr requires a maximum permeability rate of 10^{-3} cc/m^2/day.[5] A combination of the barrier, thermal, scratch resistance with flexibility, toughness, and processability of substrate materials will lead to the ideal material for flexible displays.[6] Developing barrier polymers for such applications is therefore necessary. However, it is difficult to define “barrier polymer” precisely. Whether a polymer is a barrier polymer or not, is defined by the end-use requirement. A material that

provides sufficient barrier properties for a particular application can be considered to be a barrier polymer for that application.[7]

Various polymers have been used in packaging such as polyethylene (PE), polypropylene (PP), polystyrene (PS), nylon, poly ethylene terephthalate (PET), poly (ethylene 2, 6-naphthalate) (PEN) etc. The oxygen permeability and T_g of different polymers are reported in Table 1.1. From the tabulated values, it is clear that permeability of Nylon 6, PET, and PEN offer a lower permeability compared to PE, PS, and PP.

Table 1.1: Glass transition temperature and permeability of different polymers.

Sample	**Glass transition temperature (°C)[7]**	**Permeability (cm^3.mil)/(100 $in.^2$.day.atm.) [8]**
Low density polyethylene (LDPE)	-25	498
High density poly ethylene (HDPE)	-55	185
PS	100	365
PP (biaxially oriented),	-20	150
Nylon 6	50	6.6
PET (25% crystalline)	80	4.8
PEN	120	1.2

Decreasing the permeability in polymers has been approached by annealing, biaxial stretching, copolymer ratio, filler addition, metal and/or inorganic deposition. All these approaches are based on either increase in densification of the polymer or minimizing the effect of defects. Annealing increases the crystallinity in the polymer. The higher the crystallinity, the lower the permeability as the crystalline phase has a higher density, is almost impermeable to gases. Biaxial stretching decreases permeability due to chain orientation, occurring by the stretching process. Different polymers have different affinities to gas and water vapor. Thus copolymerization is another followed approach. Benefits can be obtained from individual polymers. Relatively recently, the addition of nano fillers such as layered silicate in the polymer

has been investigated. This addition anticipated to decrease the permeability by creating a tortuous path in the polymer matrix. The economic benefits to be gained from using existing materials and technology as opposed to developing new ones make improvement by addition an attractive route. Moreover, existing polymers being already characterized, offer advantages in predicting different properties from an existing knowledge base. Though multilayer processing offers the lowest permeability, it needs one or more additional processing step(s). In contrast, nanocomposites can be processed by conventional methods such as extrusion, blow molding etc. Montmorillonite layered silicate (MLS) nano filler is used because of its nanometer scale dimension, which increases the interfacial interaction between MLS and the polymer. The resulting structure in the polymer and MLS is called a polymer nanocomposite. Another reason for studying polymer nanocomposites is because additional benefits such as improvement in mechanical properties, thermal stability, and flame resistance can be obtained. Ideally, metal and inorganic coatings are considered to be impermeable. However, coatings are always associated with defects. A very thin layer ~ (10-50) nm of metal on a polymer can reduce permeability by orders of magnitude based on the quality of the thin layer of coating.

1.1 Objectives of Dissertation

Previously our group has studied the effect of MLS on nonlinear creep[9] and crystallization[10] in different polymers. The results indicated structural evolution during deformation. The prime objective of this study is to understand the barrier properties and factors affecting in nanocomposites and can be outlined as follows

1. Effects of addition of MLS on barrier properties
2. Correlation of dispersion and crystallinity with the barrier property

3. Systematic studies of permeability using different models to understand the contributions of crystallinity changes and the effect of tortuous path in nanocomposites that contributes to either increasing or decreasing permeability

To understand the permeability results in nanocomposites, the effect of polymer-MLS interface on different properties is studied and can be outlined as follow

1. Study the interface between the polymer and MLS by force modulation atomic force microscopy (FM-AFM) and correlation of permeability to the density of the interface.
2. Examine how the increased surface area of the MLS contributes to the glass transition or coefficient of thermal expansion by examining the polymer physics of confinement.

1.2 Organization of Dissertation

Chapter 1 briefly describes the motivation, prime objectives and the scope of work. Chapter 2 explains an overview of polymer nanocomposites and the different parameters that have affect permeability. A comprehensive review of the improvement of different properties, such as barrier and mechanical properties is also attempted. The three polymers studied here are Nylon 6, PET, and PEN. The polymer nanocomposites of these polymers are processed by the extrusion method. Details relating to the processing method and experiments conducted are elaborately illustrated and explained in Chapter 3. Subsequently in Chapter 4, dispersion, crystallinity, permeability, and mechanical properties of the nanocomposites are studied and compared with a pure host matrix. The permeability of the processed film is measured using a permeability measurement system built in-house.[11] The helium and oxygen permeabilities of nanocomposites are analyzed and compared with a pure polymer. The permeabilities of fatigued and biaxially stretched films as well as the effect of moisture on permeability of the films are

also studied. The effects of processing, and variations using a single screw and twin screw extruder on the properties of PEN nanocomposite are also carried out. The permeability is predicted based on crystallinity changes and/or MLS presence to understand the significant factor that contributes to permeability in nylon and PET nanocomposites.

In Chapter 5, the possible reasons associated with increased permeability in PET nanocomposite are probed by examining the interface. Atomic force microscopy images in the force modulation mode are used to understand the effect of MLS in the polymer matrix. The FM-AFM images are studied to see the relative densification effects of MLS, bulk polymer matrix, and their interface. A weak interface at the polymer and MLS is observed, and this leads to an increase in permeability. This results in mitigating the benefits of the tortuous path created by MLS in the matrix.

The issue of interface is also approached from the perspective of chain mobility or hindered mobility as a function of distance from the substrate. The properties of thin films in the range of nanometer or tens of nanometers often differ substantially from the bulk polymer. The possible reasons for differences in the properties of thin film and bulk film are confinement, size, substrate interaction or interface, free surface, and density effects. A confinement study of thin films of PET and an amorphous PETG and their nanocomposites is carried out in Chapter 6. The glass transition and thermal expansion in the thin film is analyzed with a range of thickness varying from 25 to 710 nm and an MLS concentration varying from 0, 1, 2, 3, and 5% to understand the confinement effect. Chapter 7 provides an overall conclusion of the dissertation.

1.3 References

[1] Forsythe, E. W. Invited seminar, University North Texas (2006)

[2] Lim, S. F.; Ke, L.; Wang, W.; Chua, S.J.; Appl Phys Lett **78** (2001) 2116.

[3] Nguyen, T. P.; Jolinat, P.; Destruel, P.; Clergereaux, R.; Farenc, J. Thin Solid Films **325** (1998) 175.

[4] Weaver, M. S.; Michalski, L. A.; Rajan, K.; Rothman M. A.; Silvernail, J. A.; Brown, J. J.; Burrows, P. E.; Graff, G. L.; Gross, M. E.; Martin, P. M.; Hall, M.; Mast, E.; Bonham, C.; Bennett, W.; Zumhoff, M. Appl Phys Lett **81** (2002) 2929.

[5] Raetzold, R.; Winnacker, A.; Henseler. D.; Cesari, V.; Heuser, K. Rev Sci Instrum **74** (2003) 5147.

[6] Burrows, P. E; Graff, G. L.; Gross, M. E.; Martin, P. M.; Shi, M. K.; Hall, M.; Mast, E.; Bonham, C.; Bennett, W.; Sullivan, M. B. Displays **22** (2001) 65.

[7] Dhoot, S. N.; Freeman, B. D.; Stewart, M. E.; Encyclo Polym Sci Tech (2002).

[8] Pinnavaia, T. J.; Beall G. W. Polymer-Clay Nanocomposites, John Wiley & Sons (2001).

[9] Ranade, A. PhD Dissertation, University of North Texas, 2004.

[10] Pendse S., Masters Thesis, University of North Texas, 2005.

[11] Ranade, A.; D'Souza, N. A.; Wallace, R. M.; Gnade, B. E. Rev Sci Instru **76** (2005) 013902.

CHAPTER 2

FACTORS AND PROPERTIES OF POLYMER NANOCOMPOSITES

2.1 Polymer Nanocomposite

A polymer nanocomposite is a composite in which one or more of the components are in the nanometer scale. Polymer nanocomposites have attracted significant interest because of their improved properties over the unmodified polymer. Improved barrier properties[1] and flame retardance[2,3] have been observed in polymer nanocomposites by different groups. Benefits in the mechanical properties[4,5,6] and dimensional stability[7,8] are also observed. Multifunctional property enhancements have led the nanocomposites to increased applications in various fields such as the packaging industry (bottles and containers), automobile parts (both interior and exterior), the electronic industry (packaging materials), and the aerospace industry. Among the early reports of engineering nanocomposites, Nylon 6 nanocomposite was studied by Usuki et al.[4, 9] from the Toyota research group. Before the discovery of nanocomposites, MLS was used as fillers, as natural MLS platelets is hydrophilic and therefore does not interact with most hydrophobic polymer matrices. MLS platelets coagulate in the polymer matrix. Toyota research group discovered that surfactant-treated MLS to synthesize nanocomposites MLS is treated with an organophilic surfactant prior to mixing with polymers to enhance the interaction with polymers. Polymer chains migrate and interact with the surfactant molecules, and a well-dispersed structure can be formed. Nylon 6 nanocomposites were processed by in-situ polymerization. The COOH end groups present in MLS initiate polymerization. They observed an intercalated dispersion from using x-ray diffraction (XRD) and transmission electron microscopy (TEM). The improved tensile, flexural strength, modulus was observed in nanocomposites compared to pure nylon. The MLS-polymer interaction plays an important role

in determining the properties in nanocomposites. Therefore, the properties of polymer nanocomposites are dependent on the base polymeric material, chemistry, processing method, and structure. This is schematically shown in Figure 2.1.

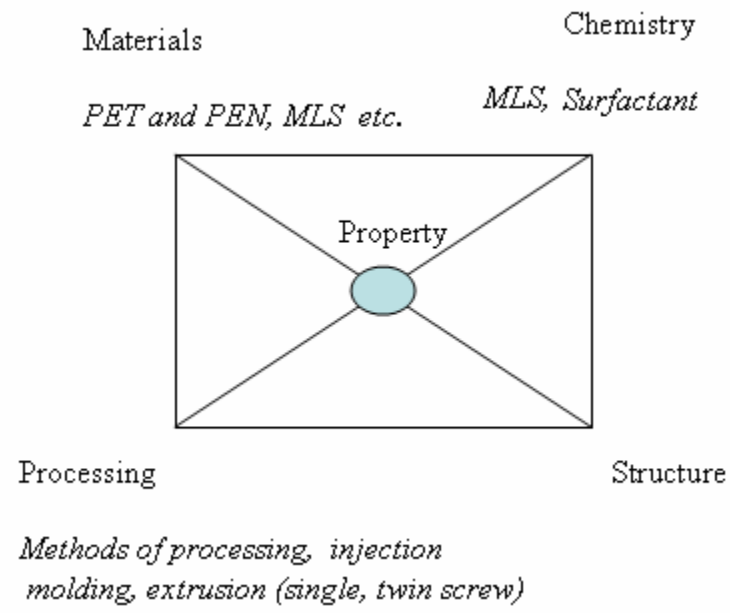

Figure 2.1: Schematic showing the relationship of materials, chemistry, processing, and structure on properties in polymer nanocomposites.

2.1.1 Polymer Matrix

In this study, three different materials (nylon 6, PET, and PEN) are studied based on their thermal transitions, mechanical properties, and barrier properties. Of these, the most widely used thermoplastic barrier polymer is poly (ethylene terephthalate) (PET).[9] It has a lower permeability than other polymers like polyethylene (PE). Another thermoplastic polymer that is used for packaging is nylon. Nylon is mostly used as blow molded bottles for industrial and household chemical markets. Compared to nylon, PET is more transparent and has been used for food packaging. These polymers have a relatively higher glass transition temperature compared to few other polymers, e.g., PE. Poly (ethylene 2, 6-naphthalate) (PEN) has a higher glass transition

temperature compared to nylon and PET; however, it is more expensive. PEN and PET are non-polar polymers. On the other hand, nylon is a polar polymer. The polar nature of nylon makes it more hydrophilic than PEN and PET. The structure and some of the general properties of these polymers is presented below.

. The chemical structure of nylon 6 is shown in Figure 2.2. [9] It is processed by the polymerization of caprolactam A Nylon has good gas barrier properties but poor moisture barrier properties. It belongs to a family of aliphatic polyamide and contains polar -CONH- group spaced out at regular intervals so that the polymers crystallize with a high intermolecular attraction. The aliphatic chain segment in the polymer chains give flexibility in the amorphous region. Therefore, this polymer has a combination of high interchain attraction in the crystalline zones and flexibility in the amorphous zones leading to polymers which are tough above their T_g. Some of the typical values of a nylon polymer are reported in Table 2.1.

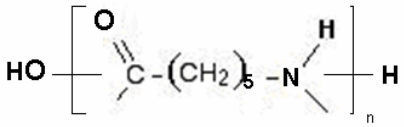

Figure 2.2: Chemical structure of Nylon 6.

Table 2.1: Some of f the typical properties of Nylon.[10]

Properties	Values
Tensile stress at yield	76 MPa
Tensile modulus	2.8 GPa
Glass transition temperature	49 ºC
Melting point	215 ºC

The chemical structure of PET is shown in Figure 2.3.[9] PET can be prepared by the reaction between ethylene glycol and terephthalic acid. Some of the typical values of a PET polymer are reported in Table 2.2. Due to the comparatively low gas barrier and ease of

processabiltiy permitting, PET is a plastic produced in high volume that has been used in food and beverage packaging. PET has been widely used for products such as soft drink containers, and sports drinks. In PET, adding a small quantity of nanoclay (0.5-5 weight %) can improve the various properties such as strength, rigidity, heat resistance, and gas and moisture barrier, while at the same time maintaining transparency and allowing for recycling.[11] The barrier to gas is not sufficient for other applications like beer or wine product packaging. Therefore, further study for improving the barrier properties is of considerable interest.

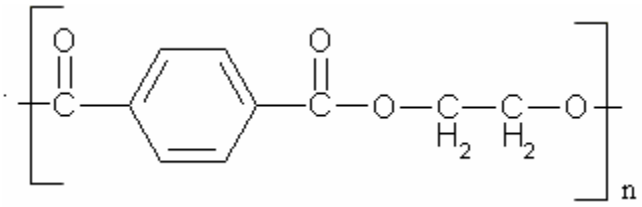

Figure 2.3: Chemical structure of PET.

Table 2.2: Some of the typical properties of PET.

Property	Values
Amorphous density	1.33 g/cm^3
Density of oriented polymer	1.38-1.39 g/cm^3
Crystalline melting point	265 ºC
Maximum rate of crystallization at	170 ºC
Glass transition temperature	67 ºC
Water absorption (24 hr immersion)	0.55 %

The chemical structure of PEN is shown in Figure 2.4. [9] PEN is processed from dimethyl-2, 6-naphthalene dicarboxylate (NDC) and ethylene glycol. PEN offers lower permeability to gases and water vapor than PET and can be classified as a high barrier polyester. The extra ring structure in PEN provides increased mechanical strength and heat stability. PEN has higher temperature resistance, tensile properties, UV resistance and improved oxygen and moisture barrier properties compared to PET. The additional ring in PEN also increases the chain stiffness, and that leads to an increase in T_g. The T_g and T_m in PEN are 124 and 270-273 ºC, respectively.

Like PET, the main markets for PEN are fibers, films, bottles, and other blown containers. Replacing PET with PEN increases the range of materials that may be packed because of the higher process temperatures and lower permeability. Because of higher cost, the market is currently limited to low-volume high cost applications such as medical applications. Relatively recently, MLS is added to lower the permeability in polymer. In the following section, MLS has been explained in detail.

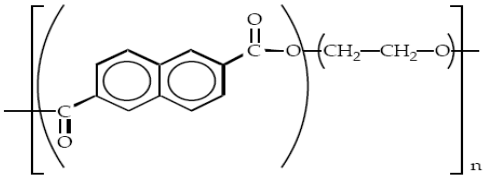

Figure 2.4: Chemical structure of PEN.

2.1.2 Montmorillonite Layered Silicate (MLS)

Montmorillonite is named after the French town of Montmorillon, where it was first discovered. It is the common name for hydrated sodium calcium aluminum silicate. MLS is the most commonly used nano-filler for processing the nanocomposites. The unit cell of MLS is shown in Figure 2.5. It is a mineral of the smectite clay group, in the structural family of phyllosilicates.

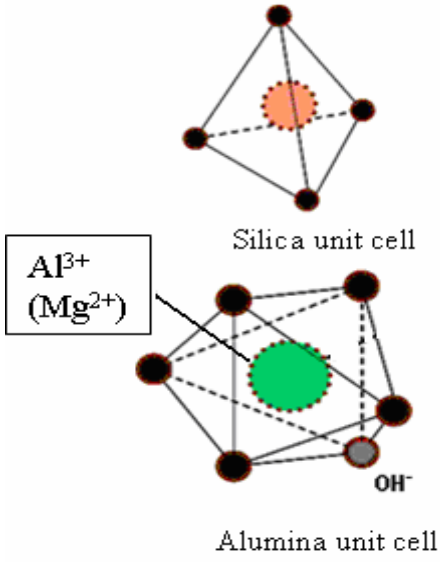

Figure 2.5: Unit cell structures in montmorillonite layered silicate (MLS).

Montmorillonite is a smectite with a dioctahedral silica/alumina sandwich structure. In the ideal, uncharged dioctahedral sheet, trivalent Al^{3+} occupies two out of every three available octahedral cells, leaving one vacant. In montmorillonite, some of the Al^{3+} sites in the octahedral are replaced by Mg^{2+} and/or other divalent cations. These substitutions are the primary source of permanent charges within MLS. MLS is in fact the specific smectite with the most ideal swelling properties and comparatively higher cation exchange capacity (CEC) of the group. The CEC of different clays varies from 77 to 140 meq/100g. The CEC of some of the surfactant-modified MLS is tabulated in Table 2.3.

Table 2.3: CEC and d spacing of different types of MLS.[12]

Nanoclay (Cloisite)	Organic modifier	CEC, meq/100gm	d(001) Å
10 A	2MBHT	125	19.2
15 A	2M2HT	125	31.5
20 A	2M2HT	95	24.2
25 A	2MHTL8	95	18.6
30B	MT2EtOH	90	18.5
93 A	M2HT	90	23.6
Cloisite Na+	-	-	11.7

where 2MBHT: dimethyl, benzyl, hydrogenated tallow, quaternary ammonium

2M2HT: dimethyl, dehydrogenated tallow, quaternary ammonium

2MHTL8: dimethyl, dehydrogenated tallow, 2-ethylhexyl quaternary ammonium

M2HT: methyl, dehydrogenated tallow ammonium

MT2EtOH: methyl, tallow, bis-2-hydroxyethyl, quaternary ammonium

The MLS crystal structure consists of layers made up of two silica tetrahedra fused to an edge-shared octahedral sheet of either aluminum or magnesium hydroxide as shown in Figure 2.6. Van der Waals force separates these layers referred to as interlayer or gallery region. One of the important issues in synthesizing the nanocomposite is treatment of the clay, which will govern the dispersion of clay in the nanocomposites. The most commonly used process is the ion exchange method. MLS is hydrophilic; therefore, it must be modified by an organophilic surfactant before mixing with polymers. The surfactants are cationic and migrate into the galleries where they are substituted in place of hydrated cations. The most common surfactants used with MLS are alkylammonium and alkylphosphonium salts. The role of alkylammonium cations in the organosilicates is to lower the surface energy of the inorganic host and improve the wetting characteristics with the polymer. These cations can also provide functional groups that can react with the polymer to improve the strength of interface between the inorganic layered silicate and the organic polymer. The cations play an important role in the dispersion of MLS in nanocomposites. Processing methods also play an important role in the dispersion of MLS. For example, processing using a single or a twin screw extruder will result in materials exhibiting different properties.

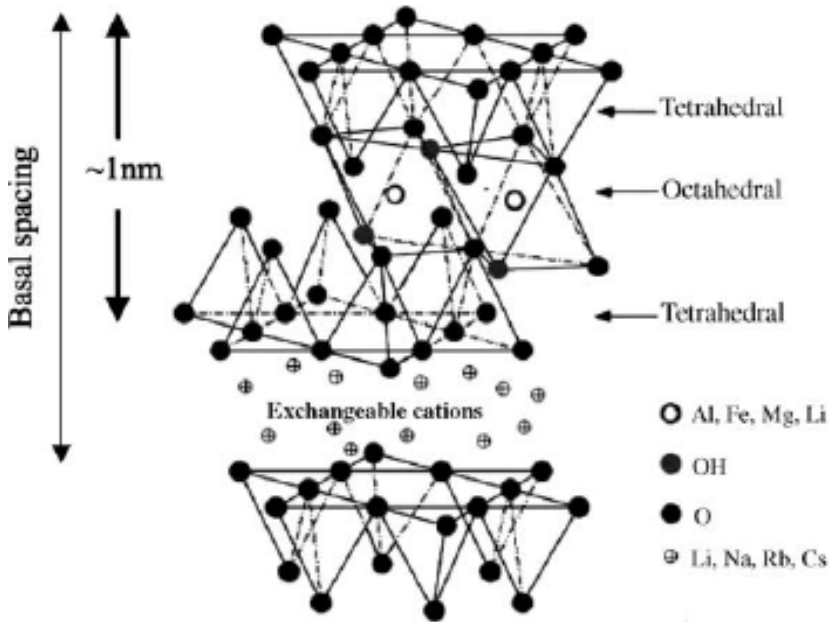

Figure 2.6: Structure of montmorillonite.[13]

2.1.3 Processing

Polymer nanocomposites can be manufactured by adding the MLS in the polymer matrix with a polymerization reaction (in-situ intercalative polymerization) to a solvent-swollen polymer (solvent method) or to a polymer melt (melt blending). Another method has been recently developed where nanocomposites are prepared by polymerizing the layered silicate precursors in the presence of the polymer. The in-situ intercalative polymerization has been studied in detail because it provides the highest level of polymer-MLS interaction.[14,15] In the polymer melt intercalation method, the polymer is melted and mixed with the MLS. The primary advantage of this method is that it is compatible with high-volume plastic manufacturing processes such as extrusion and injection molding. In this study, Nylon 6, PET, and PEN nanocomposite films are processed by extrusion. Nanocomposite pellets and films can be processed by using a single screw or a twin screw extruder. In the single screw extruder, material is sheared and mixed. On the other hand, in the twin screw extruder closely intermeshing screws

result in transportation of the material in to the so-called C-shaped chambers. The C-shaped chamber is enclosed by the neighboring intermeshing screw and the barrel wall. In the twin screw extruder, the material is transported to the C-shaped chamber. The material is internally mixed and forced through the gaps or clearances of the screw or transferred to the neighboring screw, and finally the material is delivered to the die. Therefore, mixing of the material and shear history will be different in a single screw extruder and a twin screw with other parameters being same. Mixing will also vary with the specific screw elements like kneading disc and reversed pitch.[16] The screw design in the extruder has an effect on the properties of nanocomposites. For example, yield stress and the modulus of Nylon 6 processed by a single screw extruder has been reported as 43.9 MPa and 1.2 Gpa, respectively.[17] On the other hand, Nylon 6 processed by a twin screw extruder shows improved mechanical properties. Yield strength and the modulus of Nylon 6 is determined to be 64.2 MPa and 2.66 Gpa, respectively.[18] Lew et al.[19] processed nanocomposites based on Nylon-12 and synthetic fluormica using a single screw extruder. They varied the screw speed and residence time, ranged from 15 to 45 rpm and 292 to 87 sec. Lower screw speed and higher residence time resulted in a fully exfoliated structure. Dennis et al.[20] observed from the experimental data that the best delamination and dispersion resulted in the medium shear mode of the extruder and in the non-intermeshing mode when they varied the shear from low to medium and high. However, with an increased shear, a point was reached where delamination and dispersion do not increase but got worse.

Other parameters such as processing temperature and feed rate also play an important role in obtaining an exfoliated structure. If the processing temperature is high, there is more chance of degradation of surfactants that exists before wetting of the clays in the matrix leading clay agglomeration. The processing temperature should be optimum to melt the resin and

consequently in mixing but should not be high enough to avoid the degradation of surfactant. If the feed rate is high, there is greater chance of forming a mass of clay as it experiences increased pressure in the extruder and thereby forms an agglomerated structure.

Vaia et al.[21] first studied the thermodynamics approach that is favorable to form intercalated structure in a nanocomposite. In polymer nanocomposites, when polymer penetration results in finite expansion of silicate layers, it forms intercalated nanocomposites. Vaia et al. considered the intercalation process as an incompressible system with a constant density of polymer and end-tethered chain segments. It is embedded in a bath of polymer melt where the interlayer is completely occupied with end-tethered surfactant chains. Polymer melt intercalates between the MLS, and the interlayer spacing increases forming an intercalated polymer-MLS hybrid. In a mean field context, the free energy change associated with the layer separation and the polymer melt penetration is separated into an internal energy change associated with the intermolecular interactions (ΔE) and an ideal combinational entropy change associated with the configurational change (ΔS). Therefore, the total change in Helmholtz free energy is

$$\Delta F = F(h) - F(h_0) = \Delta E - T\Delta S \qquad (2.1)$$

where T is absolute temperature. ΔF, change of free energy occurs during layer separation from an unintercalated interlayer of gallery height h_0 to an intercalated nanocomposite of interlayer of gallery height h. h_0 refers to single interlayer spacing of MLS. ΔF should be negative to facilitate the intercalation. The major factors that contribute to the free energy are the relative confinement of the polymer chain, the conformational changes of the tethered chains, and the establishment of new intermolecular interactions between the polymer, the tethered chains, and the silicate layer surface. The change in configurational entropy during nanocomposite formation is due to the

change in entropy associated with the MLS and the intercalated polymer. The change in entropy in polymer is due to the confinement of a polymer in the melt and interaction of the polymer and the surfactant. For the MLS, conformational changes arise from the reorganization of the silicate layers and the tethered surfactant molecules as the polymer penetrates. The silicate layers are large in the lateral dimension (~ 1 μm). Therefore, the translational entropy is relatively small and is neglected. Relative to the unintercalated state, the tethered chains gain substantial configurational freedom as the gallery height increases. Thus, the total ΔS is due to the entropy gain of the tethered chains in the interlayer and the entropy loss in confining an initially unconstrained polymer to a gallery of height h.

$$\Delta S \approx \Delta S^{chain} + \Delta S^{polymer} \tag{2.2}$$

ΔS of chain is due to the restricted freedom of the tethered chains arising from the ionic interactions with the silicate layer and the influence of the silicate surface on the conformational freedom of the tethered chains. ΔS of chain will depend on the surfactant and its interaction with MLS.

Vaia et al. described the mean-field model, which served as the first approximation to the polymer melt intercalation process. When the total change in the process is small, the small change in internal energy will determine whether the intercalation is thermodynamically possible. When surfactants are used, a favorable energy change is accentuated by maximizing the magnitude and number of favorable polymer-surface interactions while minimizing the magnitude and number of unfavorable apolar interactions between the polymer and the tethered surfactant chains, leading to the possibility of a well-dispersed structure.

2.1.4 Structure of Polymer Nanocomposites

Structure of nanocomposite refers to the nature of dispersion of MLS in the polymer matrix. In polymer nanocomposites, phase separated, intercalated or exfoliated structure can be obtained as shown in Figure 2.7. The type of structure that forms in the nanocomposite depends on the type of clay, surfactant, polymer matrix, and processing method. The dispersion is termed as immiscible when MLS platelets coagulate in the polymer matrix. An intercalated structure is formed when single or multiple polymer chains are intercalated between the silicate layers resulting in a well-ordered multilayer morphology built by alternating polymeric and inorganic layers. An intercalated structure results in finite expansion of intergallery spacing, but the long range order of the layered silicate is retained. The degree of intercalation depends on the method of preparation, the percentage of layered silicates and miscibility between the inorganic and the organic phase. When a high degree of interaction occurs between the charged silicates and the polymer, nano-scale dispersion is observed, and the resulting structure is called exfoliated or delaminated.

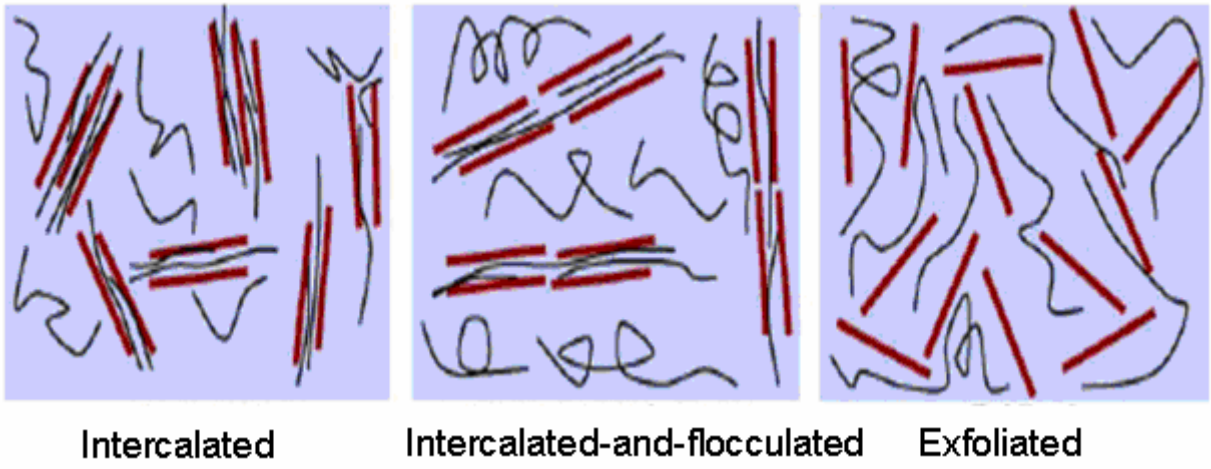

Figure 2.7: Different possible structures observed in polymer nanocomposites. [13]

2.2 Properties of Polymer Nanocomposites

The properties of nanocomposites are to a large extent, dependent on the degree of dispersion and dimension of the filler, among other factors. The most widely used filler is MLS, based on its susceptibility for potential interaction with polymers. The degree of dispersion of MLS depends on the interaction between MLS and MLS or between polymer and MLS. A completely dispersed system is preferred because it will provide more interfacial area, and therefore more interaction between MLS and the polymer. Barrier, crystallization, and the mechanical properties of polymers and their nanocomposites are reviewed because they are pertinent to this study.

2.2.1 Barrier Properties of Polymers

The permeability of a film is determined by the amount of gas that permeates through the film from one side to the other side. The permeability is characterized by the steady-state rate of the mass transport of permeant molecules through the polymer as shown in Figure 2.8. In a dense polymer, permeability, P, is defined as:

$$P = \frac{N_A L}{(P_2 - P_1)} \tag{2.3}$$

where N_A is molar flux of permeant, L is thickness of polymer, and P_1 and P_2 are the upstream and the downstream partial pressure, respectively.[22]

Permeability in a polymer is described by a solution-diffusion model. In a general way, permeability process can be decomposed into five successive stages. [23]

1. Diffusion through the limit layer of the side corresponding to the higher pressure side
2. Absorption of the gas in the polymer (by chemical affinity or by solubility)
3. Diffusion of gas inside the polymer

4. Desorption of the gas at the side of lower partial pressure
5. Diffusion through the limit layer of the down stream side

Therefore, in this process, the rate limiting step is diffusion through the film. In one dimension, the diffusion follows Fick's law:[24]

$$N_A = D\frac{dC}{dx} \tag{2.4}$$

where D is diffusion coefficient for the permeant in the polymer and dC/dx is local concentration gradient. When the permeant partial pressure in the downstream side and concentration are negligible relative to those on the upstream side i.e. p_2 is negligible then using equations (2.1) and (2.2), permeability can be expressed as

$$P = SD \tag{2.5}$$

where S is the solubility coefficient

and

$$S = \frac{C}{p} \tag{2.6}$$

where C is the equilibrium permeant concentration in the polymer and p is the permeant partial pressure adjacent to the polymer surface. Here, S describes the dissolution of a permeant molecule into a polymer, D describes movement of the penetrant molecule inside the polymer and P describes the permeation of penetrant molecules through the polymer.

The diffusion process can be Fickian and non-Fickian. For Fickian diffusion-controlled kinetics of permeant transport in a film of thickness L, the time required to reach the steady state in the permeability experiment is

$$t_{ss} = \frac{L^2}{D} \tag{2.7}$$

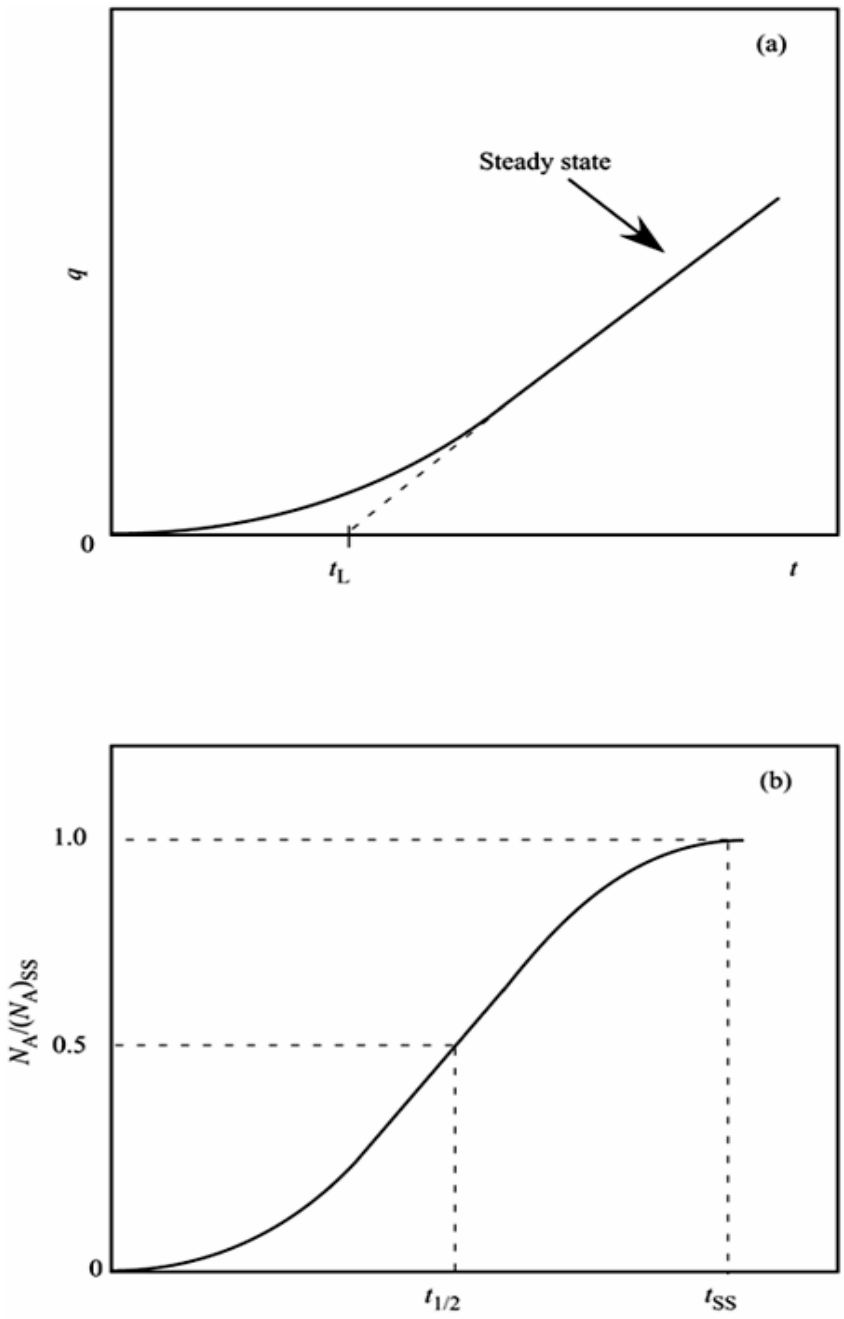

Figure 2.8: Mass of permeating permeant per unit film area (a) as a function of time (providing a measure of time lag t_L). (b) Normalized permeant flux (N_A) as a function of time (providing a measure of half time $t_{1/2}$). t_{SS} is the time required to achieve steady state.[9]

In the permeability graph in Figure 2.8, the non steady state explains the diffusion coefficient and the steady state explains the solubility coefficient. The temperature dependence of P, S, and D can be described as

$$S(T) = S_0 \exp\frac{-\Delta H_S}{RT} \tag{2.8}$$

$$D(T) = D_0 \exp\frac{-E_D}{RT} \tag{2.9}$$

$$P(T) = P_0 \exp\frac{-E_P}{RT} \tag{2.10}$$

where ΔH_S is molar heat of sorption, E_D is the activation energy of diffusion, and E_P is the apparent activation energy for diffusion. T is absolute temperature. R is molar gas constant. S_0, D_0, and P_0 are the solubility, diffusivity and permeability at room temperature, respectively. Since P = SD, therefore

$$P_0 = S_0 D_0 \tag{2.11}$$

$$E_p = \Delta H_S + E_D \tag{2.12}$$

The effect of temperature on permeability and diffusivity is studied by Polykova et al.[25] They measured the permeability in the MOCON OXTRAN permeability measurement system at 25 ºC, 1 atmosphere pressure and 0 % relative humidity. They observed a decrease in permeability and diffusivity with an increase in temperature in PET, PEN and PEI (poly (ethylene isophthalate)). With an increase in temperature, permeability, solubility and diffusivity increased and this is self explanatory from equations (2.8-2.10). Polykova et al. calculated activation energy for permeability from equation (2.10) to be 30 kJ mol^{-1}.

The solubility in polymer can be explained in terms of thermodynamic parameters such as Gibbs' free energy. If ΔG is the change in Gibb's free energy in the solubility process at constant temperature and pressure, then

$$\Delta G = \Delta H - T\Delta S \tag{2.13}$$

where ΔH is the change in enthalpy, T is the absolute temperature at which the process is carried out, and ΔS is the change in entropy in the process. If ΔG is more negative than ΔH, the process is the thermodynamically stable. For ΔG to be negative, T and ΔS should be positive. A larger positive ΔH means that the polymer and the solvent are not miscible and that they do not interact with each other. A negative ΔH means that the solvent and polymer are soluble and that a solution can be formed. Whether a solvent and a solute can be dissolved or not can also be determined from solubility parameters. In this study, a solute is a polymer and a solvent could be any gas such as oxygen, carbon dioxide and water vapor or liquid. The change in internal energy, ΔE, during the process is given by

$$\Delta E = \Phi_1 \Phi_2 (\delta_1 - \delta_2)^2 \left(\frac{cal}{cm^3 solution} \right) \tag{2.14}$$

where Φ is volume fraction

δ is solubility parameters.

The subscripts 1 and 2 refer to polymer (solute) and solvent, respectively. δ is related to cohesive energy density (CED), which is explained later in this chapter.

$$\delta = (CED)^{1/2} \tag{2.15}$$

$(\delta_1-\delta_2)^2$ is always positive because of square term. For ΔE to be negative, $(\delta_1-\delta_2)$ has to be as low as possible and the difference in solubility parameter should be less than 0.5. [26] The δ of polymer is determined by soaking lightly crosslinked polymer in a series of solvents of

known δ. The value of the solvent at which maximum swelling is observed is taken as the δ of the polymer.

The solubility parameter, δ, of PET and water is about 16 and 48 $MPa^{1/2}$, respectively. The water absorption in PET is 60 ppm at 25 ºC, when the water activity is 0.5. Water activity, A_w describes the amount of water available for hydration of materials. A value of 1 indicates pure water, and zero indicates an absence of "free" water molecules. The larger is the difference in the solubility parameter between the polymer and water, the lower the water sorption. Auras et al.[27] studied diffusivity, solubility, and permeability in PET, determined by isostatic method at 1 and 0.21 atmosphere of pressure at three different temperatures (5, 23, and 40 ºC), and A_w values of 0, 0.3, 0.6, and 0.9. They determined the permeability from the experiment. Diffusivity is determined by the half sorption time method using the equation (2.16). By knowing permeability and diffusivity, solubility (S=P/D) determined.

$$D = \frac{l^2}{7.199 t_{0.5}} \tag{2.16}$$

Figure 2.9 shows the permeability vs. water activity at different temperatures. The oxygen permeability tends to decrease as A_w in the oxygen stream increases. The opposite trend is observed in hydrophilic polymers. An increase in diffusivity is observed with an in increase in A_w as shown in Figure 2.10. This effect is more pronounced at 40 ºC compared to 5 and 23 ºC. Auras et al. attributed this increase of diffusivity with A_w to a plasticization effect of the amorphous phase in PET. This plasticization effect was confirmed with a decrease in T_g. Figure 2.11 shows the solubility coefficient as a function of A_w at different temperatures. An increase in solubility is observed with an increase in temperature and a decrease in A_w. Auras et al. explained the variation of solubility in terms of free volume. Solubility in PET is directly proportional to the free volume of amorphous matrix. [28] When A_w is increased, the amount of

water absorbed is increased and the solubility of oxygen is decreased. Since the free volume is first filled with water, an increase in diffusivity and a decrease in solubility are observed.

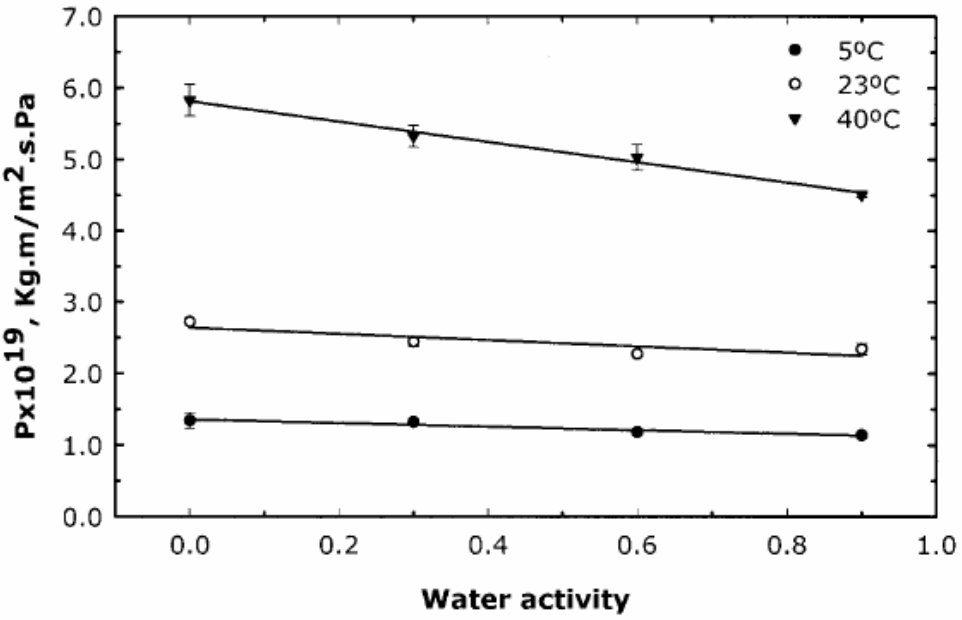

Figure 2.9: Oxygen permeability in PET vs. A_w at 5, 23, and 40 ºC.[27]

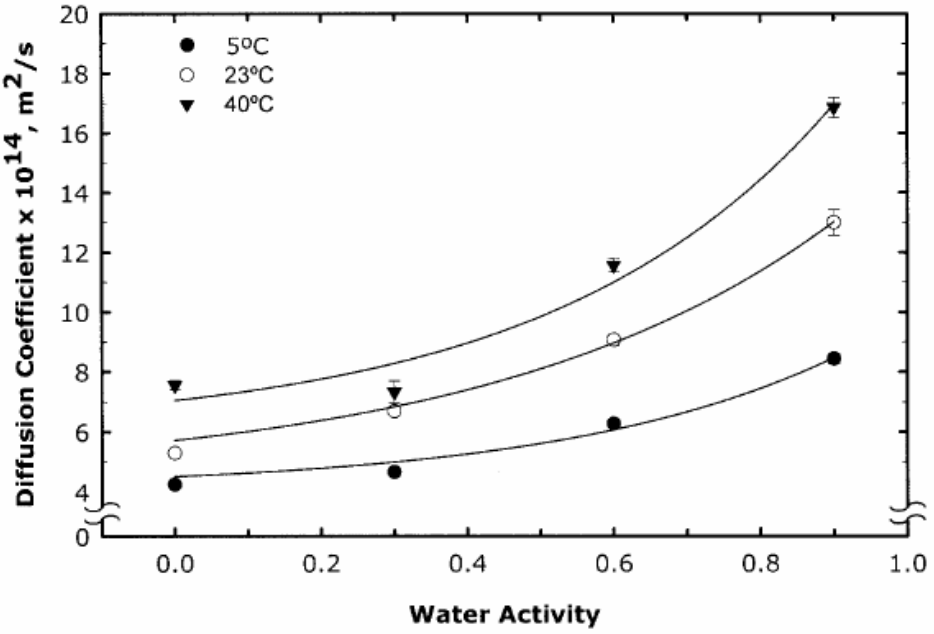

Figure 2.10: Diffusion coefficient in PET as a function of A_w.[27]

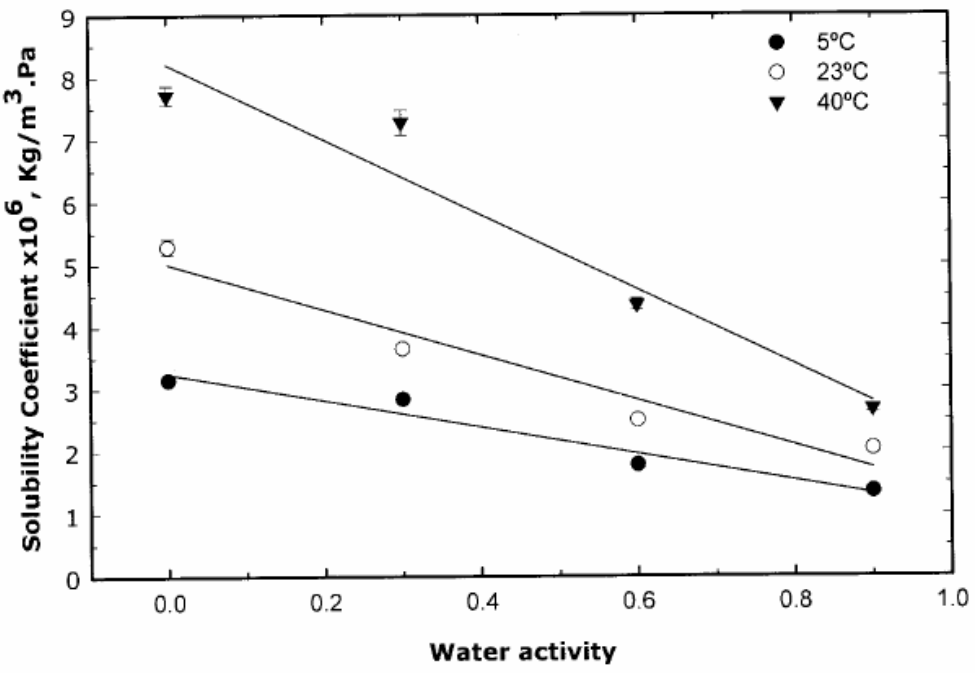

Figure 2.11: Solubility coefficient in PET as a function of A_w.[27]

Gavara et al.[29] studied the effect of water on the oxygen permeability in nylon 6 films. They observed that oxygen permeability first decreases and then increases with an increase in A_w as shown in Figure 2.12. They explained the result in terms of a bimodal diffusion mechanism. The bimodal mechanism is referred to as fast and slow. The total permeability was expressed as a linear combination of these two mechanisms ($P= P_{fast}+P_{slow}$). By using bimodal mechanism, Gavara et al. calculated the diffusivity in both mechanisms. They did not observe any significant change in diffusivity with water activity. However, the effect of temperature on the permeability was controlled mostly by the effect that temperature had on diffusivity. They assumed that oxygen molecules permeated by the slow mechanism interact with the active sites in the polymer matrix. At a very low A_w, water molecules are mainly chemisorbed in active sites due to the adsorption process. The phenomena of molecular competition between water and oxygen for these active sites are responsible for the depression of solubility of oxygen in the range of

$0<A_w<0.5$. Understanding how diffusivity and solubility affects the permeability, the different factors that affect the permeability is explained in the following section.

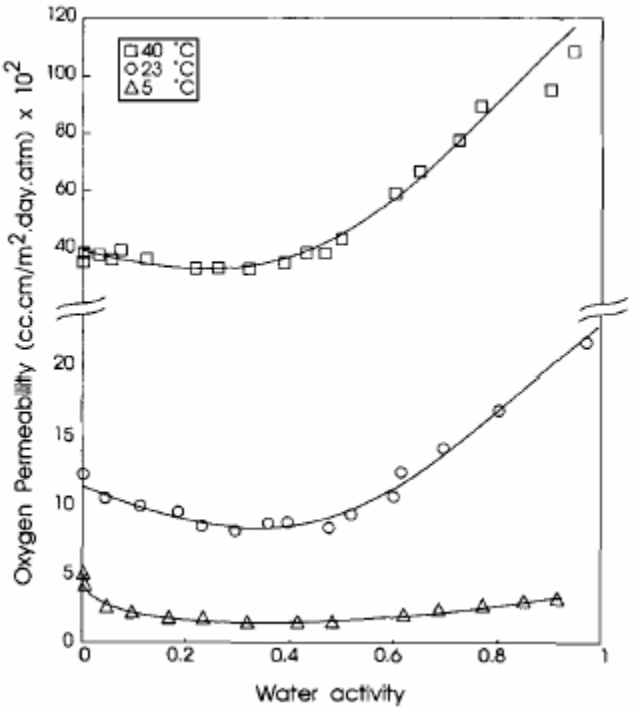

Figure 2.12: Total oxygen permeability in Nylon 6 as a function of water activity.[29]

2.2.1.1 Factors Affecting the Permeability

As permeability is governed by both the solubility and the diffusivity, the factors that affect either solubility and/or diffusivity will affect the permeability. The different factors that affect the permeability in polymers are[30,31]

Density: Structure, cross linking, co-polymerization, crystallinity, free volume, orientation, and density (all these affect the density in the polymer)

Environment: temperature and humidity

Nature of the gas molecule: size of the gas molecules and their chemical nature

2.2.1.1.1 Structure and Nature of Polymers

Permeability is dependent on the structure of the polymer as both the solubility and the diffusivity will be different for different polymer structures. The permeability of semicrystalline polymers will always be less than the permeability of amorphous polymers. It is due to the low density of the amorphous phase compared to the crystalline phase. When the structure of the polymer is further probed, the factors that affect the permeability are polarity, unsaturation, symmetry, lateral chains, steric hindrance, crosslinking, hydrogen bonding and intermolecular forces.[32] Segmental chain mobility, the degree of packing, polymer cohesive energy (i.e., chain stiffness) and, the crystallinity will affect diffusivity.

- Chain interaction can be quantified by cohesive energy density (CED). The higher the CED, the higher the activation energy of diffusion: therefore, diffusivity decreases.
- If there is any polar group in or on the chain, chain rigidity increases and the motion of the polymer segment decreases. Polymer segmental motion is the rate controlling step in permeant diffusion. The rate limiting step for permeant diffusion is the creation of transient gaps in the polymer matrix via local scale polymer segmental dynamics involving several polymer chains.
- Polymers with higher unsaturation have a higher diffusion coefficient due to chain flexibility. The presence of polar-side chains cause an increase in cohesive energy and activation energy for diffusion, leading to a decrease in diffusion.

The higher the T_g, the lower the chain mobility, and the higher the activation energy of diffusion, leading to a decrease in the permeability. The addition of plasticizers might change the macromolecular chain arrangement. Plasticizers will increase the chain mobility and thereby increase the diffusivity. The plasticizing molecules also have their own diffusion. The average

molecular weight of the polymer does not seem to affect solubility, diffusivity, and permeability except for the very low values of molecular weight, where the chain ends have significant influence on free volume.

2.2.1.1.2 Crystallinity, Free Volume, Orientation, and Density

The different factors that affect permeability such as crystallinity, free volume, orientation, and density are interrelated. Crystallinity plays an important role in the barrier properties of polymers. Permeability in semicrystalline polymer is decreased for two reasons. The crystalline region is impermeable to gases and moisture and increases the tortuosity path for the permeant gas molecule. Therefore, it facilitates a decrease in the diffusion coefficient. The presence of a crystalline region decreases the total amorphous region in the polymer. This phenomenon decreases the solubility of the permeant gas molecule. Therefore permeability decreases as both diffusivity and solubility decreases.[33]

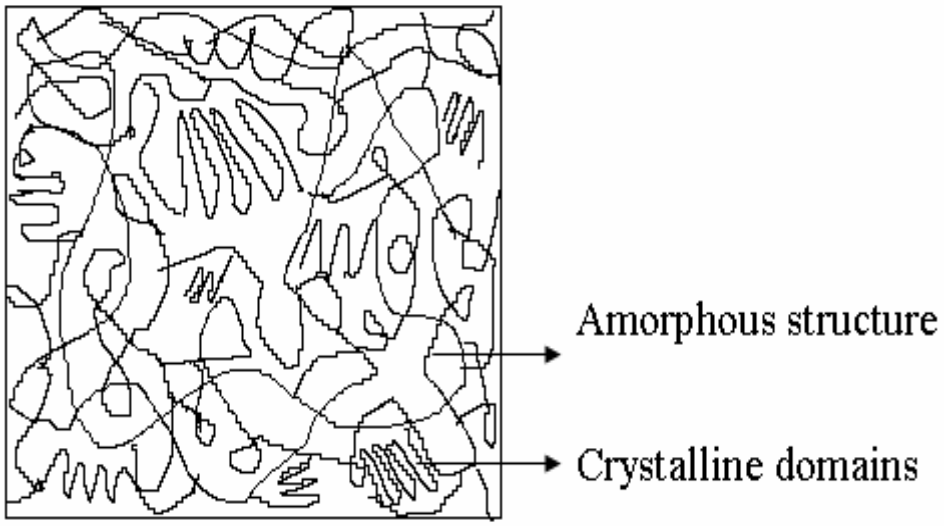

Figure 2.13: Polymer with crystalline and amorphous structure.

A typical structure showing the crystalline and amorphous region in a polymer is shown in Figure 2.13. As can be seen, some of the chains are folded and some are entangled. Being the crystalline region denser; is impermeable to gases. As seen in Figure 2.14, increasing the fraction of the amorphous phase leads to a decrease in permeability in PE at room temperature for CO_2, O_2, and N_2.

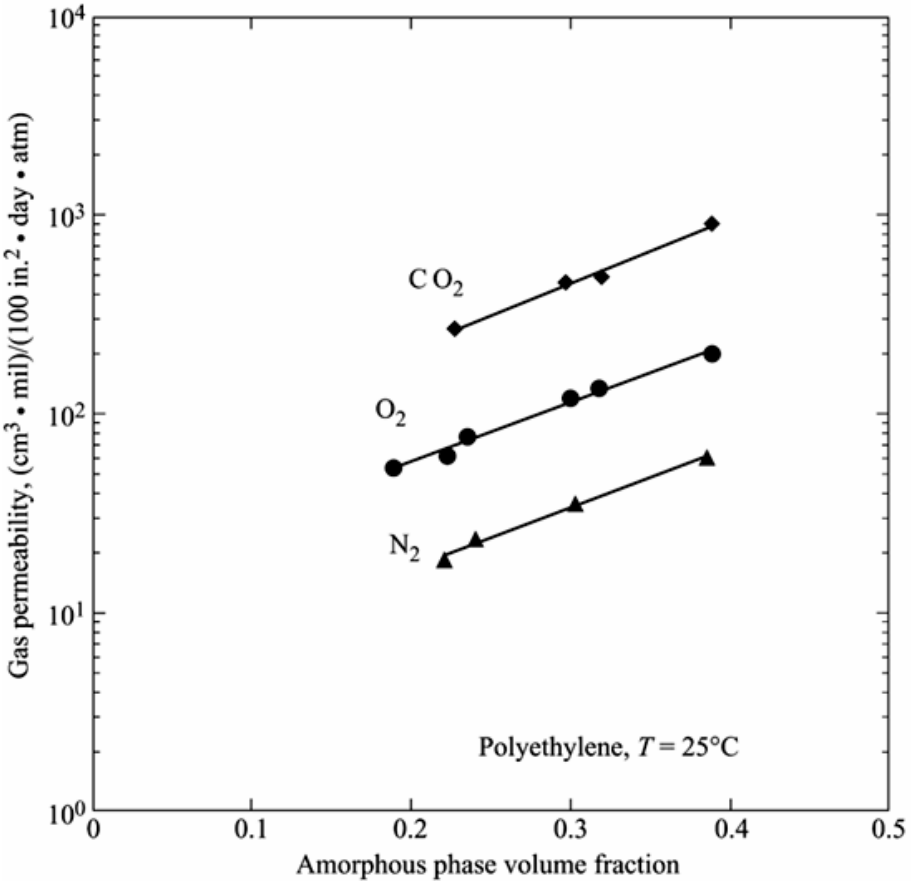

Figure 2.14: Effect of amorphous volume fraction on oxygen permeability.[9]

A decrease in solubility is not directly proportional to the crystallinity.[34, 35] Solubility is not usually affected by crystallite size, shape, and orientation. However, diffusivity is affected and it can be expressed as

$$D = \frac{D_a}{\beta\tau} \tag{2.17}$$

where D_a is the diffusion in the amorphous layer and ζ is the tortuosity factor which is defined as the distance traveled by a permeant molecule to the thickness of the sample. This is a complex function of crystallite content as well as size of crystallite and β is the chain immobilization factor.[36] If a two phase model is used (i.e., only the amorphous and crystalline phase are considered), then

$$S = S_a X_a \tag{2.18}$$

where S_a is solubility in the amorphous region and X_a is the amorphous volume fraction. This model assumes that solubility in the crystalline region is zero and the presence of crystallites does not change the solubility in the amorphous phase. However, in most cases, there are more than just two phases. The amorphous region itself is of two types: rigid amorphous fraction (RAF) and mobile amorphous fraction (MAF). The RAF generally exists in the crystalline structure of the lamella stacks, the regions where the crystalline lamellas are separated by very thin (20-40 Å) amorphous layers. On the other hand, the MAF regions are associated with the interstack amorphous region and contribute to the glass transition.

Lin et al.[37] observed that RAF in semicrystalline polymers, such as PET, do not show separate T_g in the entire range up to the melting region. They also suggested that RAF in PET become effectively vitrified upon cooling, while rest of the amorphous chains located between the lamella stacks continue to be in the melt state though it is below that. Therefore, the crystallization temperature, T_c has to be considered as an effective vitrification temperature for RAF. Figure 2.15 explains this point. Vitrification of amorphous polymers is associated with the formation of excess-hole free volume packing defects due to drastic restriction of macromolecular segmental ability. Due to these defects the solubility increases even when crystallinity increases.

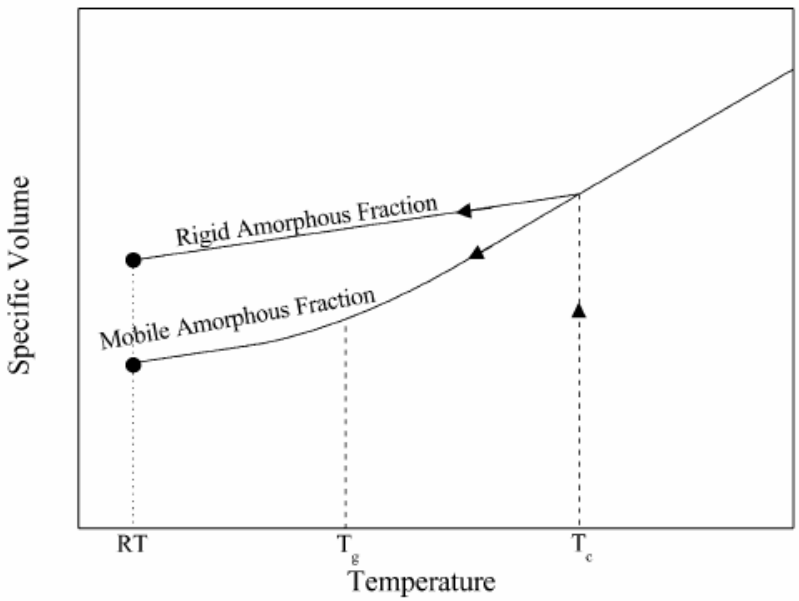

Figure 2.15: Schematic plot of specific volume as a function of temperature for rigid and MAFs.[37]

An increase in crystallinity leads to a decrease in the free volume in polymer. Free volume is the fraction of volume available in a polymer to assist permeation of permeant. The more the free volume the higher is the permeability as the permeants get more space to diffuse through it. With a decrease in fractional free volume (FFV), the permeability decreases as shown in Figure 2.16. The dependence of permeability on free volume in a cold drawn polyesters was studied by Liu et al.[38] They found that orientation of the glassy state decreases the excess-hole free volume. On the other hand, crystallization during orientation often leads to the dedensification of the amorphous phase, thereby increasing excess-hole free volume. Gas permeation depends on the number and size of holes (cavities) in the polymer matrix. This is related to static free volume and the frequency of channel formation, which is related to dynamic free volume. Since solubility and diffusivity determines the permeability, the free volume concept is important as solubility is affected by static free volume and diffusivity is affected by dynamic free volume. The relation between diffusivity and free volume is presented in equation (2.19).

$$D = A\exp\left(\frac{-B}{FFV}\right) \tag{2.19}$$

where A and B are empirical constants.

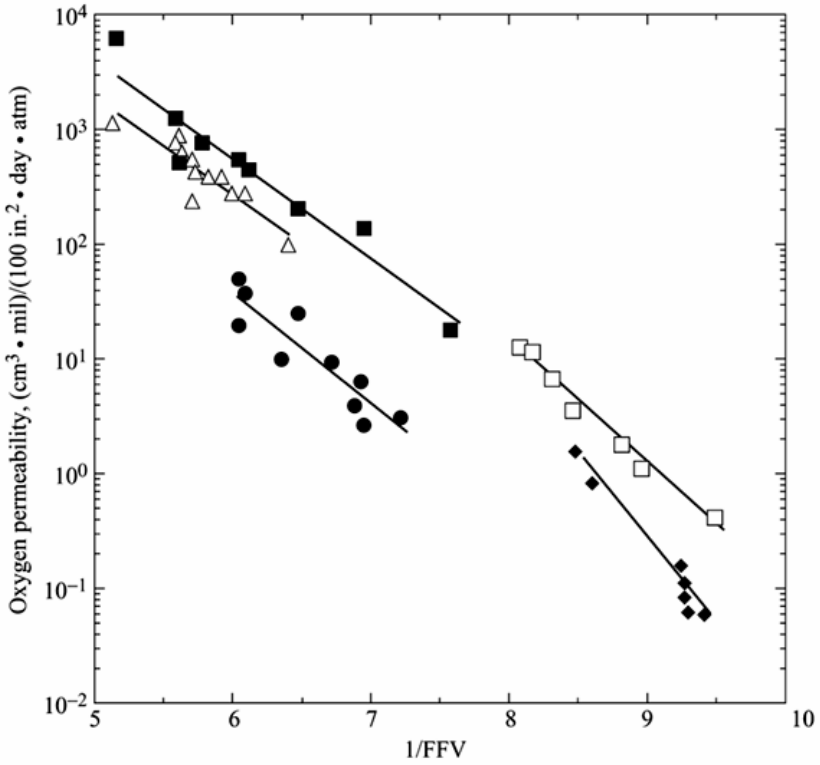

Figure 2.16: Correlation of oxygen permeability with polymer fractional free volume for several families of amorphous, glassy, and liquid crystalline polymers (■) Polystyrene (35°C), (Δ) polycarbonates (35°C), (●)polyesters (30°C), (□)polyamides (25°C), (♦) liquid crystalline polymers (35°C). [9]

The free volume of a polymer is affected in various ways. Interaction between polymer chains can lead to tighter packing of polymer molecules (i.e., less free volume), and can restrict segmental motion (i.e., less dynamic free volume). Increasing polarity, hydrogen bonding, and crystallinity reduce segmental mobility and thereby decrease the free volume. Consequently, there is an increase in the barrier ability of polymers. In many glassy polymers, free volume is

also affected by the processing. Higher cooling rates create higher free volume. The presence of polar groups with low specific volume can reduce the free volume, and thereby the permeability.

Orientation of the polymer chains also has a significant effect on permeability. If the chains are oriented, they act as a tortuous path for the permeant leading to a decrease in permeability. McGonigle et al.[39] observed that the permeability decreases in biaxially drawn films of PET and PEN. They attributed the decrease in permeability to the disentanglement and alignment of the chains, reorientation effects, higher degree of packing, and decrease in the free volume fraction of the amorphous phase. During the orientation in semicrystalline polymers, crystallites get oriented. Drawing can also increase the stress induced crystallization, thereby decreasing the permeability. Effect of drawing ratio on permeability is shown in Figure 2.17. With the increase in draw ratio, the permeability decreases. Orientation of PET without crystallization increases the density of amorphous phase therefore decreasing the permeability. If there is any crystallization then it dedensifies the amorphous phase leading to a decrease in permeability.[40]

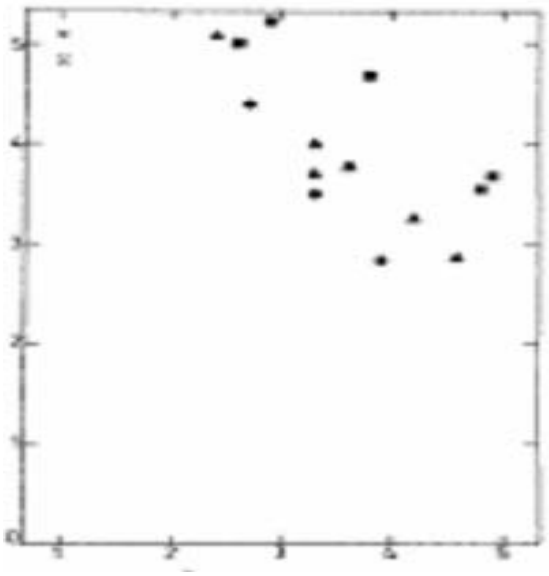

Figure 2.17: Effect of draw ratio (X-axis) on Permeability (Y-Axis). [9]

As permeability is affected by both solubility and diffusivity and studied in detail by Liu et al. They used oxygen permeability to understand the thermodynamics (solubility) and the kinetics (diffusivity). At low pressure, gas permeability is due to a "jumping" process whereby a permeant molecule spends most of the time in free volume holes and occasionally jumps into a neighboring hole by formation of a connecting channel. Gas solubility measures the amount of free volume where as diffusion measures the frequency of channel formation. Orientation increases the amorphous density due to the transformation of some gauche to trans configuration. On the other hand, crystallization decreases the amorphous phase density due to constraint on amorphous chain segments attached to chain segments in the crystals.

With the increase in density, permeability decreases. It is due to the decrease in free volume in the polymer. The increase in density could be due to an increase in crystallinity and/or higher crosslinking in the material which will eventually decrease solubility and diffusion, and therefore, permeability. The relation between the density and permeability is studied by Shah et al.[41] They observed that permeability decreases with an increase in density in ultra low density

poly ethylene as shown in Figure 2.18. They correlated further effect due to temperature change. Hu et al. studied the effect of crystallinity on permeability. They observed that permeability decreases with increase of crystallinity as shown in Figure 2.19 and attributed to increase of density with increase of crystallinity.

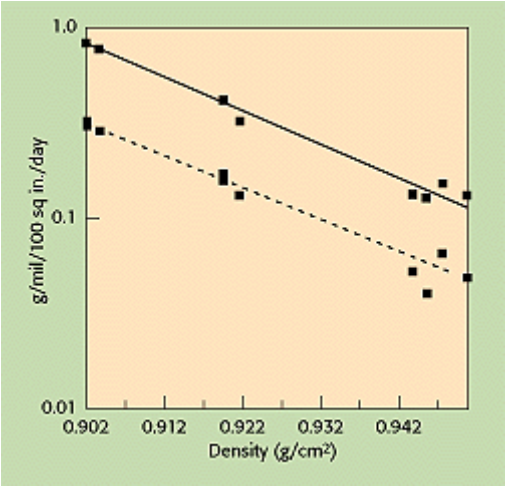

Figure 2.18: Water-vapor transmission rate vs. density for PE at 30 °C and 40°C. [41]

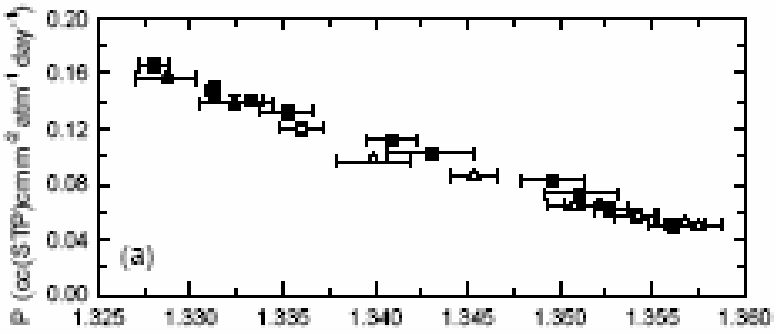

Figure 2.19: Effect of crystallinity as density on oxygen permeability in PEN. [42]

2.2.1.1.3 Humidity and Temperature

Along with different properties in the polymer, environment plays an important role in determining the permeability. Water-polymer interaction plays a significant role in the general properties and aging of polymer. The presence of water in a polymer matrix may change the way

that gas is adsorbed and diffused through the polymer.[43] The absorption of water can increase, decrease or have no effect on gas permeability. In some polymers, water acts as a plasticizer and increases the free volume in the polymer. Water vapor permeability is increased with an increase in relative humidity as observed by Tak et al.[44] However, in some amorphous polyamides and PET, with an increase in moisture leads to a decrease in permeability. The possible reason could be water occupies the free volume sites in the polymer, which lead to decrease in permeability.

Temperature also affects the permeability. The higher the temperature, the higher the permeability in the polymer. This occurs because diffusivity increases with temperature.

2.2.1.1.4 Nature of Permeant

The size and nature of the gas molecules play an important role on diffusivity. For larger gas molecules, larger free volume is necessary to diffuse. Numerous correlations suggest that diffusivity is proportional to r^{-n} where r is radius of the gas molecule. Other than the above factors, T_g, molecular weight and plasticizers also affect permeability.

Permeability of different polymers from literature is reported in Table 2.4. Though the permeability of Nylon 6, PET and PEN are lower than some of the thermoplastic polymers as reported in Table 2.4, it is not low enough for some applications such as wine packaging and substrates for flexible display. In this study the possible techniques for improving the barrier property is probed by lowering the gas permeability and two of the techniques are implemented and studied in detail.

Table 2.4: Reported permeability values of polymers

Sample	Oxygen Permeability (Source unit)	Permeability (Normalized unit) (cc/m.sec.torr)
PET	10-30 (10^{16} cm^3(STP).cm/cm^2/s/Pa)[45]	1.32-3.95X10^{11}
PET/EVOH blends	1.7-850 (10^{16} cm^3(STP).cm/cm^2/s/Pa)	6.7X10^{11}
PET (12 μm thick)	140 (cm^3/m^2/day)[46]	2.56X10^{11}
Isotropic PET	1.6E4 (10^{-18} mol/(cm.Sec.Atmo))[47]	4.71X10^{11}
Oriented PET	2.75-5.24 (cm^3(STP)/cm/cm^2/s/cm Hg)[48]	5.4X10^{13}
PET (13 μm thick)	3E-9 (cm^3(STP)/m^2/s/cm Hg)[49]	2.4X10^{13}
PET (25% crystalline)	4.8 cc.mil/100 in^2/day/atom	1.07X10^{11}
Nylon 6	0.61-0.71 cc.mm/m^2/day/atom	3.96X10^{13}
Oriented Nylon 6	0.7 cc.mm/m^2/day/atom	1.56X10^{13}
Nylon 6	6.6 cc.mil/100 in^2/day/atom	6.91X10^{12}
Nylon-6, Biaxially oriented	2.6 cc.mil/100 in^2/day/atom	1.32X10^{11}
Polyamide 6	5-25 (10^{16} cm^3(STP)/cm/cm^2/s/Pa	(3.05-30)X10^{11}
Polyamide 6/layered silicate nanocomposites	10 (10^{16} cm^3(STP)/cm/cm^2/s/Pa)	(1.52-7.61)X10^{11}
Polyimide-clay hybrid	2-20 (cc.mm/ m^2/day/Atmo)[50]	7.61X10^{12}
PET	1-5 (cc.mm/ m2/day/Atmo)[51]	(1.52-7.61)X10^{11}
PEN	0.5 (cc.mm/ m2/day/Atmo)	7.61X10^{12}

The possible techniques for improving the barrier property are:

1. Biaxial stretching: stretching of the film leads to chain orientation and decreases the permeability.
2. Annealing: it improves the crystallinity in polymer films. The higher the crystallinity, the lower the permeability.
3. Polymer Nanocomposites: expandable clay smectites creates a tortuous path in the polymer and therefore, decreases the permeability and also increases the time for permeation.
4. Multilayer processing: each layer has a different affinity for gases. By using different layers the permeability can be decreased.
5. Metal Deposition: very thin layer (~ 10-50 nm) of metal on polymer reduces the permeability by orders of magnitude. The decrease in permeability is governed by the quality of thin layer of metal. Ideal metal layer without any defects is impermeable to gas.
6. Inorganic deposition (Indium tin oxide, Al_xO_x, SiO_x): It functions similar to thin metal layer but the advantages of inorganic over metal is transparency.

This dissertation studies polymer nanocomposite in great detail as well as considers an overview of biaxial stretching of nylon and PET polymers.

2.2.1.1.5 Barrier Properties in Nanocomposites

An improvement in barrier properties is observed in different nanocomposites. Oxygen permeability is decreased with the addition of 5% MLS from 857 to 55 cc/m^2/day in PET.[52] These nanocomposites are processed by the direct polymerization with MLS supported catalyst. Ke et al.[53] also observed a decrease in permeability in PET nanocomposites. They synthesized

the nanocomposites by in situ polymerization. The composite was processed into a film by bi-axis orientation. Oxygen permeability decreased from 7.45 to 3.5 (cm^3 mm /m^2 d 0.1 MPa) with the addition of 3% MLS. PEN being relatively new material, barrier properties of PEN nanocomposites has not been reported in the literature to my knowledge.

A nanocomposite is a multiphase system in which the coexistence of phases with different permeabilities can cause complex transport phenomena.[54] It is to be noted that the polymer itself can be considered as a two phase crystalline-amorphous system, the crystalline regions being generally impermeable to the permeants. Permeability of nanocomposites with MLS content is conventionally explained within the concept of tortuous path.[55]

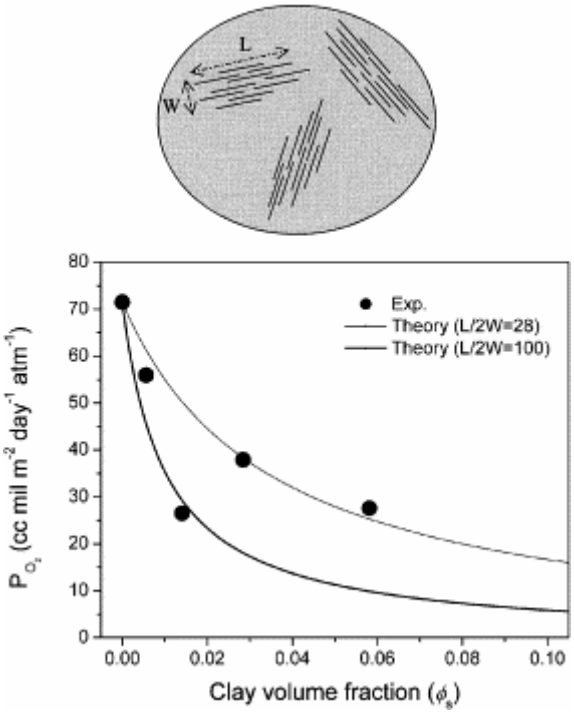

Figure 2.20: Oxygen permeability of the crosslinked polyester–clay nanocomposites as a function of clay volume fraction at 40 °C and 90% relative humidity.[58]

As the volume fraction of the clay increases, the permeability decreases as shown in Figure 2.20. This is due to an increased tortuous path with the addition of MLS. Figures 2.21and

2.22 explain the same analogy. Dispersion of clay is an important parameter in improving the barrier properties of polymers by lowering their permeability. Figure 2.23 explains the dispersion of the clay in the matrix. If clay platelets are exfoliated in the matrix, there is more interaction between the clay-matrix. However, if the clays are aggregated, the interfacial area decreases. This decrease in the permeability is low as compared to a completely exfoliated system. The aspect ratio of the clay is another important parameter, as higher the aspect ratio higher the interaction between the polymer and the MLS. The most important is higher tortuous path, therefore, lower permeability can be observed as shown in Figure 2.23.

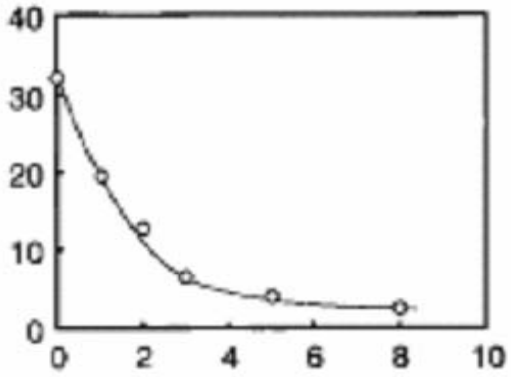

Figure 2.21: Oxygen Permeability (cc-mm/(m^2.day. atmo) as a function of MLS content in Polyimide-MLS hybrid.[1]

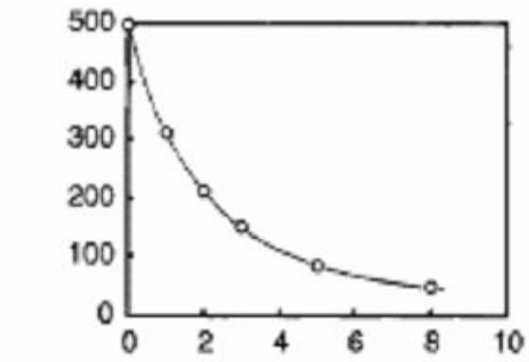

Figure 2.22: Helium Permeability (cc-mm/(m^2.day. atmo) as a function of MLS content in Polyimide-MLS hybrid.[1]

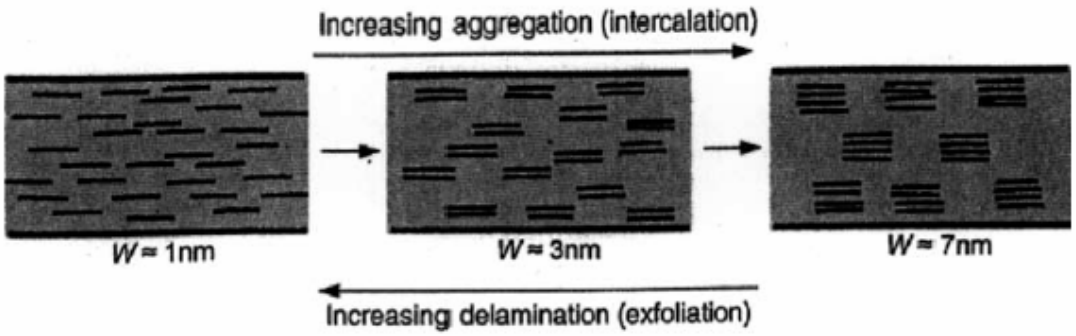

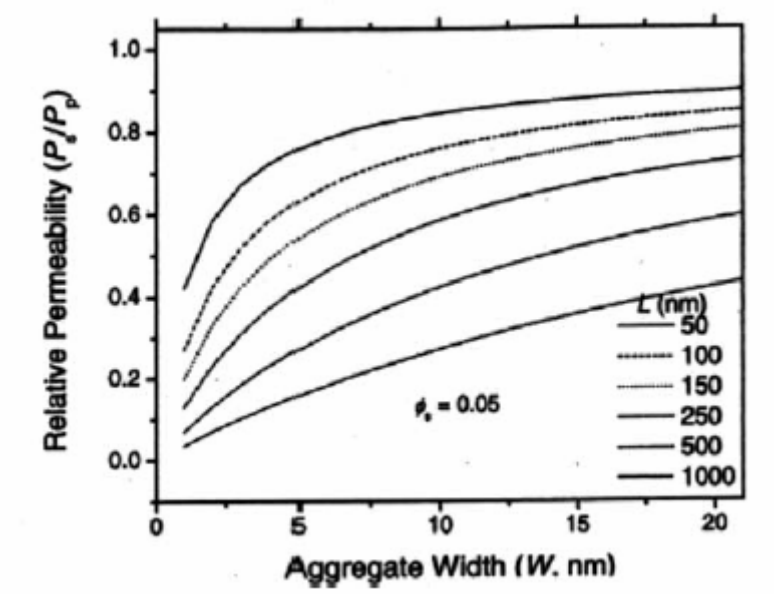

Figure 2.23: Effect of incomplete exfoliation on the relative permeability. (a)The illustrations show the effect of having one, two, and four sheet aggregates dispersed throughout the matrix. (b) The relative permeability as a function of the aggregate width at several different lengths of the sheets at φ_s 0:05.[13]

Table 2.5 summarizes the reported permeability in nanocomposites with different types of filler and weight percentage compared with pure polymer from literature.

Table 2.5: Comparison of reported permeability of polymers and their nanocomposites showing the effect of crystallinity, orientation, and MLS.

Sample	% clay	Oxygen Permeability (Source unit)	Processing method
Aromatic Nylon MXD-6[56]		$0.0518X10^{14}$ (cm^3cm/cm^2 S pa)	Extrusion cast
		$0.0547X10^{14}$ (cm^3cm/cm^2 S pa)	Biaxially oriented (2X2)
Amorphous nylon celar PA 3426		$0.19X10^{14}$ (cm^3cm/cm^2 S pa)	Extrusion cast
		$0.16X10^{14}$ (cm^3cm/cm^2 S pa)	Uniaxially oriented (2X)
		$0.14X10^{14}$ (cm^3cm/cm^2 S pa)	Biaxially oriented (2.5X2.5)
HDPE (X_c=0.6)		$41.25X10^{14}$ (cm^3cm/cm^2 S pa)	
HDPE (X_c=0.69)		$15.75X10^{14}$ (cm^3cm/cm^2 S pa)	
HDPE (X_c=0.78)		$8.25X10^{14}$ (cm^3cm/cm^2 S pa)	
HDPE (X_c=0.81)		$7.95X10^{14}$ (cm^3cm/cm^2 S pa)	
PETN[57]	0	$6.6X10^{11}$(cc/cm^2.sec.cm.Hg)	Melt intercalation-compression molding
	2 (Cloisite 30B)	$3.2X10^{11}$(cc/cm^2.sec.cm.Hg)	
	4	$3.6X10^{11}$(cc/cm^2.sec.cm.Hg)	
	6	$2.9X10^{11}$(cc/cm^2.sec.cm.Hg)	
Crosslinked polyester[58]	0.006 vol % (Cloisite 30B)	~55 ($cc.mil/m^2$.d.atm)	
	0.03 vol%	~38 ($cc.mil/m^2$.d.atm)	
		~28 ($cc.mil/m^2$.d.atm)	
PLA[59]	0	777 (cc/m^2.day)	Solution mixing
	4 (C_{16}-MLS)	449(cc/m^2.day)	
	6	340(cc/m^2.day)	
	10	327 (cc/m^2.day)	
	4 DTA-MLS	455 (cc/m^2.day)	
	6	353 (cc/m^2.day)	
	10	330 (cc/m^2.day)	
	6 (Cloisite 25A)	430 (cc/m^2.day)	
	10	340 (cc/m^2.day)	
PCL [60]		3.1 Barrer	
	PCL/(MLS-Na)	2.62 Barrer	Melt blending
	PCL/(MLS-$(OH)_2$)	1.62Barrer	Melt blending
	PCL/(MLS-$(OH)_3$)	1.12Barrer	In situ polymerization

where, C16-MLS is hexadecylamine-montmorillonite and

DTA-MLS is dodecyltrimethyl ammonium bromide-montmorillonite

2.2.1.1.6 Barrier Properties in Multilayered Structure

The addition of MLS in polymers improves their permeability. The improvement in barrier property depends on several parameters as explained before. However, it does not meet the requirement of polymer materials to be used as a substrate for flexible display. Therefore, developing multilayered structures is needed to have the required barrier properties for such applications. In the multilayered structure, a combination of both organic and inorganic different thin layers can be deposited and different layers will have different affinity for the gas. The ideal inorganic layer is impermeable to any gas. However, there are always some defects associated with deposition. To achieve a satisfactory coating on polymer substrates several problems must be identified and solved. The micro structural and gas barrier properties of the polymers and transparent oxide layers deposited on polymer substrate are of great importance to the food packaging industries and flat panel display industries and are previously studied in detail. The important properties that have to be considered for this kind of application are explained in the following Figure 2.24.

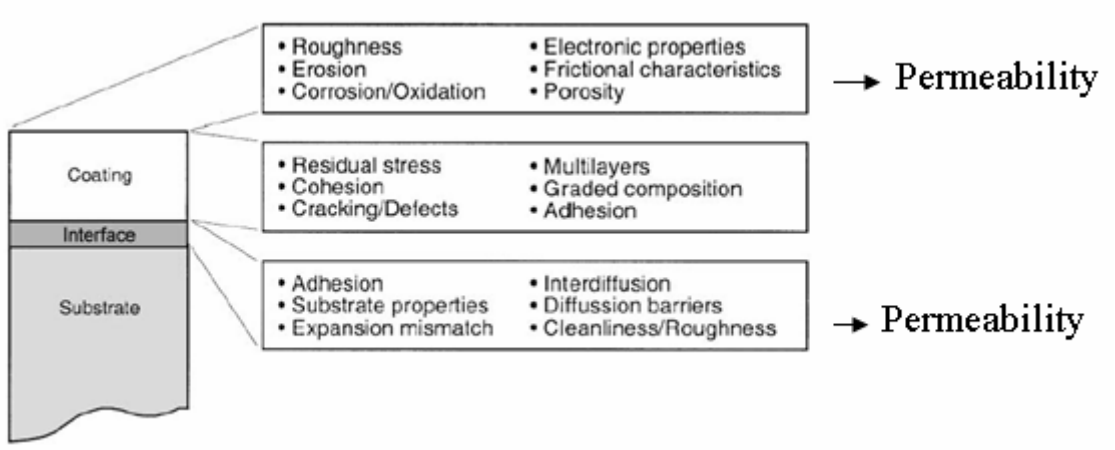

Figure 2.24: Important coating/substrate properties for technological applications.[61]

Different factors that affect the permeability in a multilayered structure in a coated polymer film are

- Thickness of the coating
- Density of coating
- Density, distribution, and size of defects

The permeability of polymer and with different types of coating is reported in Table 2.6.

Table 2.6: Oxygen permeability of polymers and multiphase polymer systems.

Polymer Coating Permeability	**PO_2 (10^{16} $cm^3.cm/cm^2/s/Pa$)**
PET/EVOH blends	5.1
Poly(ethylene terephthalate) (PET)---- Al<15nm React. Evaporation	0.15
SiN (PECVD)	0.15
ZnO (Reactive sputtering)	1.2
SiO_x 12nm (PECVD)	0.15
SiO_x (PECVD)	0.04
SiO_x70nm(Reactive evaporation)	0.3

Since polymeric substrates have a low melting temperature, the coating must be deposited or sputtered at lower temperature, which might result in low packing density and film porosity. [62] The thickness of the coating should be optimum to take care of defects and surface roughness in the substrate. Coating should be ideally free of defects and the microstructure should be dense to improve the barrier properties. Scanning Electron Microscopy (SEM) is used to study the microstructure of the film. During coating the thermal stresses might form from the difference between the coefficients of thermal expansion of the coating and the substrate. The intrinsic stresses are also induced in the deposit during growth and arose from sources such as impurity incorporation and structural reordering.[63] The stress on coating may cause delamination of the film. Therefore, the stress in the film should be as low as possible. Stress in the thin film can be found by radius of curvature method. In order to improve the coating durability, it is necessary to increase the bond strength between the substrate and the film. This can be achieved by modifying the substrate surface properties by ion bombardment. The interface properties of polymer and thin coating are generally studied to understand the adhesion. Permeability of the polymer film with a coating depends on thickness of coating as explained below.

Thickness of the coated film is one of the most important characteristics to tailor barrier properties and cost optimization. Reduced thickness down to a nanometer range is often

associated with growth heterogeneities and high residual stresses generated during the deposition process, whereas thicker film is prone to crack. Therefore, thickness of the film should be optimum which is clear from Figures 2.25 and 2.26.

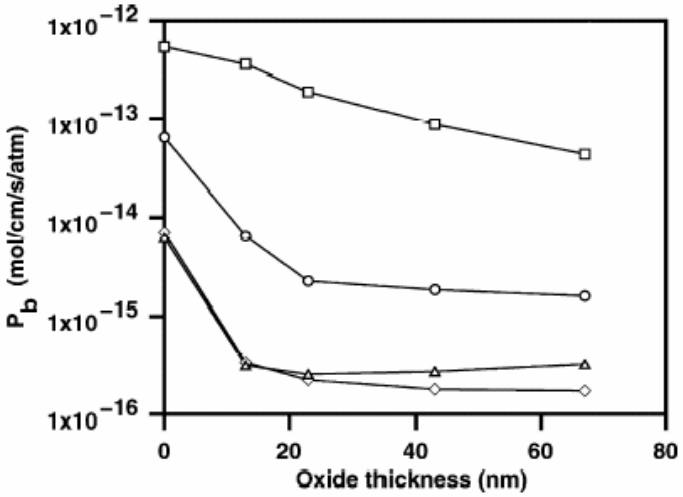

Figure 2.25: Barrier permeability as a function of oxide thickness and permeant species: helium (□), neon (○), argon (Δ) and oxygen (◊).[64]

The ideal coating will be completely impermeable to gases. However, there are always some defects in the coated inorganic layers. As the defect density in the coating increases, permeability decreases as shown in Figure 2.26. There are different types of defects such as macro, micro and nano defects. For oxygen permeation, it is believed that practically all the transport occurs through macro-defects[65], although for lower permeability films, some role has been attributed to the SiO_x layer.[66] Assuming the oxygen permeates chiefly in molecular form (since atoms would be subject to severe chemical constraints), the lattice and nano-defects are simply too small to allow significant transport.

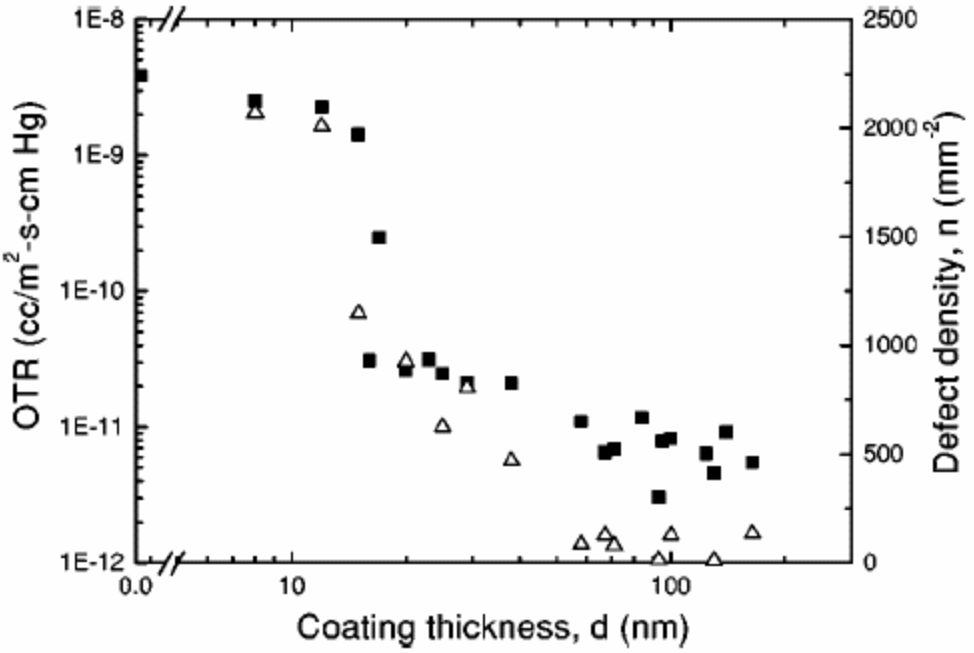

Figure 2.26: Defect density (Δ) and oxygen permeation rate OTR (□) plasma-deposited SiO_2 coating thickness, d, on PET. [67]

2.2.2 Effect of MLS on Crystallization

Crystallization in PET depends on molecular weight of PET, catalyst used, presence of nucleating agent, thermal history, the nature of the polymerization, and copolymer units.[68, 69] PET is characterized by a low degree of crystallinity and low crystallization rate.[70] This slow crystallization rate can be used to improve the optical clarity of the material. For highly barrier application large crystalline fraction in polymer is preferred as with the increase in crystalline fraction, barrier properties will be improved. The improvement will depend on their structure, size, and distribution. The crystallization in PET is temperature dependent and the maximum rate of crystallization is found in the range of 150 to 180 ^{o}C.

In DSC, there is one reference pan and one sample pan and both of them are heated at a constant heating rate. The change in the heat flow or the specific heat of a sample with

temperature with respect to reference plan is measured. The specific heat of a material changes when there is any physical transition such as glass transition, crystallization and melting.. Glass transition is defined as the temperature at which the material changes from the glassy state to rubber state. Glassy state refers to relatively hard and brittle while rubbery state refers to elastic and flexible. It is observed by differential scanning calorimetry (DSC) as a stepped increase in the heat capacity of the sample during heating due to increase of molecular motion in the polymer. In semicrystalline polymer, glass transition (because of amorphous region) and melting temperature (because of the crystalline region) is observed. The melting peak and its width explain the size and the distribution of spherulites. Enthalpy of melting (ΔH) is used to determine the crystallinity in the film by dividing by the theoretical ΔH for 100% crystalline polymer of same material. Above the melting region no crystallites is observed.

$$\%X_c = \frac{\Delta H}{\Delta H_{theoretical}} X100 \tag{2.20}$$

In some of the polymer cold crystallization is also observed and it also depends on the processing history of the polymers. Polymer matrix consists of crystalline lamellae separated by amorphous phases. The crystalline lamellae consist of polymer chains. When the crystallization process is hindered, spherulites do not grow further leaving the interspherulite region more amorphous than the interlamellar region. Therefore, crystallization from interlamellar region is easier and undergoes crystallization and it is called cold crystallization.

Crystallization in PET has been widely studied. When a polymer is stretched above its T_g but well below its melting temperature, additional crystallization is induced and the crystalline structure will generally be aligned in the direction of extension. Therefore this orientation process improves the strength of the material. This is the basis for cold drawing processing of the synthetic industry. In 1978, USA consumption of PET for bottles was in the range of 68,000-

86,000 tones. In 1998, it increased to 1430,000 tones. Semicrystalline fibers and films of PET are also produced by applying strains above the glass transition region. This stretching process generates molecular orientation, which results in strain induced crystallization. The effect of biaxial stretching on crystallinity has been studied by Chandran et al. [71] They observed the changes in crystallinity and attributed to change of density. Interestingly they observed that samples stretched in sequential mode showed higher crystallinity, with evidence of strain induced crystallization, than those stretched in a simultaneous mode where no strain induced crystallization occurred. As the stretch ratio increases, the rate of crystallization increased with subsequent decrease in activation energy for crystallization.

Chang et al. carried out isothermal DSC followed by Avrami analysis to compare the crystallinity obtained by various fillers in a PET matrix. Nucleation was inhibited by the presence of fillers. Mobility of polymers in the melt was reduced due to the presence of these fillers. As the filler changed from carbon black, titanium dioxide, glass fiber and calcium carbonate, a decreased crystallization temperature, decreased crystallization half times, increased activation energy were observed.[72] The effect of MLS on spherulitic growth was also studied by Wan et al.[73] The PET+3%MLS nanocomposites were prepared via in situ polymerization. A partially exfoliated morphology was observed in the PET nanocomposites. They observed the presence of three dimensional irregular shaped crystallites in PET nanocomposites which were smaller than neat PET. Kennedy et al.[74] studied a syndiotactic PS-silica particle system. They observed increased rate of heterogeneous nucleation and decreased spherulite growth rate with the addition of silica particles. They associated the silica particle as a quasicrosslink which hinders diffusion of polymer segments. Wang et al.[75] studied the effect of MLS on the crystallization behavior in PET with varied concentration of MLS (1, 3, and 5 %). They observed

decrease in cold crystallization temperature (T_{cc}) and the maximum decrease is observed for PET+3% MLS. For pure PET, T_{cc} is 122 ºC and for PET+3% MLS nanocomposite it is 118 ºC. Melting temperature (T_m) also decreased from 257 to 252 ºC from pure PET to nanocomposite. It is due to MLS acted as nucleating agent, and the crystallite size decreased in nanocomposites and therefore melting point decreased. Ou et al.[76,77] also studied the effect of MLS on the crystallization in PET. They varied the concentration of MLS from 1 to 15%. Melting temperature decreased from 251 to 248 ºC with 15% addition of MLS. Melting temperature width increased from 55 to 64 ºC showing the higher crystallite size distribution. The crystallization temperature increased from 190 to 205 ºC. Maximum crystallization rate is observed with the addition of MLS till 10% MLS. Further addition of MLS did not increase the crystallization rate and showed the agglomeration of MLS. Ke et al.[78] found an increase in crystallization rate and smaller crystallite sizes on addition of MLS in PET. They prepared PET-MLS nanocomposites by an in-situ polymerization process. They used MLS content of 0.5, 1, 2, 3, and 5%. It was seen that the melting temperature decreased with the addition of MLS, with 5% PET nanocomposites showing a maximum decreased melting temperature of 7^{o}C. Wan et al.[79] reported the presence of three-dimensional irregular shaped crystallites in PET nanocomposites that were smaller than neat PET. Dixon et al.[80] also observed decrease in spherulite size in nanocomposites. They observed the size of spherulite in pure PET is in the range of 20 to 50 microns, which decreased to 1 to 10 microns on addition of 0.5 wt% of talc. Pendse et al.[81] has studied the effect of MLS in the PET, the same PET that is used in this study. These PET nanocomposites are processed by extrusion method with varied concentration of MLS from 1 to 5 %. With the addition of MLS in PET smaller non uniform spherulites is observed from polarized optical microscopy in nanocomposites compared to pure PET. To explain the non

uniformity in spherulite sizes in PET nanocomposites, they calculated solid liquid surface energy by using Gibb's-Thompson equation for melting point depression. The thermodynamic behavior of fluids and organic solids confined between the glassy cylindrical pores of diameter 2-50 nm has been considered in this relationship. The phase bounded between the glassy confined boundaries is called as confined phase which is explained in more detail later in Chapter 7. This phase shows properties different from the bulk properties. Gibb's –Thompson equation for melting point depression(ΔT_m) for crystal of size d gives the value of the solid liquid interfacial energy, σsl:

$$\Delta T_m = T_m - T_m(d) = 4\sigma_{sl} T_m / (d\Delta H_f \rho_s) \quad (2.21)$$

where T_m is bulk melting temperature (Melting temperature of neat PET)

T_m (d) is melting point of crystal of size d (Melting temperature of nanocomposite)

ΔH_f is bulk enthalpy of fusion (enthalpy of neat PET)

ρ_s is density of the solid.

Spherulitic dimensions are measured from optical microscopy by comparing the spherulitic dimensions with a predetermined scale.

The surface energy is calculated using equation (2.21) and reported in Table 2.7. They observed significantly increase in surface energy with the addition of MLS suggesting the decrease in crystal size near the MLS surfaces. The higher the surface energy the more difficult it is to grow the bigger spherulites at the expense of smaller ones. They also performed DSC experiment with different cooling rate to understand the effect on crystallization with the addition of MLS. They observed decrease in cold crystallization temperature in nanocomposite and the maximum decrease is observed for PET+5% MLS nanocomposite from 192 to 157 ^oC. Further heating cycle did not show any cold crystallization. It could be related to the processing

history. During the processing the interspherulitic region can be more amorphous than the interlamellar region and undergoes crystallization giving a characteristic cold crystallization peak in PET. The decrease in cold crystallization temperature indicated the more of cold crystalline region in nanocomposite compared to pure PET. In this region the density is less and could lead to increase in permeability and decrease in mechanical properties which is experimentally obtained and presented in Chapter 4 and explained in Chapters 6 and 7.

Table 2.7: Calculation of solid-liquid interphase surface energy of PET nanocomposites.

Sample	T_m(d) ^{o} C	d (μm)	Density (kg/m^2)	σ_{sl} (mJ/m^2)
PET+1%MLS	241	0.046	1236.8	15.3
PET+2%MLS	238	3.87	1093.9	2263.7
PET+3%MLS	239	3.51	1354	2116.1
PET+5%MLS	235	3.29	1332.1	3520.1

They also calculated Avrami constant (n) using Avrami analysis. For a cooling rate of 1 ^{o}C/min, the Avrami constant (n) was 1.6 for pure PET. This intermediate value of n denotes circular lamellar geometry. These values remained almost constant for pure PET and all the nanocomposites.

Effect of MLS on crystallization is also studied in nylon. Lincoln et al. [82] observed more disordered lamellae were formed in in-situ polymerized nanocomposites whereas larger, more ordered lamellae were obtained in melt–processed nanocomposites. The in-situ polymerized nanocomposite had small crystallite structure as the polymer chains were attached to silicate surface which reduces the chain mobility. While in melt processed nanocomposite, polymer chains weakly interacting with silicate layer were not impeded and were easier to incorporate in the crystal surface. They also showed that the interfacial area between the polymer and silicate layer had an effect on the short range order of the crystallites. In spite of the disordered crystallites in nanocomposites, the extent of crystallinity was higher on addition of silicate.

Ranade et al.[83] also observed decreased spherulite size in nylon nanocomposites. In the nanocomposites the MLS was varied from 1 to 5 % by weight. Pure nylon showed larger crystallites with an average diameter of 15 μm. Nylon nanocomposite showed fine and uniform spherulites with an average diameter of 5-8 μm. Pure Nylon 6 has only α-type crystalline structure. Liu et al.[84] and Ranade et al. among others have shown that in the presence of MLS platelets, nylon crystallizes in the γ form instead of the usual and more stable α form. Kojima et al.[85] reported that the presence of MLS induced the formation of the γ-crystalline form in nylon 6. Addition of MLS in Nylon 6 forms the γ-crystalline as reported by many authors.[86- 89] Akkapeddi prepared Nylon 6 nanocomposites in a twin screw extruder and observed an increase in the degree of crystallinity compared to pure Nylon 6.[90] Liu et al. correlated the γ-phase formation with the cooling rate and they observed that γ-phase increased with cooling rate. The increase in crystallinity was related to the nucleating ability of the silicate layer surface. The induced γ-crystalline form helped to improve the mechanical properties and heat distortion temperature of Nylon 6 nanocomposites. Lincoln et al. did not observe any increase in crystallinity in Nylon 6 nanocomposite compared to pure Nylon 6. In fact decrease in crystallinity is observed from 38% to 28.6 % with layered silicate addition. These films were processed by compression molding from extruded nanocomposites pellets. From the studies it is observed that addition of MLS forms a new type of γ-crystalline structure besides α-type crystalline structure in pure nylon. Due to this new type of crystal structure in nanocomposites the properties of nanocomposites differ from pure nylon. .

The addition of MLS also affects crystallization in PEN. Wu et al.[91] did not observe any change in crystalline structure in PEN when MLS is added. Chua et al.[92]studied the effect of different modified clay on crystallization. They observed that both pristine MLS and

imidazolium-treated MLS enhanced the formation of the β-crystal phase under melt crystallization at 200 ºC. However, at 180 ºC, the imidazolium-treated MLS was found to favor the formation of α-crystal.

2.2.3 Effect of MLS on Mechanical Properties

Mechanical properties of polymer nanocomposites are expected to be higher than pure polymers because the second component filler has higher mechanical properties. Advantages of polymer nanocomposites containing uniformly dispersed silicate layers in a nylon polymer matrix was first obtained by a group at the Toyota Research Center in Japan. [15, 93, 94] Higher the degree of exfoliation, larger is the improvement in properties. Ray et al.[Error! Bookmark not defined.] observed the difference in the extent of exfoliation in Nylon 6 nanocomposites strongly influenced the mechanical properties. They also explained that exfoliated layers are the main factor in improving the stiffness in the nanocomposite. Zilg et al.[95] explained the main stiffness improvement resides in the formation of molecular assemblies obtained by the presence of dispersed anisotropic laminated nanoparticles. Intercalated particles, having a less important aspect ratio, play a minor role. Wang et al.[96] also observed mechanical properties of nanocomposites are better than that of pure polymers. They also attribute the improvement of property is due to dispersion of particles. The improved mechanical property is also observed in different nanocomposites by different groups.[95, 97,98] Dennis et al.[20] observed an increase in modulus from 2.7 GPa for pure polyamide 6 to 3.3 GPa for a poorly dispersed and delaminated nanocomposites and 4 GPa for a well dispersed and delaminated nanocomposites with 5 wt% of Cloisite 15A as shown in Figure 2.27. The films were processed by extrusion method. On the other hand, nanocomposite with Cloisite 30B showed poor elongation and impact strength. Table 2.7 summarizes the effect of MLS on mechanical properties of nanocomposite with percentage

of clay and processing method. In most of the cases improvement in mechanical properties of is observed except in few cases like recycled PET. Improvement in mechanical properties is observed in Nylon 6 as studied by Shelley et al. With the addition of 5% MLS, the yield strength increased from 43.9 to 76.1 MPa. Modulus also increased from 1.2 to 2.43 GPa. Modulus increased from approximately 2.7 to 3.7 GPa with the addition of 5% MLS in Nylon 6.[99] Mechanical properties of PETG (Eastman) nanocomposites are studied by Ranade et al.[100] Increase in MLS content increased the yield stress. Pure PET has yield strength and modulus of 44 MPa and 1.1 GPa. PET with 1% of Cloisite 20A MLS shows yield strength and modulus of 48 MPa and 1.2 GPa respectively. PET with 5% MLS of Cloisite 20A shows yield strength and modulus of 48 MPa and 1.2 GPa respectively. When Cloisite 15A is added higher improvement is observed in nanocomposites compared to pure PETG. With the addition of 1% of Cloisite 15A MLS shows yield strength and modulus of 55 MPa and 1.7 GPa respectively PETN is a copolymer of PET and PEN. The addition of 4% of clay increased ultimate tensile strength from 36 to 94 MPa and modulus increased from 1.57 to 4.34 GPa. Therefore, very small amount of clay improves the mechanical properties by more than 150%.[101] Kim et al.[102] studied mechanical properties of PEN nanocomposites consisting of multiwall carbon nanotube (MWCNT), processed by melt blending process in a twin-screw extruder. They observed increases in storage modulus and loss modulus in nanocomposites compared to pure PEN even with a very small quantity of MWCNT. Tensile strength and modulus increased approximately from 65 to 83 MPa and 1.68 to 1.88 GPa respectively.

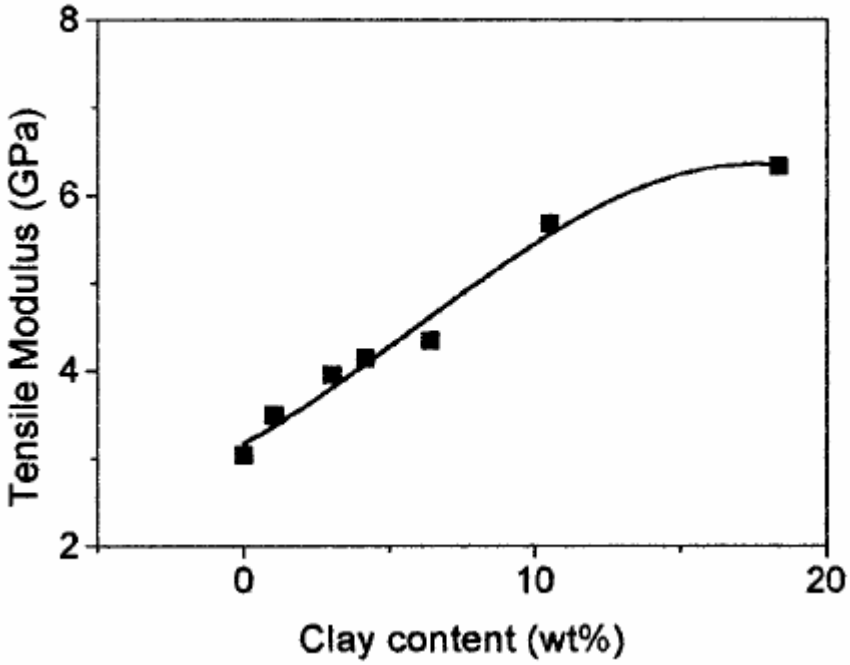

Figure 2.27: Effect of sodium montmorillonite MLS content on tensile modulus of Nylon 6 nanocomposite.[103]

Table 2.8: Effect of MLS on the mechanical properties of polymer from literature.

Sample	% clay	YS (MPa)	UTS (MPa)	E (GPa)	Elongation at break (%)	Processing method
PETN[104]	0		36	1.57	7	Solution intercalation method
	1		75	3.66	6	
	2		79	3.78	5	
	3		89	4.12	5	
	4		94	4.34	5	
	6		66	3.19	2	
Recycled PET[105]	0	~60	~37	~2.5	~380	Melt intercalation process
	1 (Cloisite Na+)	~60	~30	~2.62	~220	
	3	~60	~25	~2.7	~150	
	5	~60	~48	~2.75		
	1 (Cloisite 25 A)	~60	~28	~2.82	~410	Melt intercalation process
	3	~60	~25	~3.05	~270	

	5	~60	~48	~3.3	-	
PETG (Eastman)	0	44	51	1.1	-	
	1 (Cloisite 20A)	48	55	1.2	-	
	2	47	54	1.2	-	
	3	47	54	1.2	-	
	5	48	55	1.2	-	
	1 (Cloisite 15 A)	55	62	1.7	-	
	2	55	62	1.7	-	
	3	54	61	1.7	-	
	5	53	60	1.7	-	
Polyamide 6(Capron B135 WP)		64		2.7	-	Single screw extruder
	30 B (5wt%)	79		3.7	-	Single screw extruder
	15 A (5 wt%)	77		3.3	-	Single screw extruder
	Low shear 15 A	78		3.5	-	Twin screw extruder co-rotating intermeshing
	Medium shear 15 A	81		3.7	-	Twin screw extruder co-rotating intermeshing
	Low shear 15 A	77		3.7	-	Twin screw extruder counter-rotating intermeshing
	Medium shear 15 A	75		3.6	-	Twin screw extruder counter-rotating intermeshing
	High shear 15 A	89		4.4	-	Twin screw extruder counter-rotating intermeshing
	Medium shear 30 B	69		3.4	-	Twin screw extruder counter-rotating intermeshing
	Low shear 15 A	78		3.6	-	Twin screw extruder counter-

						rotating non-intermeshing
	Medium shear 15 A	85		4.0	-	Twin screw extruder counter-rotating non-intermeshing
	High shear 15 A	80		3.6	-	Twin screw extruder counter-rotating non-intermeshing
Nylon-6[106]		43.9		1.2	-	Single screw extruder
	2% clay (not clear which type of clay)	58.9		1.65	-	Single screw extruder
	5 wt% clay	76.1		2.43	-	Single screw extruder
Nylon 6[107]		64.2		2.66	-	Twin screw
	5 wt% organoclay	74		3.47	-	Single screw
	5 wt% organoclay	82.1		3.66	-	Twin screw
Nylon 6		68.2		3.0	-	Twin screw
	4.2 wt% Sodium montmorillonite	91.3		4.1	-	Twin screw

2.2.4 Conclusions

Different factors that affect permeability of polymers and polymer nanocomposites are explained in this chapter. Crystallinity, density, free volume, and orientation are interrelated and affect permeability. With the increase in crystallinity and density, permeability decreases. Large free volume in polymer results in increase in permeability. With the addition of filler, a decrease in permeability is observed. The decrease in permeability depends on the filler content and the

nature of dispersion. In most cases improvement in the mechanical properties is also obtained in nanocomposites. Multilayered structures on polymers further decrease the permeability based on the quality of the coating. The thickness and defect density in the film governs the permeability in the inorganic coated film on the polymer.

2.3 References

[1] Yano, K.; Usuki, A.; Okada, A.; Kurauchi, T.; Kamigaito, O. J Polym Sci Part A: Polym Chem **31** (1993) 2493.

[2] Gilman, J. W.; Jackson, C. L.; Morgan, A. B.; Harris, R.; Manias, E.; Giannelis, E. P.; Wuthenow, M.; Hilton, D.; Phillips, S. H. Chem Mater **12** (2000) 1866.

[3] Vaia, R. A.; Price, G.; Ruth, P. N.; Nguyen, H. T.; Lichtenhan, J. Appl Clay Sci **15** (1999) 67.

[4] Usuki, A.; Kojima, Y.; Kawasumi, M.; Okada, A.; Fukushima, Y.; Kurauchi, T.; Kamigaito, O. J Mater Res **8** (1993) 1179.

[5] Kojima, Y.; Usuki, A.; Kawasumi, M.; Okada, A.; Fukushima, Y.; Kurauchi, T.; Kamigaito, O. J Mater Res **8** (1993) 1185.

[6] Kojima,Y.; Usuki, A.; Kawasumi, M.; Okada, A.; Kurauchi, T.; Kamigaito, O.; Polym Sci A: Polym Chem **31** (1993) 983.

[7] Zeng, C.; Lee, J. L. Macromolecules **34** (2001) 4098.

[8] Gilman, J. W. Appl Clay Sci **15** (1999) 31.

[9] Dhoot, S. N.; Freeman, B. D.; Stewart, M. E. Encyclopedia of Polymer Science and Technology.

[10] Brydson, J. Plastic Materials, Elsevier, Seventh Edition (1999).

[11] Pinnavaia, T. J.; Beall G. W. Polymer-Clay Nanocomposites, John Wiley & Sons (2001).

[12] http://www.nanoclay.com/

[13] Ray, S. S.; Okamoto, M. Prog Polym Sci **28** (2003) 1539. Bharadwaj, R. K.; Macromolecules **34** (2001) 9189.

[14] Zeng, Q. H.; Wang, D. Z.; Yu, A. B.,; Lu, G. Q. Nanotechnology **13** (2002) 549.

[15] Okada, A.; Kawasumi, M.; Usuki, A.; Kojima, Y.; Kurauchi, T.; Kamigaito, O. Mater Res Soc Proc **45** (1990) 171.

[16] Van Zuilichem, D. J.; Kuiper, E.; Stolp, W.; Jager, T. Powder Tech **106** (1999) 147

[17] Shelley, J. S.; Mather, P. T.; De Vries, K. L. Polymer **42** (2001) 5849.

[18] Cho, J. W.; Paul D. R. Polymer **42** (2001) 1083.

[19] Lew, C. Y.; Murphy, W. R., McNally, G. M., Yanai, S.; Abe, K. Annual Technical Conference (ANTEC), Conference Proceedings (2003) 178.

[20] Dennis, H. R.; Hunter, D. L.; Chang, D.; Kim, S.; White, J. L.; Cho, J. W.; Paul. D. R. Polymer **42** (2001) 9513

[21] Vaia, R. A.; Giannelis, E. P. Macromolecules **30** (1997) 7990.

[22] Ghosal, K.; Freeman, B. D. Polym Adv Technol **5** (1994) 673.

[23] Crank, J.; Park, G. S. Diffusion in Polymers, Academic press (1968)

[24] Crank, J. The Mathematics of Diffusion, 2nd edition, Clarendon Press, Oxford (1975) 414.

[25] Polyakova, A.; Liu, R. Y. F.; Schiraldi, D. A.; Hiltner, A.; Baer, E. J Polym Sci Part B: Polym Phys **39 (**2001)1889.

[26] Rosen, S. Fundamental Principle of Polymeric Materials, John Wiley & Sons (1982).

[27] Auras, R.; Harte, B.; Selke, S. J Appl Polym Sci **92** (2004) 1790

[28] Michaels, A. S.; Vieth, W. R.; Barrie, J. A. J Appl Phys **34** (1963) 13.

[29] Gavara, R.; Hernandez, R. J. J Polym Sci Part B: Polym Phys **32** (1994) 2375

[30] Hernandez, R. J.; Selke S. E. M.; Culter, J. D. Plastics packaging: Properties, processing, applications and regulations, Hanser Publishers (2000).

[31] Ranade, A. J.; D'Souza, N. A.; Gnade, B.; Dharia, A. Annual Technical Conference (ANTEC), Conference Proceedings **2** (2003) 1956.

[32] Sangaj, N. S.; Malshe, V. C.; Prog. Org. Coat. **50** (2004) 28.

[33] Lin, J.; Shenogin, S.; Nazarenko, S. Polymer **43** (2002) 4733.

[34] Michaels, A. S.; Vieth W. R., Barrie J. J Appl Phys **34** (1963) 1.

[35] Sekelik D. J.; Stepanov, E. V.; Nazarenko, S., Schiraldi, D.; Hiltner, A.; Baer, E. J Polym Sci Part B: Polym Phys, **37** (1999) 847.

[36] Light, R. R.; Seymour, R. W. Polym Eng Sci, **22**, (1982) 857.

[37] Lin, J.; Shenogin, S.; Nazarenko, S. Polymer **43** (2002) 4733.

[38] Liu, R.Y.F.; Hiltner, A.; Baer, E. J Polym Sci Part B: Ploym Phys **42** (2004) 493.

[39] McGonigle, E. A.; Liggat, J. J.; Pethrick, R.A.R.; Jenkins, S. D.; Daly, J. H.; Hayward, D. Polymer **42** (2001) 2413.

[40] Ghosal, K.; Chern, R. T.; Freeman, B. D. J Polym Sci, Polym Phys Ed **33** (1995) 657.

[41] http://www.devicelink.com/mpb/archive/98/09/005.html (accessed in February 2006).

[42] Hu, Y.S.; Liu, R.Y.F.; Zhang, L.Q.; Rogunova, M.; Schiraldi, D.A.; Nazarenko, S.; Hiltner, A.; Baer, E. Macromolecules **35** (2002) 7326

[43] Auras, R.; Harte, B.; Selke, S. J Appl Polym Sci **71** (1999) 197.

[44] Lim, L-T.; Britt, I. J.; Tung, M. A. J Appl Polym Sci **92** (2004) 1790.

[45] Leterrier, Y. Prog Mater Sci **48** (2003) 48.

[46] Henry, B. M.; Erlat, A. G.; McGuigan, A.; Grovenor, C.R.M.; Briggs, G.A.D.; Tsukahara, Y.; Miyamoto, T.; Noguchi, N.; Niijima, T. Thin Solid Film **382** (2001) 194.

[47] Roberts, A. P.; Henry, B. M.; Sutton, A. P.; Grovenor, C.R.M.; Briggs, G.A.D.; Miyamoto, T.; Kano, M.; Tsukahara, Y.; Yanaka, M. J. Membr Sci **208** (2002) 75.

[48] Slee, J. A.; Orchard, G.A.J.; Bower, D. I.; Ward, I.M. J Polym Sci Part B: Polym Phys **27** (1989) 71.

[49] da Silva Sobrinho, A. S.; Czeremuszkin, G.; Latreche, M.; Wertheimer, M.R.J. Vac Sci technol A **18** (2000) 149.

[50] Yano, K.; Usuki, A.; Okada, A.; Kurauchi, T.; Kamigaito, O. J Polym Sci Part A: Polym Chem **31** (1993) 2493.

[51] Lange, J.; Wyser, Y. Packag Technol Sci **16** (2003) 149

[52] Choi, W. J.; Kim, H-J.; Yoon, K. H.; Kwon, O. H.; Hwang, C. L. J Appl Polym Sci **100** (2006) 4875

[53] Ke, Z.; Yongping, B. Mater Lett **59** (2005) 3348

[54] Tortora, M.; Gorrasi, G.; Vittoria, V.; Galli, G.; Ritrovati, S.; Chiellini, E. Polymer **43** (2002) 6147.

[55] Drozdov, A. D.; Christiansen, J deC.; Gupta, R.K.; Shah, A.P. J Polym Sci Part B: Polym Phys **41** (2003) 476.

[56] Sangaj, N. S.; Malshe, V. C. Prog Org Coat **50 (**2004) 28.

[57] Lai, M.; Kim, J. K. Polyme **46** (2005) 4722.

[58] Bharadwaj, R. K.; Mehrabi, A. R.; Hamilton, C.; Trujillo, C.; Murga, M.; Fan, R.; Chavira, A.; Thompson, A. K. Polymer **43** (2002) 3699.

[59] Chang, J-H; Yeong, UK. AN; Gil, Soo Sur J Polym Sci Part B: Polym Phys **41 (**2003) 94.

[60] Gain, O.; Espuche, E.; Pollet, E.; Alexandre, M.; Dubois, Ph. J Polym Sci Part B: Polym Phys **43 (**2005) 205.

[61] Leterrier, Yves. Prog Mater Sci **48** (2003) 1.

[62] Martin, P.J.; Netterfield, R.P.; Cuomo, In : J.J.; Rossnagel, S.M.; Kaufman, H.R, Handbook Of Ion Beam Processing Technology, Noyes Publications, New Jersey, (1989).

[63] Bunshah, R.F. Deposition Technologies for Films and Coatings, Noyes, NJ (1982).

[64] Roberts, A.P.; Henry, B.M.; Sutton, A.P.; Grovenor, C.R.M.; Briggs, G.A.D.; Miyamoto, T.; Kano, M.; Tsukahara, Y.; Yanaka, M. J of Membr Sci **208** (2002) 75.

[65] Tropsha, Y.G.; Harvey, N.G.; J Phys Chem B **101** (1997) 2259.

[66] Erlat, A.G.; Wang, B.C.; Spontak, R.J.; Tropsha, Y.; Mar, K.D.; Montgomery, D.B.; Vogler, E.A. J Mater Res **15** (2000) 704.

[67] da Silva Sobrinho, A. S.; Silva, S. da; Czeremuszkin, G.; Latreche, M., Wertheimer, M. R. J Vac Sci Technol **18** (2000) 149.

[68] Dixon E.; Jackson, J. J of Mater Sci **3** (1968) 464.

[69]Jackson, J.; Longman, G. Polymer, **10** (1969) 873.

[70] Srimoaon, P. ; Dangseeyun, N.; Supaphol, P. Eur. Polym J **40** (2004) 599.

[71] P. Chandran and S. Jabarin, Advances in Polym. Techno., **12**, 153(1993).

[72] S. Chang and R.Shanks, J. Appl. Polym. Sci., **47**, 2149 (1993).

[73] T. Wan, L. Chen, Y. Chua and X. Lu, J. Appl. Polym. Sci., **94**, 1381 (2004).

[74] M. Kennedy, G.Turturro, G.Brown and L. St-Pierre, J. Polym. Sci.: Polym. Phys., **21**, (1983)1403.

[75] Wang, Y.; Gao, J.; Ma, Y.; Agarwal, U. S. Composites: Part B **37** (2006) 399.

[76] Ou, C. F.; Ho, M. T.; Lin, J R. J Polym Res **10** (2003) 127.

[77] Ou, C. F.; Ho, M. T.; Lin, J R. J Appl Polym Sci **91** (2003) 140.

[78] Ke, Y.; Yang, Z.; Zhu, C. J Appl Polym Sci **85** (2001) 2677.

[79] Wan, T.; Chen, L.; Chua, Y.; Lu, X. J Appl Polym Sci **94** (2004) 1381.

[80] Dixon E.; Jackson, J. J of Mater Sci **3** (1968) 464.

[81] Pendse S. Masters Thesis, University of North Texas, 2005.

[82] D. Lincoln, R. Vaia, Z. Wang and B. Hsio, *Polymer*, **42**, 1621 (2001).

[83] Ranade, A.; D'Souza, N.; Gnade, B.; Dharia, A. J Plastic films, **19** (2003) 271.

[84] Liu, L.; Qi, Z.; Zhu, X. J Appl Polym Sci **71**, 1133 (1999).

[85] Kojima, Y.; Matsuoka, T.; Takahashi, H.; J Appl Polym, **51** (1994) 683.

[86] Lincoln, D.; Vaia, R.; Wang; Z.; Krishnamoorti; R., Polym, **42** (2001) 9975.

[87] Wu, Z.; Zhou, C.; Zhu, N. Polym Test, **21** (2002) 479.

[88] Wu, Z.; Zhou, C.; Zhang, H.; J Appl Polym Sci **83** (2002) 2403.

[89] Liu, L.; Qi, Z.; Zhu, X.; J Appl Polym Sci **71** (1999) 1133.

[90] Akkapeddi, M. K. Annual Technical Conference (ANTEC), Conference Proceedings (1999).

[91] Wu, T.-M.; Liu C.-Y. Polymer **46** (2005) 5621.

[92] Chua, Y. C.; Lu, X.; Wan T. J of Polym Sci Part B: Polym Phys **44** (2006) 1040.

[93] Usuki A.; Kojima, Y.; Kawasumi, M.; Okada, A.; Fukushima, Y.; Kurauchi, T.; Kamigaito, O.; J Mater Res **8** (1993) 1179.

[94] Usuki, A.; Kojima, Y.; Kawasumi, M.; Okada, A.; Fukushima, Y.; Kurauchi, T.; Kamigaito, O. J Mater Res **8** (1993) 1185.

[95] Zilg, C.; Thomann, R.; Mulhaupt, R.; Finter, J. Adv Mater **11** (1999) 49.

[96] Wang, J.; Pinnavaia , T.J. Chem Mater **10** (1998) 3769.

[97] Hasegawa, N.; Okamoto, H.; Kato, M.; Usuki A.; Sato, N. Polymer, **44** (2003) 2933.

[98] LeBaron, P. C.; Wang, Z.; Pinnavaia, T. J. App Clay Sci **15** (1999) 11.

[99] Borse, N. K.; Kamal, M. R. Polym Eng Sci **46** (2006) 1094.

[100] Ranade, A.; D'Souza, N.; Christopher, T.; Ratto, J. A. Polym Int **54** (2005) 875.

[101] Chang, J. –H.; Park, D.-K. J Polymer Sci Part B: Polym Phys, **39** (2001) 2581.

[102] Kim, J. Y.; Kim, S. H., J Polym Sci Part B: Polym Phys **44** (2006) 1062.

[103] Liu, L.; Qi, Z.; Zhu, X. J App Polym Sci, **71** (1999) 1133.

[104] Chang, J. –H.; Park, D.-K. J Polymer Sci Part B: Polym Phys, **39** (2001) 2581.

[105] Pegoretti, A.; Kolarik, J.; Peroni, C.; Migliaresi, C. Polymer **45** (2004) 2751.

[106] Shelley, J. S.; Mather, P. T.; De Vries, K. L. Polymer **42** (2001) 5849.

[107] Cho, J. W.; Paul D. R. Polymer **42** (2001) 1083.

CHAPTER 3

EXPERIMENTAL TECHNIQUES

Polymer and nanocomposite films were processed by extrusion. Experiments were conducted to determine dispersion and crystallization effect in the nanocomposites of nylon, PET, and PEN. X-ray diffraction (XRD), scanning electron microscope (SEM), transmission electron microscopy (TEM), differential scanning calorimetry (DSC), and permeability characterization techniques were performed. Techniques performed to understand interfacial phenomena by atomic force microscopy and ellipsometry are described separately in Chapters 6 and 7.

3.1 Materials

The Nylon 6 (Capron B135MP) studied in the work was supplied by Honeywell. It is a lubricated, nucleated, high viscosity (melt flow ratio, MFR = 1.2), and extrusion grade homo polymer for fabricating cast or blown films. The semi-crystalline grade PET (Kosa 1101) used in this work was supplied by KOSA. It has intrinsic viscosity of 0.84. PEN pellets type 7001 with intrinsic viscosity of 0.85 was obtained from Futura Polyesters Ltd, Chennai, India. Amorphous poly (ethyelene terephthalate) glycol, PETG (6763) was obtained from Eastman.. The montmorillonite layered silicate (MLS) of type Cloisite 30B and Cloisite 20A, and was supplied by Southern Clay. It is a natural montmorillonite modified with a ternary ammonium salt with cation exchange capacity (CEC) 90.0 meq and $d_{(001)}$ spacing of 18.5 Å.

3.2 Processing

3.2.1 Processing of Nylon 6 Nanocomposite Films

Nylon 6 pellets were dried overnight in a vacuum oven at 80 ºC. A 20% by weight master-batch of MLS (30B) in nylon 6 was prepared on a Werner Pfleiderer co-rotating twin screw extruder with an L/D ratio of 30. Individual MLS concentrations of nylon 6 nanocomposites (1, 2, 3 and 5% by weight) were processed on a Leistritz counter rotating twin screw extruder with a 30 mm screw diameter and an L/D ratio of 32.5. Nylon 6 nanocomposite films of approximately 10-mil thickness were prepared on a Thermo Haake Polydrive single screw extruder with a film die attached.

3.2.2 Processing of PET Nanocomposite Films

PET pellets were dried overnight in a vacuum oven at 65 ºC. A 10% by weight master-batch of MLS was prepared on a Werner Pfleiderer co-rotating twin screw extruder with an L/D ratio of 30. Individual MLS concentrations of 1, 2, and 3 % by weight were processed on a Leistritz counter rotating twin screw extruder of 30 mm screw diameter and an L/D ratio of 32.5 with a film die attached to it.

3.2.3 Processing of PEN Nanocomposite Films

PEN pellets were dried in a vacuum oven at 120 ºC for 24 hrs. A three stage and two stage process for making PEN nanocomposite films was investigated. A master batch of PEN and 10 % MLS (Cloisite 30B) by weight was compounded on a Berstorff ZE 25 twin screw extruder with 25 mm diameter and 40 L/D. For the three stage process, the master batch was diluted using additional PEN to make 1 and 2% concentration on the twin screw extruder. The mixtures were then introduced into a Haake Polydrive single screw extruder (18 mm diameter

and 25 L/D) with a film die and films were formed. These films are named as 3S (3 stage) in nanocomposites. For the two stage process, the master batch dilution and film processing was done simultaneously on the single screw extruder. These films are named as 2S (two stage) in nanocomposites.

Nomenclature of PEN and nanocomposite films is tabulated in Table 3.1.

Table 3.1: Nomenclature of PEN and nanocomposite films.

Samples	Nomenclature
PEN	A
PEN+1%MLS-2S	B
PEN+1%MLS-3S	C
PEN+2%MLS-2S	D
PEN+2%MLS-3S	E

Different processing parameters were varied to get smoother and transparent film and the best film was obtained with the following parameters as mentioned in Table 3.2.

Table 3.2: Optimized process parameter for PEN nanocomposite films.

Variable	Optimized Parameter
Temperatures of 4 different zones	320, 310, 310, and 310 ºC
Screw speed	11 rpm
Roll speed	20 rpm
Distance between die and roll	16”
Chiller temperature	17 ºC

3.3. Characterization Techniques

3.3.1 X-Ray Diffraction (XRD)

Dispersion of the nanocomposites films were studied using x-ray diffraction (XRD). XRD of nylon, PET, PEN nanocomposites and MLS powder was performed on Scintag XDS 2000 x-ray diffractometer from 2^o- 70^o and a step size of 0.02 using Cu K_α radiation.

3.3.2 Scanning Electron Microscopy (SEM)

A focused ion beam and field emission SEM (FEI Nova 200 Dual Beam FIB/FEGSEM) was used to record images. The cross section of the sample was prepared using a focused ion beam of gallium ions at 30 KV and 1.7 nA current. SEM images were taken at 10 KV and at 5 mm working distance using a field emission electron beam. For SEM cross section, the polymer films were coated with few nanometers of gold before the sample was loaded into the SEM chamber. Dispersion of PEN nanocomposites was studied by taking images on a cross section of the sample (prepared by ion milling) in SEM.

3.3.3 Transmission Electron Microscopy (TEM)

Transmission electron microscopy (TEM) was used to study the dispersion of PET and PEN nanocomposites. TEM was performed using Philips EM 420 Transmission Electron Microscope at 120 KeV. The sample was prepared by ultra microtome method. Thin sections of polymer films were cut by a razor blade after embedding the polymer in epoxy. Thin sections of samples (less than 100 nm) from the cut section were cut using a diamond knife on a MT 6000 Sorvall microtome machine.

3.3.4 Mechanical Properties

The MTS 810 hydraulic system was used to measure tensile properties of PET and PEN nanocomposite films. A minimum of 5 samples were taken to get the average tensile properties and were measured according to the ASTM D 882-95a standard.

3.3.5 Differential Scanning Calorimetry (DSC)

To study the crystallinity of the film, differential scanning calorimetry (DSC) was done on a Perkin-Elmer DSC 6 instrument. The system was calibrated using 5–15 mg of elemental

indium sample. Heating was carried out from 30 to 280 ºC for PET and PEN films at a rate of 10 ºC/min and cooling was done at the same rate of 10 ºC /min in both the first and second cycles. In DSC, there is one reference pan and one sample pan as shown in Figure 3.1. Both of them are heated at a constant heating rate. The change in the heat flow or the specific heat of a sample with temperature with respect to reference plan is measured. The specific heat of a material changes when there is any physical transition such as glass transition, crystallization, and melting. This will be observed as a peak in the DSC graph where heat flow is plotted in the X-axis and temperature or time is plotted in the Y-axis.

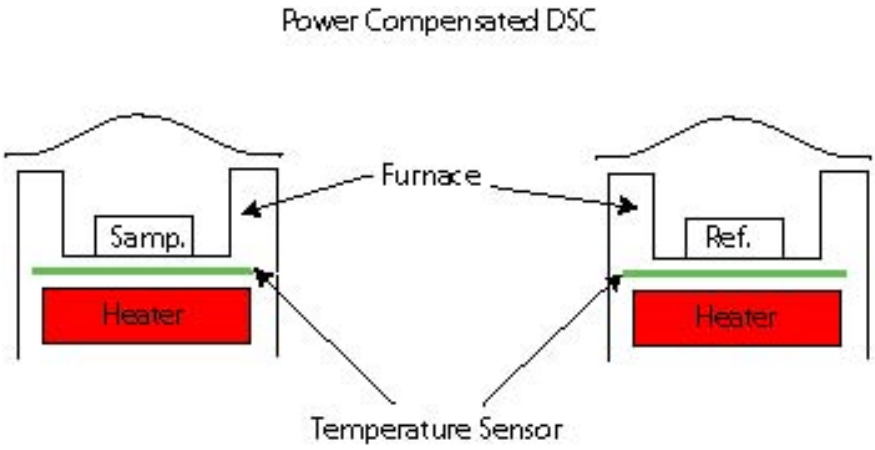

Figure 3.1: Schematic showing the principle of DSC.[1]

3.3.6 Percentage Haze Measurement

Percentage haze of the PEN and nanocomposites samples are measured in Color Quest II. It was measured at three different points and the average was determined for each sample.

3.3.7 Permeability

The oxygen permeability is most commonly measured using an OXTRAN instrument. The volume of O_2 collected in a given time is measured by a nickel–cadmium sensor.[2] In this

isostatic coulometric method, flat film samples are clamped into a diffusion cell, which is then purged of residual oxygen using an oxygen-free carrier gas such as N_2. The carrier gas is routed to the instrument sensor until a stable zero has been established. Pure oxygen is then introduced into the outside chamber of the diffusion cell. Oxygen molecules diffusing through the film to the inside chamber are conveyed to the sensor by the carrier gas. The Ox-Tran system uses a patented coulometric sensor to detect oxygen transmission through both flat films and packages. This sensor provides parts-per-billion sensitivity to oxygen even in the presence of water vapor. Modern Controls, Inc. (MOCON) also makes instruments for measuring carbon dioxide permeation. Infrared detector is used to detect carbon dioxide that permeates through the test film. Water vapor transmission rate (WVTR) can either be measured by the traditional gravimetric "cup" method. The newer method: ASTM method F1249 uses infrared detection to measure water vapor transmission through barrier films. One of the most widely used commercial WVTR systems is Permatran-W (Modern Controls Inc., Minneapolis, Minn.).

Helium and oxygen permeability of PET, PEN and nylon 6 films and their nanocomposites was measured on an in-house manufactured permeability system. Figure 3.2 shows the schematic of permeability system. It consists of two chambers, a low-pressure feed side and an ultrahigh vacuum (UHV) side, separated by the flexible polymer sample to be analyzed. The system was calibrated using a combination of a NIST traceable calibrated helium leak and a variable aperture calibrated orifice. The instrument has been previously described.[3] Both sides are separated by the polymer sample being tested. The sample was gripped using an indium seal. Experiments were carried out with varying inlet pressures of helium and oxygen gas on the feed side. The helium and oxygen was detected by a residual gas analyzer (RGA) on the UHV side and capacitance manometer and ion gauge on the low-pressure side. The experiments

were carried out for sufficient time until equilibrium partial pressure was observed on the UHV side. Oxygen or helium gas diffuses through plastic film to UHV side and over a period of time the permeation rate stabilizes, which reflects directly into a constant partial pressure on the UHV side. A typical pressure vs. time graph during permeability experiment is shown in Figure 3.3. By using partial pressure of gas and calibration factor, permeability of the gas was determined quantitatively. The error range of the all the measured permeability values are in between 5-10 %. Water vapor transmission rate (WVTR) of PEN and nanocomposite film was measured in PERMATRAN-W® Model 398 at Army Research Laboratory, Natick, MA.

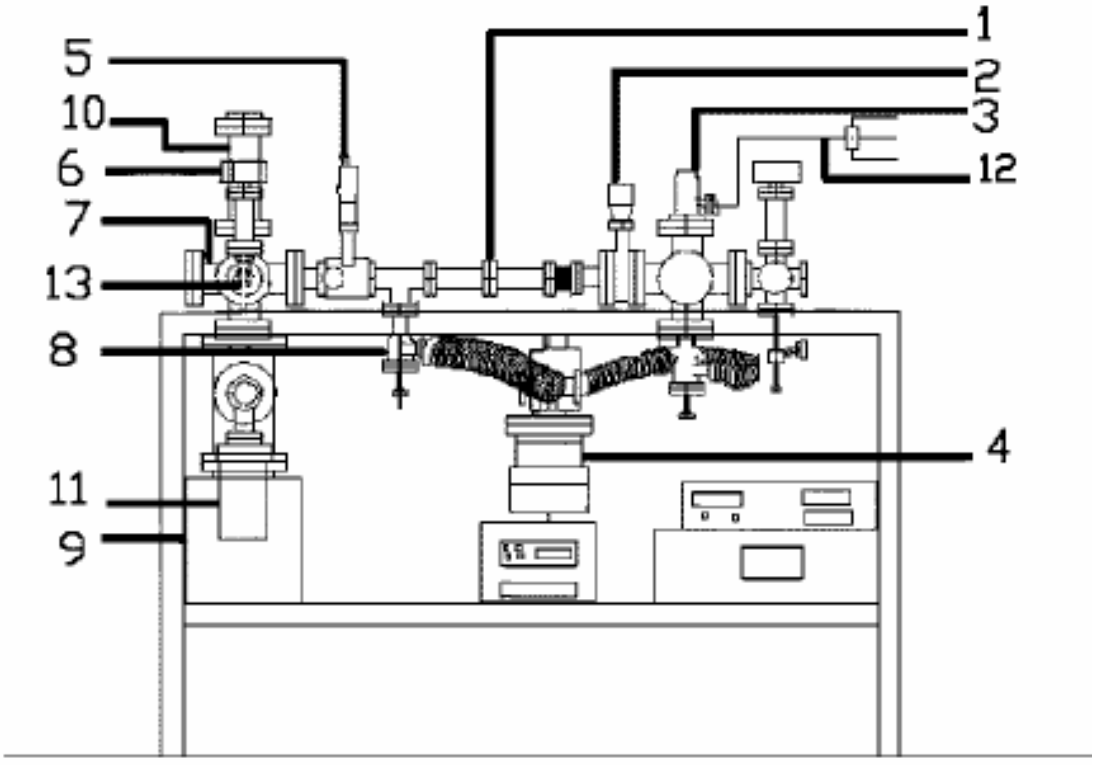

Figure 3.2: Schematic of Permeability Measurement System.[3]

The critical parts of the system are labeled as follows: (1) Sample holder, (2) Gate valve, (3) Gas leak valve (4) Turbo-molecular pump (150 l/s), (5) Three position/apertured gate valve, (6) Residual gas analyzer, (7) 4 ½ in. six way cross, (8) Turbo pump gate valve, (9) Ion pump, (10)

Titanium sublimation pump, (11) Turbo pump (65 l/s), (12) Line for introducing gas into high pressure side, and (13) NIST calibrated helium leak valve

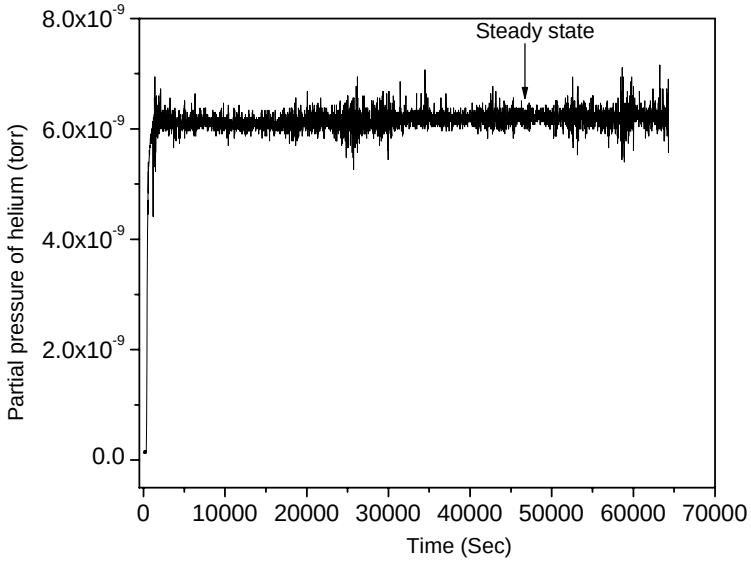

Figure 3.3: Typical pressure vs. time curve for the helium permeability experiment

3.3.8 Fatigue and Stretching of PET and Nylon Films

The MTS 810 hydraulic system was used to subject the samples to undergo the fatigue of 50 and 10,000 cycles. Fatigue of the sample was done by flexing the sample in MTS. It is done in the compression mode at the rate of 10 mm/sec.

Biaxial stretching of the sample is done by first stretching the sample in one direction. The sample is then rotated by 90º and stretched again. Nylon 6 and PET films are stretched biaxially in the same system at the rate of 0.2 mm/sec at room temperature. Nylon 6 films were stretched by 5 % and PET films were stretched by 3.3% in both the directions, as PET films were fragile. The permeability of these samples was then measured immediately.

3.3.9 Water Absorption

To study water absorption, samples of 1cm× 1cm dimensions were cut and completely immersed in water for a definite time period. The weight of the samples was measured before and after the test and the percentage change in weight was calculated.

3.3.10 Annealing

As processed nylon samples are annealed at 120 ºC for 24 hrs and permeability of the sample was measured immediately. Permeability of these samples was then compared with as processed sample

3.4 References

[1] http://en.wikipedia.org/wiki/Image:PowercompenstatedDCS.jpg

[2] Roberts, A. P.; Henry, B.M.; Sutton, A. P.; Grovenor, C.R.M.; Briggs, G.A.D.; Miyamoto, T.; Kano, M.; Tsukahara, Y.; Yanaka, M. J Membr Sci **208** (2002) 75.

[3] Ranade, A.; D'Souza, N. A.; Wallace, R. M.; Gnade, B. E. Rev Sci Instru **76** (2005) 013902.

CHAPTER 4

STRUCTURE PROPERTY EVALUATION OF THE BULK NANOCOMPOSITES: DISPERSION, CRYSTALLINITY, AND PERMEABILITY OF NYLON, PET, AND PEN NANOCOMPOSITES

As explained in Chapter 2, the permeability in nanocomposites is affected by MLS content, nature of MLS dispersion in the matrix, and crystallinity. The dispersion of MLS and influence of MLS addition on crystallinity in the nanocomposites is studied here and correlated with barrier properties (permeability). Dispersion in the nanocomposite films is studied using either one or a combination of the following techniques of x-ray diffraction, scanning electron microscopy cross section using focused ion beam (FIB), and transmission electron microscopy. The effect of MLS on crystallinity in polymers is studied using differential scanning calorimetry. Results of the permeability experiments and discussions correlating the barrier properties with the dispersion of MLS and crystallinity are explained in this chapter.

4.1 Nylon Nanocomposites

Previous results on dispersion and crystallinity of Nylon nanocomposite are included in this chapter to correlate with barrier properties in nanocomposites. [1]

4.1.1 Dispersion of MLS in Nanocomposites

Dispersion of MLS in nylon nanocomposites was studied by x-ray diffraction. Figure 4.1 shows the XRD diffraction pattern of nylon, MLS, and nylon nanocomposites. The XRD of MLS shows a sharp peak for MLS at 2Θ of 5 º. This corresponds to a d spacing of 1.76 nm. This differed from the material datasheet but was reproducible in multiple runs. Pure nylon does not have any characteristic peak in the 2Θ range of 2-15 º. XRD of nylon nanocomposites, with varied

concentration of MLS (1, 2, 3, and 5 by wt %) did not show the presence of the (001) reflection peak in MLS in the 2-15 º region. Therefore, an exfoliated structure can be inferred.

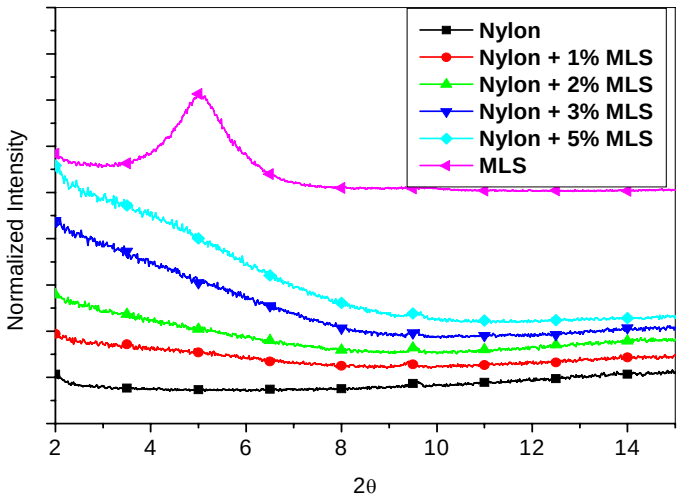

Figure 4.1: XRD of nylon, MLS, and nanocomposites. [1]

4.1.2 Effect of MLS on Thermal Transitions in Nylon

Crystallization in nylon and nylon nanocomposites was studied by using DSC. As-processed samples were heated from 5 to 250 ºC at 10 ºC/min. The nylon used had a glass transition of 49 ºC and melting point of 223 ºC as shown in Figure 4.2 and the values are reported in Table 4.1. When MLS is introduced into the nylon, the glass transition showed an increase relative to the nylon. For nylon+1% MLS film, the T_g increased to 54 ºC. For nylon+2% MLS and nylon+3% MLS, T_g are 53 and 52 ºC, respectively indicating no further increase in T_g. When 1% MLS is added in nylon, the T_g increased by 5 ºC. The melting point did not change but the enthalpy of melting showed a substantial drop. After annealing the sample at 250 ºC for 30 minutes, the cooling scans were recorded from 250 ºC to 5 ºC at 10 ºC/min. The cooling scans are shown in Figure 4.3 and fusion peaks analyzed in Table 4.2. Nylon had a fusion temperature of 167 ºC. The width of fusion temperature is 19 ºC in the first cooling cycle. The fusion temperature

of nylon+1% MLS is 189 ºC. This indicates an increase of ~20 ºC. Additional MLS did not impact the T_f further and the enthalpy of fusion remained similar to that of nylon. The enthalpy of fusion dropped relative to the nylon. When the samples were reheated from 5 to 250 ºC at 10 ºC/min, the nylon had a melting temperature of 220 ºC as shown in Figure 4.4. When the MLS is added, the melting temperature did not vary. However, the enthalpy of melting increased from pure nylon to nanocomposites and the results are reported in Table 4.3. The crystallinity fraction in all the films is calculated as explained in Chapter 3 using the theoretical enthalpy value for 100% crystalline nylon (240 J/g)[2]. The crystallinity fraction in pure nylon and films containing 1, 2, 3, and 5% MLS was determined to be 0.3, 0.41, 0.41, 0.32, and 0.35, respectively. The total crystallinity in all the nanocomposites is higher than that of pure nylon. Cooling scans were recorded from 250 ºC to 5 ºC at 10 ºC/min. The second cool showed the same fusion temperature of 167 ºC for nylon and ~188 ºC for all nanocomposites. This is similar to the first cool (Figure 4.5 and Table 4.4). The width of fusion temperature for nylon was 19 ºC. However, the width of fusion temperature is 11-13 ºC for all nanocomposites. The width of fusion temperature decreased by 6-8 ºC in nanocomposites compared to pure nylon. Figures 4.6 and 4.7 show the melting and fusion temperature in the first and second DSC scan of nylon and nanocomposites. In both scans the difference in melting and fusion temperature is large for nylon compared to nylon nanocomposites. Comparing the first and second heat, there is slight decrease in melting temperature and width of melting region in the second heat. Comparing the first and second cooling thermogram the fusion temperature did not change much in nylon and nylon nanocomposites.

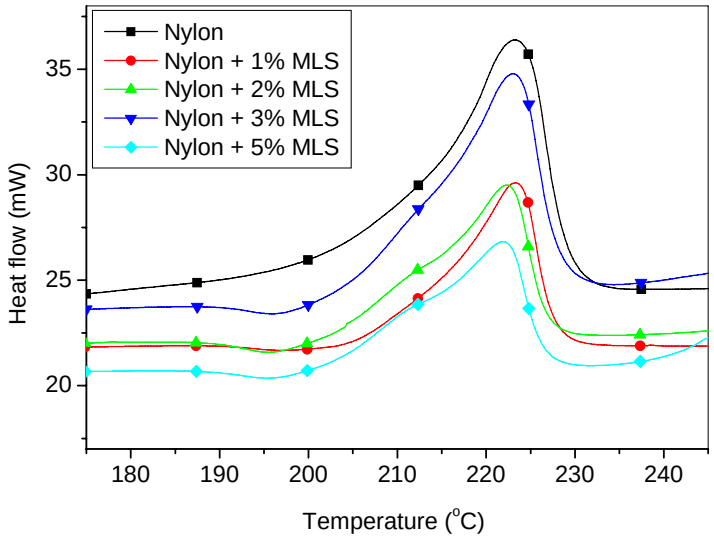

Figure 4.2: DSC of nylon and nanocomposites (first heat).[1]

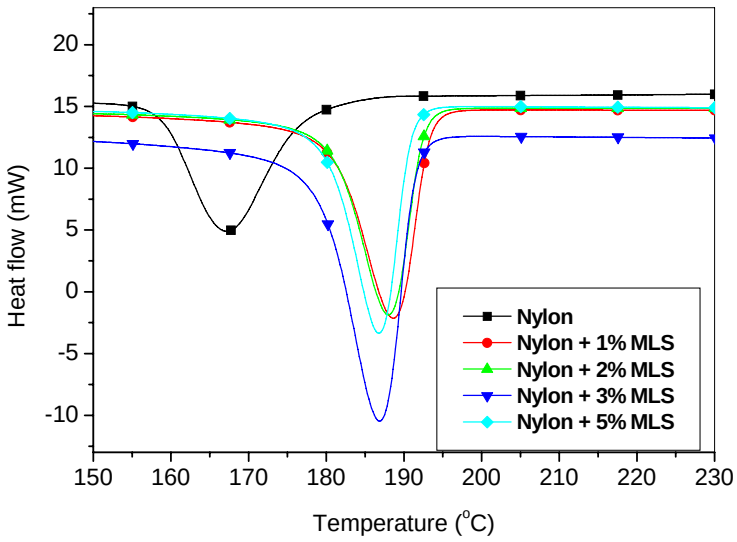

Figure 4.3: DSC of nylon and nanocomposites (first cool).[1]

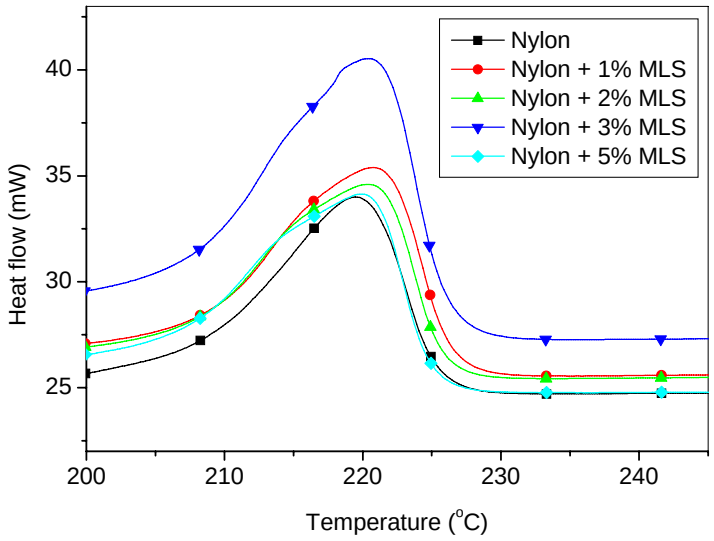

Figure 4.4: DSC of nylon and nanocomposites (second heat).[1]

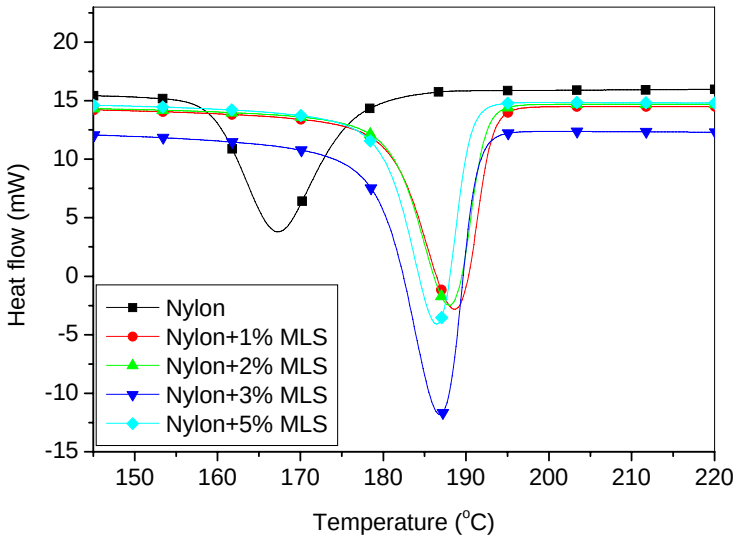

Figure 4.5: DSC of nylon and nanocomposites (second cool).[1]

Table 4.1: DSC data analysis of nylon and nanocomposites in the first heat.[1]

Samples	**T_g (°C)**	**T_m –onset (°C)**	**T_m–end (°C)**	**T_m –width (°C)**	**T_m (°C)**	**ΔH_m (J/gm)**
Nylon	49	210.6	229.1	18.5	223.2	116.6
Nylon +1%MLS	54	211.7	227.6	15.9	223.4	48.4
Nylon +2%MLS	53	209.9	226.8	16.9	222.4	58.7
Nylon +3%MLS	52	210.4	228.1	17.7	222.9	57.0
Nylon +5%MLS	52	207.2	226.3	19.1	221.8	45.3

where T_m_onset, T_m_end, T_m_width, T_m, and ΔH_m are onset of melting temperature, end of melting temperature, width, melting temperature, and enthalpy of melting, respectively.

Table 4.2: DSC data analysis of nylon and nanocomposites in the first cool.[1]

Samples	T_f_onset (ºC)	T_f_end (ºC)	T_f_width (ºC)	T_f (ºC)	ΔH_f (J/gm)
Nylon	177.3	158.6	18.7	167.2	-81.0
Nylon +1%MLS	193.4	180.7	12.7	188.7	-83.9
Nylon +2%MLS	192.6	180.6	11.9	188.0	-81.7
Nylon +3%MLS	191.6	179.1	12.5	186.9	-76.4
Nylon +5%MLS	191.0	179.9	11.1	186.7	-76.8

where T_f_onset, T_f_end, T_f_width, T_f, and ΔH_f are onset of fusion temperature, end of fusion temperature, width, fusion temperature, and enthalpy of fusion, respectively.

Table 4.3: DSC data analysis of nylon and nanocomposites in the second heat.[1]

Samples	T_m_onset (ºC)	T_m_end (ºC)	T_m_width (ºC)	T_m (ºC)	ΔH_m (J/gm)	X_c
Nylon	207.4	225.3	17.9	219.5	72.1	0.30
Nylon +1%MLS	207.3	226.3	19.0	220.8	98.7	0.41
Nylon +2%MLS	206.2	225.7	19.5	220.5	98.4	0.41
Nylon +3%MLS	206.3	226.0	19.8	220.5	77.6	0.32
Nylon +5%MLS	206.0	224.8	18.8	220.0	84.3	0.35

Table 4.4: DSC data analysis of nylon and nanocomposites in the second cool.[1]

Samples	T_f_onset (ºC)	T_f_end (ºC)	T_f_width (ºC)	T_f (ºC)	ΔH_f (J/gm)
Nylon	176.7	159.2	17.5	167.3	-86.4
Nylon +1%MLS	193.3	180.5	12.9	188.7	-87.0
Nylon +2%MLS	192.5	180.4	12.1	188.0	-86.1
Nylon +3%MLS	191.4	179.2	12.2	186.9	-82.1
Nylon +5%MLS	190.6	179.7	10.9	186.4	-77.8

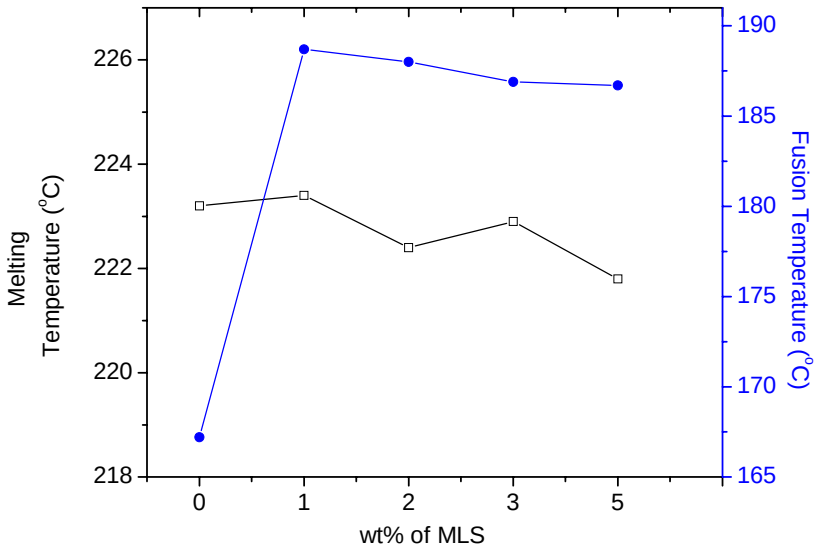

Figure 4.6: Fusion and melting temperatures in the first DSC scan in nylon and nylon nanocomposites.

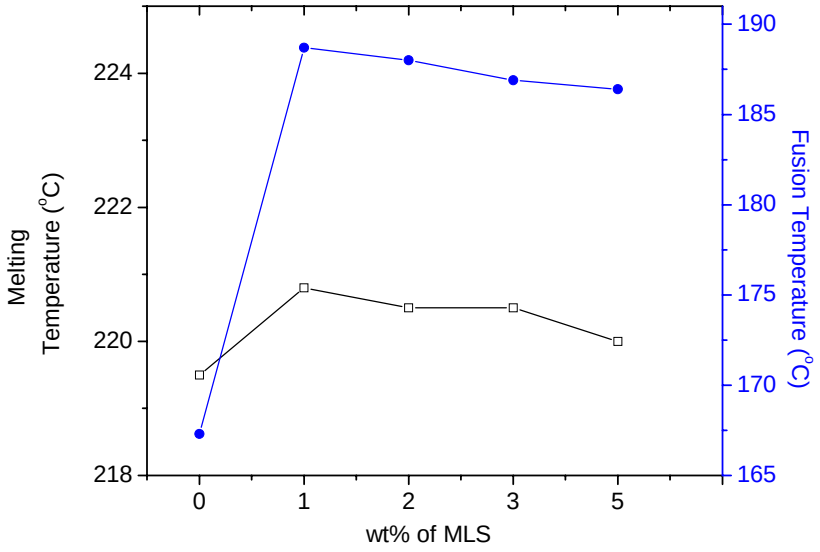

Figure 4.7: Fusion and melting temperature in the second DSC scan in nylon and nylon nanocomposites.

4.1.3 Water Absorption in Nylon

Water absorption in nylon and nylon nanocomposites is measured with time. Figure 4.8 shows the water absorption in the nylon films with time. The maximum percentage of change in weight for nylon is ~ 7% which is observed in ~24 hr. For nylon+3% MLS film, approximately the same percentage of water absorption is observed in ~ 24 hr. The water absorption is saturated after ~ 24 hr for both nylon and nylon nanocomposite films.

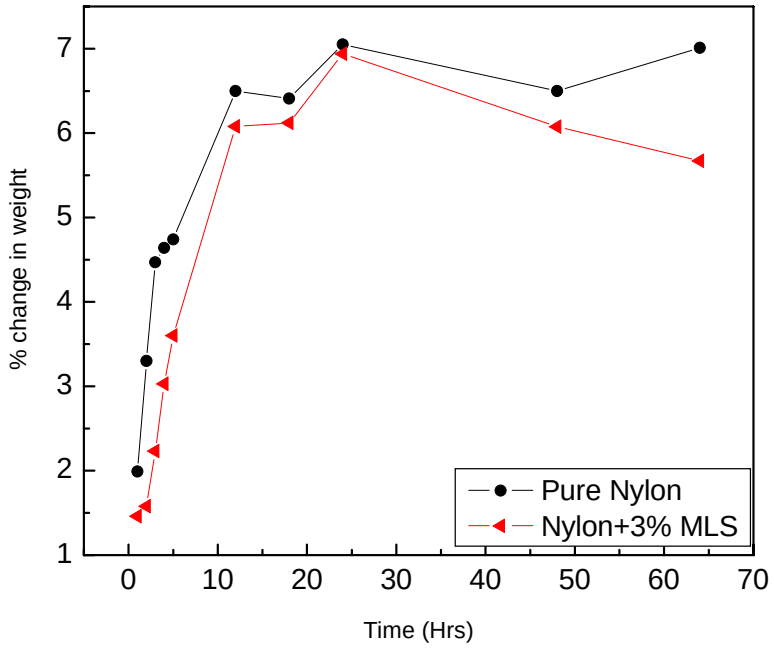

Figure 4.8: Percentage change in weight in pure nylon and nylon+3% MLS samples vs. time in water.

The substantial amount of water absorption could be associated with polar and comparatively higher hydrophilic nature of nylon. The adsorption of water could be more in nylon. Water in the polymer acts as a plasticizer. A small amount of water in a hydrophilic polymer may disrupt the intermolecular bonds, enhancing the main chain mobility. This disruption leads to a decrease in T_g compared to a polymer without water. This decrease in T_g in nylon and

nanocomposite is confirmed from DSC data as shown in Figure 4.9. The T_g of as-processed nylon+2% MLS is 53 ºC. On the other hand, the T_g of annealed nylon+2% MLS is ~120 ºC. When there is no moisture in the sample, the glass transition temperature is more than that of as-processed samples. Such an increase in glass transition (~ 70 ºC) could be due to increase in crystallinity in the annealed sample leaving a lower amorphous fraction in the material.

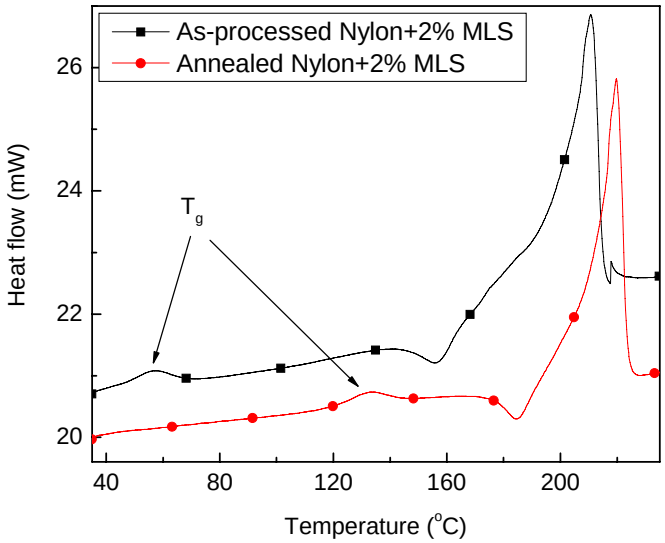

Figure 4.9: Effect of moisture on T_g in nylon+2% MLS nanocomposite films.

The presence of water in the polymer also affects the barrier properties. Water vapor plasticizes the polymer, leading to high mobility of the polymer chains which could affect permeability. The presence of water in the polymer matrix may change the way that gas is adsorbed and diffused through the polymer. The adsorption and diffusion affects the permeability. The tortuous path might vary because of the presence of water molecules in the polymer matrix, which will also affect the permeability. Since 7% water absorption in nylon was observed, the effect of moisture on permeability was studied for nylon films. As-processed nylon samples were annealed at 120 ºC for 24 hr and the permeability of the samples was measured immediately.

4.1.4 Permeability

The permeability of the pure nylon and nanocomposite films was measured on permeability system built in-house as explained in the Chapter 3.[3] There are different units of permeability that has been reported in the literature. For our permeability data, the cc/(m.sec.torr) unit is used. Figure 4.10 shows the permeability as a function of MLS content. Permeability of pure nylon is 7.89 cc/(m.sec.torr). With the addition of 1 wt% MLS, permeability decreased from 7.89E-10 to 5.41E-10 cc/(m.sec.torr). There was no additional decrease in permeability for films containing 2 wt% and 3 wt% MLS. When the MLS content increased by 5wt%, the permeability decreased from 7.89E-10 to 3.22E-10 cc/(m.sec.torr). A maximum drop of 59% in permeability was observed in nylon nanocomposite (nylon+5% MLS) compared to pure nylon.

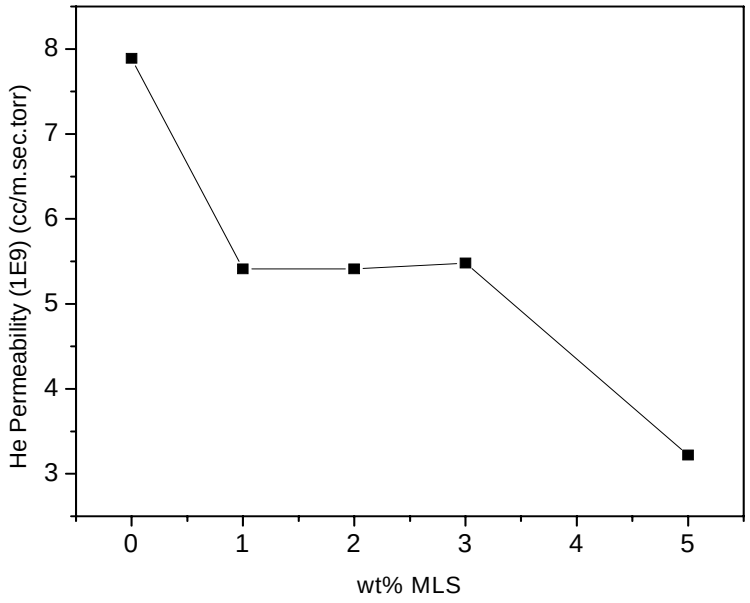

Figure 4.10: Helium permeability of nylon and nanocomposites.[1]

4.1.4.1 Permeability of Fatigued and Biaxially Stretched Nylon Films

The permeability of the fatigued samples is measured immediately after fatigue cycling to avoid aging of the samples. Only one composition of nanocomposite is chosen for fatigue and biaxial stretching to compare with the pure polymer. Permeability of 50 and 10,000 post-fatigue cycled sample was measured Permeability of as-processed pure nylon and nylon+3% MLS are 0.79E-9 and 0.55E-9 cc/m.sec.torr, respectively. Permeability of 50 fatigued cycles of pure nylon and nylon+3% MLS are 0.77E-9 and 0.66E-9 cc/m.sec.torr, respectively. On the other hand, permeability of 10,000 fatigued cycles of pure nylon and nylon+3% MLS are 0.64E-9 and 0.45E-9 cc/m.sec.torr, respectively. The sample after 50 fatigue cycle shows an increase in permeability in nylon+3% MLS as shown in Figure 4.11. For 10,000 fatigue-cycled films, the permeability of pure nylon and nylon+3% MLS films drops by 19 % and 18%, respectively. This indicates that the MLS interfaces enhance defect generation under low cycle fatigue. When subjected to higher fatigue cycles, the permeability for both nylon and its nanocomposite decreased and a possible explanation could be thermal healing and rearrangement of polymer chains.

The permeability of biaxially stretched samples was also measured. By stretching the film in the draw direction followed by in the transverse direction, the permeability of both nylon and its nanocomposite are 0.69E-9 and 0.47E-9 cc/m.sec.torr, respectively. The permeability of biaxially stretched samples showed lower permeability compared to unstretched films in nylon. The maximum drop of 15% in permeability is observed for stretched nylon +3% MLS film. This drop reflects the orientation of polymer chains.

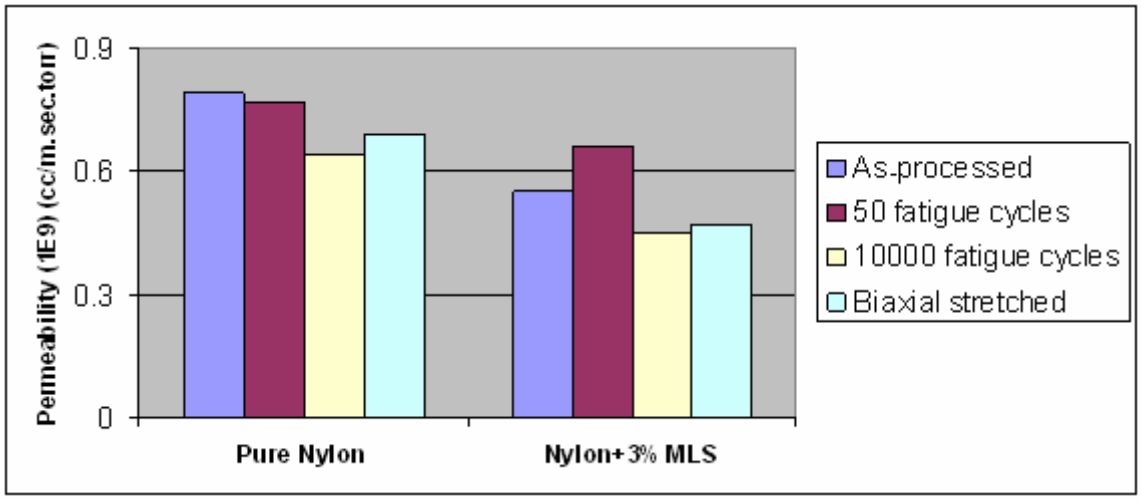

Figure 4.11: Permeability of as-processed, fatigued, and stretched nylon and nanocomposites to helium.

4.1.4.2 Effect of Annealing on Permeability in Nylon

The permeability of the annealed samples was measured similar to the as-processed samples. The permeability of annealed samples was compared with the permeability of as-processed samples. The permeability of as-processed pure nylon is 7.89E-10 cc/(m.sec.torr). The permeability of annealed pure nylon is 10.8E-10 cc/(m.sec.torr). With the addition of 1% MLS in nylon, the permeability of as-processed and annealed samples are 5.4E-10 and 13.8E-10 cc/(m.sec.torr), respectively. With 5% MLS addition in nylon, the permeability of as-processed and annealed samples are 3.2 E-10 and 4.1E-10 cc/(m.sec.torr), respectively. The results reflect that the nylon annealed sample showed higher permeability to the helium gas than the as-processed sample as shown in Figure 4.12. A 37% increase in permeability is observed for annealed samples as compared to as-processed pure nylon samples. However, a 28% increase in permeability is observed for annealed samples as compared to as-processed nylon+5% MLS samples. A possible reason could be that moisture in the sample occupies the free volume and does not let the gas permeate through. Though an increase in permeability is observed both in annealed nylon and

nanocomposites, a lower percentage increase in permeability is observed in annealed nanocomposites compared to annealed pure nylon. An increase in T_g is also observed in annealed samples. If the increase in T_g is due to increase in crystallinity in the annealing process, a decrease in permeability is expected. However, an increase in permeability is observed in annealed samples and the reason is not clear.

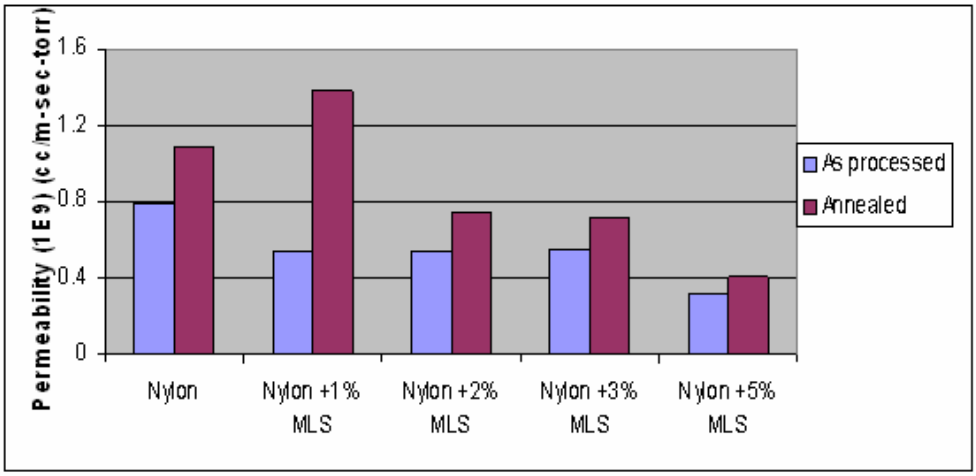

Figure 4.12: Comparison of permeability of as-processed and annealed nylon nanocomposites.

4.1.5 Tensile Properties of Nylon and Nanocomposites

The tensile properties of nylon and nanocomposites are measured and tabulated in Table 4.5. The yield strength and the modulus of pure nylon are 23 MPa and 1.2 GPa, respectively. The yield strength increased from 23 to a maximum of 28 MPa with the addition of 5 wt% MLS. The addition of MLS improved the yield strength of nylon. UTS also increased from 28 to a maximum of 36 MPa for PET to nanocomposite film containing 5% MLS. The modulus of pure nylon and nylon+1% MLS are 1.2 and 0.9 GPa, respectively. The improvement in yield stress and UTS is observed for all the compositions of nanocomposites. On the other hand, a decrease in modulus is observed for films with 1 and 2 wt% MLS, but films with 5 wt% MLS showed a slight increase in modulus.

Table 4.5: Tensile properties of nylon nanocomposite.[1]

Samples	Yield strength (MPa)	UTS (MPa)	Modulus (GPa)
Nylon	23	28	1.2
Nylon+1% MLS	25	31	0.9
Nylon+2 % MLS	26	32	1.0
Nylon+3 % MLS	27	35	1.2
Nylon+5 % MLS	28	36	1.3

4.1.6 Summary for Nylon Nanocomposites

To summarize, for nylon nanocomposites, an exfoliated structure can be inferred from the XRD data. When MLS is introduced in nylon, an increase in nucleation rate is observed. A decrease of 59% in permeability was obtained with the addition of 5% MLS. An improvement in mechanical properties was also observed.

4.2 PET Nanocomposites

4.2.1 Dispersion of MLS in Nanocomposites

An experimental assessment of the dispersion of PET nanocomposites was first done by XRD. Figure 4.13 shows the diffraction pattern of PET, MLS, and nanocomposites. MLS has two characteristic peaks at low 2Θ equal to 4.6 º (001) and 9 º (002). The peak (001) and (002) corresponds to an original platelet spacing of 1.9 and 1 nm, respectively. In the PET nanocomposite, there are two different MLS peaks, at 2Θ of ~2 and 5 º is observed. Though a sharp peak of MLS is not observed, two small peaks corresponding to the (001) and (002) are observed for films containing more than 1 % MLS. In PET nanocomposites, the intensity of the (001) peak is observed at lower 2Θ than the pure MLS peaks, indicating an increase in d spacing. $d_{(001)}$ and $d_{(002)}$ are determined to be 4.4 and 1.76 nm. Therefore, an intercalated dispersion can be inferred. Further dispersion analysis was performed using TEM as shown in Figures 4.14 and 4.15.

It confirms the presence of an intercalated structure. The width of the MLS is determined by using Image J ® software and is found to be in the range of 13-15 and 65-70 nm. Therefore, a combination of intercalated and exfoliated dispersion is inferred in PET nanocomposites.

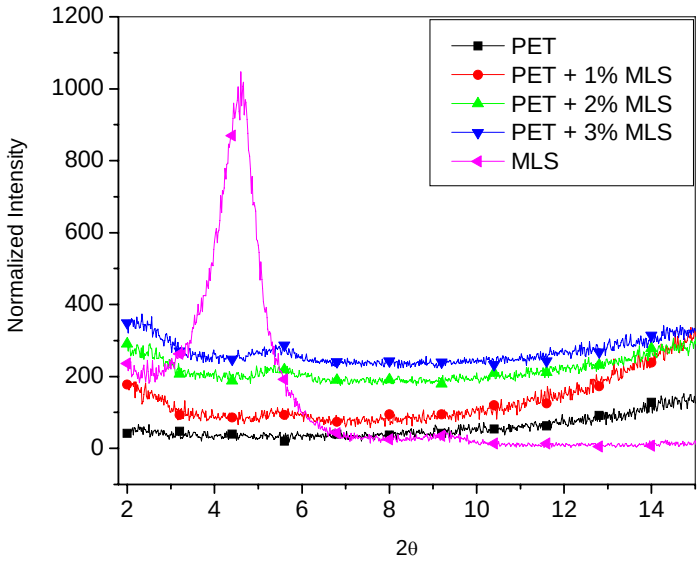

Figure 4.13: XRD of PET, MLS, and nanocomposites.

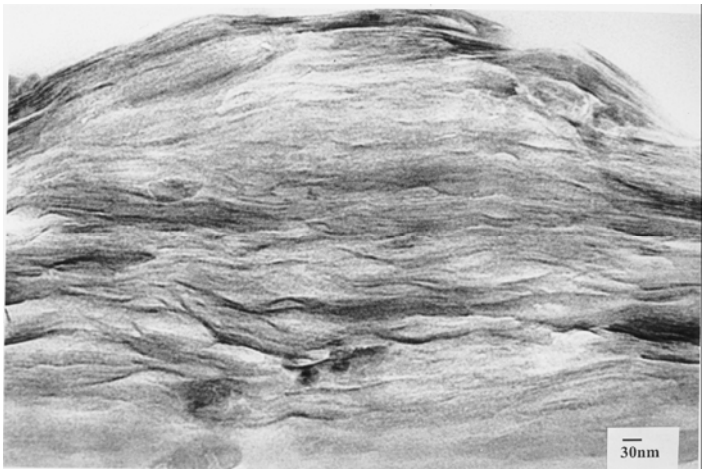

Figure 4.14: TEM micrographs of PET nanocomposites.

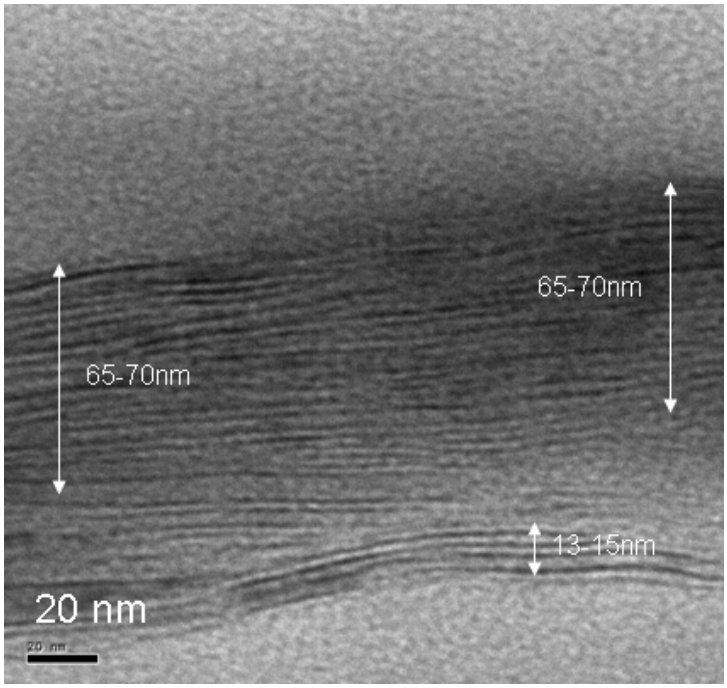

Figure 4.15: TEM micrographs of PET nanocomposites.

4.2.2 Effect of MLS on Thermal Transitions in PET

The effect of MLS on thermal transitions and crystallization in PET are studied. Samples were heated from 30 to 280 ºC at 10 ºC/min. The glass transition and melting point of PET in the first heat are 69 and 245 ºC, respectively. The glass transition of PET+1% MLS is 67 ºC (Tables 4.6-4.7) and did not change with the addition of 1% MLS. Cold crystallization is observed in the first heat. The cold crystallization temperature (T_{cc}) of pure PET in the first heat is 133 ºC. The cold crystallization temperature decreased by ~10 ºC with 3% MLS addition. The melting point of PET+1% MLS is 248 ºC as shown in Figure 4.16. A very slight increase in melting point is observed when MLS is introduced into PET. The width of melting temperature decreased from 21 to 12 ºC with the addition of 1% MLS. Therefore, the smaller size of crystallites can be inferred in nanocomposites. After the samples were annealed for 30 minutes at 280 ºC, they were cooled from 280 ºC to 30 ºC at 10 ºC/min. In the cooling scan, the fusion point was analyzed. Figure 4.17

shows the DSC heat flow of PET and its nanocomposites while cooling. The fusion temperature of pure PET in the first scan is 211 ºC (Table 4.8). When 1% MLS is introduced, the fusion temperature is 208 ºC. Again samples were heated from 30 to 280 ºC at 10 ºC/min and melting point of PET and nanocomposites are studied. Melting point of PET is 246 ºC and when 3% MLS is introduced melting point decreased to 241 ºC (Figure 4.18, Table 4.9). While cooling the sample from 280 ºC to 30 at 10 ºC/min, fusion temperature is recorded. The fusion temperature of pure PET is 211 ºC and it decreased to 205 ºC with the addition of 3 % of MLS as shown in Figure 4.19 and reported in Table 4.10. The melting temperature of PET+1% MLS in the first and second heat is 248 and 244 ºC, respectively. With the addition of MLS, change in T_m is observed as shown in Figure 4.17. The fusion temperature of pure PET remained same in first and second heating cycle. The fusion temperature of PET+1% MLS also did not vary in the first and second heat. The fusion and melting temperature vs. MLS concentration is plotted for PET for both first and second scan as shown in Figures 4.20 and 4.21. In the first heat the difference in melting and fusion temperature increases with addition of 1%MLS. Therefore, the addition of MLS has affected supercooling in PET. There is not significant variation in difference in melting and fusion temperature in the second scan. Cold crystallization is observed only in the first heat and it did not show any peak in the second heat. The enthalpy of cold crystallization also increased from 35 to 37 J/gm from pure PET to PET+1% MLS nanocomposite. Though ΔH did not increase much from pure PET to nanocomposites, however, the combination of decrease in T_{cc} and ΔH shows the crystallites did not grow fully, therefore, hindered growth of crystallites can be inferred. Pendse et al. [4] used Gibb's-Thompson equation to determine the solid liquid interfacial surface energy as presented in Chapter 2, it increased with increase in MLS content. It is 15, 3520 mJ/m^2 for PET+1%MLS and PET+3%MLS, respectively. The higher the surface energy, the more difficult it is to grow the

bigger the spherulites which correlates well this cold crystallization temperature and enthalpy of cold crystallization. If the cold crystallization fraction is normalized to pure PET, it increased from 1 to 1.07 for PET+1% MLS nanocomposite. Therefore, the amorphous region surrounding the crystallites increased and thereby, density decreased (It is proved experimentally and explained later in this dissertation in Chapter 5). Both the cold crystallization temperature and fusion temperature decreased by ~ 5 ºC with the addition of MLS in PET. Our group had probed the effect of MLS addition on crystallization in PET.[4] When observed in the polarized optical microscopy, pure polymer showed bigger spherulites, but when the MLS is introduced, it acts as a nucleating agent and small uniform spherulites are formed. Crystallinity fraction is calculated as explained in Chapter 3 using the theoretical value for 100% crystalline PET (140 J/g)[5]. Crystallinity fraction of pure PET and films containing 1, 2, and 3% MLS are 0.43, 0.43, 0.42 and 0.46, respectively. Crystallinity did not vary in PET+1% MLS and PET+2% MLS compared to pure PET, however, it increased from 0.43 to 0.46 in PET+3% MLS.

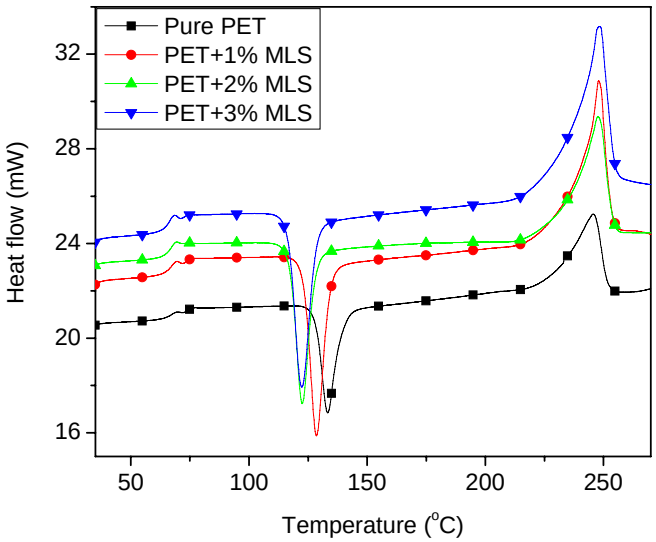

Figure 4.16: DSC of PET and nanocomposites (first heat).

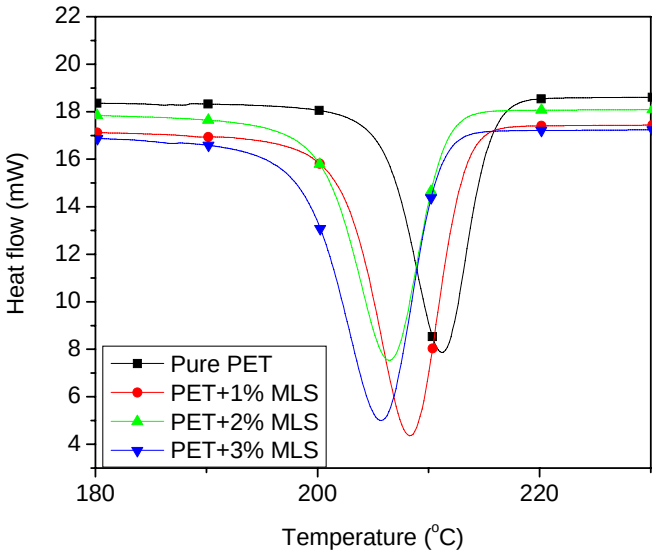

Figure 4.17: DSC of PET and nanocomposites (first cool).

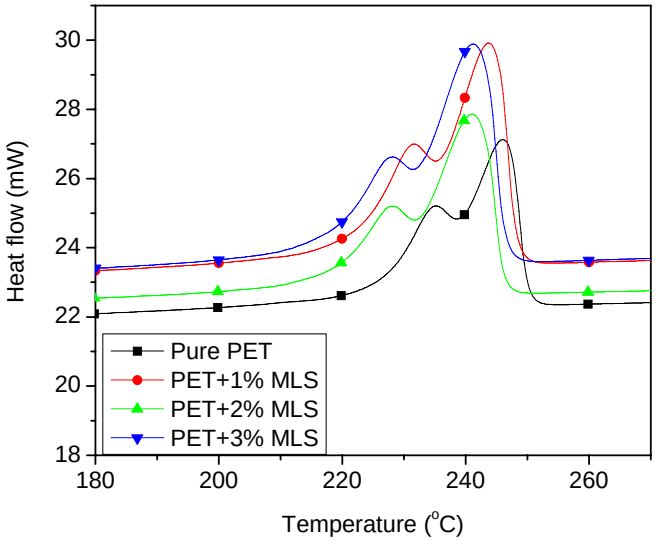

Figure 4.18: DSC of PET and nanocomposites (second heat).

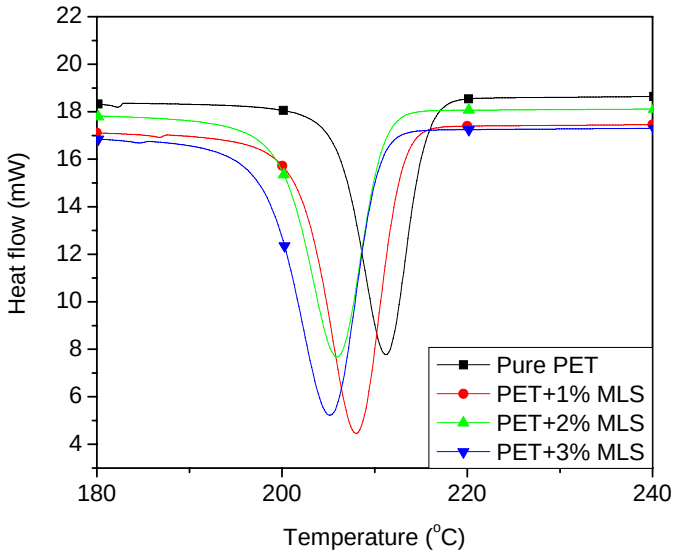

Figure 4.19: DSC of PET and nanocomposites (second cool).

Table 4.6: DSC data analysis of PET and nanocomposites in the first heat.

Sample	T_g (°C)	T_{cc}_onset (°C)	T_{cc}_end (°C)	T_{cc}_width (°C)	T_{cc} (°C)	ΔH_{cc} (J/gm)	X_{cc}
PET	67.0	128.2	139.5	11.3	133.3	-35.2	1.00
PET + 1%MLS	67.5	123.2	134.3	11.1	128.5	-37.6	1.07
PET + 2%MLS	67.2	117.4	128.1	10.7	122.5	-37.4	1.06
PET + 3%MLS	66.7	116.7	128.5	11.8	122.3	-34.3	0.97

where T_{cc}_onset, T_{cc}_end, T_{cc}_width, T_{cc}, and ΔH_{cc} are onset of cold crystallization temperature, end of cold crystallization temperature, width, cold crystallization temperature, and enthalpy of cold crystallization, respectively. X_{cc} refers to cold crystallization fraction normalized to pure PET

Table 4.7: DSC data analysis of PET and nanocomposites in the first heat for melting peak.

Sample	T_m_onset (°C)	T_m_end (°C)	T_m_width (°C)	T_m (°C)	ΔH_m (J/gm)
PET	230.8	251.8	21.0	245.6	50.1
PET + 1%MLS	240.8	253.0	12.0	248.0	57.8
PET + 2%MLS	236.0	253.7	18.0	247.6	57.8
PET + 3%MLS	239.1	254.5	15.0	248.2	62.0

Table 4.8: DSC data analysis of PET and nanocomposites in the first cool.

Sample	T_f_onset (ºC)	T_f_end (ºC)	T_f_width (ºC)	T_f (ºC)	ΔH_f (J/gm)
PET	205.9	215.6	9.8	211.2	-69.9
PET + 1%MLS	202.1	213.2	11.1	208.3	-66.5
PET + 2%MLS	200.3	211.4	11.2	206.5	-62.6
PET + 3%MLS	198.7	211.0	12.2	205.7	-60.3

Table 4.9: DSC data analysis of PET and nanocomposites in the second heat.

Sample	T_m_onset (ºC)	T_m_end (ºC)	T_m_width (ºC)	T_m (ºC)	ΔH_m (J/gm)	X_c
PET	234.8	250.1	15.0	246.1	60.2	0.43
PET + 1%MLS	231.9	248.2	16.0	243.9	60.2	0.43
PET + 2%MLS	229.3	246.2	17.0	240.9	58.8	0.42
PET + 3%MLS	228.7	246.4	18.0	241.3	64.4	0.46

Table 4.10: DSC data analysis of PET and nanocomposites in the second cool.

Sample	T_f_onset (ºC)	T_f_end (ºC)	T_f_width (ºC)	T_f (ºC)	ΔH_f (J/gm)
PET	206.0	215.6	9.6	211.2	-68.4
PET + 1%MLS	201.7	212.9	11.2	207.9	-67.5
PET + 2%MLS	199.7	210.9	11.3	206.0	-62.1
PET + 3%MLS	198.2	210.4	12.3	205.3	-59.3

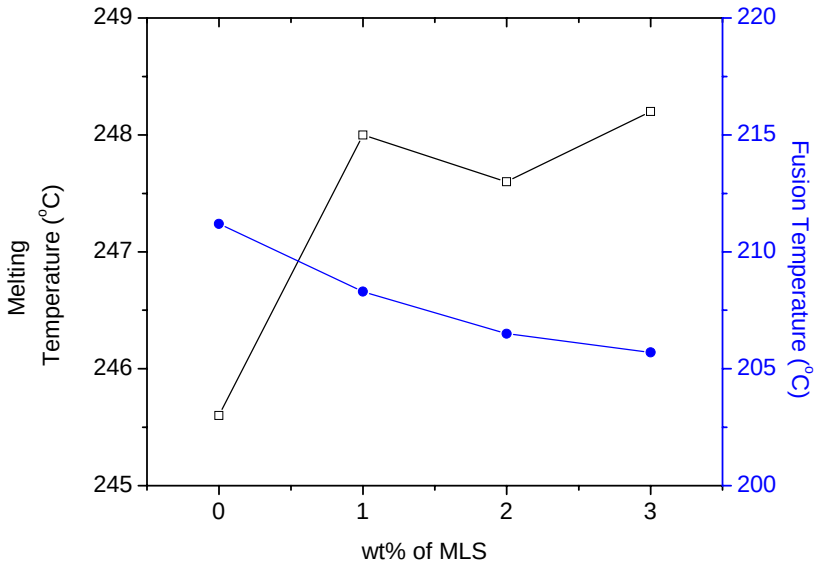

Figure 4.20: Fusion and melting temperature in the first DSC scan in PET and PET nanocomposites.

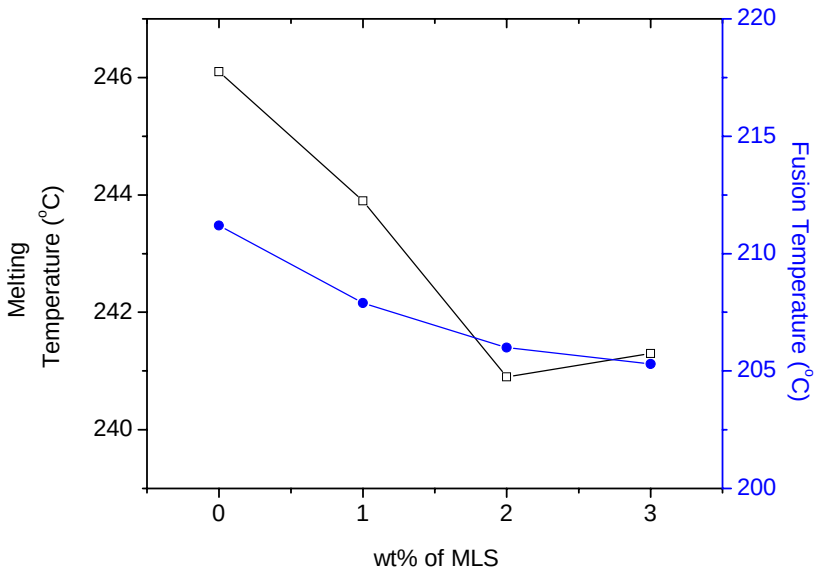

Figure 4.21: Fusion and melting temperature in the second DSC scan in PET and PET nanocomposites.

4.2.3 Water Absorption in PET

Water absorption is measured as a function of time in PET and nanocomposites. Figure 4.22 shows water absorption in the films with time. For pure PET sample, the maximum water absorption is only 0.62% and for PET+3% MLS sample it is still less (0.42 %). For both PET and PET nanocomposite, the maximum water absorption is less than 1%. The maximum percentage change in weight due to water absorption is observed at ~24 hr and it decreases after that. PET films show less water absorption even after 64 hrs.

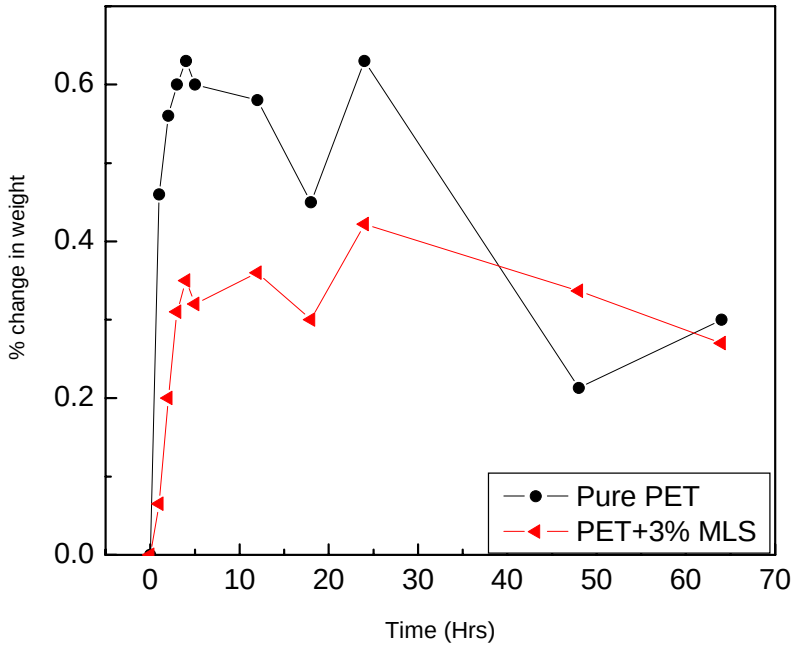

Figure 4.22: Percentage change in weight in pure PET and PET+3% MLS vs. time in water.

4.2.4 Permeability

The permeability is studied as a function of MLS in PET. For pure PET, the permeability is 3.7E-9 cc/(m.sec.torr) and for PET+3% MLS film, it is 1.35E-9 cc/(m.sec.torr). Permeability as a function of MLS is plotted (Figure 4.23). Helium permeability increased in PET+1% MLS film; however, the permeability is decreased in PET+2% MLS and PET+3% MLS film. Oxygen

permeability of pure PET is 9.53E-12 cc/(m.sec.torr). Oxygen permeability in the polymer is always less than helium permeability, oxygen being a larger gas molecule compared to helium. Solubility of oxygen in the polymer is also different from helium. Therefore, permeability to oxygen in a given polymer is different from helium. Permeability in PET+1% MLS and PET+2% MLS are 10E-12 and 10.2E-12 cc/(m.sec.torr), respectively. Permeability in nanocomposites containing 1 and 2 % MLS are higher than the base PET. However, permeability of PET+3% MLS is 7.92E-12 cc/(m.sec.torr). Oxygen permeability of PET nanocomposites increased in PET+1% MLS and PET+2% MLS and decreased in 3%MLS composition compared to pure PET as shown in Figure 4.24. Since helium permeability decreases and oxygen permeability increases in PET+2% MLS film, it is not the tortuosity factor but solubility that that play a role in determining the permeability. The decrease and increase in permeability in nanocomposites is analyzed later in this chapter.

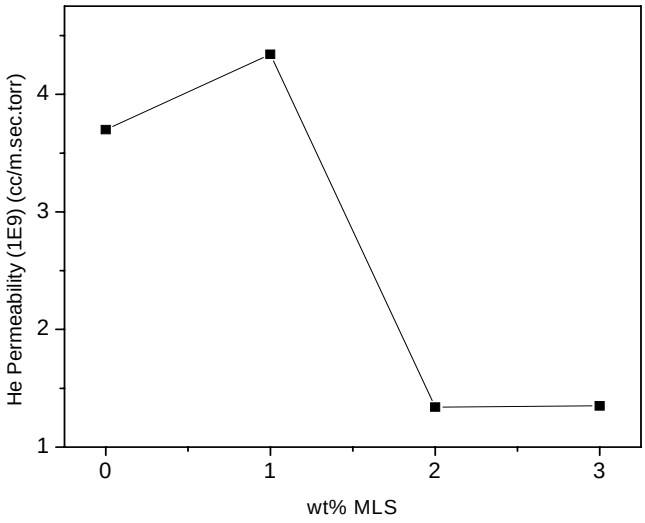

Figure 4.23: Helium permeability of PET and nanocomposites.

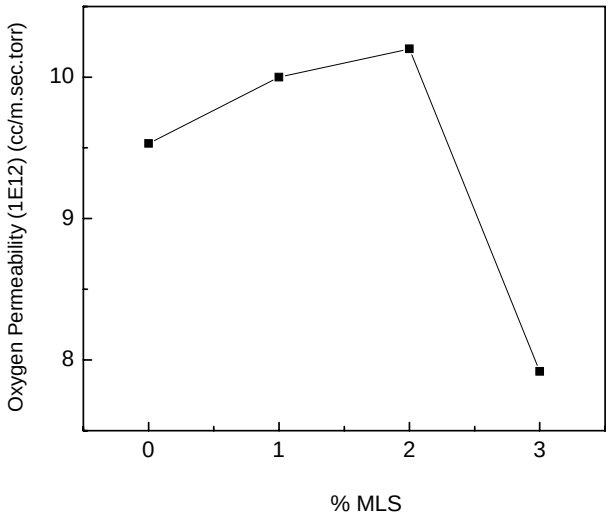

Figure 4.24: Oxygen permeability of PET and nanocomposites.

4.2.4.1 Permeability of Fatigued and Biaxially Stretched Films

Permeability of post-fatigued sample was measured. Permeability of as-processed pure PET and PET+3% MLS are 3.7E-9 and 1.35E-9 cc/m.sec.torr, respectively. Permeability of 50 fatigued cycles of pure PET and PET+3% MLS are 6.92E-9 and 3.45E-9 cc/m.sec.torr, respectively. Permeability increased when the sample was subjected to 50 fatigue cycles compared to as processed sample. Permeability of 10,000 fatigued cycles of pure PET and PET+3% MLS are 3.47E-9 and 3.61E-9 cc/m.sec.torr, respectively. For 10,000 fatigue cycled films, an increase in permeability is observed when MLS is added into PET. However, permeability of pure PET drops by 6% compared to permeability of as-processed PET. For PET+ 3% MLS film, an increase in permeability is evident as shown in Figure 4.25.

Oxygen permeability of pure PET and PET+3% MLS are 9.53E-12 and 7.92E-12 cc/(m.sec.torr), respectively. Permeability of 50 and 10,000 post fatigued PET sample is 5.02E-12 and 5.79E-12 cc/(m.sec.torr), respectively as reported in Table 4.11. Therefore, permeability of

post fatigued PET sample is decreased compared to as-processed PET. Permeability of 50 and 10,000 post fatigued PET+3% MLS sample is 2.16E-12 and 4.6E-12 cc/(m.sec.torr), respectively. Both 50 and 10000 fatigue cycled PET and PET+3% MLS nanocomposite showed a decrease in oxygen permeability compared to as-processed samples. However, an increase in permeability is observed for 10,000 post fatigued sample compared to 50 post fatigued sample. This decrease in permeability could be reflective of molecular chain rearrangement during the fatigue cycling in the materials. The behavior of the helium permeability in fatigued nanocomposite sample is different than the oxygen permeability and again the reason could be solubility of oxygen in sample.

The helium permeability of biaxial stretched PET and its nanocomposite are 4.68E-9 and 3.65E-9 cc/m.sec.torr, respectively. Biaxial stretching increased the permeability in both PET and nanocomposite as compared to as-processed samples. Oxygen permeability of PET and stretched PET are 9.53E-12 and 9.57E-12 cc/m.sec.torr, respectively. There is not much change in oxygen permeability in as-processed and stretched PET. Comparing the permeability of as-processed to stretched PET+3% MLS sample, a decrease in permeability from 7.92E-12 to 6.03 E-12 cc/m.sec.torr is observed (Table 4.11). An increase in permeability for helium is observed in stretched PET and nanocomposite, on the other hand, a decrease in oxygen permeability is observed.

From the experimental data it shows that a drop in oxygen permeability for 10,000 fatigued samples is more than the stretched films when compared to as-processed films for PET. Therefore, to verify if any additional crystallization occurred during fatigue, the DSC test was performed. The results did not show any crystallization when the sample flexes for both 50 and 10000 cycles. Unlike nylon, any mechanical force contributed to increased permeability in the nanocomposite compared to the as processed film. Thus it appears that the PET host does not have a strong

interfacial strength to the MLS and no thermal healing or recrystallization occurs under mechanical loads in PET nanocomposites.

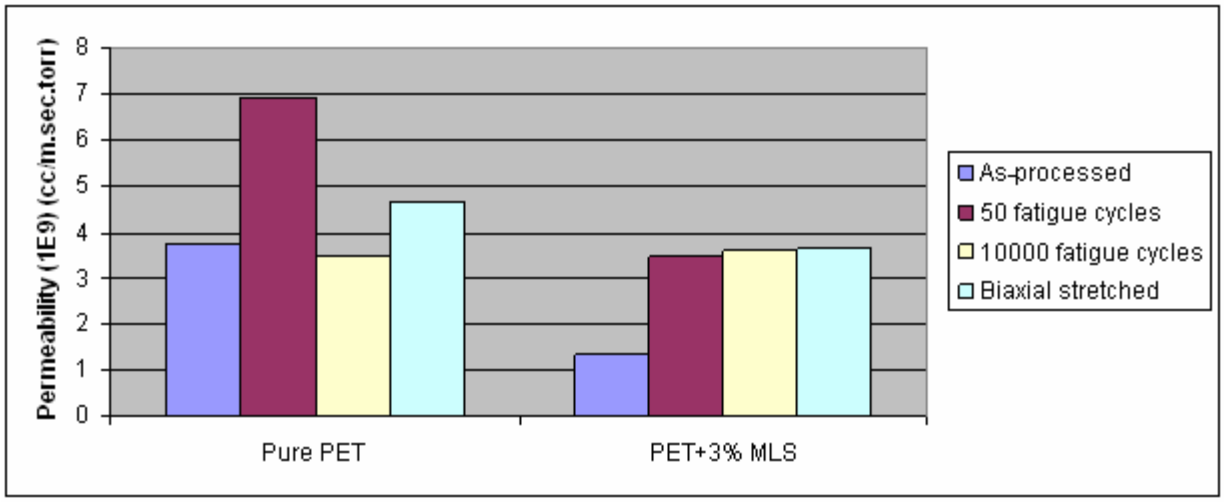

Figure 4.25: Permeability of as-processed, fatigued, and stretched PET and nanocomposites to helium.

Table 4.11: Permeability of as-processed, fatigued, and stretched PET and nanocomposites for oxygen.

Sample	**As-processed Permeability (1E12) (cc/m.sec.torr)**	**Fatigued (50 cycles) Permeability (1E12) (cc/m.sec.torr)**	**Fatigued (10,000 cycles) Permeability (1E12) (cc/m.sec.torr)**	**Stretched Permeability (1E12) (cc/m.sec.torr)**
PET	9.53	5.02	5.79	9.57
PET+3% MLS	7.92	2.16	4.60	6.03

4.2.5 Tensile Properties of PET and Nanocomposites

Tensile properties of PET and nanocomposites were determined. The yield strength and modulus of PET are 44 MPa and 2 GPa, respectively. The yield strength decreased from 44 to 35 MPa with the addition of 3% MLS. PET has a higher yield strength compared to the

nanocomposites. The UTS also followed the same trend. On the other hand, modulus of PET+3% MLS 2.3 GPa and it is higher than that of PET. Tensile results of PET and nanocomposites are tabulated in Table 4.12. Chang et al. [6] observed that with the increase in clay, initially the mechanical properties increases but with an increase in MLS content, mechanical properties started deteriorating in PETN. Pegoretti et al. observed a decrease in mechanical properties with increase in clay in recycled PET which is reported in Table 2.5 in Chapter 2.[7] In all these tensile data, the percentage error is 10-15 % based on the results from the average of 5 tests for one sample.

Table 4.12: Tensile properties of PET nanocomposites.

Samples	Yield stress (MPa)	Elastic modulus (GPa)	UTS (MPa)
PET	43.5±2	2±0.2	58.8±2.5
PET + 1%MLS	36.7±3.1	2.6±0.3	48±2
PET + 3%MLS	35.2±2.5	2.3±0.3	49.4±2

4.2.6 Summary for PET Nanocomposites

To summarize, for PET nanocomposites, a combination of intercalation and exfoliation was inferred. An increase in permeability was observed in some compositions of nanocomposites unlike nylon nanocomposites though the same MLS and processing steps were used to process the nanocomposites. An increase in fusion temperature was observed in nylon. On the other hand, a decrease in fusion temperature was observed in PET nanocomposites. With the addition of MLS, an improvement in mechanical properties was obtained in nylon nanocomposite. A decrease in yield strength and UTS was observed in PET. From the above results, it is clear that nylon nanocomposites showed improved properties unlike PET nanocomposites compared to the base matrix. To understand the effect of MLS on the matrix and permeability further, another semicrystalline polymer, PEN was studied.

4.3 PEN Nanocomposites

4.3.1 Dispersion of MLS in Nanocomposites

To understand the dispersion of MLS in PEN, XRD, SEM, and TEM of PEN nanocomposites were studied. XRD of PEN nanocomposites are shown in Figure 4.26. For the MLS, the peak is observed at 2Θ of 5.11 º for (001) corresponding to 1.73 nm interlayer spacing. In our nanocomposites, the characteristic peaks for MLS are shifted to the right (i.e., 2Θ increased) compared to pure MLS. Therefore, decreased d spacing is observed in nanocomposites. The distance between the individual layers of the MLS (basal spacing or the d spacing) was calculated by using Bragg's equation, $n\lambda = 2d\sin\Theta$, where λ is wavelength of Cu K_α radiation (0.154056 nm), Θ is the angle of diffraction and d is the platelet spacing. The (001) peak is observed in all the nanocomposites from 6.24 to 6.39 º. In all the nanocomposites, the d spacing is decreased from 1.73 to (1.38-1.41) nm. A sharp reflection peak is observed in all nanocomposites except for PEN+1%MLS–3S indicates intercalated nature of nanocomposites. The d spacing calculation from Bragg's equation shows that MLS layers are dispersed in the PEN matrix (Table 4.13). This was further investigated from images using SEM cross section and TEM.

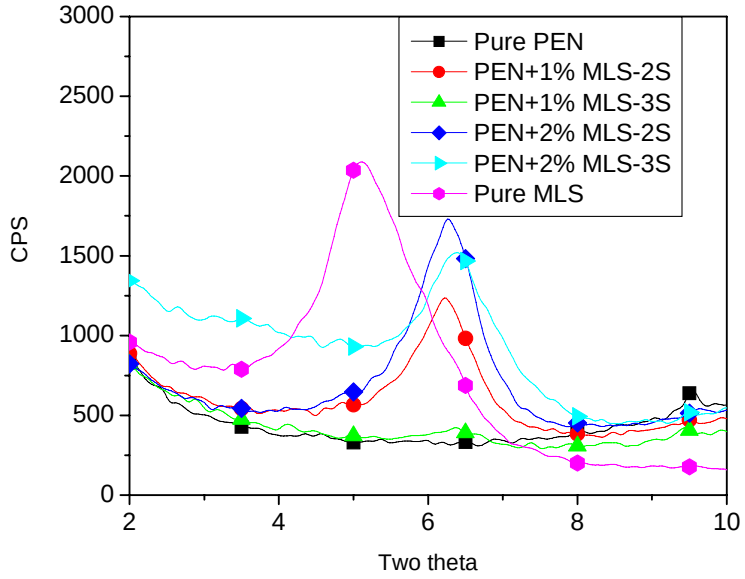

Figure 4.26: XRD of PEN, MLS and nanocomposites.

Table 4.13: d spacing of PEN nanocomposites.

Sample	**2Θ (º)**	**d(nm)**	**Average thickness of plates (from SEM) nm based on number of MLSs**	**Distance between plate aggregates**
Pure MLS	5.11	1.73	-	-
PEN+1%MLS-2S	6.24	1.41	15±5 (5 MLSs)	650±300
PEN+1%MLS-3S	6.36	1.39	13±8 (4 MLSs)	900±150
PEN+2%MLS-2S	6.26	1.41	20±10 (13 MLSs)	150±100
PEN+2%MLS-3S	6.39	1.38	20±15 (10 MLSs)	600±200
PEN+10%MLS master batch	-	-	10±5 (10 MLSs)	-

After observing a sharp (001) reflection peak, further dispersion analysis was performed by SEM and TEM for one sample. SEM cross sections of all PEN nanocomposites are shown in Figures 4.27-4.30. All nanocomposites also show well dispersed structures. The thickness of platelets is calculated at various points on the MLSs using Image J ® software and is reported in Table 4.13. The highest MLS percentage in the master batch, PEN+10%MLS shows a combination of intercalated and exfoliated dispersion (Figure 4.27). The average thickness of the platelets is

determined to be ~10 nm with a range of 8-15 nm. After dilution with PEN, in PEN+1% MLS-2S sample, the average thickness of platelets was found to be 15 nm with a range of 10-20 nm (Figure 4.28). Separating mixing from film processing stages for the same concentration PEN +1%MLS-3S are shown in Figure 4.29. Marginal change in average plate thickness 13 nm was observed but the range changed to (5-15) nm. With increased concentration of MLS, (PEN+2% MLS-3S) the average thickness is determined to be ~20 nm with a range of (10-25) from Figure 4.30 The two stage processed sample, PEN+2% MLS-2S for the same composition had same average plate thickness of 20 nm with a range of (10-30) nm.

The master batch shows the lowest average thickness of MLS platelets compared to all other nanocomposites. For the diluted samples, with increase in MLS concentration, the thickness of MLS platelets also increases.

Only one PEN nanocomposite sample was investigated in TEM. TEM images of PEN+1%MLS-2S nanocomposites also show dispersed structures as shown in Figures 4.31- 4.33. The average thickness of MLS from Figure 4.31 is determined to be ~6 nm with a range of (3-7) nm. Similarly the average thickness of MLS plates from Figure 4.32 is ~2.5 nm with a range of (2-3) nm. Figure 4.33 showed similar result to Figure 4.32.Though the ideal thickness of MLS from XRD is determined to be 1.7 nm, the SEM and TEM image shows the thickness to be ~ (10-15) nm i.e. 5-8 MLSs are agglomerated in nanocomposites. Given that the XRD peak also shifts to the right indicating decreased d-spacing, we conclude that MLS platelet collapse is occurring similar to reported in the literature presumably due to loss of organofunctional layers from within the galleries. This increase in thickness of MLS could be collapse of OH group in the surfactant in Cloisite 30B clay (methyl, tallow, bis-2-hydroxyethyl, quaternary ammonium), therefore, having more than one MLS platelets instead of just one. The driving force for this collapse could be

related to miscibility of PEN and the methyl, tallow, bis-2-hydroxyethyl, quaternary ammonium of the MLS. The distances between the plates indicate that while intercalated, the layers are well dispersed in the matrix. The distance between the neighboring clay is calculated. The distance between the MLSs in PEN+1%MLS film-2S is varied from 500-1000 nm. The interplate distances are considerable as indicated in Figure 4.28. The average distance between two neighboring plates is ~ 550 nm. The thickness of plates is ~15 nm indicating that around 8 to 9 plates remain undispersed. The TEM image showed the average thickness is ~10 nm. It could be two different regions of sample are investigated in SEM and TEM separately. Based on TEM and SEM images, the average thickness ((10+15)/2=12.5) 12.5 nm. Similarly, for PEN+1%MLS-3S, the interplate distances are considerable as indicated in Figure 4.29. Excluding the two MLS plates at the edge in the Figure 4.29, the average distance between plates is ~900 nm. The thickness of MLS plates is ~13 nm indicating that around 7 to 8 plates remain undispersed. For PEN+2%MLS-1S, the distance between plates is ~600 nm and the average thickness of plates is ~ 20 nm (Figure 4.30 (a)). In PEN+2% MLS- 3S film, the platelets are separated from each other randomly as intercalated platelets are well dispersed randomly (Figure 4.30). The minimum distance was observed between platelets 9 and 10 and it was 240 nm. The longest distance is observed between 2 and 7 and it was 650 nm. The corresponding line thickness is ~20nm indicating that around 11 to 12 plates remain undispersed. This distance indicates that the MLSs are dispersed randomly giving a good dispersion of intercalated structure.

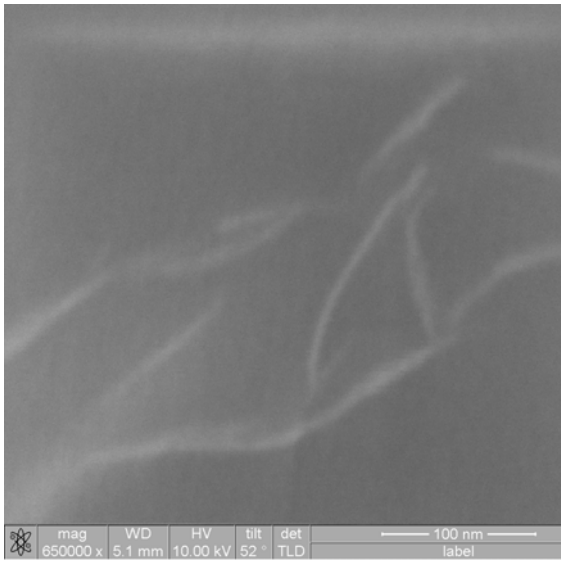

Figure 4.27: SEM of FIB cross section of PEN+10%MLS master batch.

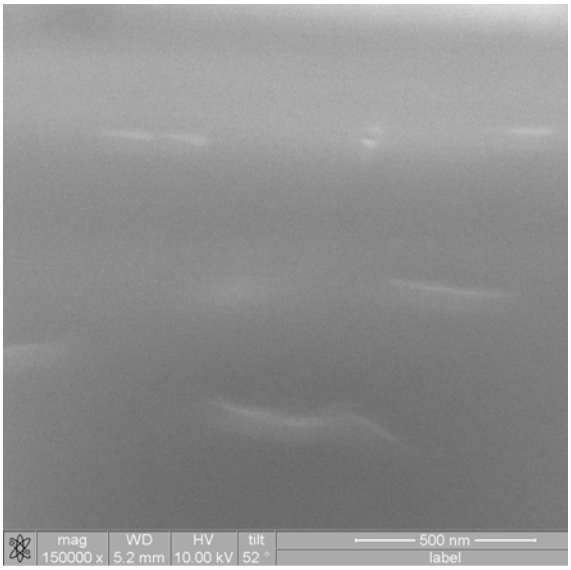

Figure 4.28: SEM of FIB cross section of PEN+1% MLS-2S.

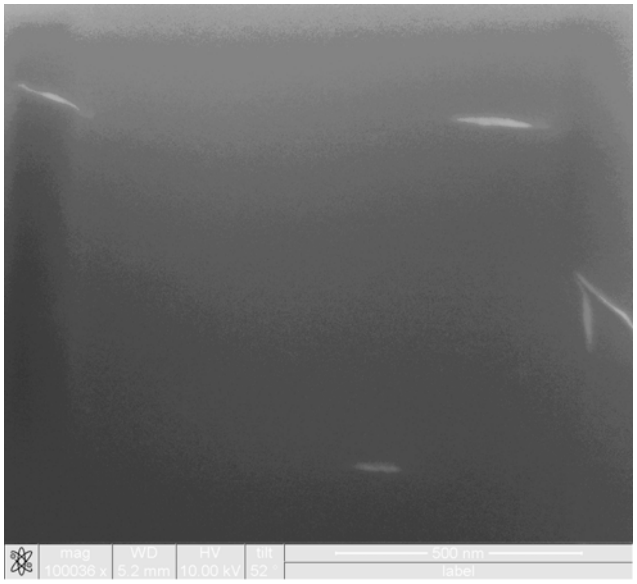

Figure 4.29: SEM of FIB cross section of PEN+1% MLS-3S.

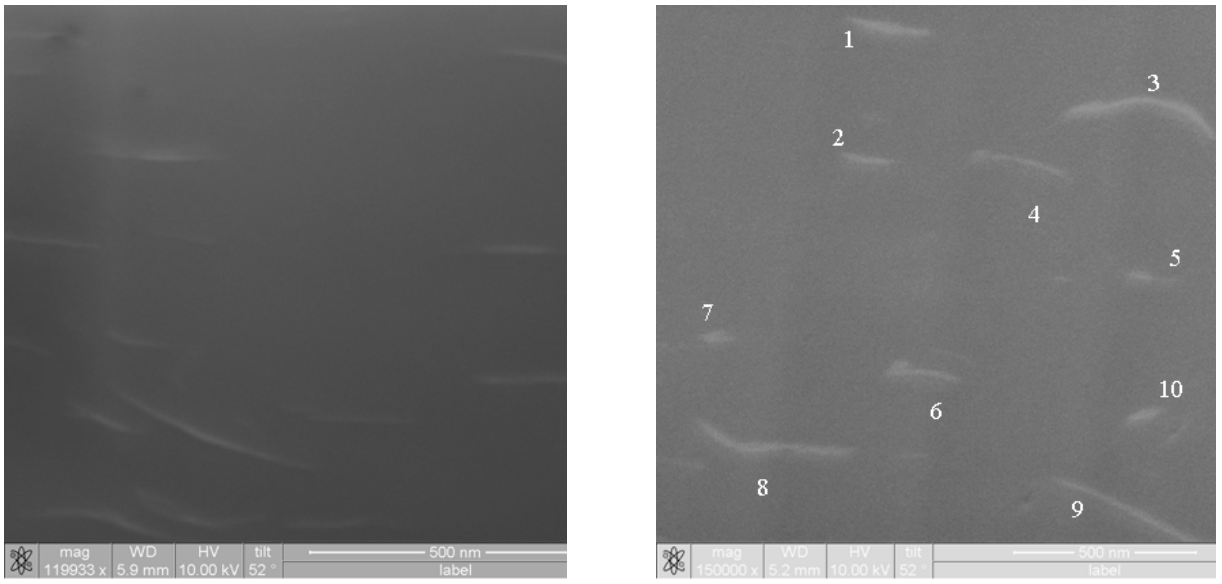

(a) (b)

Figure 4.30: SEM of FIB cross section of (a) PEN+2% MLS-2S and (b) PEN+2% MLS-3S.

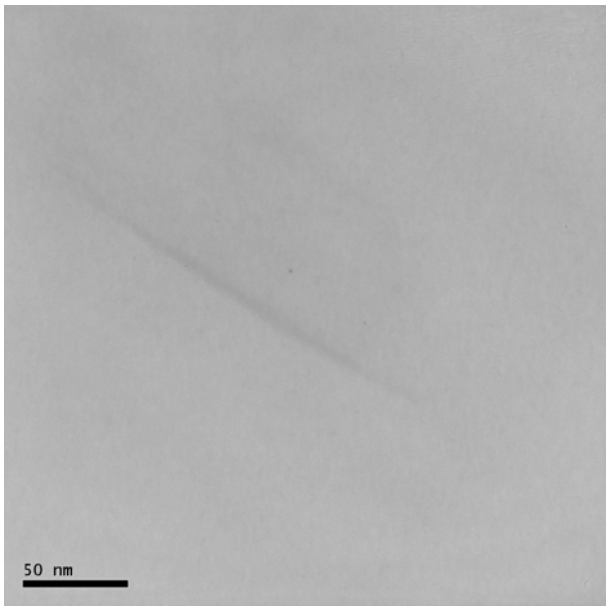

Figure 4. 31: TEM images of PEN+1%MLS-2S.

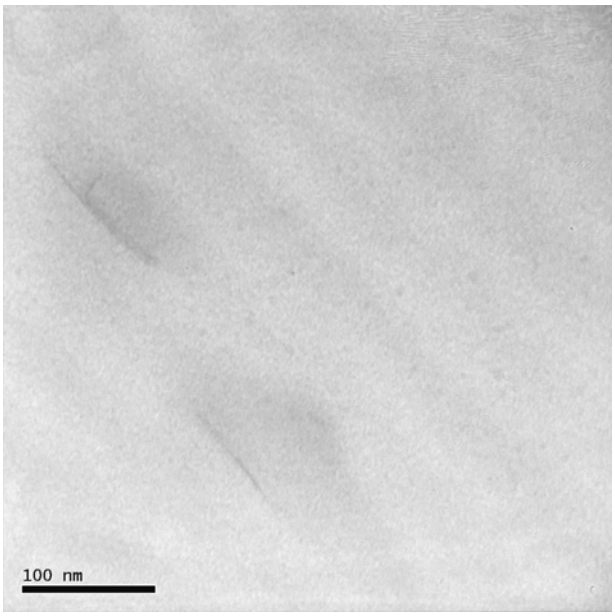

Figure 4.32: TEM images of PEN+1%MLS-2S.

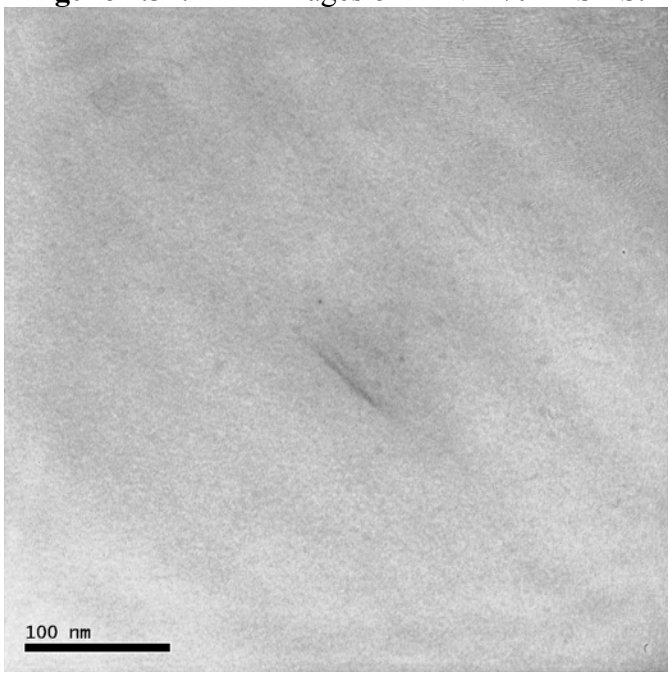

Figure 4.33: TEM images of PEN+1%MLS-2S.

4.3.2 Effect of MLS on Thermal Transitions in PEN

The effect of MLS on thermal transitions in PEN and nanocomposites was studied using DSC. Samples were heated from 30 to 280 ºC at 10 ºC/min and glass transition and melting temperature of samples were recorded. A very small peak associated with the cold crystallization

temperature is observed in pure PEN in the first heat. The T_g, T_{cc}, and T_m of pure PEN in the first heat are 121, 220, and 264 ºC, respectively. The T_g, T_{cc}, and T_m of PEN+1% MLS are 121, 195, and 265 ºC, respectively. With the addition of 1% MLS, the glass transition temperature and melting temperature did not change significantly as shown in Figure 4.34 and reported in Tables 4.14-4.15. Cold crystallization temperature decreased with the addition of MLS as shown in Figure 4.35. With the addition of MLS, a sharp cold crystallization peak is observed. The temperature is decreased by ~25 ºC for 1%MLS film and ~30 ºC for 2% MLS. This temperature difference is large. The width of cold crystallization temperature decreased from 48 to 18 ºC with the addition of 1% MLS. PEN+1% MLS-3S sample shows wider cold crystallization temperature (30 ºC) compared to all other nanocomposites. The enthalpy of cold crystallization temperature increased from 33 to 38 J/gm with 1% addition of MLS. The samples were annealed for 30 minutes at 280 ºC and cooled from 280 ºC to 30 ºC at 10 ºC/min. The fusion temperature of pure PEN in the first cool is 193 ºC. It increased by ~ 35 ºC with the addition of 1% MLS (Figure 4.35 and Table 4.16). The enthalpy of fusion also increased from 33 to 40 J/gm. The width of fusion temperature decreased from 43 to 11 ºC from pure PEN to PEN+1% MLS-2S sample. It shows the secondary nucleation behavior in nanocomposites. However, different behavior is observed for PEN+1%MLS-3S nanocomposite sample which is similar to pure PEN though there is increase in fusion temperature compared to pure PEN. Diffused fusion and no secondary nucleation is observed in PEN+1%MLS-3S sample. The sample was heated second time from 30 ºC to 280 ºC at 10 ºC/min. T_g appeared for only pure PEN and disappeared for all nanocomposites. A very small cold crystallization peak is observed for pure PEN in the second heat. On the other hand, no cold crystallization peak was observed for all other nanocomposites in the second heat. The melting temperature of pure PEN in the second heat is 266 ºC. When 1 and 2% MLS are introduced into

PEN, the melting temperature did not change (Table 4.17). Pure PEN shows only one melting peak in the second heat and the addition of MLS in nanocomposites forms a doublet in the melting peak as shown in Figure 4.36. However, PEN+1%MLS-3S shows a very small second peak compared to all other nanocomposites. The double melting point observed in the second heat is related to lamellar reorganization. The doublet in the melting peak could be correlated to bimodal crystallinity i.e. two domain of crystallites. Pure PEN has an α crystal structure. This indicates that addition of MLS enhances the formation of the β crystal structure. Wu et al.[8] observed that formation β crystal structure is enhanced with the addition of clay in PEN. This results of PEN nanocomposites correlates well with nylon nanocomposites, studied by our group. The addition of MLS in nylon 6 formed the γ-crystalline structure in nylon. The width of melting region also decreased from 15 to 9 ºC from pure PEN to nanocomposite. Smaller crystallites can be inferred in the nanocomposites. While cooling the sample from 280 ºC to 30 ºC at 10 ºC/min, the fusion temperature of pure PEN in the second cool is determined to be 208 ºC as reported in Table 4.18 and shown in Figure 4.37. The fusion temperature of PEN+1% MLS in the first cool and second cool are 228 and 231 ºC, respectively. With the addition of MLS, the fusion temperature is shifted to the right i.e. an increase in fusion temperature is observed. The increase is 20-35 ºC for the nanocomposites in both first and second heat. ΔH for fusion also increased with the addition of MLS in the first heat and decreased in the second heat. From all these heating and cooling scans it is very clear that PEN+1%MLS-3S sample behaved differently compared to all other nanocomposites. Figure 4.38 and Figure 4.39 show the melting and fusion temperature of PEN and PEN nanocomposites in the first and second DSC scan. The difference in melting and fusion temperature is affected by the addition of MLS in PEN. Both in the first and second scan, the

difference in melting and fusion temperature, i.e. effect of supercooling is decreased with addition of MLS.

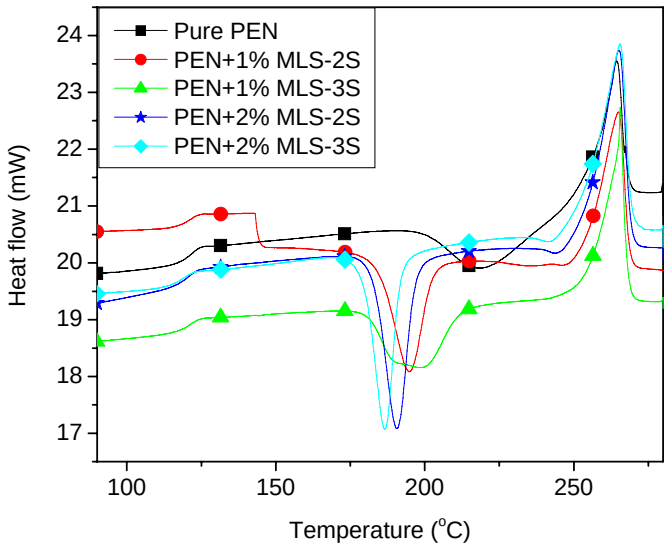

Figure 4.34: DSC of PEN and PEN nanocomposites (first heat).

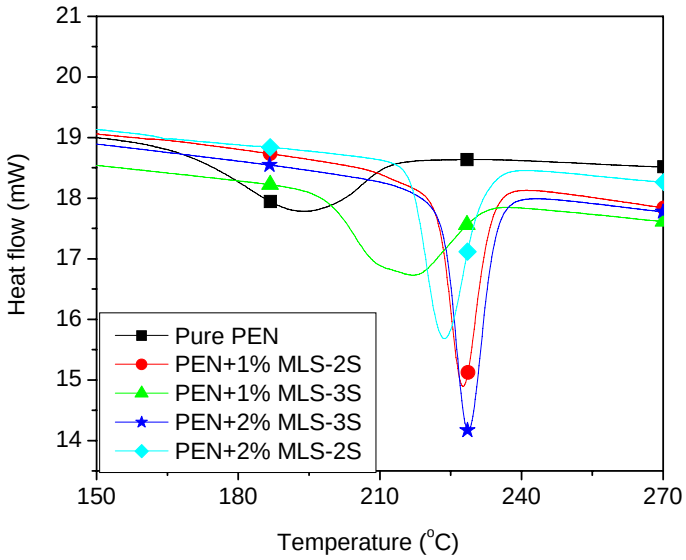

Figure 4.35: DSC of PEN and PEN nanocomposites (first cool).

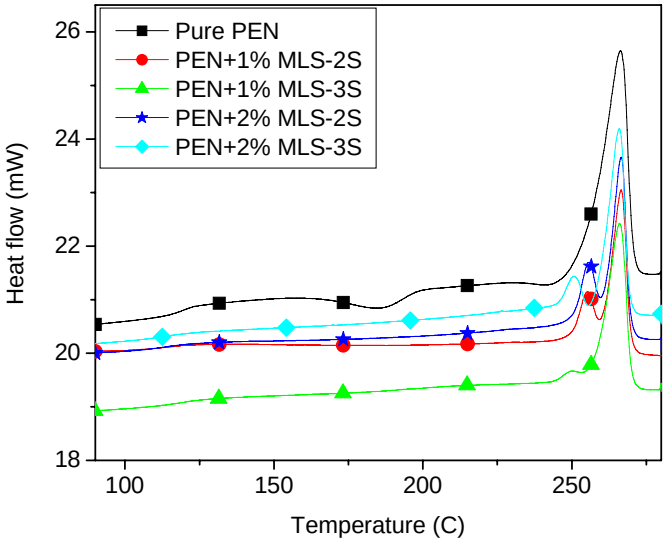

Figure 4.36: DSC of PEN and PEN nanocomposites (second heat).

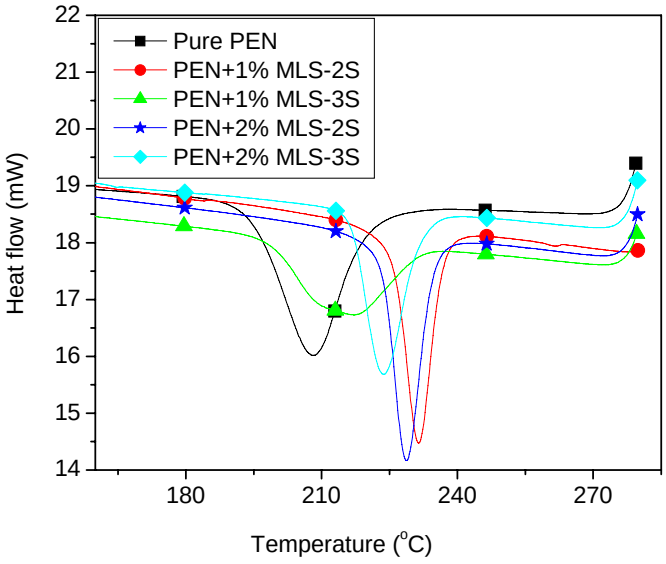

Figure 4.37: DSC of PEN and PEN nanocomposites (second cool).

Table 4.14: DSC data analysis of PEN and nanocomposites in the first heat.

Sample	T_g (ºC)	T_{m_onset} (ºC)	T_{m_end} (ºC)	T_{m_width} (ºC)	T_m (ºC)	ΔH_m (J/gm)
Pure PEN	120.8	255.9	267.7	11.8	264	27.54
PEN+1%MLS-2S	120.8	254.1	268.6	14.5	265	39.3
PEN+1%MLS-3S	121.1	262.9	267.8	4.9	266	37.6
PEN+2%MLS-2S	120.2	253.8	269	15.2	265	49.1
PEN+2%MLS-3S	118.4	252.6	269.2	16.6	266	52.6

Table 4.15: DSC data analysis of PEN and nanocomposites in the first heat for cold crystallization peak.

Sample	T_{cc_onset} (ºC)	T_{cc_end} (ºC)	T_{cc_width} (ºC)	T_{cc} (ºC)	ΔH_{cc} (J/gm)
Pure PEN	198.9	246.6	47.7	219.6	-33.19
PEN+1%MLS-2S	184.7	202.7	18	194.58	-37.6
PEN+1%MLS-3S	181.2	211.2	30	198.73	-38.7
PEN+2%MLS-2S	182.7	196.97	14.27	190.68	-40.45
PEN+2%MLS-3S	179.5	191.93	12.43	186.5	-38.43

Table 4.16: DSC data analysis of PEN and nanocomposites in the first cool.

Sample	T_{f_onset} (ºC)	T_{f_end} (ºC)	T_{f_width} (ºC)	T_f (ºC)	ΔH_f (J/gm)
Pure PEN	212	169.3	42.7	193	-33
PEN+1%MLS-2S	233.7	222.09	11.6	227.6	-40
PEN+1%MLS-3S	231	198.9	32.1	216.5	-45
PEN+2%MLS-2S	234.6	223.5	11.1	228	-39
PEN+2%MLS-3S	233.9	221.4	12.5	227.5	-40

Table 4.17: DSC data analysis of PEN and nanocomposites in the second heat.

Sample	T_{m_onset} (ºC)	T_{m_end} (ºC)	T_{m_width} (ºC)	T_m (ºC)	ΔH_m (J/gm)
Pure PEN	255.3	270.5	15.2	266	270.5
PEN+1%MLS-2S	260.2	269.6	9.4	266.4	73.64
PEN+1%MLS-3S	257.8	269.8	12	266.1	40.67
PEN+2%MLS-2S	260.6	269.6	9	266.6	35.3
PEN+2%MLS-3S	259.5	268.8	9.3	265.7	31.4

Table 4.18: DSC data analysis of PEN and nanocomposites in the second cool.

Sample	T_f_onset (ºC)	T_f_end (ºC)	T_f_width (ºC)	T_f (ºC)	ΔH_f (J/gm)
Pure PEN	219.6	194.8	24.8	207.9	-52
PEN+1% MLS-2S	236.7	225.9	10.8	231.3	-42
PEN+1% MLS-3S	234.3	208.3	26	221	-43
PEN+2% MLS-2S	237	226.7	10.3	232	-43
PEN+2% MLS-3S	233.9	221.4	12.5	227.5	-41

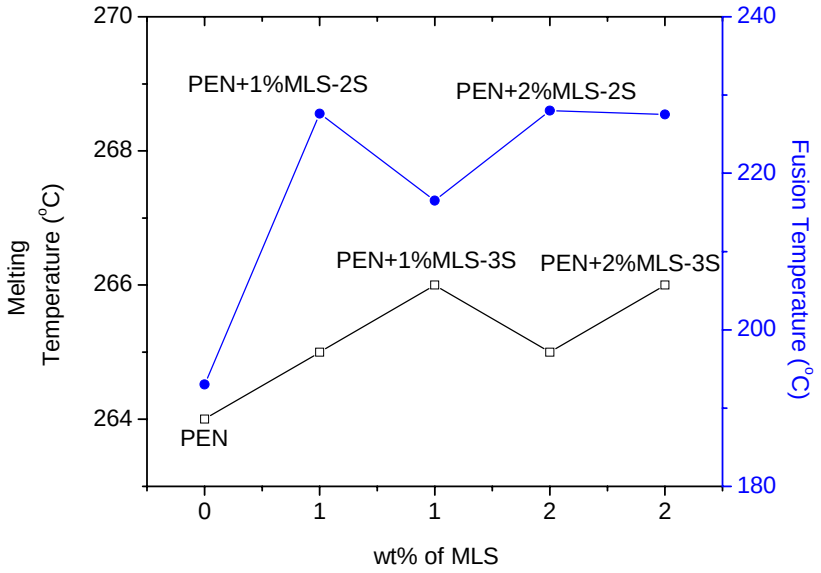

Figure 4.38: Fusion and melting temperature in the first DSC scan in PEN and PEN nanocomposites.

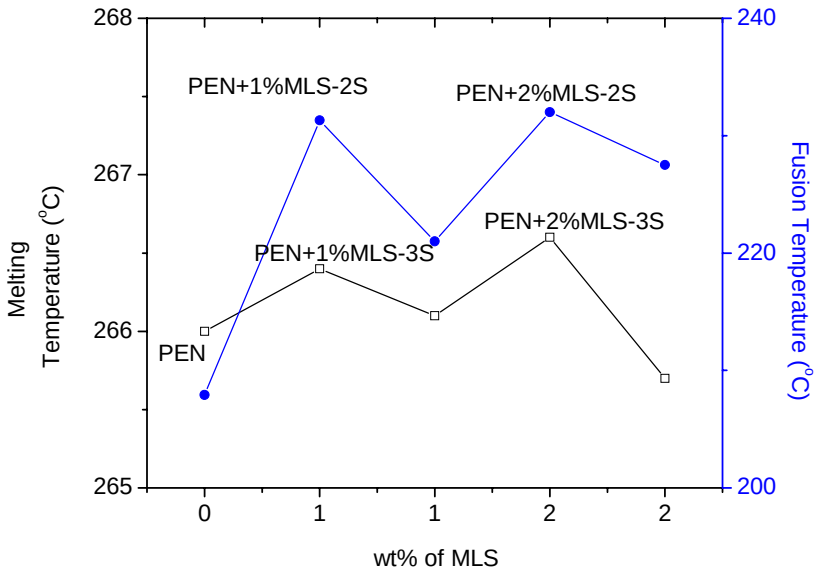

Figure 4.39: Fusion and melting temperature in the second DSC scan in PEN and PEN nanocomposites.

4.3.3 Permeability

Helium permeability of pure PEN is 4.07E-9 cc/(m.sec.torr). Helium permeability of all the samples is tabulated in Table 4.19. The experiment was repeated for two sets of sample to understand the consistency and variability in permeability from sample to sample. The maximum error was determined to be 15%. The average permeability is calculated for each sample and that permeability was used to compare with other samples. Permeability of PEN+1% MLS-2S film and PEN+1% MLS-3S are 3.38E-9 and 3.21E-9 cc/(m.sec.torr), respectively. However, permeability of PEN+2% MLS-SS film and PEN+2% MLS-3S are 4.21E-9 and 4.05E-9 cc/(m.sec.torr), respectively. There is not much decrease in helium permeability in nanocomposites except for a small decrease in PEN+1% MLS-2S film and PEN+1% MLS-3S. PEN+1% MLS-3S film showed the lowest permeability compared to all the films. Water vapor transmission of pure PEN is 43 g-mil/(m^2-d). Water vapor transmission of PEN+1%MLS-2S and PEN+1%MLS-3S are 40 and 41 g-

mil/(m^2-d) and that of PEN+2%MLS-2S and PEN+2%MLS-3S are 42 g-mil/(m^2-d). For nanocomposite containing 2% MLS, water vapor transmission remained same irrespective of different screw configuration while processing the films. Water vapor transmission of all the nanocomposites also did not show much decrease in permeation compared to pure PEN as shown in Figure 4.40.

Oxygen permeability of pure PEN is 1.09E-11 cc/(m.sec.torr). Permeability of PEN+1% MLS-2S film is 0.2E-11 cc/(m.sec.torr). Oxygen permeability of all nanocomposites is observed to be less than that of PEN as shown in Figure 4.41. The permeability of 2%MLS-2S sample shows approximately 45% less than that of pure PEN. If the permeability of only two stages processed PEN nanocomposite films is compared, films follows PEN+2%MLS-2S < PEN+1%MLS-2S < PEN order. On the other hand, the three stage processed PEN nanocomposite films did not follow the order of decreasing permeability with increase in MLS content. PEN+1% MLS-3S nanocomposite sample showed the lowest oxygen permeability and it is approximately 5 times lower than that of pure PEN.

Table 4.19: Helium permeability of PEN and nanocomposites.

Sample	Expt #	He (1E9) Permeability cc/(m.sec.torr)	Average He (1E9) Permeability cc/(m.sec.torr)
PEN	1	4.07	4.07
PEN+1%MLS-2S	1	3.39	
PEN+1%MLS-2S	2	3.38	3.38
PEN+1%MLS-3S	1	3.48	
PEN+1%MLS-3S	2	2.93	3.21
PEN+2%MLS-2S	1	4.09	
PEN+2%MLS-2S	2	4.34	4.21
PEN+2%MLS-3S	1	4.07	
PEN+2%MLS-3S	2	4.04	4.05

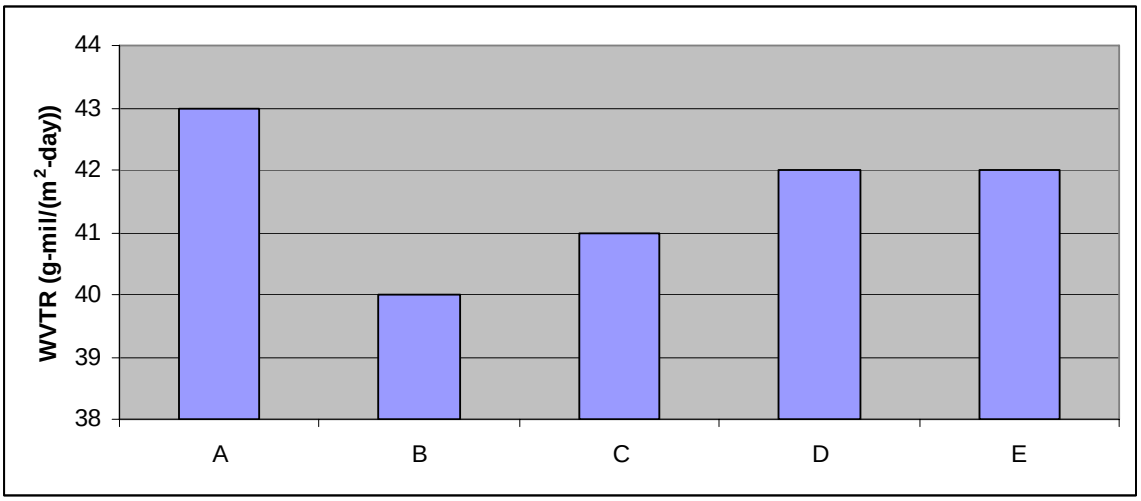

Figure 4.40: Water vapor transmission rate (WVTR) of PEN and nanocomposites.

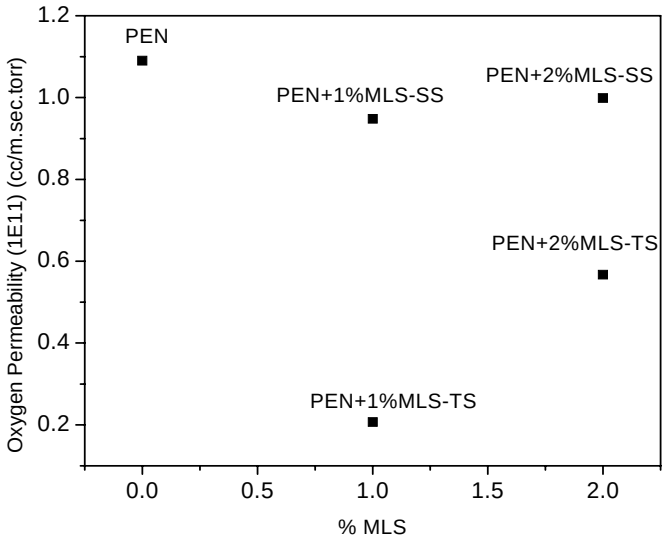

Figure 4.41: Oxygen permeability of PEN and nanocomposites.

4.3.4 Tensile Properties of PEN and Nanocomposites

The yield stress of pure PEN is 50 MPa. The yield stress of PEN+1% MLS -TS sample is 61 MPa. An improvement in tensile properties of nanocomposites is observed compared to pure PEN as shown in Table 4.20 and Figure 4.42. PEN+1%MLS-2S sample did not show much improvement in yield stress where as all other nanocomposites have a higher yield stress compared to pure PEN. A maximum yield stress of 62.3 is observed for PEN+2% MLS-2S films corresponding to 25% improvement in yield stress. The UTS of pure PEN is 68.6 MPa. The UTS of all nanocomposites are higher than pure PEN and they varied from 71.4 to 84.9 MPa, respectively. Again the maximum improvement of 24% in UTS is observed for PEN+2% MLS-2S. The modulus of pure PEN is determined to be 1.98 GPa. Modulus of PEN+1%MLS-2S is 2.12 GPa. All nanocomposites have a higher modulus except for PEN+1%MLS-3S film. The PEN+1%MLS-3S film showed a decrease in modulus though improved yield stress and UTS is observed. The maximum modulus is observed for PEN+2% MLS-2S film. All nanocomposite

films show higher tensile strength and modulus compared to pure PEN. The error range of the tensile properties of all the sample is 10-15 % based on the results from the average of 5 tests for one sample. The improvement in tensile properties of nanocomposites compared to pure PEN is due to the presence of MLS platelets which act as load transfer media leading to improvement in mechanical properties compared to pure PEN.

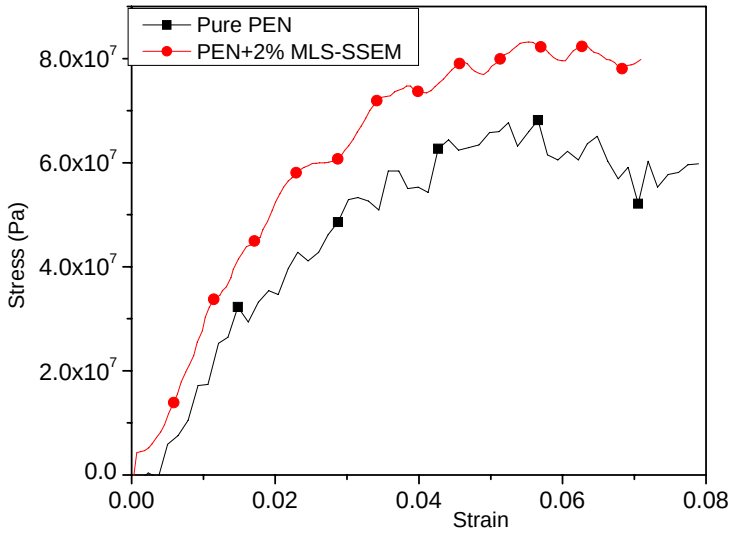

Figure 4.42: Tensile overlay of PEN and PEN+2%MLS-2S.

Table 4.20: Tensile properties of PEN and nanocomposites.

Sample	YS (MPa)	E (GPa)	UTS (MPa)
Pure PEN	50±2	1.98±.1	68.6±1.5
PEN+1%MLS-2S	51.4±3	2.12±.1	71.4±3
PEN+1%MLS-3S	60.9±2.3	1.76±.2	71.6±2
PEN+2%MLS-2S	62.3±3	2.27±.1	84.9±2
PEN+2%MLS-3S	56.5±1	2.12±.2	78.85±3

4.3.5 Haze

Haze describes the opaqueness of polymer film. Haze results are shown in Table 4.21. The percentage haze of pure PEN is 1.74. PEN+1% MLS-2S showed 23 % of haze. On the other hand,

PEN+1% MLS-3S showed 4 % of haze. The pure polymer has the lowest percentage Haze of 1.74%. Films processed in two stages show higher % haze compared to 3S films. Therefore, processing makes a difference in the optical property of the films.

Table 4.21: Effect of MLS on optical properties (haze) of PEN and nanocomposites.

Sample	% Haze
PEN	1.74
PEN+1%MLS-2S	23.32
PEN+1%MLS-3S	4.05
PEN+2%MLS-2S	9.1
PEN+2%MLS-3S	6.41

4.3.6 Summary for PEN Nanocomposites

To summarize, for PEN nanocomposites, well dispersed intercalated structure is observed in all the nanocomposites. Addition of MLS has increased the fusion temperature. Oxygen permeability is decreased in PEN+1% MLS-3S nanocomposite. Improvement in mechanical properties is obtained.

4.4 Permeability Model

PET+3% MLS films exhibited a decrease in permeability compared to pure PET as shown in Figure 4.23. However, helium permeability increased in PET+1% MLS film. Oxygen permeability increased in PET+1% MLS and PET+2% MLS and decreased in PET+3%MLS film compared to pure PET as shown in Figure 4.24.

PET+3% MLS and nylon+5 % MLS showed a drop in helium permeability by 63 % and 59% in PET and nylon, respectively compared to pure PET and nylon. The possible reason could be due to the presence of MLS platelets which act as a barrier layer and thus increases the tortuous path for the permeant to permeate through to the other side of the film. The presence of a rigid barrier such as MLS can be expected to impede this natural chain mobility. Thus lower dynamic

free volume explained in Chapter 2 becomes an additional contribution to decrease in permeability. From experimental data, it is clear that for some compositions of nanocomposites, a decrease in permeability is observed. On the other hand, for some compositions, an increase in permeability is observed. From the dispersion investigation, PET nanocomposites did not show highly exfoliated structure. Even though MLS platelets are not very well dispersed, the permeability should not increase compared to the base matrix based on any additive function prediction. Tortuosity factor, which is defined earlier in the Chapter 2, is calculated in this chapter. A speculative value of less than one is obtained for some compositions. Unless there is some indirect effect of MLS on the host matrix, the permeability should not increase in nanocomposites. Therefore, the contribution of crystallinity with the addition of MLS in the host matrix is probed to understand the increase in permeability instead of predicted decrease. In semicrystalline polymers, the higher the crystallinity, the lower the permeability as the crystalline phase is almost impermeable to the gases. In semicrystalline polymer nanocomposites, the barrier effect is the combined contributions of the tortuous path and the crystallinity. In this study, the permeability of nylon and PET nanocomposites is predicted to understand the effect of MLS and crystallinity by using different additive functions.

Permeability in nanocomposites is explained using the tortuous path theory detailed in Chapter 2. The tortuosity factor will depend on the effective dispersion of MLS in the polymer matrix. The better the dispersion of MLS, the larger the tortuosity factor, and consequently improved barrier properties of nanocomposites can be obtained. An exfoliated system gives the highest tortuosity factor, and consequently the lowest permeability in the film. Tortuosity factor can be calculated quantitatively using the Nielsen model.

4.4.1 Nielsen Model

Nielsen predicted the minimum permeability that can be expected in a polymer filled with plate like particles.[9] Nielsen assumed the MLS particles are almost parallel to the film surface. If plates of length, L and width, W are dispersed parallel in a polymer matrix as shown in Figure 4.43, the tortuosity factor, τ is given by

$$\tau = 1 + \left(\frac{L}{2W}\right) V_{MLS} = \frac{d'}{d} \tag{4.1}$$

$$d' = d\tau \tag{4.2}$$

where d and d' are corresponding distance when the permeant molecule travels without and with the tortuous path.

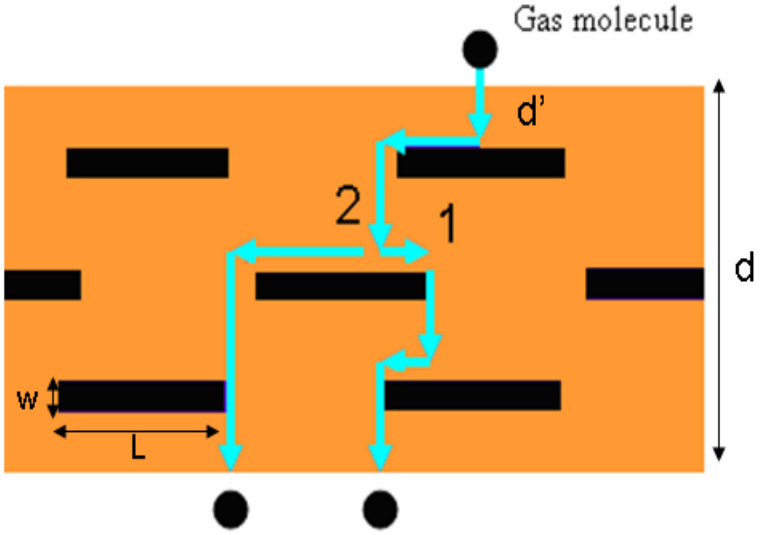

Figure 4.43: Schematic explaining Nielsen theory.

The relative permeability coefficient is given by

$$\frac{P_n}{P_{poly}} = \frac{1}{\tau} = \frac{1}{1 + \left(\frac{L}{2W}\right) V_{MLS}} \tag{4.3}$$

where V_{MLS}, represents the volume fraction of plates, and P_n and P_{poly} are the permeability of nanocomposites and polymer film.

Rearranging the above equation,

$$P_n = \frac{P_{poly}}{1 + \left(\frac{L}{2W}\right) V_{MLS}} \tag{4.4}$$

where V_{MLS} is theoretical volume fraction of MLS.

For determining the V_{MLS} from the experimental value, the following equation can be used.

$$V_{MLS(Expt)} = \left(\frac{P_{poly(Expt)}}{P_{n(Expt)}} - 1\right)\frac{2W}{L} \tag{4.5}$$

$$\tau = \frac{P_{poly}}{P_n} = \frac{d'}{d} \tag{4.6}$$

For determining the tortuosity factor from the experimental permeability values, the following equation can be used.

$$\tau_{Expt} = \frac{P_{poly}}{P_{n(Expt)}} = \frac{d'_{Expt}}{d} \tag{4.7}$$

$$d'_{Expt} = d\,\tau_{Expt} \tag{4.8}$$

The ideal width of MLS is 1 nm. The length of MLS varies. Giannelis [10] and Lan et al.[11] have reported the length of MLS could be 1000-2000 nm. Therefore, the ideal length of MLS is taken as the average of this range and it is 1500 nm. Volume of MLS layer is calculated from weight fraction and density of polymer and MLS. Density of PET and nylon are 1.35, 1.14 g/cc. Density of crystalline and amorphous PEN are 1.4 and 1.34 g/cc, [12] respectively. ~25% of crystallinity is calculated in PEN from the DSC experiment. Using mixture rule, density of PEN is calculated to be 1.355 g/cc. Density of MLS is 1.98 g/cc.[13] The ideal permeability in a

nanocomposites considering the ideal dimension and the volume fraction is calculated using Nielsen theory and reported in Table 4.22. To understand the deviation of the predicted permeability from the experimental permeability, ΔP is calculated. ΔP refers to the difference of predicted permeability from the experimental one i.e. $\Delta P = (P_{Expt} - P_{Predicted})$.

Table 4.22: Ideal permeability in PET nanocomposites using Nielsen theory.

Samples	**P_{Expt} (1E9) (cc/m.sec.torr)**	**Ideal P_{n1} (1E9) (cc/m.sec.torr) (L=1500nm, W=1) nm)**	**ΔP_1(1E9) (cc/m.sec.torr)**	**Ideal P_{n2} (1E9) (cc/m.sec.torr) (L=150nm, W=1) nm)**	**ΔP_2(1E9) (cc/m.sec.torr)**
PET	3.7	3.70	0	3.7	0
PET+1%MLS	4.34	0.6	3.74	2.44	1.9
PET+2%MLS	1.34	0.32	1.02	1.82	-0.48
PET+3%MLS	1.35	0.22	1.13	1.45	-0.1

In PET nanocomposite films, the value of L and W were determined from TEM image (Figure 4.15) and determined to be L = ~ 150 nm, W was varied from 13-70 nm. P_n is calculated using the equation (4.4) and compared with the experimental values as shown in Figure 4.42. For PET nanocomposites (PET+2% MLS and PET+3% MLS), from the permeability data, width of MLS is predicted to be less than what is observed from TEM image. Therefore, crystalline lamellae in semicrystalline polymer might have increased the effective tortuosity path. In addition, the higher weight percentage of MLS might have increased the tortuosity factor further to decrease the permeability in case of PET+2%MLS and PET+3%MLS films.

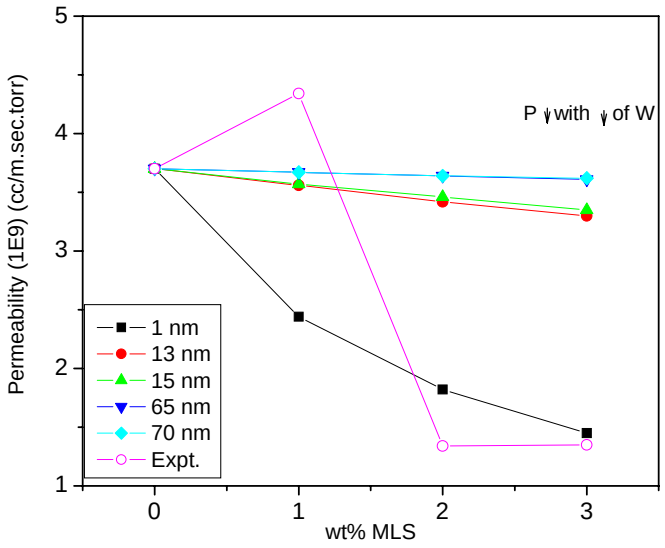

Figure 4.44: Range of helium permeability for different width in PET nanocomposites.

Permeability is also predicted for nylon nanocomposites considering the ideal dimension (L=1500 nm and W=1nm) and when L=150 nm, W=1 nm. Permeability values are reported in Table 4.23. For nylon+5% MLS, the experimental, P_n (considering L=1500nm, W=1nm) and P_n (considering L=150nm, W=1nm) are .32E-9, 0.03E-9 and 0.25E-9 cc/m.sec.torr, respectively. It is clear that predicted permeability is lower than the experimental values (Table 4.23) as presented by ΔP. The maximum deviation (ΔP) is observed for nylon+3% MLS. When ideal dimension is considered permeability is one order of magnitude lower than the experimental value. 20% decrease in predicted permeability is observed when L=150 nm is used to determine permeability. If MLS platelets are of L= ~150 nm and W= ~1 nm, other then tortuous path, crystallinity plays a role in lowering the permeability in nanocomposites. For PEN nanocomposite, permeability is predicted using Nielsen theory. From SEM and TEM images, the width of MLS varied from 5-15 nm. Therefore, the minimum width of 5 nm is considered to predict the permeability. Permeability

is calculated considering the ideal dimension of MLS and when L=150 nm and W=1 and 5 nm and compared with the experimental results as reported in Tables 4.24 and 4.25.

Table 4.23: Ideal permeability in nylon nanocomposites using Nielsen theory.

Unit of permeability is cc/m.sec.torr**.**

Samples	**P_{Expt} (1E9)**	**Ideal P_{n1} (1E9) (L=1500 nm, W=1) nm)**	**ΔP_1 (1E9)**	**Ideal P_{n2} (1E9) (L=150 nm, W=1 nm)**	**ΔP_2 (1E9)**
Nylon	0.79	0.79	0.00	0.79	0.00
Nylon+1% MLS	0.54	0.15	0.39	0.55	-0.01
Nylon+2% MLS	0.54	0.08	0.46	0.42	0.12
Nylon+3% MLS	0.55	0.06	0.49	0.34	0.21
Nylon+5% MLS	0.32	0.03	0.29	0.25	0.07

Table 4.24: Ideal permeability in PEN nanocomposites using Nielsen theory. Unit of permeability is cc/m.sec.torr.

Samples	**P_{Expt} (1E9)**	**Ideal P_{n1} (1E9) (L=1500nm, W=1 nm)**	**ΔP_1 (1E9)**	**Ideal P_{n2} (1E9) (L=150nm, W=1 nm)**	**ΔP_2 (1E9)**	**Ideal P_{n3} (1E9) (L=150nm, W=5 nm)**	**ΔP_3 (1E9)**
Pure PEN	4.07	4.07	0.00	4.07	0.00	4.07	0.00
PEN+1% MLS-2S	3.38	0.66	2.72	2.69	0.69	3.69	-0.31
PEN+1% MLS-3S	3.21	0.66	2.55	2.69	0.52	3.69	-0.48
PEN+2% MLS-2S	4.21	0.36	3.85	2.00	2.21	3.37	0.84
PEN+2% MLS-3S	4.05	0.36	3.69	2.00	2.05	3.37	0.68

Table 4.25: Ideal oxygen permeability in nanocomposites using Nielsen theory.

Unit of permeability is cc/m.sec.torr**.**

Sample	P_{Expt} (1E9)	Ideal P_{n1} (1E11) (L=1500nm, W=1 nm)	ΔP_1 (1E11)	Ideal P_{n2} (1E11) (L=150nm, W=1 nm)	ΔP_2 (1E11)	Ideal P_{n3} (1E11) (L=150nm, W=5 nm)	ΔP_3 (1E11)
PEN	1.08	1.08	0.00	1.08	0.00	1.08	0.00
PEN+1%MLS-2S	0.95	0.18	0.77	0.71	0.24	0.98	-0.03
PEN+1%MLS-3S	0.21	0.18	0.03	0.71	-0.50	0.98	-0.77
PEN+2%MLS-2S	0.57	0.10	0.47	0.53	0.04	0.89	-0.32
PEN+2%MLS-3S	1.00	0.10	0.90	0.53	0.47	0.89	0.11

The different parameters that affect permeability are already explained in Chapter 2. When the chemical structures and permeant are the same, crystallinity (which can be expressed in term of density) and tortuosity are the contributions to the permeability. To separate the effect of MLS and crystallinity, permeability considering only MLS and only crystallinity fraction is predicted separately in the films. Permeability is predicted based on Maxwell's theory considering MLS and crystalline separately and then combining MLS and crystallinity. Based on continuum theory, permeability is also predicted considering only MLS and all these predicted permeability values are compared with the experimental permeability.

4.4.2 Permeability Model Based on Maxwell's Theory

4.4.2.1 Permeability Considering Only Crystalline Phase

In semicrystalline polymer there are two different phases: amorphous and crystalline. Amorphous phase can be again rigid and mobile as explained in Chapter 2. Crystallinity in the polymer offers a tortuous path to the permeant resulting in an additional decrease in permeability. In addition, an increase in the crystalline portion lowers the amorphous volume fraction. Thus a lower fraction of polymeric volume is available for the permeant to diffuse through it. Let P is

permeability of system containing A and B phases as shown in Figure 4.45. Phase A is crystallites in the amorphous phase B. V_A and V_B are the volume fractions of phases A and B, respectively. P_A is permeability of system without phase B and P_B is permeability of system without phase A. Assuming the phase A is spherical, well separated, and do not interact with each other, permeability can be written by replacing with dielectric permeability in Maxwell's equation.[14,15]

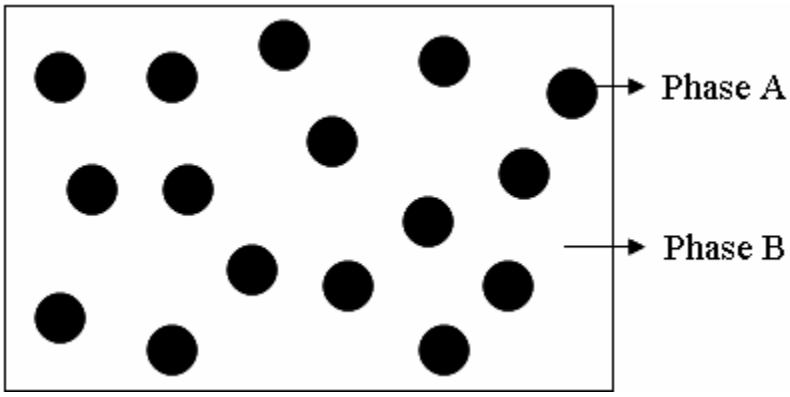

Figure 4.45: Crystallites and amorphous matrix in polymer.

$$\frac{P}{P_B} - 1 = 3V_A\left(\left(\frac{P_A + 2P_B}{P_A - P_B}\right) - V_A\right)^{-1} \tag{4.9}$$

Dividing the equation by P_B both in numerator and denominator on right hand side,

$$\frac{P}{P_B} - 1 = 3V_A\left(\left(\frac{\left(\frac{P_A}{P_B}\right) + 2}{\left(\frac{P_A}{P_B}\right) - 1}\right) - V_A\right)^{-1} \tag{4.10}$$

By replacing $\left(\frac{P_A}{P_B}\right)$ with α in the equation (4.10)

$$\frac{P}{P_B} - 1 = 3V_A\left(\left(\frac{\alpha + 2}{\alpha - 1}\right) - V_A\right)^{-1} \tag{4.11}$$

Rearranging the above equation

$$\frac{P}{P_B} = 1 + 3\left(\frac{V_A}{\left(\left(\frac{\alpha+2}{\alpha-1}\right) - V_A\right)}\right) \tag{4.12}$$

If crystallites are assumed to be impermeable, then P_A=0.

Therefore, α=0.

Putting α=0 in the equation (4.12)

$$\frac{P}{P_B} = 1 + 3\left(\frac{V_A}{(-2 - V_A)}\right) \tag{4.13}$$

Rearranging the above equation

$$P = 2P_B\left(\frac{1 - V_A}{2 + V_A}\right) \tag{4.14}$$

Since V_A is the volume fraction of phase A, therefore replacing with crystalline fraction, V_{cr} and replacing P_B with permeability in amorphous phase, P_{am}, permeability in semicrystalline polymer can be written as

$$P_{ac} = 2P_{am}\left(\frac{1 - V_{cr}}{2 + V_{cr}}\right) \tag{4.15}$$

where Pac is the effective permeability considering both amorphous and crystalline phase.

Rearranging equation (4.15)

$$P_{am} = \frac{P_{ac}}{2\left(\frac{1 - V_{cr}}{2 + V_{cr}}\right)} \tag{4.16}$$

For nylon,

$$P_{am,nylon} = \frac{P_{ac,nylon}}{2\left(\frac{1-X_c}{2+X_c}\right)} \quad (4.17)$$

For determining the P_{am}, permeability of pure amorphous PET is experimentally measured and determined to be 7.89E-9 cc/m.sec.torr. Crystalline fraction for each sample was calculated from the DSC experiment. Considering both the amorphous and crystalline fraction of the polymer, permeability is predicted using equation (4.15) and presented in Table 4.26. For nylon films, permeability of pure amorphous nylon is calculated using the V_{cr} and the experimental permeability value of pure semicrystalline nylon using equation (4.17) and determined to be 1.3E-9 cc/m.sec.torr. P_{am} is then put back in equation (4.15) to calculate permeability, P_{ac} for all the compositions and permeabilities are presented in Table 4.27. The predicted permeability is more than the experimental permeability for nylon nanocomposite samples as presented by ΔP. However, for PET nanocomposites except PET+1% MLS, the predicted permeability is more than the experimental permeability values.

Table 4.26: Permeability considering crystalline fraction in PET nanocomposites.

Unit of permeability is cc/m.sec.torr**.**

Samples	**V_{cr}**	**P_{ac} (1E9)**	**P_{Expt} (1E9)**	**ΔP (1E9)**
PET	0.43	3.70	3.7	0.00
PET+1% MLS	0.43	3.70	4.34	0.64
PET+2% MLS	0.42	3.78	1.34	-2.44
PET+3% MLS	0.46	3.46	1.35	-2.11

Table 4.27: Permeability considering crystalline fraction in nylon nanocomposites**.**

Unit of permeability is cc/m.sec.torr**.**

Samples	**V_{cr}**	**P_{ac} (1E9)**	**P_{Expt} (1E9)**	**ΔP_3 (1E9)**
Nylon	0.30	0.79	0.79	0.00
Nylon+1% MLS	0.41	0.63	0.54	-0.09
Nylon+2% MLS	0.41	0.64	0.54	-0.10
Nylon+3% MLS	0.32	0.76	0.55	-0.21
Nylon+5% MLS	0.35	0.72	0.32	-0.40

4.4.2.2 Permeability Considering Only MLS

Effect of MLS on permeability is explained in Chapters 2 and 4. If V_{MLS} is the volume fraction of MLS, P_{poly} is permeability of polymer matrix; P_n is permeability of nanocomposite,[14]

$$P_n = P_{poly}\left(1+\left(\frac{(1+A)V_{MLS}}{\left(\frac{\alpha+A}{\alpha-1}\right)-V_{MLS}}\right)\right) \tag{4.18}$$

where $\alpha=\frac{P_{MLS}}{P_{poly}}$

Assuming MLS is impermeable, $P_{MLS}=0$

Therefore, $\alpha=0$

To determine the value of A for MLS, assuming MLS as long transverse cylinders (A=1)[14]

Putting the values in the above equation,

$$P_n = P_{poly}\left(\frac{1-V_{MLS}}{1+V_{MLS}}\right) \tag{4.19}$$

For PET and nylon P_{poly} are 3.7E-9 and 7.89E-10 cc/m.sec.torr, respectively. These values are determined from the experiment. Permeability in nanocomposites is calculated using the equation (4.19) and presented in Tables 4.28 and 4.29 for PET and nylon, respectively.

Table 4.28: Permeability considering only MLS phase in PET nanocomposites.

Unit of permeability is cc/m.sec.torr.

Sample	V_{MLS}	$\left(\frac{1-V_{MLS}}{1+V_{MLS}}\right)$	P_n (1E9)	P_{Expt} (1E9)	ΔP (1E9)
PET	0	1.0	3.70	3.7	0.00
PET+1%MLS	0.0068	0.986	3.65	4.34	0.69
PET+2%MLS	0.0137	0.973	3.60	1.34	-2.26
PET+3%MLS	0.02	0.961	3.55	1.35	-2.20

Table 4.29: Permeability considering only MLS phase in nylon nanocomposites.

Unit of permeability is cc/m.sec.torr**.**

Sample	V_{MLS}	$\left(\frac{1-V_{MLS}}{1+V_{MLS}}\right)$	P_n (1E9)	P_{Expt} (1E9)	ΔP (1E9)
Nylon	0.000	1.000	0.79	0.79	0.00
Nylon+1%MLS	0.006	0.989	0.78	0.54	-0.24
Nylon+2%MLS	0.012	0.977	0.77	0.54	-0.23
Nylon+3%MLS	0.017	0.966	0.76	0.55	-0.21
Nylon+5%MLS	0.029	0.943	0.74	0.32	-0.42

4.4.2.3 Permeability Considering Both Crystalline and MLS

Observing the predicted permeability data based on only MLS and only crystallinity, neither MLS nor V_{cr} individually dominate in determining permeability as both the predicted value considering only MLS and only V_{cr} deviate more from the experimental. Hence, the model is used considering amorphous, crystalline phase and MLS content to find the effective permeability, P_{Mac} of the film. Here the subscript Mac refers to MLS (M), amorphous (a), and crystalline (c) phase. For predicting the permeability considering both crystalline and MLS phase, the equation (4.18) can be written as

$$P_{Mac} = P_{am}\left(1+\left(\frac{(1+A)V_{MLS+cr}}{\left(\frac{\alpha+A}{\alpha-1}\right)-V_{MLS+cr}}\right)\right) \quad (4.20)$$

Volume fraction of crystalline phase V_{cr}^{0} is first calculated from DSC in all pure polymer and nanocomposite films. Volume fraction of MLS is subtracted from the matrix. From this volume fraction of matrix (which excludes the V_{MLS}) volume fraction of crystalline phase is calculated and denoted by V_{cr}. Here $V_{cr} = V_{cr}^{0} V_{poly}$. For pure polymer $V_{cr} = V_{cr}^{0}$ as $V_{poly} = 1$. For nanocomposites, $V_{poly} = 1 - V_{MLS}$. Volume fraction of MLS and crystalline phase is added to determine volume fraction of amorphous phase. For crystallites (assuming spheres), A=2 and for MLS (assuming transverse cylinders), A=1. Since both crystalline and MLS phases are considered, A can be taken as the average of 1 and 2 to predict the permeability. Therefore, A= (1+2) = 3/2=1.5.

Putting the value of α=0, and A=1.5 in equation (4.20)

$$P_{Mac} = 1.5P_{am}\left(\frac{1-V_{MLS+cr}}{1.5+V_{MLS+cr}}\right) \quad (4.21)$$

Permeability in nanocomposites is calculated using equation (4.21) and presented in Tables 4.30 and 4.31 respectively. For PET film the predicted permeability is decreased from 3.5E-9 to 3.18E-9 cc/m.sec.torr with the addition of 3% MLS. From ΔP it is clear that for PET+2% MLS and PET+3% MLS predicted permeability are much higher than experimental one. For nylon films, the predicted permeability is decreased from 0.76E-9 to 0.669 cc/m.sec.torr with 5% addition of MLS. ΔP in these prediction, considering MLS and crystallinity shows less for nylon nanocomposites and the maximum deviation is observed for nylon+5% MLS and it is (0.34 E9 cc/m.sec.torr)

Table 4.30: Permeability considering both crystalline and MLS phase in PET nanocomposites.

Unit of permeability is cc/m.sec.torr**.**

Sample	Wt % MLS	V_{MLS}	V_{poly}	V_{cr}^0	V_{cr}	$V_{MLS}+V_{cr}$	V_{am}	P_{Mac} (1E9)	P_{Expt} (1E9)	ΔP (1E9)
PET	0	0.000	1.000	0.430	0.430	0.430	0.570	3.50	3.7	0.20
PET+1%MLS	1	0.007	0.993	0.430	0.427	0.434	0.566	3.46	4.34	0.88
PET+2%MLS	2	0.014	0.986	0.420	0.414	0.428	0.572	3.51	1.34	-2.17
PET+3%MLS	3	0.020	0.980	0.460	0.451	0.471	0.529	3.18	1.35	-1.83

Table 4.31: Permeability considering both crystalline and MLS phase in nylon nanocomposites.

Unit of permeability is cc/m.sec.torr**.**

Sample	Wt % MLS	V_{MLS}	V_{poly}	V_{cr}^0	V_{cr}	$V_{MLS}+V_{cr}$	V_{am}	P_{Mac} (1E9)	P_{Expt} (1E9)	ΔP (1E9)
Nylon	0	0.000	1.000	0.300	0.300	0.300	0.700	0.76	0.79	0.03
Nylon+1%MLS	1	0.006	0.994	0.411	0.409	0.415	0.585	0.59	0.54	-0.05
Nylon+2%MLS	2	0.012	0.988	0.410	0.405	0.417	0.583	0.59	0.54	-0.05
Nylon+3%MLS	3	0.017	0.983	0.323	0.318	0.335	0.665	0.70	0.55	-0.15
Nylon+5%MLS	5	0.029	0.971	0.351	0.341	0.370	0.630	0.66	0.32	-0.34

4.4.3 Bilayer Series Model Considering Only MLS

To model the effect of MLS, the bilayer series equation based on continuum theory is also used to predict the permeability of nanocomposites. Permeability using the individual permeability of MLS and pure polymers can be written as

$$\frac{L_n}{P_n} = \frac{L_{MLS}}{P_{MLS}} + \frac{L_{poly}}{P_{poly}} \tag{4.22}$$

Rearranging the equation

$$P_{MLS} = \frac{L_{MLS}}{\left(\frac{L_n}{P_n} - \frac{L_{poly}}{P_{poly}}\right)} \tag{4.23}$$

where L_n, L_{MLS} and L_{poly} represent the total nanocomposite films, MLS, and polymer thickness, respectively.[16] The thickness of all the PET and nanocomposites and all the nylon and

nanocomposites films is 0.15 mm and 0.36 mm, respectively. P_n is the apparent permeability of the nanocomposite films. P_{MLS} and P_{poly} are the permeability of the MLS and pure matrix. Here P_{poly} is permeability of pure PET and nylon which is determined experimentally and they are 3.7 E-9 and 7.9E-10 cc/m.sec.torr. As explained, volume of MLS is calculated from weight fraction and density of polymer and MLS. The effective thickness of the MLS is then calculated from volume fraction as surface area is same for MLS and polymer and reported in Tables 4.32 and 4.33 for nylon and PET nanocomposites, respectively. Permeability of nanocomposite films is calculated using equation (4.22). P_{MLS} was determined using equation (4.23) from the pure PET and PET+3% MLS nanocomposite experimental permeability values and determined to be 4.34E-11 cc/m.sec.torr. For nylon films, experimental permeability of pure nylon and nylon+5% MLS films is used to calculate the P_{MLS}. Equation (4.23) is used only to calculate P_{MLS} and it determined to be 0.94E-11 cc/m.sec.torr. Using the above calculated permeability value of MLS, the permeability of other nanocomposite films is predicted by using equation (4.22) and permeability in nylon and PET nanocomposites are presented in Tables 4.32 and 4.33. For determining the permeability in PEN nanocomposites, permeability of MLS is taken as 4.34E-11 cc/m.sec.torr (determined from PET and nanocomposites using equation 4.23). The calculated permeability is presented in Table 4.34.

Table 4.32: Thickness of MLS and permeability in PET nanocomposites from bilayer model.

Samples	L (mm)	L_{MLS} (mm)	L_{poly} (mm)	P_n (1E9) (cc/m.sec.torr)	P_{Expt} (1E9) (cc/m.sec.torr)	ΔP (1E9) (cc/m.sec.torr)
PET	0.15	0	0	3.70	3.7	0.00
PET+1%MLS	0.15	1.03E-03	0.149	2.35	4.34	1.99
PET+2%MLS	0.15	2.06E-03	0.148	1.72	1.34	-0.38
PET+3%MLS	0.15	3.10E-03	0.147	1.35	1.35	0.00

Table 4.33: Thickness of MLS and permeability in nylon nanocomposites from bilayer model.

Samples	L (mm)	L_{MLS} (mm)	L_{poly} (mm)	P_n (1E9) (cc/m.sec.torr)	P_{Expt} (1E9) (cc/m.sec.torr)	ΔP (1E9) (cc/m.sec.torr)
Nylon	0.36	0	0.36	0.79	0.79	0.00
Nylon+1%MLS	0.36	2.08E-03	0.358	0.61	0.54	-0.07
Nylon+2%MLS	0.36	4.18E-03	0.356	0.50	0.54	0.04
Nylon+3%MLS	0.36	6.30E-03	0.354	0.42	0.55	0.13
Nylon+5%MLS	0.36	1.06E-02	0.349	0.32	0.32	0.00

Table 4.34: Permeability considering only MLS in PEN nanocomposites.

Sample	L (mm)	L_{MLS} (mm)	L_{poly} (mm)	P_n (1E9) (cc/m.sec.torr)	P_{Expt} (1E9) (cc/m.sec.torr)	ΔP (1E9) (cc/m.sec.torr)
PEN	0.14	0	0.14	4.07	4.07	0.00
PEN+1% MLS-2S	0.14	9.86E-6	0.139	2.46	3.38	0.92
PEN+1% MLS-3S	0.14	9.86E-6	0.139	2.46	3.21	0.75
PEN+2% MLS-2S	0.15	2.12E-5	0.149	1.76	4.21	2.45
PEN+2% MLS-3S	0.15	2.12E-5	0.149	1.76	4.05	2.29

4.5 Discussion on Permeability Models

Permeability is predicted considering different assumptions as explained in section 4.4. These predicted permeability values are compared with experimental and presented in Figures 4.46 and 4.47. To study the effect of crystallinity on permeability, permeability is predicted based on only crystallinity using Maxwell's approach. The predicted permeability is more than the experimental permeability for nylon nanocomposite samples. It is 7.15E-10 cc/m.sec.torr compared to the experimental value of 3.22E-10 cc/m.sec.torr. However, for PET nanocomposites

except PET+1% MLS, the predicted permeability is more than the experimental permeability. The predicted permeability for PET+3% MLS is 3.46 E-9 cc/m.sec.torr compared to experimental value of 1.35E-9 cc/m.sec.torr. The similar trend is observed when permeability is predicted considering only MLS using Maxwell's approach. Therefore, neither MLS nor crystallinity alone is a dominant factor in determining the permeability; both of them play a significant role in determining the permeability When permeability is predicted considering both MLS and crystallinity using Maxwell's approach, it is 6.55E-10 compared to the experimental value of 3.22E-10 cc/m.sec.torr. The predicted permeability for PET+3% MLS is 3.55 E-9 cc/m.sec.torr compared to experimental value of 1.35E-9 cc/m.sec.torr The predicted permeability can be some what comparable to experimental value when it is predicted considering both MLS and crystallinity. In this case the deviation from the experimental result is less compared to all other predictions. Comparing all the predicted values based on different consideration and comparing with the experimental permeability, it is clear that when the permeability is determined using bilayer series model, permeability of nylon nanocomposites shows closer to the predicted ones. However, having an increased permeability in PET+1% MLS nanocomposite, the experimental permeability did not correlate with the experimental permeability.

For PEN nanocomposites, the experimental helium permeability of PEN+1%MLS-2S is 3.38E-9 cc/m.sec.torr. Predicted permeability considering the ideal dimension is more than an order of magnitude less than that of experimental permeability. When L=150 nm and w=5nm, the predicted permeability is 3.69E-9 cc/m.sec.torr (Figure: 4.48) and it is closer to the experimental value. The similar trend is observed for oxygen permeability. For PEN+1%MLS-3S, the experimental permeability is 0.21E-11 cc/m.sec.torr (Figure 4.49). Ideal Nielsen permeability is 0.18E-11 cc/m.sec.torr which is closer to the experimental value. However, the SEM and TEM

image did not show the dimension of ideal dimension. Other than MLS, there is some other factor that is contributing in lowering the permeability. However, helium permeability results shows permeability of PEN+1%MLS-3S is much higher than the predicted experimental values. When permeability is calculated considering L=150nm and W=5 nm, it is closer to the experimental value. The width of MLS as 5 nm which is experimental determined for some of MLS platelets from the SEM and TEM images. For PEN+2%MLS-2S, oxygen permeability correlates well when permeability is predicted considering width of MLS as 1 nm. However, helium permeability shows a higher than predicted value. For PEN+2% MLS-TS film, both oxygen and helium permeability shows that width of MLS is slightly more than 5 nm. Compared to all the three materials studied here, permeability of PEN is best suited with Nielsen predicted value.

The predicted value based on ideal L and W factors of MLS geometry are fitted into the Nielsen equation and predict the lowest permeability that can be expected in the nanocomposites. The predicted values tell us the ideal permeability value when each and every MLS layer is well dispersed thus contributing to the barrier properties. It is found to be much less than an experimental value for some of the samples and it is especially true for PET+1% MLS nanocomposite. From the experimental helium permeability value in PET+1%MLS, and oxygen permeability in both the PET+1% MLS and PET+2% MLS films, it is clear that the tortuosity factor did not play any significant role to lower the permeability. Therefore, tortuosity factor is calculated from the experimental permeability value for PET and nylon nanocomposites and reported in Tables 4.35 and 4.36, respectively. In these Tables V_{MLS} is calculated using equation (4.4) and tortuosity factor (TF) is determined using equation (4.1). Once TF is determined, d' is calculated by multiplying TF with thickness of the film, d. The ideal TF, d' are compared with the predicted ones, determined from experimental permeability. The predicted tortuosity factor based

on the volume fraction of MLS in PET and nylon nanocomposites is 5-7 times more than that of determined from the experimental permeability (Tables 4.35 and 4.36).

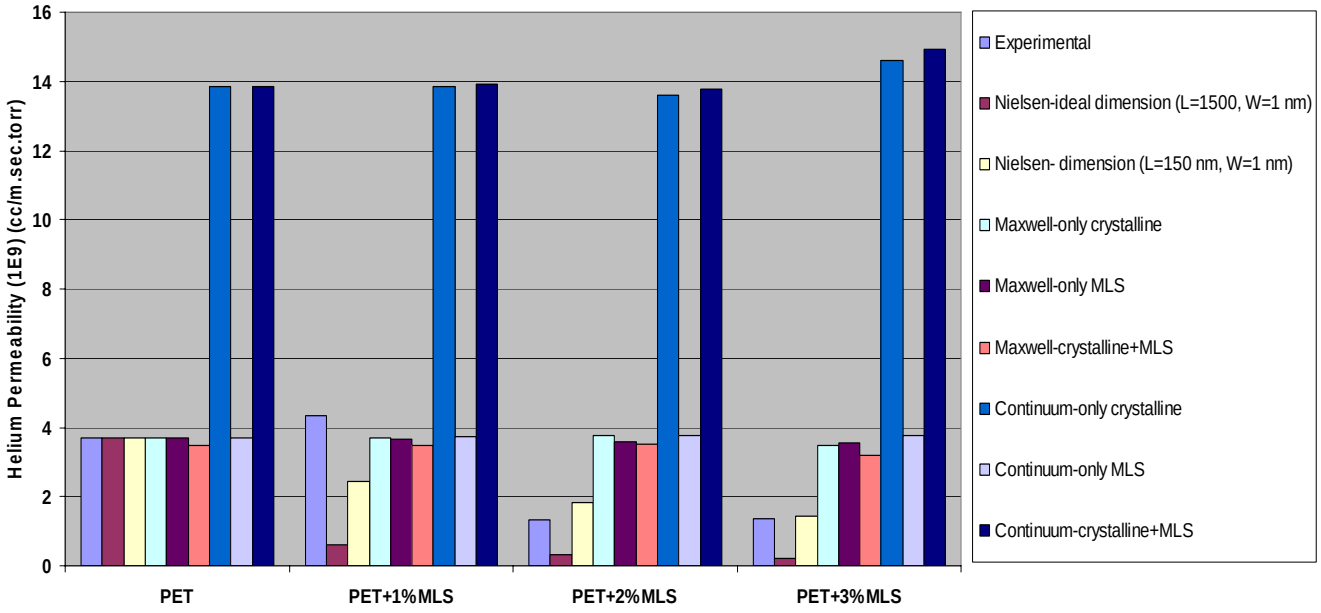

Figure 4.46: Comparison of different predicted permeability with the experimental measured values for PET nanocomposites.

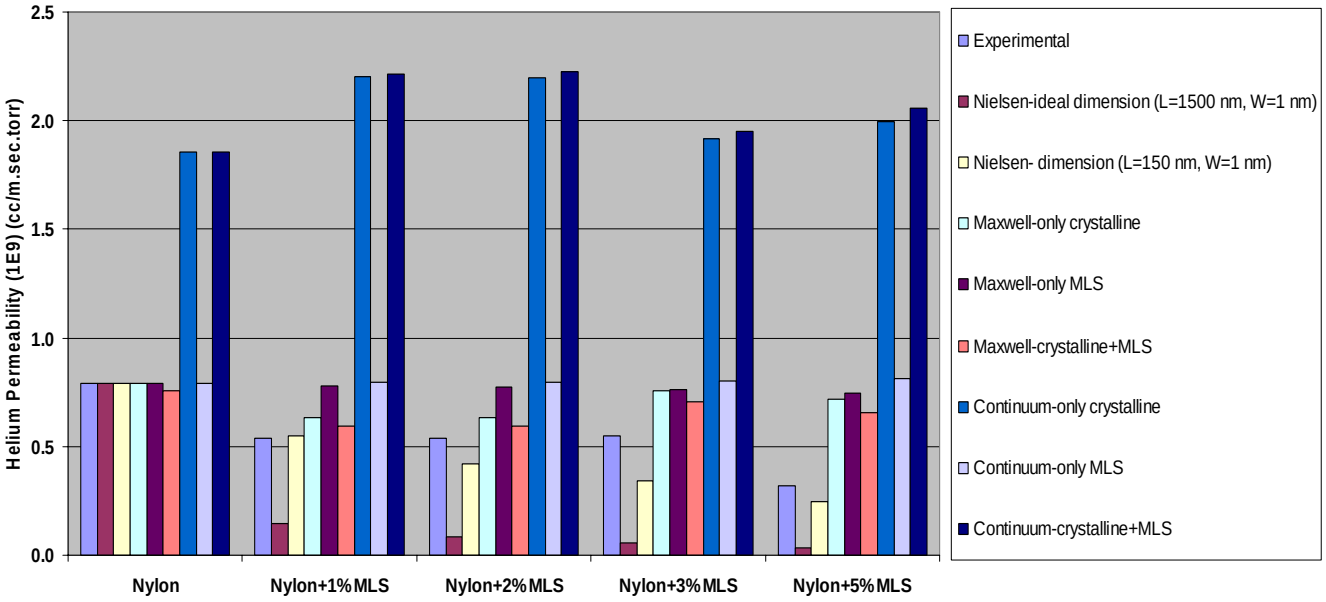

Figure 4.47: Comparison of different predicted permeability with the experimental measured values for nylon nanocomposites.

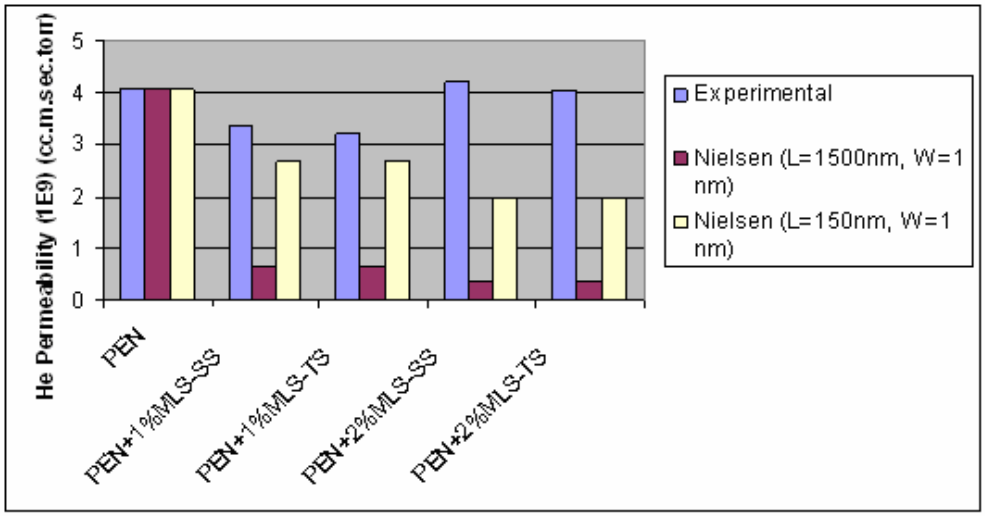

Figure 4.48: Helium permeability of PEN nanocomposites.

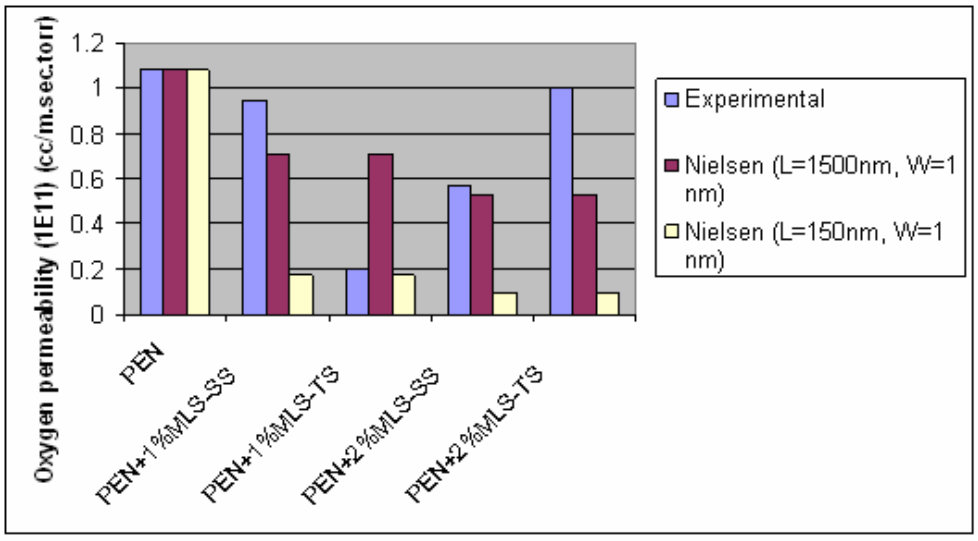

Figure 4.49: Oxygen permeability of PEN nanocomposites.

Table 4.35: Comparison of experimental and theoretical TF in PET nanocomposite films.

Samples	Expt. P (1E9)	V_{MLS}	Predicted TF, using eq. (4.1)	TF (d'/d) from expt. P, using eq. (4.6, 4.7)	Predicted d', using eq. (4.2)	d' from expt. P, using eq. (4.6, 4.7)
PET	3.7	0	1	1	0.15	0.15
PET+1%MLS	4.34	0.056	5.245	0.85	0.79	0.13
PET+2%MLS	1.34	0.108	9.115	2.76	1.37	0.41
PET+3% MLS	1.35	0.155	12.6475	2.74	1.90	0.41

Table 4.36: Comparison of experimental and theoretical TF in nylon nanocomposite films.

Samples	Expt. P (1E9)	V_{MLS}	Predicted TF, using eq. (4.1)	TF (d'/d) from expt. P, using eq. (4.6, 4.7)	Predicted d', using eq. (4.2)	d' from expt. P, using eq. (4.6, 4.7)
Nylon	7.89	0	1	1	0.36	0.36
Nylon+1% MLS	5.41	0.0482	4.615	1.46	1.66	0.53
Nylon+2% MLS	5.41	0.0929	7.9675	1.46	2.87	0.53
Nylon+3% MLS	5.48	0.1344	11.08	1.44	3.99	0.52
Nylon+5% MLS	3.22	0.209	16.675	2.45	6.00	0.88

The deviation in predicted permeability from the experimental results is observed. One of the possible reasons could be that Nielsen model emphasizes only the MLS content and its

distribution in the matrix. Other than MLS content and its distribution, the effect of MLS on the polymer matrix and the interface also affects the permeability value as reflected in our experimental value. This is also explained by the conceptual model described by Beall.[17] A nanocomposite has four distinct phases: MLS, surface modified phase, constrained polymer phase and a polymer phase similar to the pure polymer. Beall explained polymer-MLS interface as the dominant factor that contributes in improving the properties (mechanical, barrier etc.) in comparison to the pure polymer. The Nielsen model takes only the distribution of MLS into consideration, but the effect of MLS addition on the polymer matrix is not considered. While the MLS contributes to the tortuous path, the deviation from the predicted values may be dominated by an increase in a low density polymer-MLS interphase. The possible reason could be low density crystallite-amorphous interphase near MLS. To probe further the effect of crystallinity resulting from the addition of MLS, the crystallization in nanocomposites is analyzed. Pendse et al. [4] in our group the effect of MLS on crystallization. When observed in polarized optical microscopy, pure polymer shows bigger spherulites. When the MLS is introduced, it forms smaller spherulites. This shows that nucleation is affected by the presence of MLS. Since MLS has acted as nucleating agent and enhanced nucleation rate, therefore regions at the interface of MLS and polymer will have smaller spherulites. The MLS-polymer interface could be of low density (due to the low density crystalline-amorphous regions near MLS). If the nanocomposites have an increased low density interfacial area, higher permeability than predicted permeability can result. Therefore, modification of the host matrix near the interface of MLS due to MLS addition plays important role in the barrier properties. The effect of the interface in terms of relative densification is probed in Chapter 5 and effect of interface on glass transition and thermal expansion by investigating the polymer physics of confinement is studied in Chapter 6.

4.6 Conclusions

The dispersion of MLS in nylon nanocomposites was studied using X-Ray Diffraction (XRD) techniques. Transmission Electron Microscopy (TEM) was used to characterize both PET and PEN nanocomposites. Due to the availability of the dual beam scanning electron microscopy (SEM), the tedious sample preparation method by ultra microtome method for TEM is avoided. Therefore, all the compositions of PEN nanocomposites studied to investigate the dispersion of MLS by using the dual beam SEM. Nylon nanocomposites showed an exfoliated structure and PET nanocomposites showed a combination of intercalation and exfoliation. A decrease in permeability is observed for all the nanocomposites in nylon where as an increase in permeability is observed for some compositions of PET nanocomposites. Permeability of fatigued and stretched samples was also studied. In fatigued sample, defect generation and subsequent thermal healing played a significant role in determining the permeability in nylon nanocomposites. Oxygen permeability stretched and fatigued samples were lower than that of unstretched and as-processed PET samples. Higher water absorption is observed in nylon compared to PET films in the same time period. As- processed nylon films showed lower permeability to gases compared to annealed films. In PET nanocomposite, with lower concentration of MLS, crystallinity played a significant role in determining permeability. However, with higher concentration of MLS in PET nanocomposites, MLS played a significant role in determining the permeability. An increase in helium permeability is observed for fatigued and stretched samples. On the other hand, decreased oxygen permeability is observed. PEN+1% MLS-3S nanocomposites sample showed the lowest permeability compared to all other nanocomposites. This is approximately five times lower than that of pure PEN. Based on the glass transition temperature and barrier property of the material PEN+1% MLS-3S nanocomposite is a best material compared to all materials studied here.

Permeability of PET and nylon nanocomposites are predicted considering amorphous, crystalline, and MLS content. Total crystallinity did not decrease in PET nanocomposites but an increase in permeability is observed. The Models do not explain the effect of the presence of MLS decrease in permeability of the nanocomposite. If a weakened interface is hypothesized, there is a possibility of increase in permeability. This could be due to the dominance of weak interface. In Chapter 5 the characteristics of the interface of MLS-polymer in two different systems such as PET and PEN is studied to probe the possible reason of increase in permeability. Chapter 5 explains the interface study of MLS-polymer by using Atomic Force Microscope (AFM) in the force modulation mode. Chapter 6 explains the interface and confinement effect in the thin PET polymer and nanocomposite films.

4.7 References

[1] Ranade, A.; D'Souza, N. A; Gnade, B.; Dharia, A. , Annual Technical Conference (ANTEC) Conference Proceedings **2** (2003) 1938

[2] Fornes, T. D.; Paul, D. R. Polymer **44** (2003) 3945.

[3] Ranade, A.; D'Souza, N. A.; Wallace, R. M.; Gnade, B. E. Rev Sci Instru **76** (2005) 013902.

[4] PENdse, S.; Ranade, A.; D'Souza, N.; Ratto, J. O. Annual Technical Conference (ANTEC) Conference Proceedings **2** (2004) 2343

[5] Mancini, S. D.; Zanin, M. Mater Res **2** (1999) 33.

[6] Chang, J. –H.; Park, D.-K. J Polym Sci Part B: Polym Phys **39** (2001) 2581.

[7] Pegoretti, A.; Kolarik, J.; Peroni, C.; Migliaresi, C. Polymer **45** (2004) 2751.

[8] Wu, T-M.; Liu, C-Y. J Macromol Sci **43** (2004) 1171

[9] Nielsen, L. E. J. Macromol. Sci Chem **1** (1967) 929.

[10] Giannelis, E. P. Adv Mater **8** (1996) 29.

[11] Lan, T.; Kaviratna, P. D.; Pinnavaia. T. J. Chem Mater **6** (1994) 573.

[12] Patcheak, T. D.; Jabarin, S. A. Polymer **42** (2001) 8975.

[13] www.nanoclay.com

[14] Petropoulos, J. H. J Polym Sci Polym Phys Ed **23** (1985) 1309.

[15] Crank, J.; Park, G. S. Diffusion in Polymers, Academic press (1968).

[16] Leterrier, Y. Prog Mater Sci **48** (2003).

[17] Pinnavaia T. J.; Beall, G. W. Polymer-clay nanocomposites (2001).

CHAPTER 5

POLYMER-MLS INTERFACE STUDY USING ATOMIC FORCE MICROSCOPY (AFM) IN POLYMER NANOCOMPOSITES

The effects of MLS concentration and dispersion, and crystallinity on permeability were studied in previous chapters. The increase in permeability was observed in some nanocomposites of PET as explained in Chapter 4. In this chapter, the role of the interface on the increase in permeability of nanocomposites is explored. Atomic force microscopy (AFM) images in the force modulation mode are used to understand the relative densification or hardness at the interface.

5.1 Atomic Force Microscopy (AFM)

Atomic force microscopy is conventionally used for acquiring topographic images with high resolution up to a few nanometers. It has been used to characterize the different phases in materials. A schematic of AFM is shown in Figure 5.1. The sample is mounted on a piezoelectric scanner which can be precisely moved in X, Y and Z directions. The sample is scanned in the X and Y direction with a tip attached to the free end of the cantilever. The radius of the tip is a few nanometers. The laser beam is focused on the tip with the help of a mirror. The beam is reflected from the back of the cantilever to a set of four photosensitive diodes. These diodes detect deflection of laser beams from the cantilever.

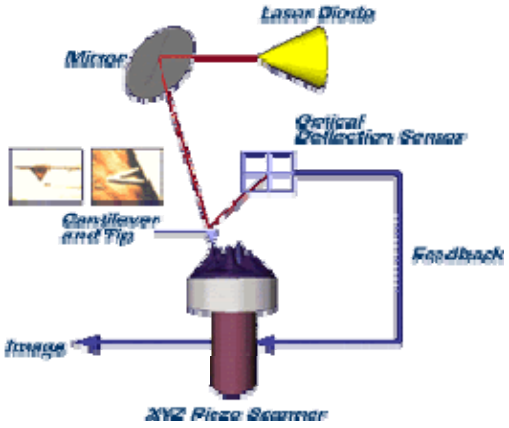

Figure 5.1: Schematic of AFM explaining principle.

5.1.1 Modes of Operation of AFM

There are different modes of operation in AFM. They are contact, non-contact, and tapping mode. Any of these modes can be used for imaging depending on the type of image and the resolution required.

5.1.1.1 Contact Mode

In the contact mode, the tip scans in close contact with the sample surface. Therefore, the force on the tip is repulsive since the distance is small as shown in Figure 5.2. It is in the order of 10^{-9} N. This force is set by pushing the cantilever against the sample with a piezoelectric positioning element. In the contact mode, deflection of the probe is measured. This measured deflection is compared with the desired deflection. The DC feedback amplifier applies a voltage to the piezo to raise or lower the sample relative to the cantilever to restore the desired value of deflection. The voltage that the feedback amplifier applies to the piezo is a measure of height of different features of the sample. This is displayed as a function of the position of the sample.

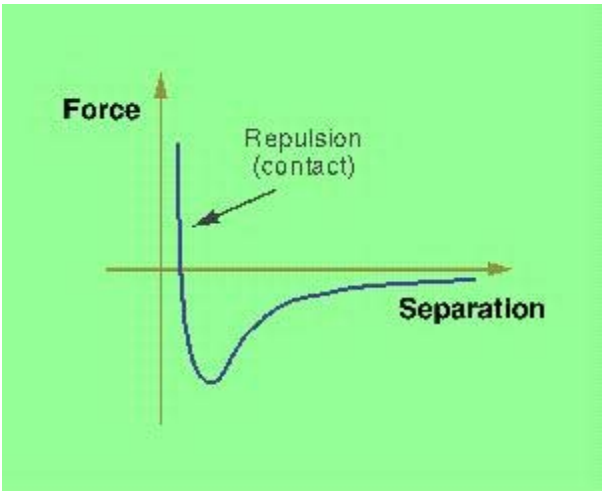

Figure 5.2: Region of contact mode operation (very close to the sample surface, therefore repulsive force is experienced).

5.1.1.2 Non-contact Mode

In the non-contact mode, the tip is not in contact with the sample surface. It is 5-15 nm above the sample surface. Therefore, attractive van der Waals forces acting between the tip and sample are detected. The magnitude of the force is very small; therefore the tip must be given a small oscillation so that the AC detection methods can be used to detect the small forces between the tip and the sample surface.

5.1.1.3 Tapping Mode

In the tapping mode, the tip is not continuously in contact with the sample surface unlike in the contact mode. It is alternately in contact with the surface to provide high resolution and not in contact to avoid dragging across the surface. Depending on the frequency of the probe, the tip alternately contacts the surface and lifts off. When the tip comes in contact with the surface, the cantilever oscillation is reduced due to the energy loss caused by tip contact. This variation in amplitude change of oscillation (Figure 5.3) is detected to characterize the sample surface. The

advantage of tapping mode is that the tip does not wear like in contact mode and therefore, the life of the tip increases, and also reproducible results can be obtained.

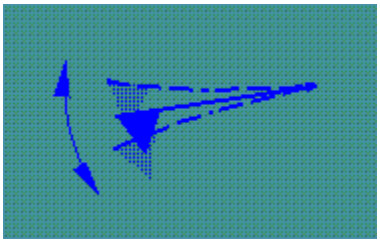

Figure 5.3: Variation in amplitude change of oscillation during contact mode.

5.1.2 Phase Imaging

This is an extension of tapping mode AFM. Topography and phase differences can both be imaged. In the phase imaging AFM method, the phase difference between the oscillations of the cantilever driving piezo and the detected oscillations is measured. This phase lag is very sensitive to material properties such as modulus or density.

Force modulation (FM) AFM is an extension of the AFM techniques, which can be used to map the difference of elasticity of material in a blend, composite etc. It allows the simultaneous acquisition of both topographic and material property (elasticity) maps. In the contact mode the probe, which includes the cantilever and the tip, scans in x-y direction. In the force modulation technique the probe also moves with small oscillation (modulates) in the z direction.[1] The modulation will depend on the properties of the sample. If the material has low elasticity, the probe oscillation will be lower compared to the material with higher elasticity as shown in Figure 5.4. In the FM-AFM mode when the probe is modulated, with the tip in contact with a sample, the sample surface resists the oscillation and the cantilever bends. Since it applies the same force in all the regions of the material, a stiff area in the sample deforms less than a soft area. Hence, stiffer areas put up higher resistance to the cantilever's vertical oscillation and,

consequently cause large bending of the cantilever. Therefore, the relative stiffness of the material is reflected as a variation in the cantilever deflection amplitude at the frequency of modulation. In other words, damping of the oscillation amplitude due to interaction of tip with the surface is used to produce the force modulation image. Imaging polymers in tapping mode is advantage as polymer samples are soft. If the images are taken in the contact mode, the tip-sample interaction could exert forces in the sample that results in plastic deformation around the tip.

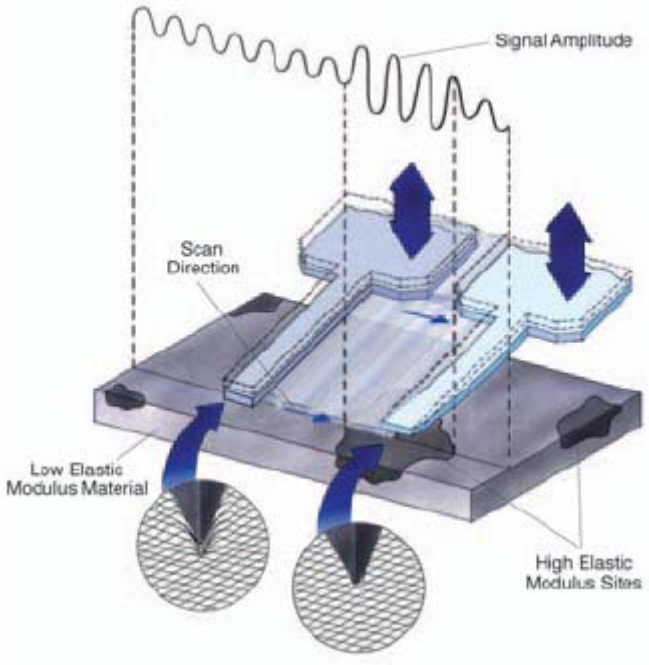

Figure 5.4: Figure illustrating the principle of FM-AFM.

5.2 Role of Interface

At the MLS-polymer interface, the creation of an interphase can be inferred. Interphase characterization in composites has been studied using nano-scratch, nano-indentation, AFM by different groups. [2- 6] The property of an interphase is governed mainly by the thermodynamic compatibility, chemical, and morphological nature between the filler and matrix. Functional

performance such as mechanical and the structural integrities can be tailored by altering the properties of the interphase. Nano-indentation and nano-scratch instruments are used to measure the mechanical properties of a fiber matrix interphase. Mader et al.[7] studied the interphase to predict the properties of composites. They formed the glass fiber from γ–aminopropyltriethoxysilane(APS) with PU and PP. They studied γ–aminopropyltriethoxysilane(APS) in polyurethane (PU) and polypropylene (PP) forming glass fiber in polypropylene matrix. They studied the properties of the interphase by using AFM technique in the nano-indentation mode. They observed the average moduli of the interphase are more than half and three times larger than the matrix value for APS/PU-PPm and APS/PP-PPm systems. The modulus profile[7] (modulus at different distance from the fiber) as shown in Figure 5.5 shows that the interphase of APS/PU and APS/PP glass fiber reinforced in PP matrix shows different behaviors. . At the interphase with APS/PU glass fiber in Figure 5.5 (a) explains that modulus at x (distance) less than and at zero is less. When x is greater than zero, modulus increases due to the modulus of fiber. On the other hand, at the interphase with the APS/PP glass fiber shows at x less than and zero, modulus starts increasing. The increase is 40 GPa in the softer APS/PU interface while it is 60 GPa in the stiffer APS/PP interface.

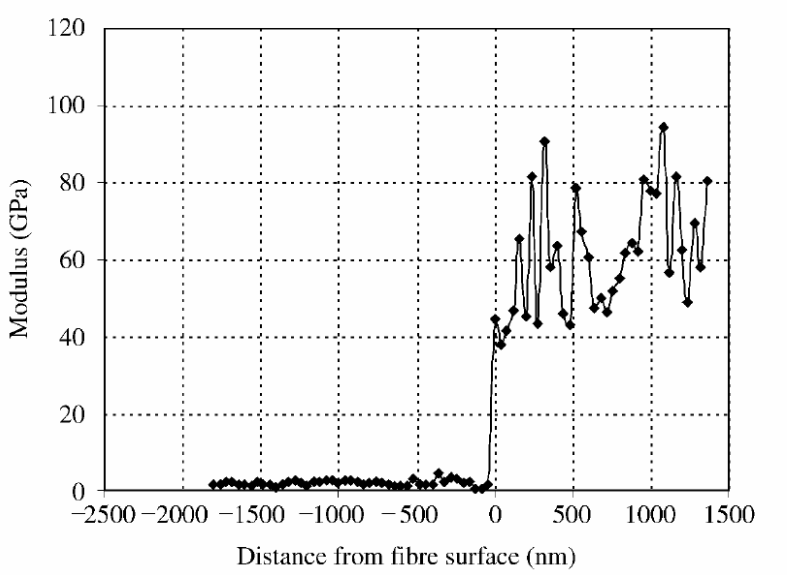

(a)

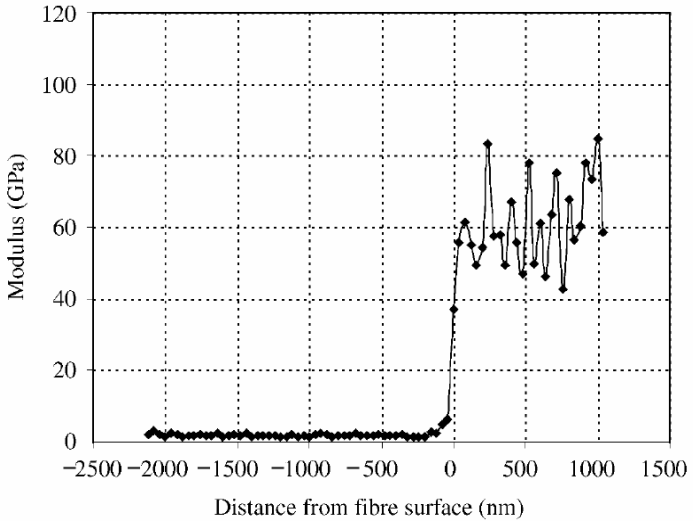

(b)

Figure 5.5: The profile of moduli across the matrix/interphase/fiber region in: (a) APS/PU sized; and (b) APS/PP sized fiber/PP composites.[7]

Hodzic et al.[8] studied the interphase by using nano-indentation and nano-scratch techniques. They studied the interphase both in dry and water aged conditions. Hardness was calculated using Berkovich tip by taking load and depth into consideration. The width of interphase increased from ~0.8 to 1.5 μm from dry to aged condition. Hodzic et al. observed that

hardness value decreased with aging and reached its saturation after ten weeks of aging as shown in Figure 5.6. They attributed this due to the interdiffusion of water into the interphase regions.

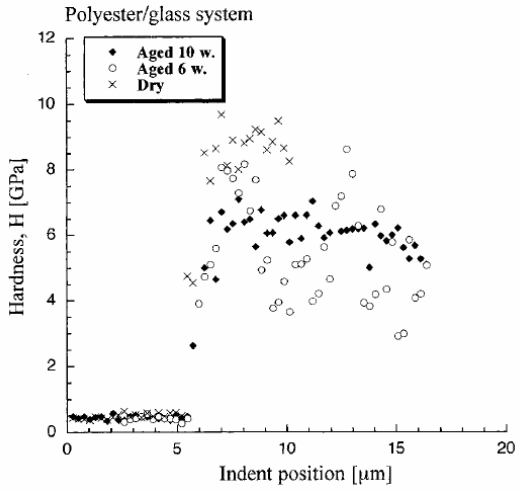

Figure 5.6: Hardness for polyester/glass system in dry and aged condition in dry conditions and after 3 and 10 weeks of aging in water. The transition zone from the matrix on the left to the glass fiber on right.[8]

In this study the polymer-MLS interface is studied using atomic force microscopy in the force modulation mode. The interface is the boundary between the polymer matrix and MLS. The interphase is the intermediate region between the polymer and MLS. The relative variation in local hardness at MLS, polymer matrix, and interface is shown in Figure 5.7. The Y-axis can be either hardness or density. The interface can be weak or strong. Figure 5.7 shows the hardness of different phases in two different cases. The hardness values are not to scale. If the interface is strong then improvements in barrier and mechanical properties are expected. The highest density or hardness is observed at the MLS. Density of different regions will follow in the order of MLS>Interface>polymer. If the interface is weak then improvement in properties can not be obtained as predicted. Since hardness and density are directly related, density will be expressed in terms of hardness as force modulation AFM images are expressed in terms of relative hardness.

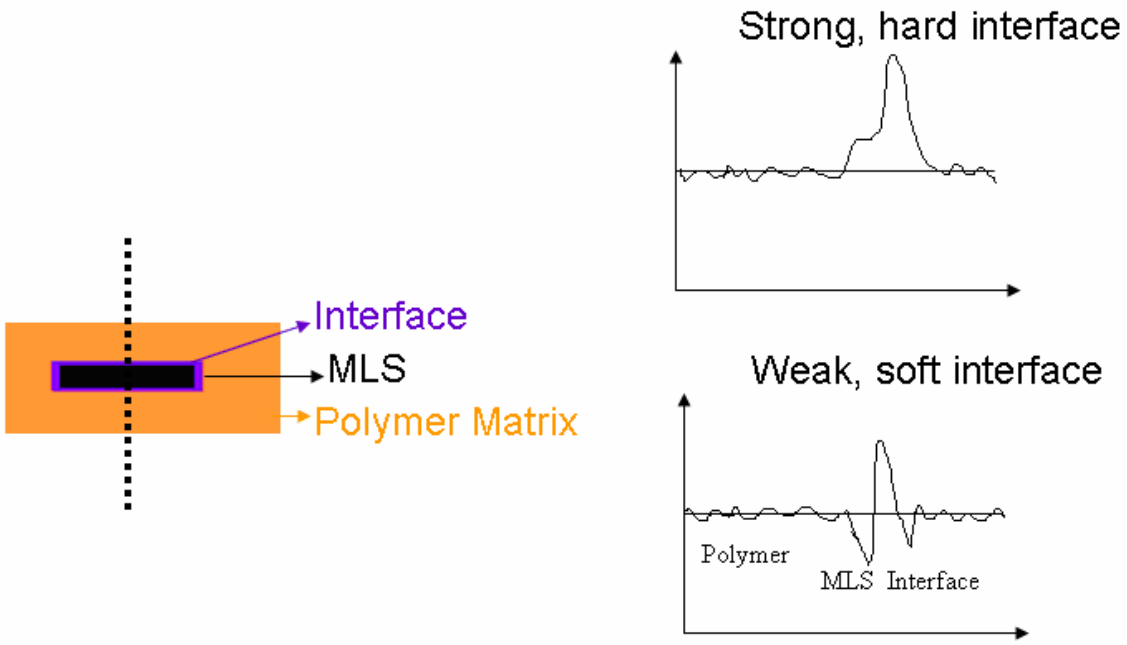

Figure 5.7: Different phases in nanocomposites and their relative hardness in two different cases (strong and weak interface).

5.3 Experimental

Atomic Force Microscopy (AFM), force modulation (FM) images are taken using FESP tip in the force modulation deflection mode in Nanoscope III, Veeco Instruments, USA. Specifications of FESP tip (Model: BS multi 75, Budget sensors) are reported in Table 5.1.

Table 5.1: Specification of the probe.

Specification	Values
Resonant frequency	75 kHz
Force constant	3N/m
Length	225 μm
Width	28 μm
Thickness	3 μm
Tip height	17 μm
Tip radius	< 10 nm

The usual method for displaying the data is in terms of color mapping. The different colors will show different regions in the materials. Images obtained in the force modulation mode are height and amplitude images.

Force modulation AFM images are studied to understand the MLS dispersion and their relative hardness in the different regions in the polymer nanocomposite. Nanoscope software is used to analyze the AFM images such as to calculate the amplitude in the different region in the polymer nanocomposites. The amplitude at different points through the section is obtained. This amplitude can be related to the hardness of the material, and hardness is related to density. Therefore, relative hardness and density is calculated at different points. Dimensions of the MLS are determined using the Nanoscope software® and Image J® software.

5.4 Issues Related to Quality of Image

There are various factors that need to be taken care of to get a good image of the film sample. The image quality is affected by tip quality, moisture in the environment, and dirt on the sample. Better resolution of the image can be obtained with smaller tip radius. A very sharp tip results in very good quality images with good resolution. When the tip is used repeatedly, the sharpness of the tip is reduced and the tip starts broadening which is called tip broadening. Tip broadening is most commonly observed when the radius of curvature of the tip is comparable with, or greater than, the size of the feature to be imaged. Under ambient conditions, sample

surfaces are covered by a layer and one of the main components of this layer is water vapor from the ambient atmosphere. When the probe touches the sample, due to surface tension, a meniscus forms and the cantilever is pulled towards the sample surface. This surface tension could affect the quality of the image. It could distort the image. Because of tip contact, it can also destroy the sample. It is observed that the quality of the image is better on a dry day than a rainy day. On a rainy day the humidity content in the environment increases and therefore, the quality of the image deteriorates. In addition, the sample surface should be clean. It is always recommended to clean the surface with compressed air or nitrogen or dust remover. If there is any dirt in the sample, it may get attached or stick to the tip surface. Depending on the type of dirt, the tip radius will be affected.

Once the image is obtained, it needs to be carefully analyzed. For example, if the shape of the tip has changed during the experiments. Two different samples with some variability are imaged during this change of shape of tip. In this case the analysis might not be correct. So after every image the quality of the tip is judged by using nanoscope software®. For all images that are used for analysis, a fresh tip is used for each sample.

5.5 Results and Discussions

5.5.1 FM-AFM Image of PET Nanocomposite

Force modulation images of polymer nanocomposites are obtained using a fresh tip. The parameters that gave optimum image are: set point (1.4 V), driving amplitude (350 mV), integral gain (0.2) and proportional gain (0.3), and scan speed (3 μm/sec). In polymer nanocomposites, the MLS and polymer have different elastic moduli. Because of this difference in elasticity, MLS and the polymer matrix appear as two distinct phases in the FM AFM images as shown in Figure 5.8.

Force modulation images are taken in a 10μmX10μm region as shown in Figure 5.8. They clearly show both the MLS and the matrix. The amplitude at the MLS and interface and bulk matrix is calculated from the amplitude image by section analysis using nanoscope software ® [1] as well as WSxM software® [9] as shown in Figure 5.9. Section analyses through different MLSs are presented in Figure 5.10 and 5.11. The section analysis provides amplitude at different points in the image in that section. To understand the variation in amplitude near the MLS region, section is analyzed from different angles. Section analysis through MLS # from different angle is plotted as shown in Figure 5.12. It shows that all the sections from different angles follow the same trend and the magnitude differs slightly when compared to each section separately. The amplitude of the matrix is calculated at three different points as reported in Table 5.2 and average amplitude is determined to be 34 mV. It is used to calculate the relative hardness of the MLS and the interphase region with respect to matrix. In polar polymers the relationship between the modulus (elasticity) and hardness is found to be linear as explained by Gimenez et al.[10] Hence, the elasticity can be explained in terms of hardness or vice versa as here all the relative values are discussed rather than absolute values. MLS has a higher modulus than matrix. Therefore, a higher hardness of the MLS is expected compared to hardness of the base matrix The MLS in the matrix are marked with a number. The MLS shows higher amplitude than the polymer with a sharp peak like crest wherever the MLS is present. Since MLS has the higher modulus material than the polymer, the signal from the MLS in the terms of amplitude of oscillation observed is higher. The interesting point that was observed from the section analysis was a trough near to the crest like region of the MLS. The trough like region is next to the MLS and it is the interphase. Therefore, the interphase shows a trough like region with negative amplitude. This negative amplitude explains the lower elasticity or lower hardness (the softer)

region at the interface. In addition in Figure 5.9, at distance ~1.5 μm i.e. ~ 5 μm from MLS # 7, a trough like region is observed. This indicates that the interphase composition is shared by the bulk matrix. Previous polarized microscopy results by Pendse et al.[11] indicate diffuse crystallites in PET nanocomposites. The cold crystallization region represents a region formed around crystallites. The AFM results indicate that chain folding around the crystallite and MLS is occurring to form the cold crystalline regions.

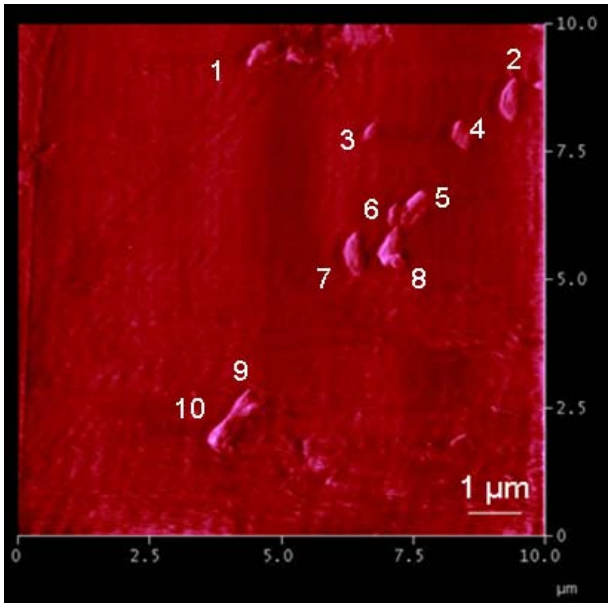

Figure 5.8: Force modulation AFM image of PET+1% MLS.

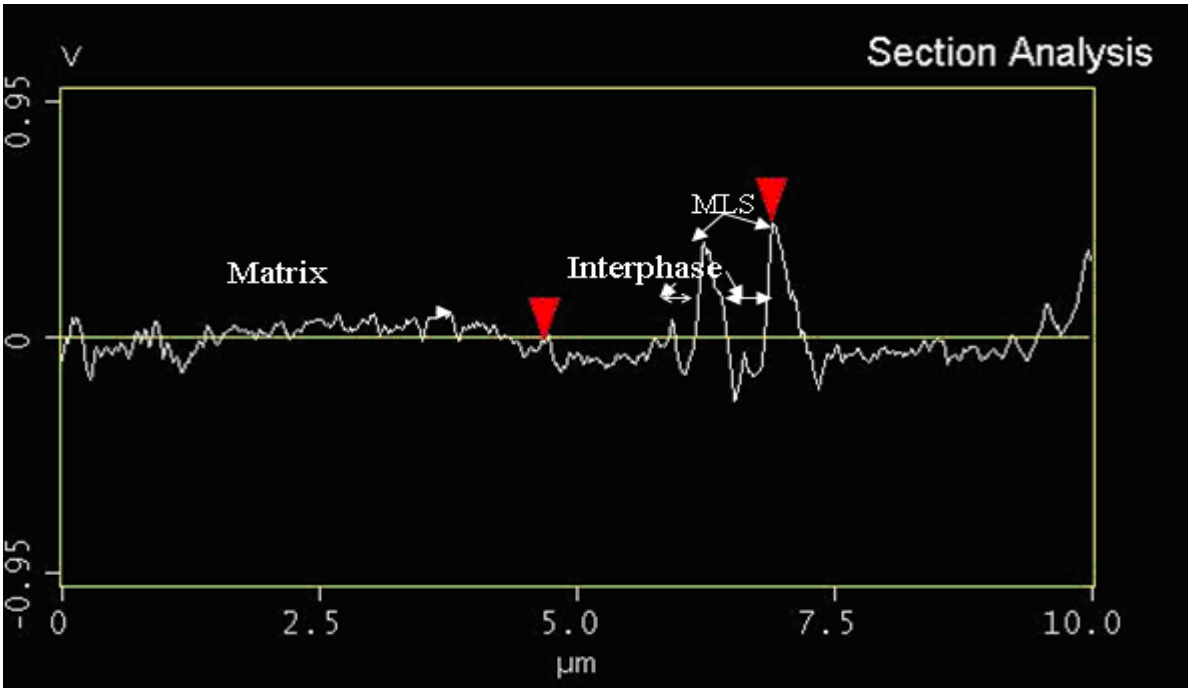

Figure 5.9: Example showing section analysis (amplitude vs. distance) through MLSs # 7 and 8 in PET+1% MLS nanocomposite.

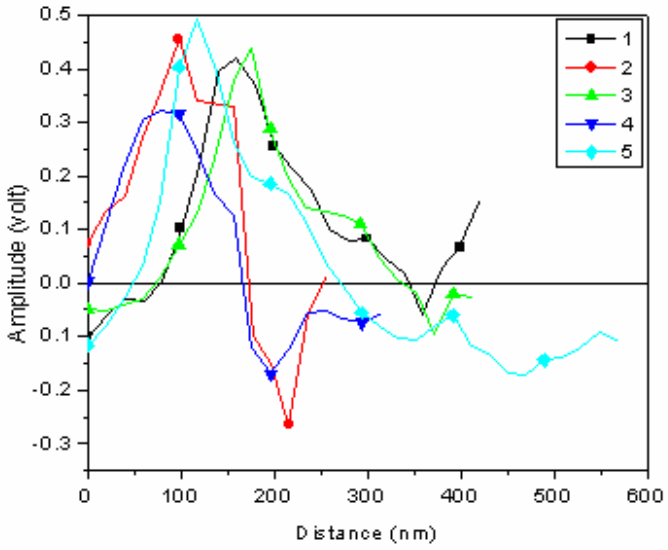

Figure 5.10: Example showing section analysis (amplitude vs. distance) through MLSs # 1-5 in PET+1% MLS nanocomposite.

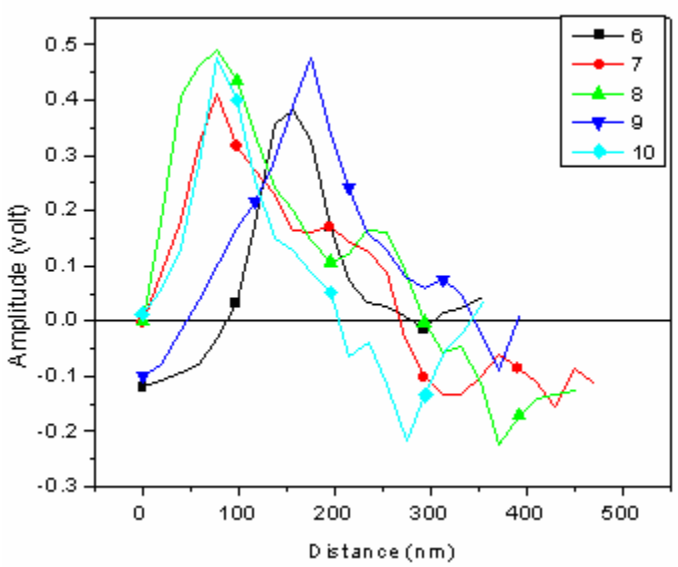

Figure 5. 11: Example showing section analysis (amplitude vs. distance) through MLSs # 6-10 in PET+1% MLS nanocomposite.

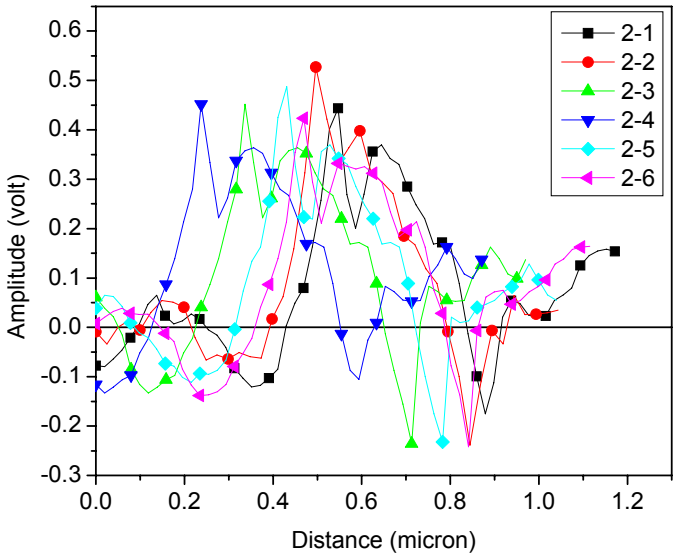

Figure 5.12: Amplitude plot of MLS # 1 in PEN+1% MLS nanocomposite at different sections.

Table 5.2: Calculation for average amplitude of the matrix from Figure 5.8.

Serial #	Average amplitude of polymer matrix (Ra) (mV)
1	31.46
2	37.69
3	33.35
Average	34.16±3.2

To calculate the relative hardness of MLS, the maximum amplitude is determined which is the highest point in the crest like region at the MLS in the section analysis plot (Figure 5.9). To calculate the relative softness of interface, the minimum amplitude is determined which is the lowest point in the trough like region at the interface, next to MLS in the section analysis plot (Figure 5.9).

Relative hardness of MLS = Amplitude of MLS/ Amplitude of polymer (34 mV).

Relative softness of interface adjacent to MLS= (-1) Amplitude of the interface/ Amplitude of polymer (34 mV).

The average relative hardness of MLS and softness of the MLS-polymer interface compared to polymer matrix is calculated for different MLSs and presented in Tables 5.3 and 5.4.Amplitude of MLS is a positive number; however, amplitude of interface is a negative number. Therefore, relative softness of interface is multiplied by -1. The amplitude of MLS # 1 is ~420mV and the relative hardness compared to the base matrix is 12.3. In this chapter, the relative hardness explains hardness with respect to host matrix. Therefore, hardness (modulus, density) of MLS # 1 is ~12.3 times harder than that of host matrix. Similarly, the relative hardness of MLSs # 2 and 3 are 13.3 and 12.8. The amplitude of MLS # 4 is ~ 317 mV. The relative hardness of MLS # 4 is 9.3 which is less than that of other three MLSs. The relative

hardness of 9 out of 11 MLSs are in the range of 11-14.5. The two MLSs that show lower relative hardness are 4 and 11 and they are approximately 9.3 and 7. The minimum amplitude at the interface next to MLS # 1 is ~58. The relative softness of interface is calculated to be 1.7. In this chapter, the relative softness explains softness at the interface with respect to the host matrix. Interface is ~1.7 times softer than the host matrix. The relative softness at the interface next to MLS # 2 is ~7.7. Similarly, the relative softness of MLSs # 3, 4, and 5 are approximately 2.8, 4.9, and 4.9, respectively. The softest interface among all the interface is the one that is next to MLS # 2. It could be due to presence of another MLS adjacent to it (top right corner of MLS # 2) which is clear from Figure 5.8. Larger softness is also determined at the interface of MLS # 8 and this could be due to the same reason as that of interface of MLS # 2. Another MLS (bottom right corner) is observed adjacent to MLS # 8. The approximate dimension and position of these MLS are also tabulated in Table 5.5. It is clear that the MLSs near to number 5, 6, 7, 8, 9, and 10 are more agglomerated compared to number 1, 3 and 4. However, there is a variation in the softness of interface region. MLSs # 8 and 10 show more softness because of the additional effect of MLS from the neighboring region. As explained, interface of MLS # 2 is the softest among all MLS. The length of this MLS is ~1180nm where as all other lengths of MLS are ~600 nm. Thus increased length could be from the combination of two or more MLSs. MLS overlap may be a contributing factor to increase the negative amplitude and therefore, dedensification. The relative softness of interface of MLSs # 8 and 10 are approximately 6.7 and 6.17. Such high relative softness could be due to the additional effects of neighboring MLSs. From Figure 5.8, the average distance between MLSs 2-4, 4-5, 5-7, 7-8, and 9-10 is less than 1 μm. If the distance between the two MLSs is less than ~1.7 μm, higher negative amplitude at the interface is observed. On the other hand, in most of the cases if two MLSs are separated by more than ~1.7

μm, the negative amplitude at the interface is decreased and therefore, a less weaker region i.e. less dedensification is observed. From the statistical analysis using Microsoft excels ® the relative hardness of the MLS and interface with respect to matrix are 12 and 4.5, respectively. This weaker interface at the MLS and polymer is responsible for increased permeability in nanocomposites. This can be explained in terms of Figure 5.13.

Table 5.3: Amplitude of different MLS and their relative hardness with respect to (w.r.t.) polymer matrix.

MLS #	Amplitude from the amplitude image at MLS (mV)	Relative hardness w.r.t. polymer matrix
1	420±24	12.3±0.7
2	455±20	13.3±0.6
3	437±20	12.8±0.6
4	317±17	9.3±0.5
5	494±23	14.5±0.7
6	380±20	11.1±0.6
7	408±24	12±0.7
8	489±24	14.4±0.7
9	474±16	13.9±0.5
10	475±24	13.9±0.7
11	241±17	7.1±0.5

Table 5.4: Amplitude at interface next to different MLS and their relative softness with respect to polymer matrix.

MLS #	Amplitude from the amplitude image at Interface (-mV)	Relative softness w.r.t. polymer matrix
1	58±7	1.7±0.2
2	264±17	7.7±0.5
3	98±10	2.8±0.3
4	169±15	4.9±0.4
5	167±15	4.9±0.4
6	-	-
7	134±10	3.9±0.3
8	229±15	6.7±0.4
9	65±7	1.91±0.2
10	210±14	6.17±0.4
11	140±10	4.11±0.3

Table 5.5: Approximate dimension and coordinates of MLS platelets from Figure 5.8.

Serial #	Length (nm)	Width (nm)	X Coordinate (µm)	Y Coordinate (µm)	Relative hardness compared to matrix	Relative softness ompared o matrix	Distance from neighboring MLS
1	624	60	4.49	9.43	12.3	1.70	5 µm from 2
2	1180	60	9.26	8.67	13.4	7.7	2.76 µm from 3 1.2 µm from 4
3	412	35	6.64	7.89	12.8	2.9	1.7 µm from 4 2.76 µm from 2
4	519	40	8.32	7.91	9.32	5	1.7 µm from 5
5	526	30	7.52	6.54	14.5	4.9	1.7 µm from 4
6	450	40	7.09	6.21	11.2	No soft region is observed	-
7	750	30	6.27	5.63	12	3.9	1.1 µm from 6 0.65 µm from 8 3.7 µm from 9
8	700	40	6.97	5.64	14.4	6.7	0.65 µm from 7 0.52 µm from 6
9	625	35	4.18	2.54	13.9	1.91	3.7 µm from 7
10	650	80	3.75	1.95	13.97	6.18	<0.5 µm from 9
11	450	25	8.36	1.86	7.09	4.1	4.8 µm from 10

Figure 5.13 explains the weak interface in the nanocomposite film samples. Since hardness is related to density, therefore from the FM-AFM image it is clear that density is higher at MLS than polymer matrix than interphase. In this case MLS does not provide a tortuosity path as the permeant permeates through the low density interface. Figure 5.13 (a) explains that permeant gas molecule permeates through the interface and Figure 5.13 (b) explains that permeant gas molecule directly permeates through as it does not find any denser phase compared to base matrix. Correlation between density and permeability is explained in Figure 2.12 in

Chapter 2. When density decreases, permeability increases. Due to this low density interphase, permeability is increased in PET nanocomposite.

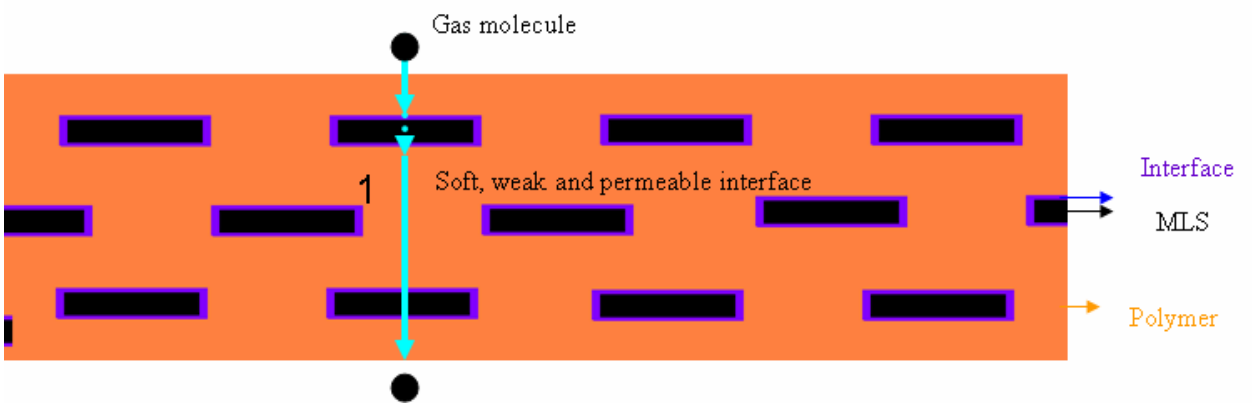

(a)

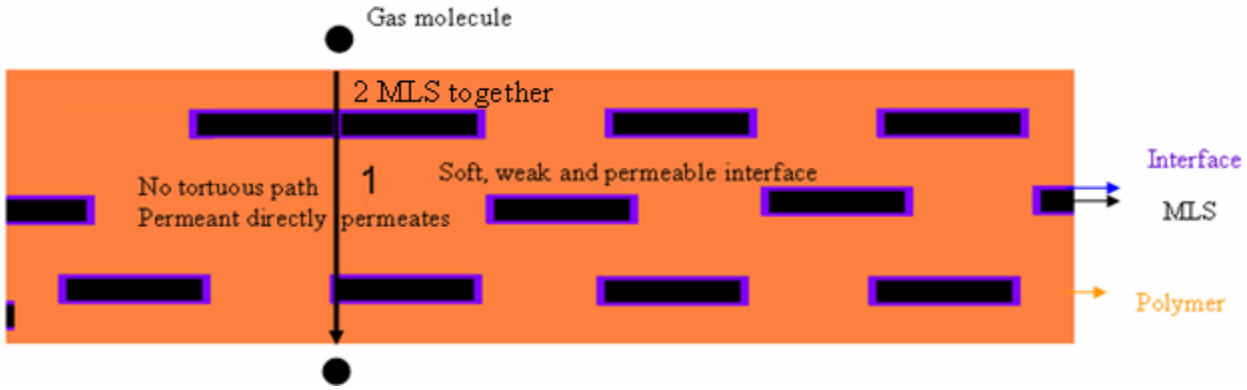

(b)

Figure 5.13: Tortuosity path of permeant in a weak interface nanocomposite system (PET).

5.5.2 FM-AFM Image of PEN Nanocomposite

The same experimental procedure is followed to get FM-AFM image of PEN nanocomposite like PET nanocomposite. The parameters that gave optimum image are: set point (1.2 V), driving amplitude (50 mV), integral gain (0.2) and proportional gain (0.3), and scan speed (3 μm/sec). FM-AFM image of PEN nanocomposites is shown in Figure 5.14. It shows MLSs are very well separated from each other which correlate well with FIB cross section and

TEM images showing exfoliated structure as described in Chapter 4. Like PET nanocomposite section analysis for PEN nanocomposite is analyzed. The amplitude at the center of MLS and polymer is determined by section analysis. From section analysis, amplitude vs. distance is plotted for pure PEN matrix as shown in Figure 5.15. PET nanocomposite showed a weak soft region at polymer and MLS interface by showing negative amplitude. On the other hand, PEN nanocomposite did not show such negative amplitude region compared to the base matrix. MLS shows higher amplitude compared to pure polymer matrix and no negative amplitude is observed at the interface as shown in Figure 5.16 and 5.17. Therefore, MLS has the highest density and the matrix has the lowest density. This explains the interface does not have any weak or soft region unlike PET nanocomposite for the same composition and the processing method. The negative amplitude or weak interface region is not observed for 8 MLSs out of 10 MLSs region. Section analysis is also conducted for MLS # 1 at different angles. The same amplitude is observed from the different angles as shown in Figure 5.18. Figure 5.19 shows the magnified image of 5.14. Table 5.6 shows all the MLS have positive peak amplitude and the base matrix has amplitude similar to polymer matrix. In PEN nanocomposites, the interface result correlates very well with our permeability of PEN nanocomposite.

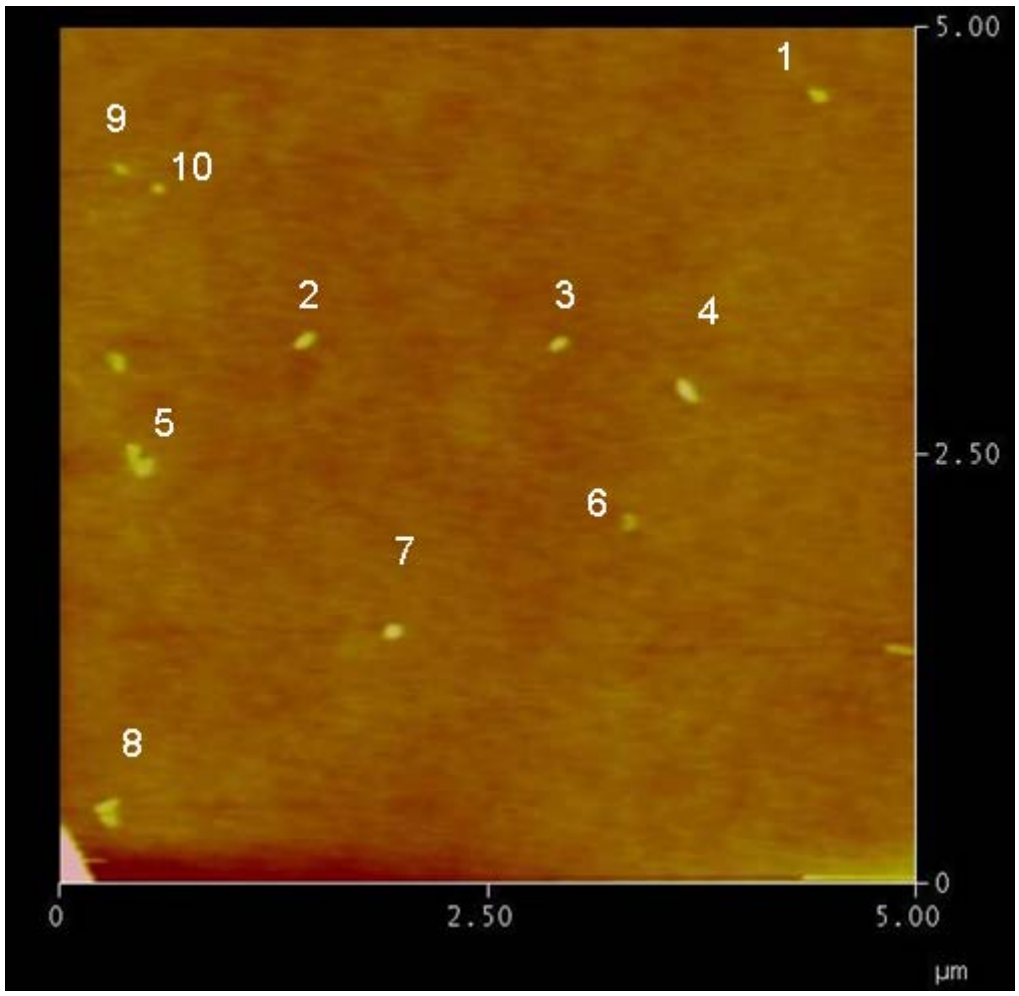

Figure 5.14: Height plot of FM-AFM image of PEN+1%MLS-3S nanocomposite.

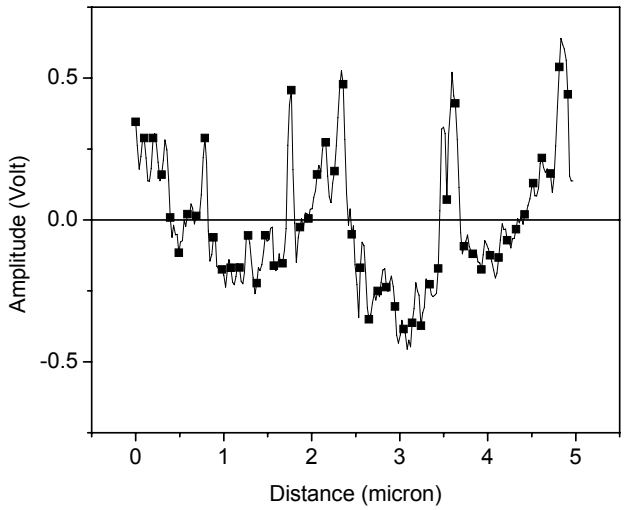

Figure 5.15: Amplitude plot of polymer matrix.

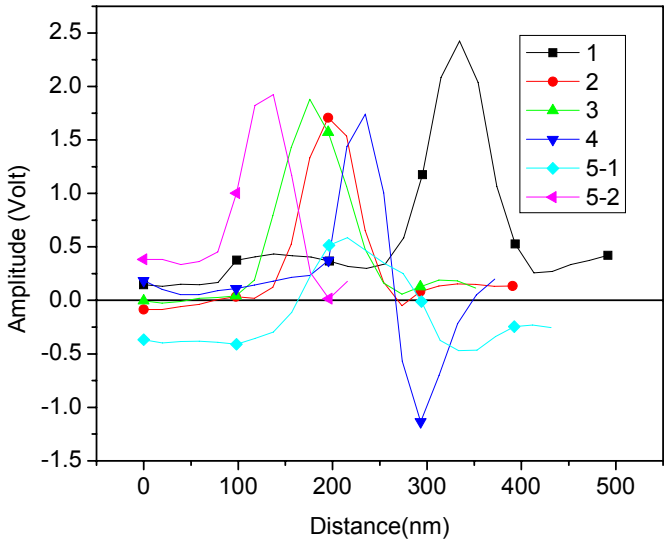

Figure 5.16: Amplitude plot of MLSs # 1-5 in PEN+1% MLS nanocomposite.

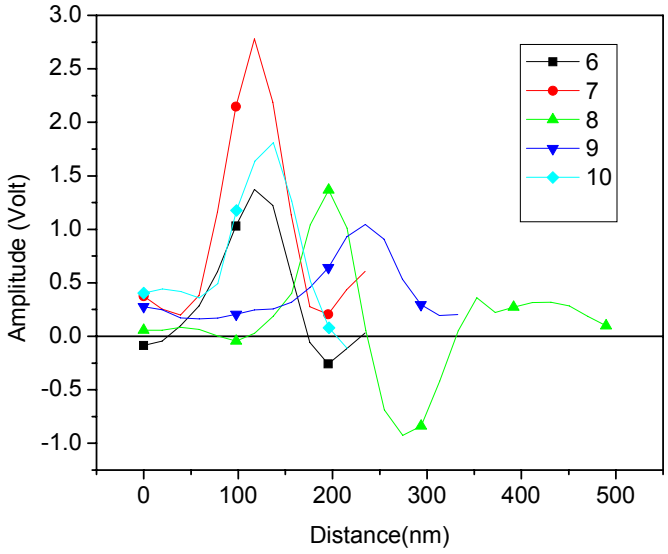

Figure 5.17: Amplitude plot of MLSs # 6-10 in PEN+1% MLS nanocomposite.

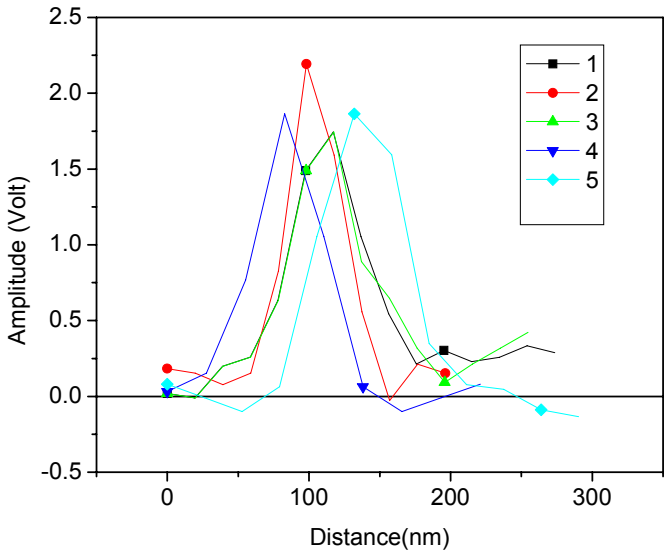

Figure 5.18: Amplitude plot of MLS # 1 in PEN+1% MLS nanocomposite at different sections.

Table 5.6: Maximum amplitude of MLS.

MLS #	Maximum amplitude (V)
1	2.42±0.3
2	1.72±0.3
3	1.85±0.2
4	1.71±0.2
5--1	0.56±0.1
5--2	1.9±0.2
6	1.36±0.2
7	2.75±0.3
8	1.36±0.5
9	1.02±0.2
10	1.78±0.2

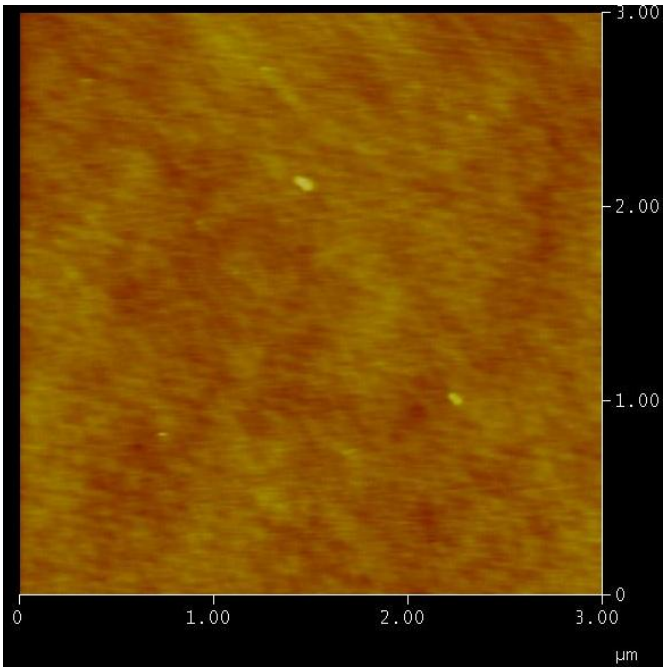

Figure 5.19: Magnified height plot of FM-AFM image of PEN+1%MLS-3S nanocomposite (3µmX3µm).

Relative hardness at the interphase is in between the MLS and polymer matrix. Therefore, density is higher at MLS than interphase than polymer matrix. When a permeant gas molecule permeates through the polymer matrix as shown in Figure 5.20, MLS provides tortuous path without letting it permeate through the other side of the film, therefore, contributing to decrease in permeability in nanocomposite. In PEN+1% MLS-3S, permeability was decreased by approximately one order of magnitude than that of pure PEN.

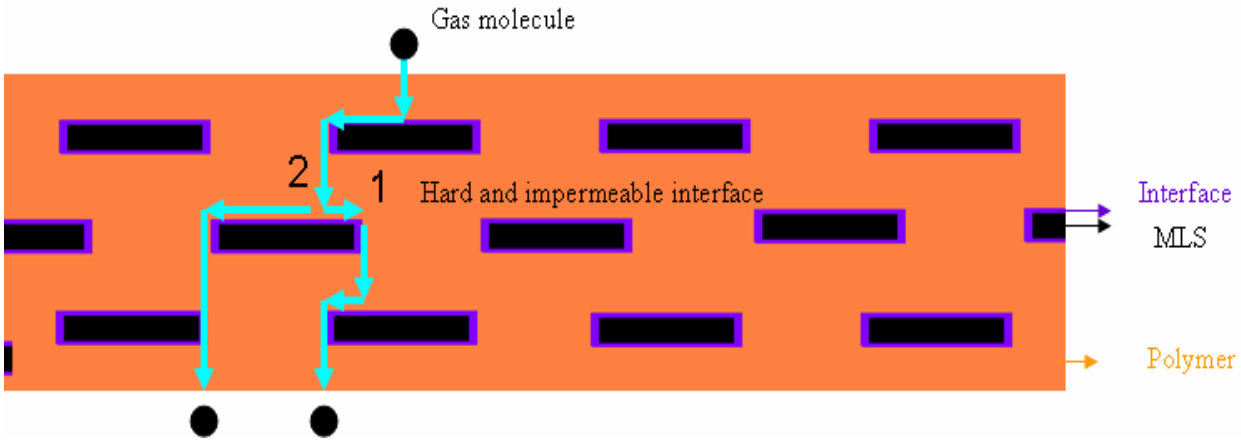

Figure 5.20: Tortuosity path of permeant in a hard interface nanocomposite system (PEN).

5.5.3 Correlation between Cold Crystallization and FM-AFM Images in PET

From the DSC result it is observed that pure PET shows cold crystallization temperature. It explains that the crystallites did not grow completely. Therefore, the crystallites have amorphous region around it. The cold crystallization in pure PET is observed at 133 ºC. From Table 2.6 in Chapter 2, the cold crystallization temperature is decreased by ~10 ºC in nanocomposite. Increase in low density amorphous region can be inferred from this decrease of cold crystallization temperature in nanocomposite. The relative cold crystallization fraction is also increased from 1 to 1.07 in PET nanocomposite compared to pure PET as shown in Figure 5.21. Since MLS acted as nucleating agent, therefore, crystallites are formed on or near the MLS.

Therefore, these low density regions are observed at the polymer-MLS interface which is proved from the force modulation-AFM images. This low density, weak region is responsible for an increase in permeability. The cold crystalline fraction has slightly decreased from 1 to 0.97 in PET+3% MLS. The possible reason of lower permeability in this composition of nanocomposites could be less region of low density phase compared to pure PET.

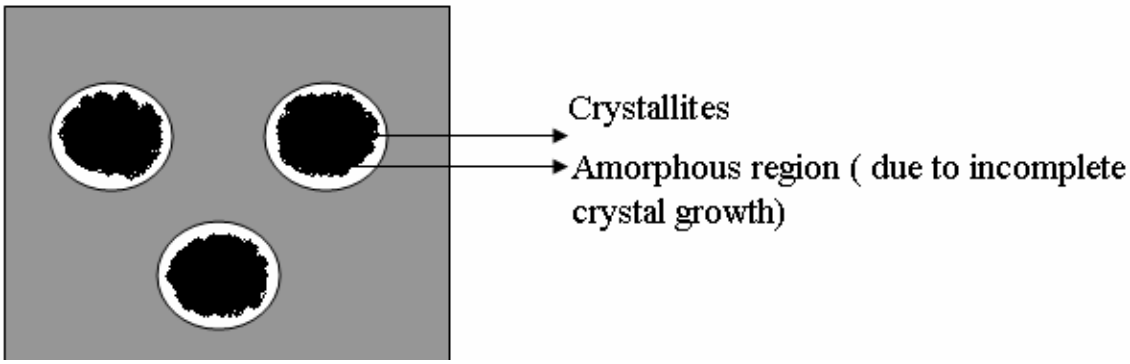

(a): Schematic showing the cold crystalline region in pure PET (less amorphous region around the crystallites).

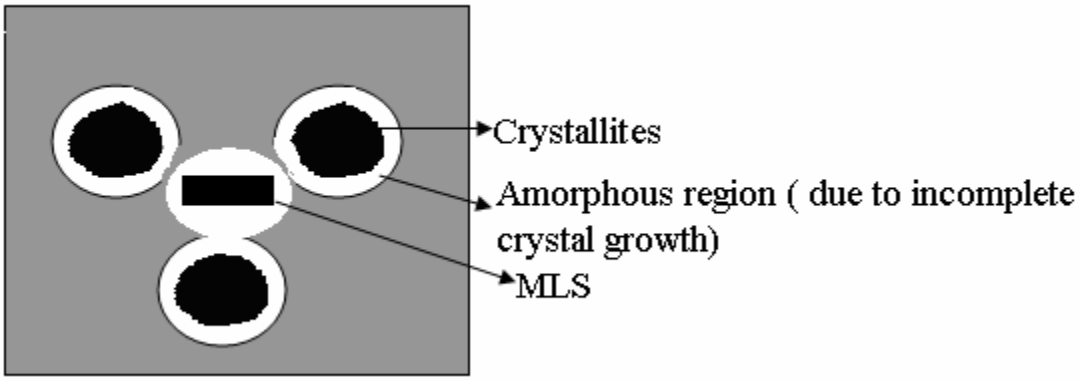

(b): Schematic showing the cold crystalline region in PET +1% MLS nanocomposite (comparatively more amorphous region around the crystallites).

Figure 5.21: Schematic showing the cold crystalline region in PET and nanocomposite.

5.6 Conclusions

The increase in permeability in PET+1% MLS nanocomposite is probed by analyzing the force modulation AFM images. The density at the interface determined was less than the density of matrix. The lowest dense region was observed at the interface in PET nanocomposite. Therefore, it did not provide any tortuous path to lower the permeability and improving the barrier properties. This lowest density interface region contributed to increase in permeability in PET+1%MLS nanocomposite. On the other hand, PEN nanocomposite did not show any low density region at the interface and correlating well with the permeability data.

5.7 References

[1] www.veeco.com/pdfs.php/1 (July 2006)

[2] Kim, J-K.; Hodzic, A. J Adhes **79** (2003) 383.

[3] Mader, E. ; Gao, S.; Planka, R. Adv Eng Mater **6** (2004) 147.

[4] VanLandingham, M. R.; Dagastine, R. R.; Eduljee, R. F.; McCullough, R. L.; Gillespie, J. W. Compos: Part A **30** (1999) 75.

[5] Downing, T. D.; Kumar, R.; Cross, W. M.; Kjerengtroen, Kellar, J. J. J Adhe Sci Tech **14** (2000) 1801.

[6] Mai, K.; Mader, E.; Muhle, M. Compos Part A **29A** (1998) 1111.

[7] Mader, E. ; Gao, S. J Adhe Sci Tech **15** (2001) 1015.

[8] Hodzic, A.; Kim, J. K.; Stachurski, Z. H. Polymer **42** (2001) 5701.

[9] http://www.nanotec.es/

[10] Gimenez, E.; Lagaron, J. M.; Gavara, R.; Saura, J. J., Polym Int **52** (2003) 1243.

[11] Pendse, S.; Ranade, A.; D'Souza, N.; Ratto, J. O. Annual Technical Conference (ANTEC) Conference Proceedings **2** (2004) 2343

CHAPTER 6

INTERFACIAL EFFECTS OF POLYMER NANOCOMPOSITES ON SUBSTRATES

In chapter 6, the effect of MLS interface is studied using the AFM technique and correlated with the barrier properties in nanocomposites. The effect of increased surface area of MLS on the glass transition and thermal expansion is studied in nanocomposites by examining the physics of confinement. The differences between bulk and confined geometry dynamics have been associated with interference of intrinsic length scales with the dimensions of imposed geometry.[1] The free surface of a supported film is more mobile than the bulk polymer film.[2] The mobility of the interface is dependent on the interaction between the film and the substrate. However, weak or unfavorable interactions between the film and the substrate results in increased mobility at the interface. Strong interactions with the substrate may lead to few layers of the molecules being strongly immobilized.[3,4]

The glass transition has been considered in much detail, especially in terms of how it affects either supported,[5-8] or free standing films or glass forming liquids confined in nanoscopic pores. [9,10] Different groups observed that the glass transition has been shown to increase, decrease or not change with decreasing thickness. [11-13] The differences have been attributed to confinement geometry, the particular polymer investigated, experimental method, and measurement technique sensitivity. Green et al.[14] explained that, this effect is due to the range of relaxation times in polymers at the interface and away from the substrate. Next to a substrate, the polymer chains bend and fold over leading to higher density. Decreased mobility, and higher glass transition temperatures occur at the substrate-polymer interface. At the free surface higher mobility, increased relaxation times due to entropic effects such as disentanglements, confinement effects or by chain-end segregation occur. In the intermediate region, the polymer chains have intermediate

mobility. When the substrate-polymer interaction is noninteracting, the free surface mobility dominates leading to decreased T_g's with decreasing film thickness. Next to highly interacting surfaces, the lower mobility fraction dominates and the T_g's increase with decreasing film thickness. This has been ascribed to specific chain organization such as conformation, orientation or chain packing due to a fluctuation in local density[3] and is supported by the molecular simulations,[15] as well as experimental results. This molecular mobility at the interface, in the bulk of the film, and at the free surface affects various properties.

The differences in chain mobility with film thickness and surface interaction has have effect on coefficient of thermal expansion (CTE). The dependence is more pronounced for ultra thin films and arises due to structural density and differences. Prior results have shown that as the samples become thicker, the thickness dependence is diminished and the effective CTE approaches bulk properties. The CTE of polymers is generally lowered by the addition of ceramic fillers. The CTE of bulk polymer composites is influenced by the filler shape, size, concentration and their dispersion.[16-18] In this study, the effects of MLS dispersion on the CTE and T_g of PET polymer thin films of varying thicknesses are examined. PET is a semicrystalline polymer. To understand the crystallinity effect in thin film, the result from PET is compared with poly (ethylene terephthalate) glycol (PETG) which is an amorphous polymer. In this chapter, PET refers to semicrystalline PET and PETG refers to amorphous PET. Before proceeding to the results, a background on confinement is briefly discussed.

6.1 Effect of Confinement on the Glass Transition

Both liquids in nanoporous media and thin films are investigated and presented each separately.

6.1.1 Glass Transition of Liquids Confined in Nanoporous Media

Controlled pore glass (CPG) or Vycor^{TM}glass are most commonly studied as the confining media. These porous media generally have a very narrow size distribution. If very small molecules are confined in nanopores then it is considered "hard" confinement, and if spheres or nanodroplets are suspended in a fluid environment then it is considered "soft" confinement. Polymer thin film confinement is considered as a 2D confinement since one dimension i.e. thickness is confined to nanometer size scale. The liquid confined in CPG or Vycor^{TM}glass Vycor.TM.glass is considered to be between two and three dimensional confining geometry.

Jackson and McKenna[19] have studied the T_g of ortho-terphenyl confined in nanopores in CPG media using DSC. They observed a decrease in T_g with a decrease in pore size as shown in Figure 6.1. They attributed this reduction in T_g to intrinsic size effect.

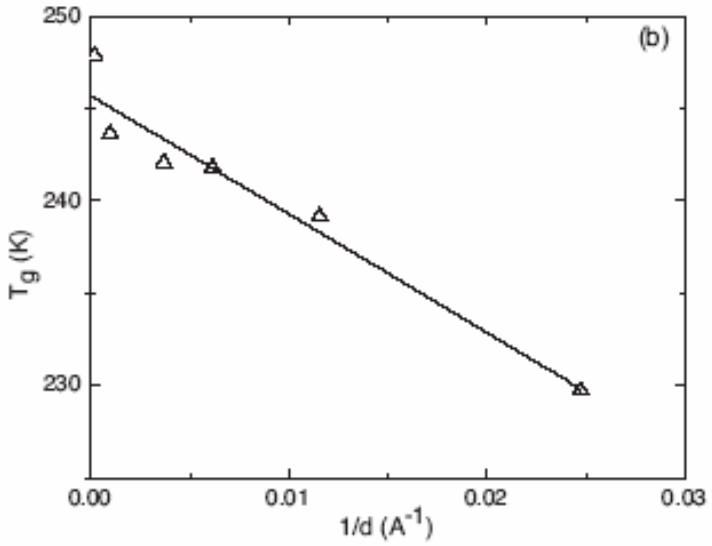

Figure 6.1: A plot showing reduction in T_g with decreasing pore diameter (increasing 1/*d*) for the *o*-TP in CPG.[10]

Alba-Simionesco and co-workers[20,21] performed T_g measurement of toluene and benzene confined in a cylindrical pores of synthesized silicates using adiabatic calorimeter. This nature of

non-monotonic variation of T_g is only observed for confined fragile liquids such as benzene and toluene as proposed by Alba-Simionesco and co-workers. They observed that T_g decreased with a decrease in pore size and then increased. The large increase in T_g by 37K in very small pore diameters of 2.4 nm was explained in terms of a surface effect due to the interaction between the confined molecules and the pore. The reduction in T_g in large pore diameters was due to intrinsic size effects where a decrease in the surface to volume ratio occurs. If the difference in density between the bulk and confined liquid were taken, then the surface effect can be stronger and the T_g of the bulk with the same density as the confined liquid would be lower than T_g of confined molecule in nanopores. This is shown in the dotted line in the Figure 6.2.

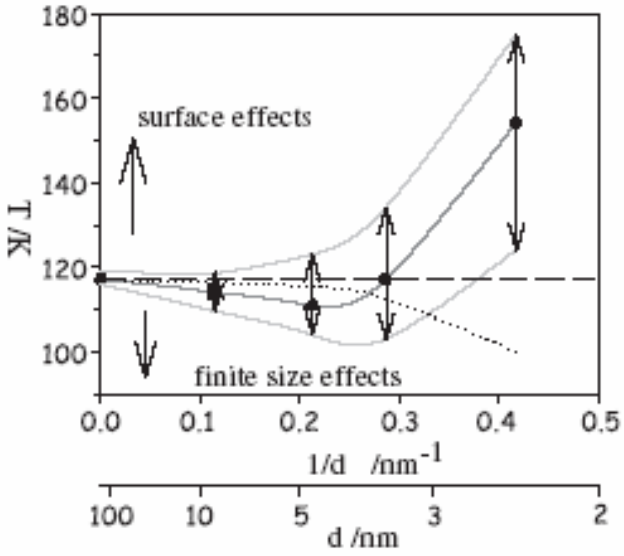

Figure 6.2: Glass transition versus pore diameter for toluene confined in nanopores.[20]

Pissis et al. [22] studied the confinement of polypropylene glycol in Vycor™glass using thermally stimulated depolarization current (TSDC) technique. They observed that the temperature of the α relaxation peak is close to the T_g measured by calorimetry but in comparison to the bulk film lowered T_g is observed. Pissis et al. explained the reduction in T_g in terms of cooperative length scale. The mobility of the small confined molecules increases because the decrease in the

size of the system causes a decrease in the number of molecules rearranging collectively to infer a glass transition.

6.1.2 Glass Transition in Thin Films

Results in thin films have differed from the liquids confined in pores. Keddie et al.[23] studied the T_g of polystyrene (PS) on silicon by using the ellipsometry technique. They observed a depression in T_g for films below 100 nm thickness compared to bulk film. A larger depression in T_g was observed for films of thickness below 40 nm as shown in Figure 6.3. Keddie et al. [24] also observed a depression in T_g for poly methyl methacrylate (PMMA) on gold substrate. However, the same polymer on silicon oxide substrates showed a small increase in T_g due to higher interaction with the substrate. When PMMA is processed on a hydrophobic surface, a depression in T_g is observed as expected.[25] A decrease in T_g with a decreasing film thickness was observed by Green et al. [26] when the thickness is less than 50 nm. They attributed this to the weak interaction between the substrate and the polymer film. Green et al. [27] explain that the change in T_g from the bulk film is due to the range of relaxation times in polymers at the interface and away from the substrate. Ellison et al. addressed the effect of confinement on the gradient of T_g with distance from the free surface of thin film. They explain that both the free surface and substrate confinement are important. T_g decreases near the free surface and this decrease in T_g can extend to 10-14 nm distance away from the surface. The magnitude of the decrease depends on the film thickness. It remains challenging to quantify the variation in T_g in polymer thin films. Computer simulation plays an important role in developing the theoretical basis for a decrease or an increase in T_g observed experimentally.

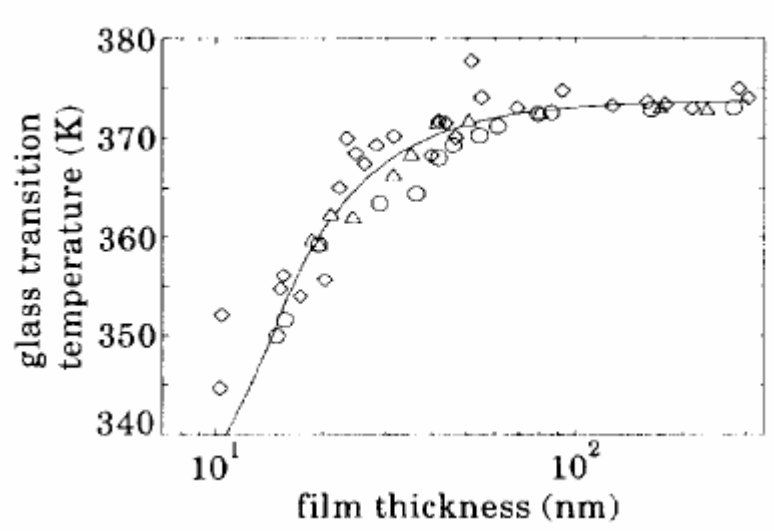

Figure 6.3: T_g as a function of film thickness of PS of three different molecular weights. The solid line is a best fit to the data using equation (12) described later in this chapter.[23]

6.2 Thermal Expansion in Thin Films

Along with the T_g the next important property that has been studied in detail in polymer thin films is thermal expansion. The CTE has been determined to have thickness dependence. The dependence is more pronounced for ultra thin films and arises due to structural differences and density. Prior results have shown that as the samples become thicker, the thickness dependence is diminished and the effective CTE approaches bulk properties. CTE of the PS films also decreased with a decrease in thickness as observed by Keddie et al. as shown in Figure 6.4. Kim et al. [28] also demonstrated that the CTE is thickness dependent. They observed that CTE initially decreases drastically and then begins to plateau with increasing film thickness. If the mobility of the polymer near the substrate is significant, then CTE decreases with increasing film thickness. On the other hand, if the mobility of the polymer near the surface of the film is increased and the free surface mobility is dominant, CTE increases with increasing film thickness. The spin coating process leads to an orientation in the in-plane direction, which gives a strong covalent bond while the interchain

forces out-of plane is dominated by weak Vander walls force. Thus most volumetric expansion is directed in the thickness direction and this effect is more pronounced for thinner films. Thus initially thinner films have higher CTE. The CTE decreases for thicker films due to their higher density. CTE is therefore strongly thickness dependent.

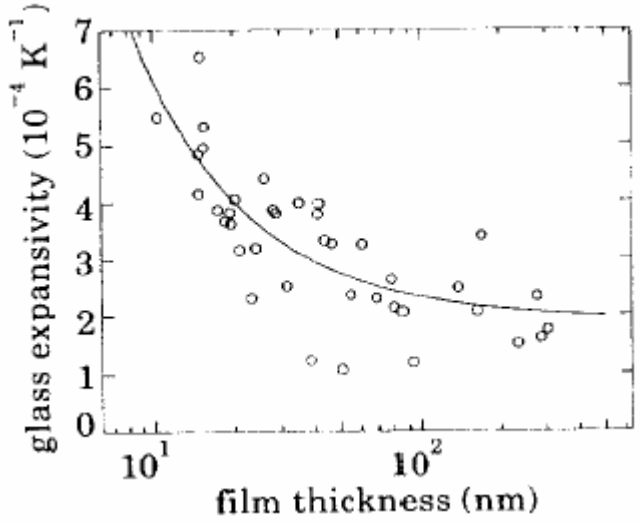

Figure 6.4: Linear CTE below the T_g as a function of film thickness. The solid line is fitted to equation (6), described later on this chapter.[23]

6.3 The Nature of the Glass Transition

One important point is that the bulk T_g itself is not fully understood and it is not clear whether T_g is a thermodynamic second-order transition or a kinetic transition.[29] In thermodynamic measurements a break or jump in the thermodynamic property such as heat capacity or volume with temperature would indicate a first order phase change. Sometimes pseudo-thermodynamic measurements are also included to determine T_g. Pseudo-thermodynamic measurements are defined as a measurement of properties such as film thickness, Brillouin frequency, lateral force microscopy response considering one frequency, fluorescence probe intensity etc. that vary with

temperature. In dynamic measurements relaxation time and viscosity with temperature are studied to understand the T_g. [11]

Differential scanning calorimetry is generally used for bulk films. However, recently it has also been used to characterize ultra thin films. Dynamic measurements such as dielectric spectroscopy are used to understand the relaxation phenomena in thin films. By using these techniques, confinement in nanoporous structures and thin films are studied. In this study ellipsometry is used to determine the thickness of the films over a temperature range.

6.3.1 Ellipsometry

Ellipsometry is used to measure the film thickness. Different parts of the ellipsometry are the light source (for e.g. xenon lamp that projects light in the UV/vis or infra red spectral range), a polarizer, sample holder, an analyzer, and a detector. The light is projected from the light source and the polarizer polarizes it by rotating normal to the beam of light. Light is reflected off the sample and the angle between the transmitted light and the incident plane is measured by the analyzer. The detector measures the intensity of the light that passes through the analyzer. Ellipsometry measures the change in the polarization state of the reflected light from a sample surface to determine thickness of the film as shown in Figure 6.5. This state of polarization after reflection is measured experimentally. The change in amplitude and phase before and after reflection determines Δ and ψ. Polarization of light is characterized by an amplitude ratio A_p/A_s, where p is plane of reflection and s is perpendicular to this plane, and phase difference (dp-ds) of the two components p and s. The angle ψ is defined by the ratio of the amplitude ratios before and after reflection.[30] The ellipsometric angles are determined as a function of wavelength and angle of incidence. A model is constructed using different layers such as, the substrate, film, and ambient and using this model ellipsometric angles are predicted. The predicted and experimental

ellipsometric angles are compared and then the model is adjusted until the difference between the two is minimized. So the ellipsometry technique is a model dependent technique.

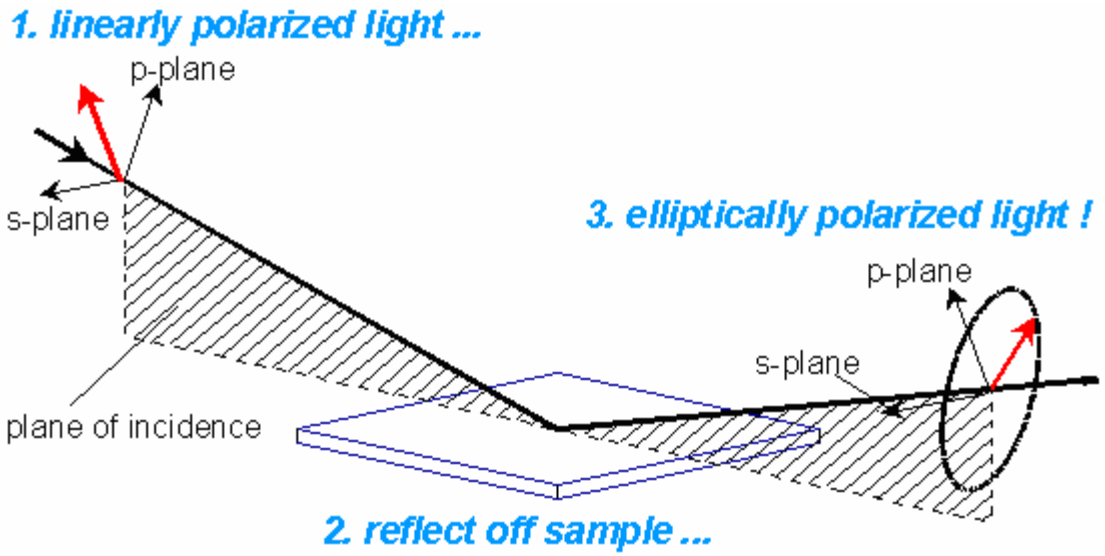

Figure 6.5: Illustration of principle of ellipsometry.[31]

Ellipsometry is most accurate at the Brewster angle – the angle at which the difference between R_p and R_s (the Fresnel coefficients) is the greatest. The change in the amplitude and the phase change of the polarized light after reflection are used to find the values of delta (Δ) and psi (Ψ). The amplitude change and phase change are found in two different planes: the p-plane which is the plane parallel to the plane of incidence and the s-plane which is perpendicular to the plane of incidence. Δ is defined by

$$\Delta = \left(d_p^r - d_s^i\right) - \left(d_p^i - d_s^r\right) \tag{6.1}$$

where r and i corresponds to reflected light and incident light, and p and s correspond to the parallel and perpendicular planes. Ψ is defined by

$$\tan\psi = \left(\frac{\left(\frac{A_p^r}{A_s^r} \right)}{\left(\frac{A_p^i}{A_s^i} \right)} \right) \tag{6.2}$$

Ψ and Δ can also be related according to the Fresnel coefficients by the formula

$$\rho = \left(\frac{R_p}{R_s} \right) = \tan(\Psi) e^{i\Delta} \tag{6.3}$$

where ρ is a complex number called ellipticity. The two optical constants can be related through the equation

$$\bar{n} = n + ik \tag{6.4}$$

which describes the complex refractive index, ñ, in terms of the refractive index, n, and the extinction coefficient, k. Ψ and Δ are dependant on the refractive index and the angle of incidence, and the refractive index is dependent on the wavelength, λ, of the incident light. Therefore, Ψ and Δ is also dependant on the λ of the incident light. In these experiments, data is collected in the spectroscopic scans, which give multiple values of Ψ and Δ by using light at multiple wavelengths. Since the polymer is a transparent material, the Cauchy equation is used to model the data

$$n(\lambda) = A + \left(\frac{B}{\lambda^2} \right) + \left(\frac{C}{\lambda^4} \right) \tag{6.5}$$

where A, B, and C are constant terms based on the sample. The refractive index, n, can also be related to the Brewster angle by the equation (6.6)

$$\left(\frac{n_1}{n_0} \right) = \tan^{-1}(\varphi_B) \tag{6.6}$$

where n_1 is the refractive index of the material and n_0 is the refractive index of the ambient medium. As the refractive index for the ambient medium is known, this formula can be used to calculate the refractive index of the sample. The purpose of both these formulae is to lower the number of unknown constants. By combining three different equations, the thickness can be derived. The equations (6.7)

$$R_p = \left(\frac{(R_{p01} + R_{p12} e^{-2i\delta})}{(1\_R_{p01} R_{p12} e^{-2i\delta}} \right) \tag{6.7}$$

and

$$R_s = \left(\frac{R_{s01} + R_{s12} e e^{-2i\delta}}{1 + R_{s01} R_{s12} e^{-2i\delta}} \right) \tag{6.8}$$

and (6.8) describe the Fresnel reflection coefficients for the infinite series of multiple reflections on a film-covered substrate where the subscript 0 is for the ambient medium, 1 is for the film, and 2 is for the substrate. The equations (6.9) and (6.10)

$$R_p = \frac{n_a \cos\Phi_2 - n_b \cos\Phi_1}{n_a \cos\Phi_1 + n_b \cos\Phi_1} \tag{6.9}$$

and

$$R_s = \frac{n_a \cos\Phi_1 - n_b \cos\Phi_2}{n_a \cos\Phi_1 + n_b \cos\Phi_2} \tag{6.10}$$

describe the Fresnel reflection coefficients for a clean substrate where $Ø_1$ is the incident angle, $Ø_2$ is the reflected angle, corresponds to the ambient medium, and b corresponds to the substrate. The equation (6.11) describes phase change, δ, as a function of wavelength,

$$\delta = \left(\frac{360}{\lambda} \right) d \left(n_1^2 - \sin^2 \Phi \right)^{1/2} \tag{6.11}$$

λ, thickness, d, the refractive index of the film, n_1, and the difference between $Ø_1$ and $Ø_2$, Ø. By combining the above equations thickness can be determined as a function of Δ, Ψ, angle of incidence, indices of refraction of the film and substrate, and wavelength.

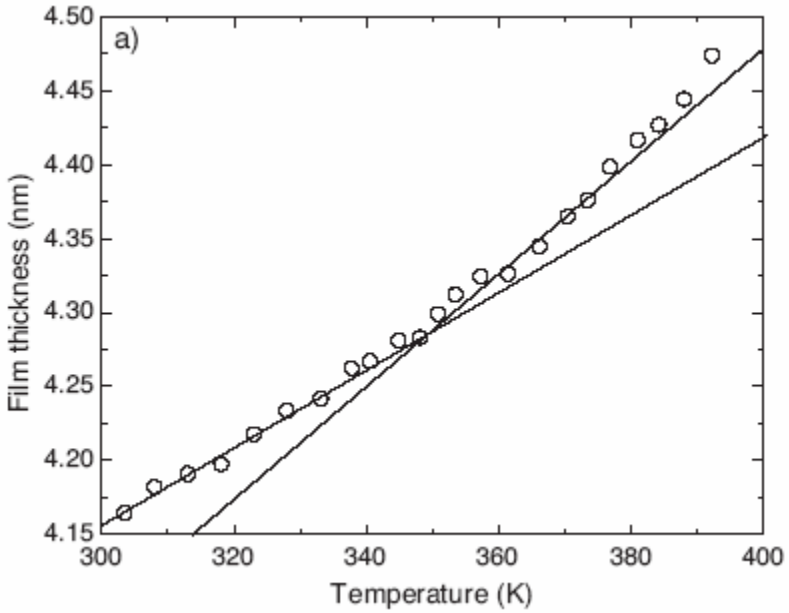

Figure 6.6: The first measurements of the thickness dependence of the glass transition in ultra thin PS films as reported by Keddie et al.[23]

Other than ellipsometry, T_g also can be measured by fluorescence probe intensity method. In this method, florescence intensity is measured as a function of temperature. Figure 6.7 shows the temperature dependence of intensity of pyrene-labelled polystyrene. The intersection of two straight lines of the glassy and liquid states of the pyrene fluorescence intensity is interpreted as T_g of PS film.[32]

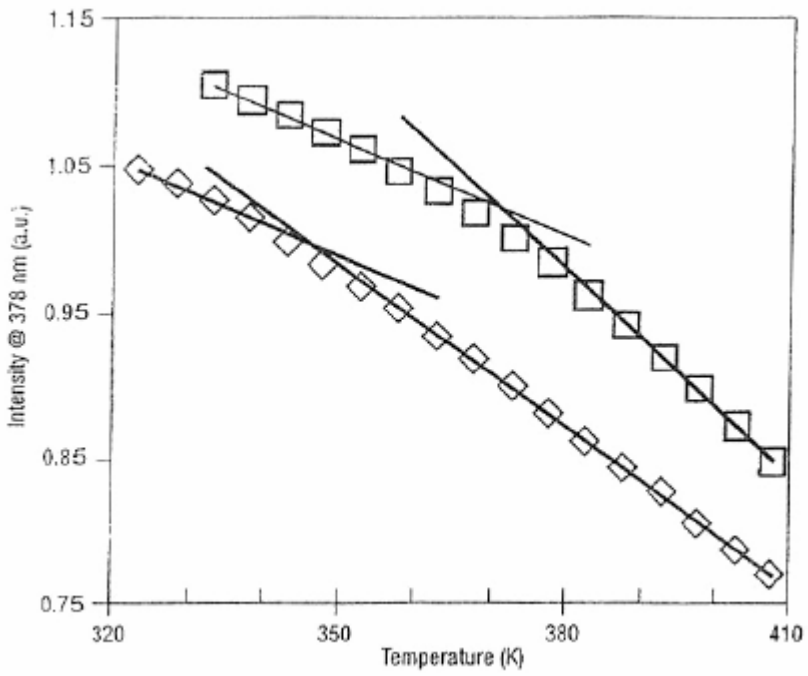

Figure 6.7: The temperature dependence of the fluorescence for pyrene-labelled PS single-layer films: 545 nm thick (□) and 17 nm thick (◊).[32]

6.4 Sample Preparation Issues for Thin Polymer Films

Thin films can be prepared by spin casting the solution onto the substrate. The films are annealed at different temperatures based on the type of materials. Due to the evaporation of the solvent, the film could be in non equilibrium condition. It has been reported that the material processed by spin casting method can undergo approximately 14% volume change in the glassy state after the solvent gets evaporated. To reach the equilibrium state, the spin cast film is annealed above T_g before the measurement on the film is started. Hence, it is very important to anneal the film for longer time at a temperature higher than T_g to equilibrate the thin film. Reiter et al. [33] studied the spin casted PS thin films of thickness less than 100nm on silicon. They observed that if the films are annealed at ~ 25 ºC below the bulk T_g, the films dewet and break up. The dewetting process consists of formation of pinhole defects, which grow into cellular

structures, eventually resulting into droplets.[33] They also observed the dewetting temperature of the film increases with increasing thickness and molecular weight.[34] This dewetting process was later confirmed by Stange et al. [35] using atomic force microscopy.

6.5 Experimental

6.5.1 Sample Preparation

The semi-crystalline grade PET used in this work was Kosa 1101 grade with intrinsic viscosity of 0.84. The filler that is used to process the nanocomposite is MLS (Cloisite 30B) supplied by Southern Clay. PET pellets were dried overnight in a vacuum oven at 65 ^{o}C. A 10% by weight master-batch of MLS was prepared on a Werner Pfleiderer co-rotating twin screw extruder with an L/D ratio of 30. Individual MLS concentrations of 1, 2, 3 and 5% by weight were processed on a Leistritz counter rotating twin screw extruder of 30 mm screw diameter and an L/D ratio of 32.5. A high shear screw with kneading block and reverse element was chosen to achieve uniform distribution of MLS to process the nanocomposite. Amorphous poly (ethyelene terephthalate) glycol, PETG (6763) was obtained from Eastman Chemical Company. MLS (Cloisite 20A) was obtained from Southern clay. PETG pellets were dried overnight in a vacuum oven at 80 ^{o}C. Master batches (15% by weight of MLS 20 A) were prepared on a Thermoprism co-rotating twin-screw extruder with a 16 mm screw diameter and a L/D ratio of 24:1. The medium/high shear screw design with good dispersion characteristic was chosen for the master batch preparation. A master batch was diluted to 5% by weight of MLS on the same twin-screw extruder. PETG nanocomposite films of 10-mil thickness were prepared on a Thermo Haake Polydrive single screw extruder with a film die attached.

PET and PETG were dissolved in dichloroacetic acid and heated at 60 ºC for 18 hours. Films were spun on silicon wafer substrates from the solution on a photo resist spinner; model PWM 32, Headway Research Inc. Texas, USA. The native oxide on the silicon wafers was etched using 2 wt % hydrofluoric acid. Immediately after removing the native oxide from the Si wafer, thin films were deposited on the Si wafer by the spin casting method, using varying speeds from 300-3000 rpm and viscosity to control the thickness. Initially the annealing was done at 60ºC for 3 hr and 120 ºC for 10 hours. Preliminary temperature scan revealed sample thickness decreased with temperature past the approximate $T_{g.}$ When the films were annealed for longer time i.e., at 60ºC for 3 hr and 120 ºC for 24 hours to remove the entrapped solvent, film thickness increased consistently with increase in temperature. Annealing was done in steps to avoid any pore formation in the thin film. Thickness of the samples was determined within a week of sample preparation using ellipsometry.

6.5.2 Characterization of Polymer Thin Films

For PET nanocomposite films, the dispersion of MLS in thin polymeric films was studied by optical microscopy and grazing angle X-ray diffraction (GAXRD). Optical microscopy images were recorded using a Nikon Eclipse ME600 (Japan). Images were taken using a Nikon Digital Camera DXM1200 (Japan). X-ray diffraction was performed using grazing angle XRD on a Rigaku Ultima III system. For PETG nanocomposite films the dispersion was studied by scanning electron microscopy (SEM). Thicknesses of the films were determined from ellipsometry. For PET films, a HSC302 hot stage from Instec, Inc. with temperature controller was connected to a Sentech SE 800 spectroscopic ellipsometer for heating the film and controlling the temperature. Heating was performed at a rate of 2 ºC/min. For PETG the thickness of the sample was measured by J.A. Woollam VASE VB-400 Spectroscopic Ellipsometry with an attached hot stage. The

linearity of the ellipsometric angle (psi) with thickness was investigated. It was determined to be linear with thickness though the results are not reported here.. Using the Cauchy model, software provided by the manufacturer,[36] thickness was determined in the normal thickness direction. The thickness obtained from ellipsometry was verified in SEM by taking a cross section. The thickness was plotted as a function of temperature over the temperature range of 30-140 ºC for some films and 30-160 ºC for some other films, and plotted. The coefficient of thermal expansion and glass transition temperature were calculated from these data. CTE and T_g values were determined for thicknesses from 25 nm to 710 nm for all compositions for PET films and from 17 to 360 nm for PETG films.

6.6 Thickness Measurement and Verification

The thickness of the film was measured as a function of temperature. The thickness obtained from ellipsometry was verified in Scanning Electron Microscopy (SEM) by taking a cross section as shown in Figure 6.8. The thickness from the SEM image was determined using Image J software at 10 different points across the image. The average thickness of the film from SEM was 39.2 nm and from the ellipsometry, the thickness for the same film was determined to be 40.31 nm. When the same procedure was tried for different film thickness the error was within 7%. First the films were annealed at 60ºC for 3 hr, then at120 ºC for 10 hours, and thicknesses were determined. The ratio of change of thickness to original thickness ($\Delta L/L$) with temperature was plotted as shown in Figure 6.9. A sharp decrease in thickness is observed at a temperature around T_g. However when the films were annealed at 60ºC for 3 hr and 120 ºC for 24 hours i.e. by increasing the annealing time, increase in thickness with temperature was observed as shown in Figure 6.10 as expected. The possible reasons for the decrease in thickness around T_g can be observed in Figure 6.10. This could be the result of non equilibrium state of the film due to residual solvent.

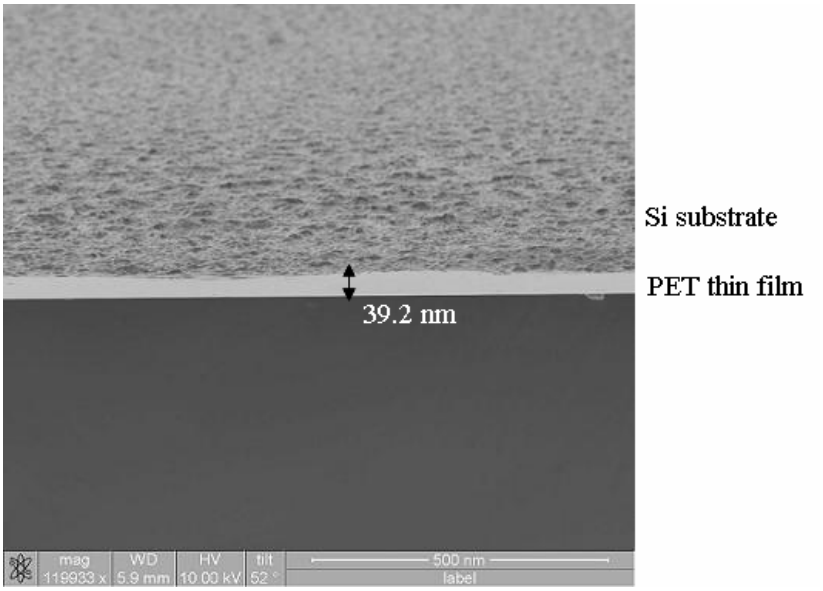

Figure 6.8: Cross section of PET thin film on silicon in SEM showing the thickness of PET thin film 39.2 nm (Ellipsometry result- 40.31 nm).

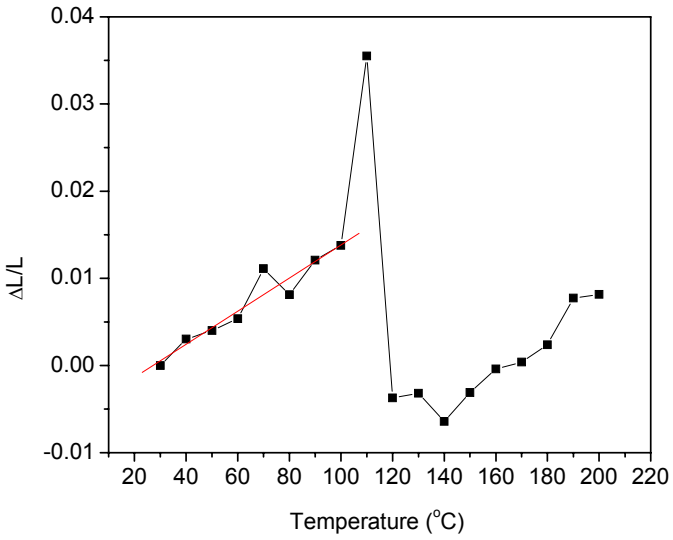

Figure 6.9: Thermal scan of thickness vs. temperature of pure PET for 415 nm thickness film when the annealing time was 10 hr, which was not sufficient.

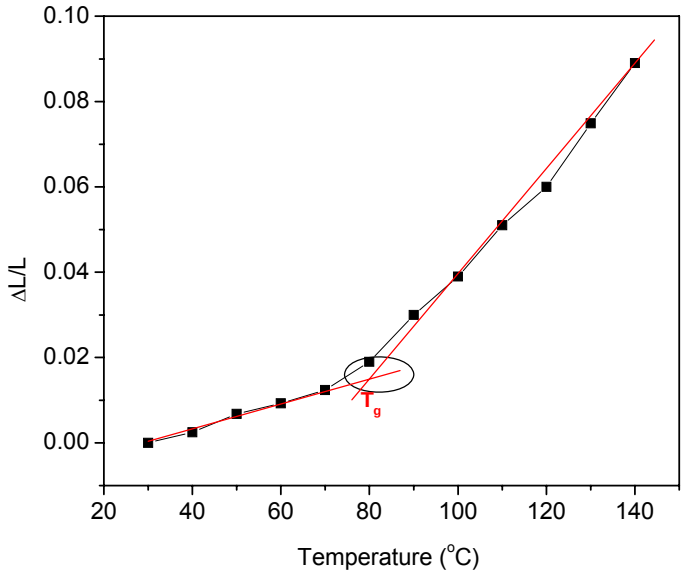

Figure 6.10: Thermal scan of thickness with temperature of PET+5 wt % MLS 30B for 150 nm thickness film.

6.7 Semicrystalline PET and Nanocomposites Results

6.7.1 Investigation of Dispersion MLS

As seen in Figure 6.11, optical microscopy images show that the dispersion of the MLS 30B in the film is uniform. The GAXRD results in Figure 6.12 show a very small broad peak of MLS 30B at 5.8º and 8.5º 2Θ for the PET+5% MLS 30B film. These peaks represent secondary reflections and confirm that the MLS 30B are well dispersed (Note the absence of the primary 001 reflection at 2.9º).

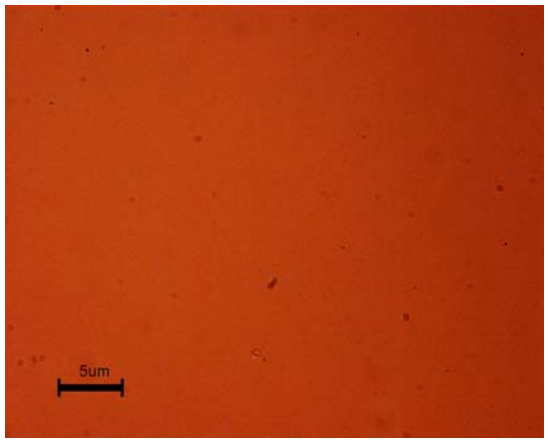

(a)

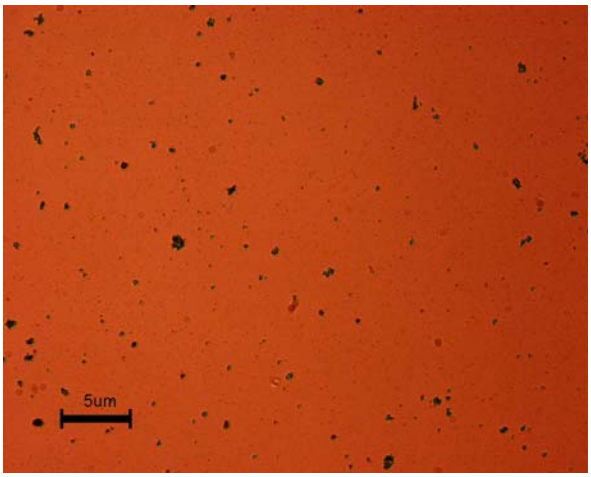

(b)

Figure 6.11: Polarized optical micrograph of (a) pure PET and (b) PET+ 5 % MLS-30B nanocomposite showing presence of MLS 30B.

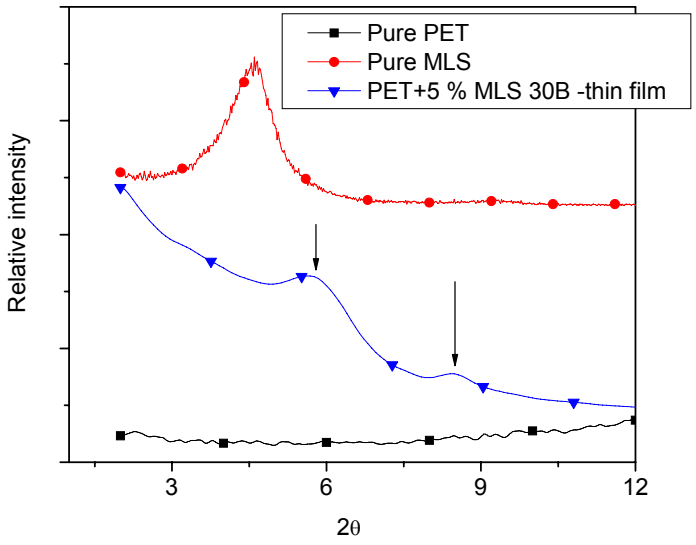

Figure 6.12: X-ray diffraction of PET nanocomposite thin film.

Figure 6.10 shows the typical thermal scan of thickness vs. temperature of a polymer film. The ratio of change in thickness to original thickness with temperature was plotted for both pure PET and the nanocomposite thin films. It clearly shows two distinct regions, one glassy and, the other rubbery region. ΔL/L over a temperature range is shown for films with different thickness and MLS 30B in the Figures 6.13 and 6.14, respectively.

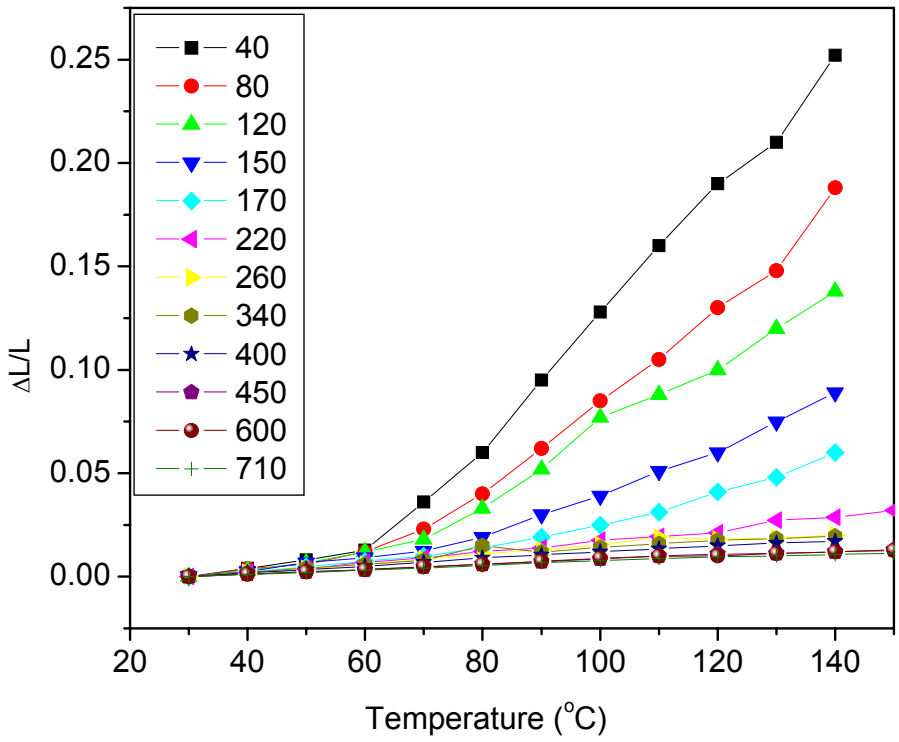

Figure 6.13: ΔL/L with temperature for different thickness for PET+5% MLS 30B thin film.

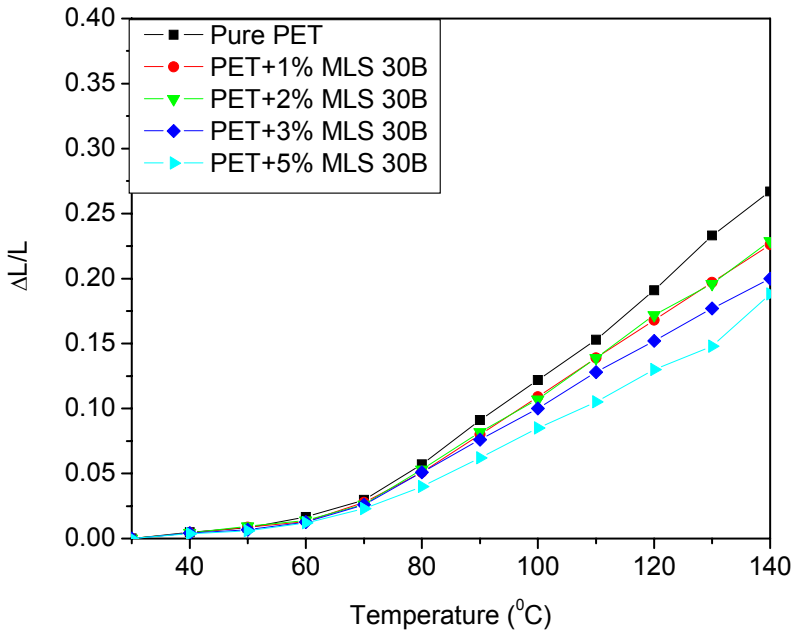

Figure 6.14: ΔL/L with temperature in pure polymer and nanocomposites for 80 nm thickness films.

6.7.1.2 Glass Transition

T_g was determined as the intersection of straight lines through the glassy and rubber regions. T_g was plotted for pure PET and for the nanocomposite film as a function of thickness as shown in Figure 6.15. CTE was calculated as the ratio of change of length to original length per unit temperature increase. Mathematically the slope of the graph in Figure 6.10 defines two CTE values, one below T_g and the other above T_g. With an increase in thickness, a decrease in slope is observed both below and above T_g. The addition of MLS 30B also affected the slope and it decreased with increase in its concentration. It is clear that T_g increases with increasing thickness, and reaches a plateau when the thickness is approximately 350 nm. The effect of MLS 30B on the glass transition temperature is not significant for the same thickness and the difference is approximately 5 º C for most film thicknesses. It is observed that the T_g decreased from 69.8 to 66

ºC when PET is compared to PET+ 5% MLS 30B nanocomposite for 80 nm thickness. Film thickness however, had a more significant impact on T_g. With an increase in thickness, T_g increased by 40 ºC for 220 nm thick film vs. an 80nm film and bulk film. We conclude that the difference in packing density with film thickness is significant. Packing density of chain segments near the free surface is lower than that of the interior of the film. This lower packing density leads to enhanced chain dynamics of segments at the free surface.[37-39] An empirical equation was proposed by Keddie et al.[23] to describe the T_g as a function of thickness

$$T_g(d) = T_g(\infty)\left[1 - \left(\frac{A}{d}\right)^{\delta}\right] \tag{6.12}$$

where d is film thickness and A is characteristic length. $T_g(d)$ is function of thickness, d and another empirical equation proposed by Kim et al.[28] is described as

$$T_g(d) = T_{g,bulk}\frac{d}{\sigma + d} \tag{6.13}$$

where $T_{g, bulk}$ is bulk glass transition temperature, σ is the measure of the rate at which the glass transition temperature decreases with decreasing d. Equation (6.13) was fitted using Origin software, the results are tabulated in Table 6.1. The model indicate that T_g decreased from 125 to 119 ºC with the addition of 5% MLS 30B. This is also observed for experimental values. A significant change of σ is not observed for pure PET films when compared to nanocomposite which correlates well with T_g data.

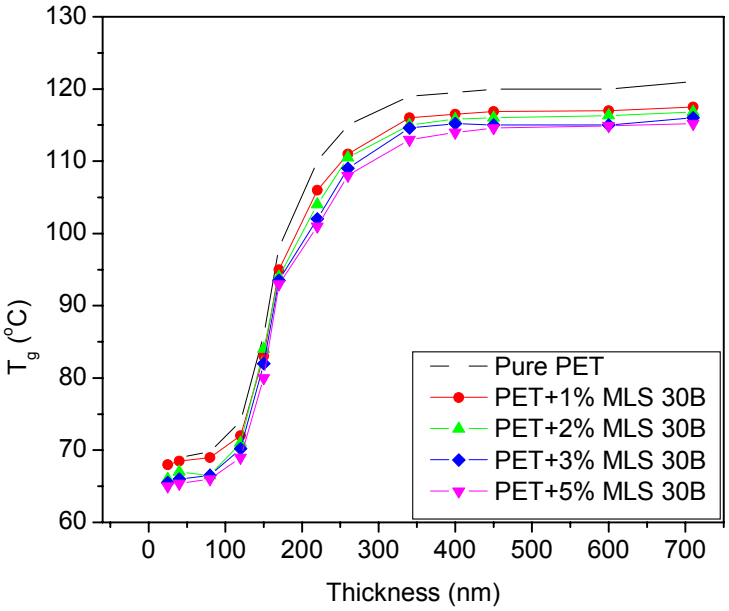

Figure 6.15: Variation of glass transition temperature (T_g) with thickness for pure PET and nanocomposite thin film.

As explained, the T_g of the nanocomposite film decreased with the addition of MLS 30B. These experimental data correlates well with a study by Ash et al.[40] They studied the effect of γ-alumina nanoparticles in poly (methyl methacryalte) (PMMA) on glass transition temperature. These nanocomposites were prepared by in situ polymerization of PMMA with nanoparticles. The sizes of these nanoparticles are 38 and 17 nm. These particles were first suspended in dry toluene through 10 minutes of sonication. Meanwhile, they added the appropriate amount of silane coupling agent to approximately 20 ml of dry toluene and swirled the suspension. The T_g was studied by using DSC. They observed a decrease in T_g with increase in nanoparticles. The T_g decreased by 25 ºC and did not decrease with further addition of nanoparticles after 1 wt% as shown in Figure 6.16. Figure 6.17 explains the effect of T_g with the ratio of surface area to

volume. With the increase in surface to volume ratio, T_g did not change initially and then it decreased. They attributed this to poor bonding of nanoparticles with the matrix.

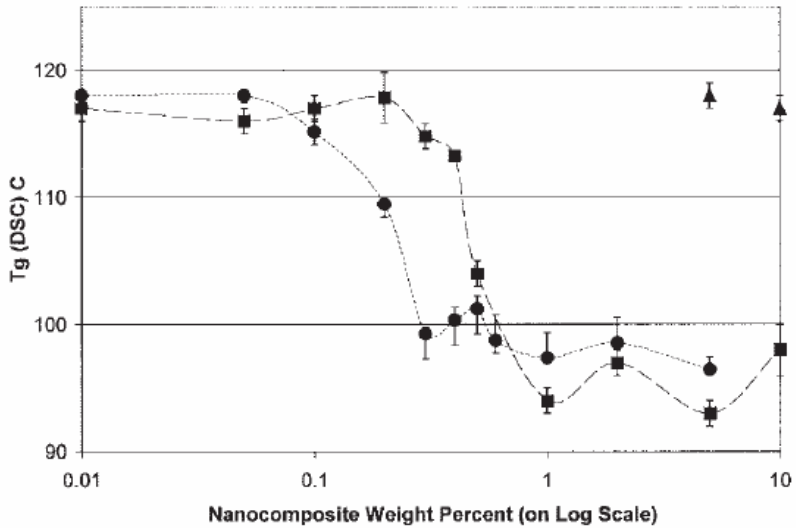

Figure 6.16: Glass-transition temperature behavior of alumina/PMMA nanocomposites (■: 38/39 nm alumina,●: 17 nm alumina). Note that the filler weight fraction is plotted on a log scale to show the behavior of the lower values more clearly. The neat PMMA is plotted as 0.01 wt % on the top graph. Following coating with GPS, the T_g returns to the neat value (▲: 3-glycidoxypropyltrimethoxysilane GPS-coated).

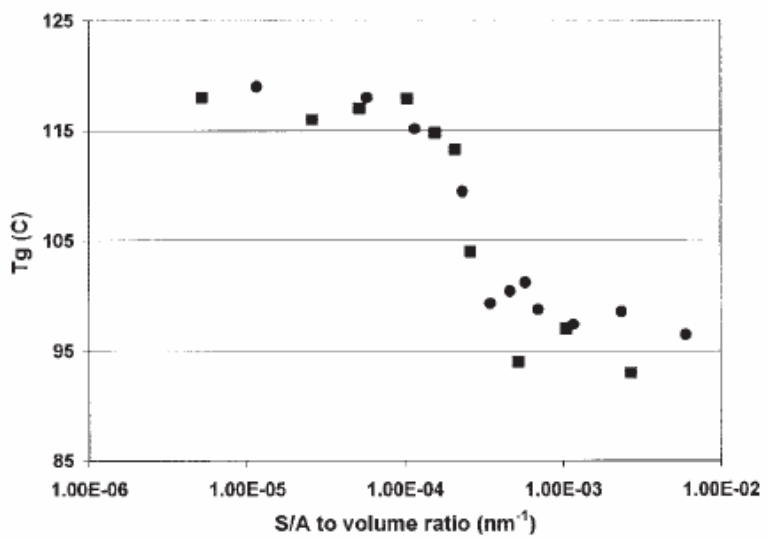

Figure 6.17: Glass-transition temperature behavior of alumina/PMMA nanocomposites (■: 38/39 nm alumina, ●: 17 nm alumina). The data are now plotted with respect to surface-area (S/A) to volume ratio, with the reported specific surface area given by the manufacturer, Nanophase Technologies Corporation (NTC).[40]

Table 6.1: T_g and σ, fitted values from equation (6.13).

Sample	T_g (°C)	σ
Pure PET	125.2	9.12
PET+1% MLS 30B	121.6	8.78
PET+2% MLS 30B	121	8.97
PET+3% MLS 30B	120	8.98
PET+5% MLS 30B	119	9.08

6.7.1.2 Thermal Expansion

The CTE for pure PET and for the nanocomposite thin films is shown in Figure 6.18. As the film thickness increases, the CTE decreased from 9.1 $X10^{-4}$ to 1.92 $X10^{-4}$ nm/nm-°C for pure PET film. The same trend is observed for the pure and nanocomposite films. The CTE decreased by 79% and 86 % for pure PET and PET +5 % MLS 30B films, respectively, when the thickness increased from 25 to 710 nm. All pure and nanocomposites CTE values are greater than the CTE of the free standing polymer film, 1.7 $X10^{-5}$ nm/nm-°C. [41] A decrease in CTE is observed with

increasing MLS 30B content for a given thickness. CTE decreased from 9.1 $X10^{-4}$ to $7.6X10^{-4}$ nm/nm-°C from the pure polymer to the nanocomposite with PET +5% MLS 30B for a 25 nm thick film. This corresponds to a 15 % decrease in CTE in the nanocomposite over the pure film, while a 40% decrease is observed for a 450 nm thick film.

CTE values above the T_g also decreased when the thickness of the film increased from 25 to 710 nm as shown in Figure 6.19. The CTE of the film is decreased by one order of magnitude when thickness of the film increased. The CTE of films with thickness up to 220 nm also showed approximately one order of magnitude higher than the CTE values below T_g for the same thickness. When the film thickness increased from 25 to 220 nm the CTE values decreased from 4.5 E-3 to 1E-3 nm/nm /°C corresponding to 77% decrease in CTE in the post T_g region. CTE of all film showed high thickness dependence. For nanocomposites films when 5% MLS 30B is added, CTE decreased by 15% for 25 nm thickness film. On the other hand, a 69% decrease is observed for 220 nm thickness film with the same 5% MLS 30B addition. The difference in (CTE below T_g) and (CTE above T_g), (yes, it is $\alpha_{rubber} - \alpha_{glass}$) ΔCTE decreases with increase in film thickness as shown in Figure 6.20. For the same thickness, increase in MLS 30B concentration resulted in a decrease in ΔCTE, indicating more of MLS 30B presence. Thus the MLS 30B surface offers additional surface for chain folding to occur leading to decrease in ΔCTE. This indicates a lower degree of super cooling.

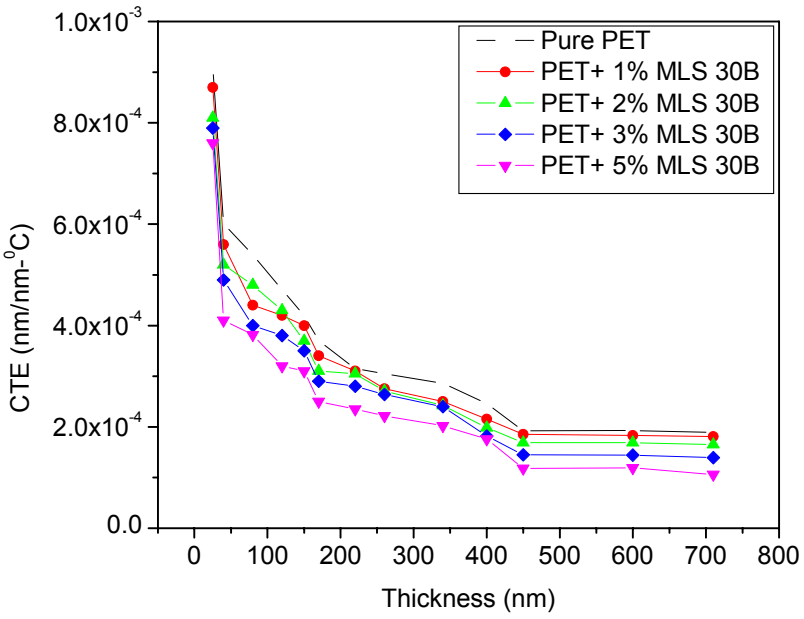

Figure 6.18: CTE as a function of thickness and MLS 30B below T_g.

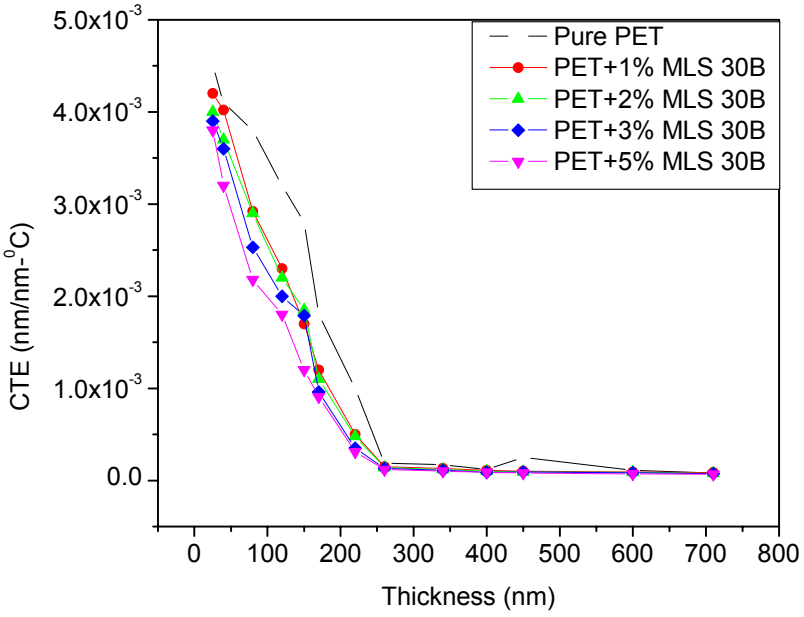

Figure 6.19: CTE as a function of thickness and MLS 30B above T_g.

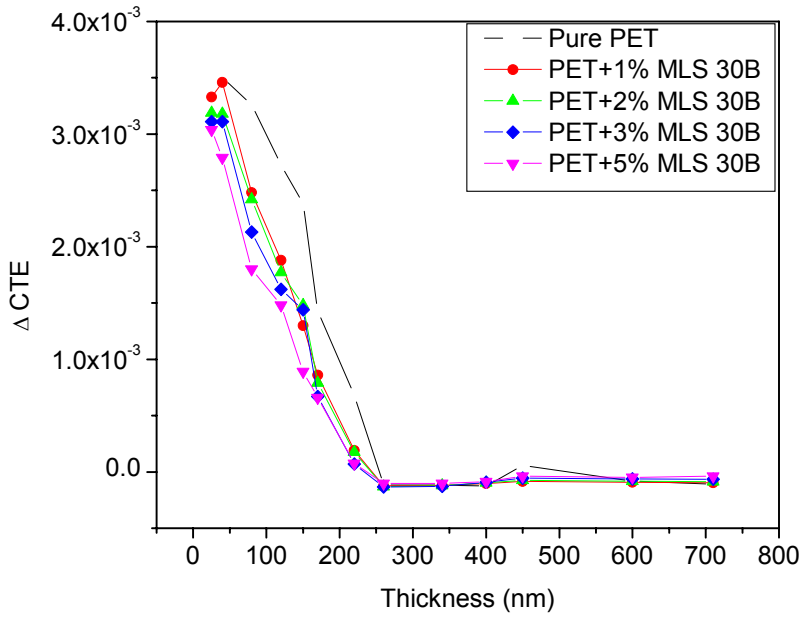

Figure 6.20: Difference of CTE as a function of thickness and MLS 30B below and above T_g.

From the PET results, it is very clear that the increase in T_g was very large (~40 ºC) for films of thickness 220 nm and above. Since PET is a semicrystalline polymer, if the crystallinity in the film is restricting the mobility and leading to an increase in T_g, is studied and compared by taking an amorphous polymer. Durell et al.[42] investigated molecular configuration and long range order at the surface of spin-cast PET thin film by studying the crystallization as a function of annealing temperature and time. They used grazing-incidence XRD to study the crystallization at the surface of the thin film. Crystallization peak was observed when the samples were annealed at and above 80 ºC. Durell et al. tried two different solvent to confirm it is not solvent induced crystallization. After 30 minutes of annealing at 95 ºC, they observed substantial local ordering with in ~ 5 nm of the surface. Crystalline ordering of the near-surface region in PET above T_g was observed while the bulk region below the surface was still amorphous.

Poly (Ethylene Terephthalate) Glycol (PETG) is an amorphous polymer, studied exactly similar to semicrystalline PET to understand the crystallinity effect in thin film. As already mentioned, here PET refers to semicrystalline PET and PETG refers to amorphous PET. Only one composition of nanocomposite (PETG+ 5wt % MLS 20A) is chosen for comparison with pure PETG.

6.8 Amorphous PET (PETG)

6.8.1 Effect of Film Thickness on Glass Transition in PETG

Figure 6.21 and 6.22 shows the plot between $\Delta L/L$ with temperature for PETG thin film and the nature of the plot is similar to semicrystalline PET showing two different slopes below and above T_g. The thickness increases with an increase in temperature. With the addition of MLS 20A, the slope decreases indicating a decrease in CTE. The T_g of PETG also decreased with MLS 20A similar to PET. T_g of PETG film increased from 73 to103 ºC with an increase in thickness from 16.8 to 216.4 nm. The decrease in T_g from PETG to nanocomposite is ~7 ºC for all films with different thickness as shown in Figure 6.23. A 30 °C increase in T_g is observed in both the pure PETG and nanocomposite films. It increased by 30 °C for the film of thickness ~220 nm which corresponds to the plateau of Tg values obtained in the PET. There was not much increase in T_g for film thickness more than ~220 nm. Therefore both PETG and PET film reach the plateau region for approximately same thickness. However, the increase in T_g for semicrystalline PET is 10 ºC more than that of amorphous PETG.

6.8.2 Thermal Expansion

Figure 6.24 shows the CTE as a function of thickness for PETG and nanocomposite film before T_g. Initially the CTE increased and then decreased with thickness. For the 17 nm film, the

CTE before T_g decreases from 2.39E-4 to 1.78E-4 nm/nm-°C from the pure polymer film to the nanocomposite film corresponding to a 26% decrease. For the 360 nm film, it decreases from 1.31E-4 to 6.08E-5 nm/nm-°C corresponding to a 53% decrease. With an increase in thickness, the CTE decreases by 45% and 59% in the pure polymer and nanocomposite, respectively.

Figure 6.25 shows the CTE as a function of thickness for PETG and nanocomposite films after T_g. For pure PETG, CTE is 1.4 E-3 nm/nm-°C for 17 nm film thickness. There is an approximately one order of magnitude difference in CTE is observed with increase in film thickness. CTE decreases from 1.4 E-3 to 3.77E-4 nm/nm-°C in the pure polymer film and from 8.89E-4 nm/nm-°C to 1.47E-4 nm/nm-°C in the nanocomposite film when the thickness is increased from ~ 17 to 360 nm. This corresponds to 73% and 84% decrease in PETG and nanocomposite, respectively. The CTE difference below T_g and above T_g decreases with increase in film thickness as shown in Figure 6.26. It follows similar trend as that of CTE above and below T_g. The ΔCTE of PETG and PETG nanocomposite are larger than the ΔCTE of PET and PET nanocomposite. Comparing the CTE data of PETG with PET, surprisingly CTE of PETG is less than PET films both below and above T_g. However, below T_g, the percentage decrease in CTE with thickness is higher in PET compared to PETG. The percentage decrease in CTE is 45 and 60% in PETG and PETG nanocomposites with increase in thickness from 17 to 220 nm. It is 80 and 86% in PET and PET nanocomposites when the thickness increased from 25 nm to 220 nm. The possible reason could be the increase in thickness of middle layer with increase in film thickness which is explained later by considering three layer model.

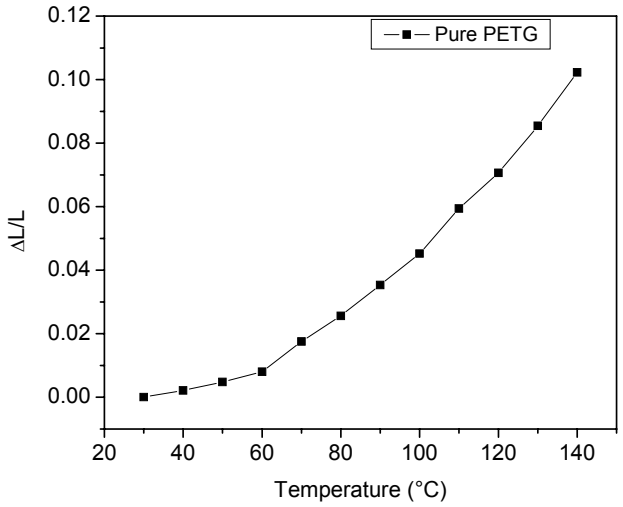

Figure 6.21: ΔL/L with temperature for the pure PETG film.

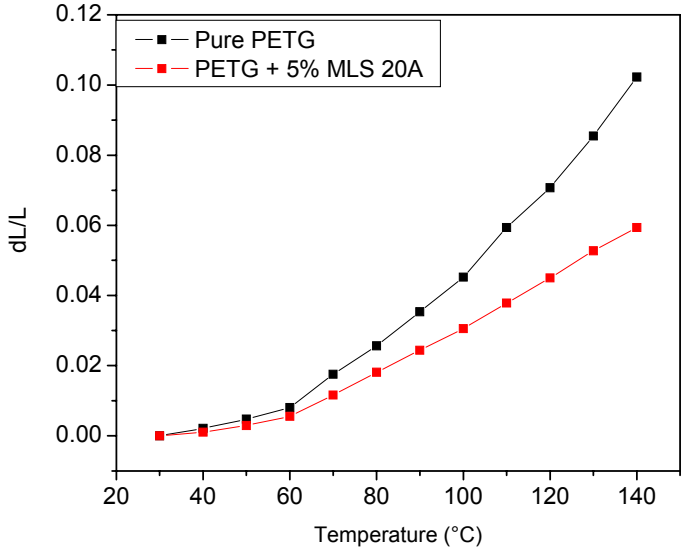

Figure 6.22: ΔL/L with temperature for different thickness for the PETG to the nanocomposite film.

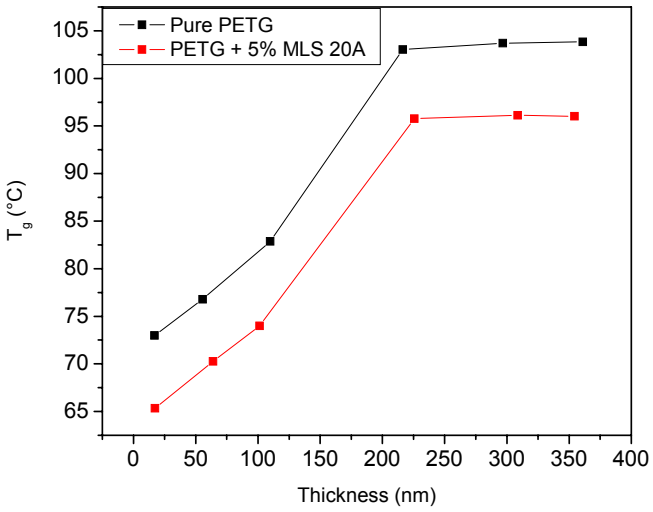

Figure 6.23: Variation of T_g with thickness for the pure PETG film to the nanocomposite film.

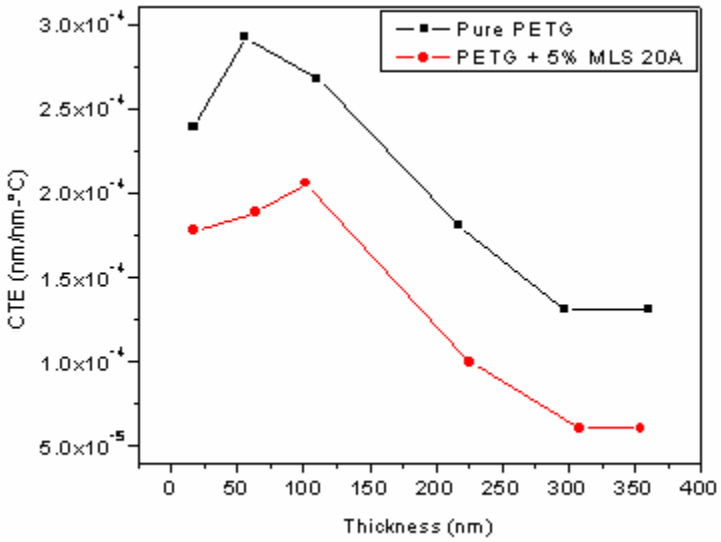

Figure 6.24: CTE as a function of thickness below T_g thickness for the pure PETG to the nanocomposite film.

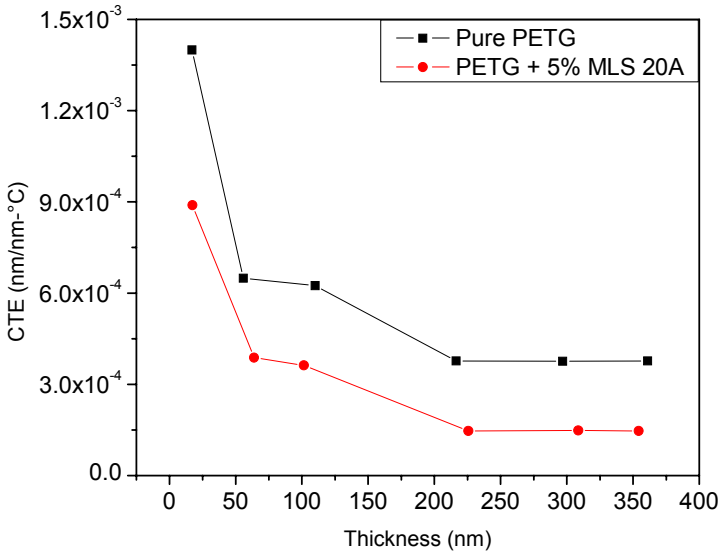

Figure 6.25: Comparison of CTE as a function of thickness above T_g thickness for the pure PETG to the nanocomposite film.

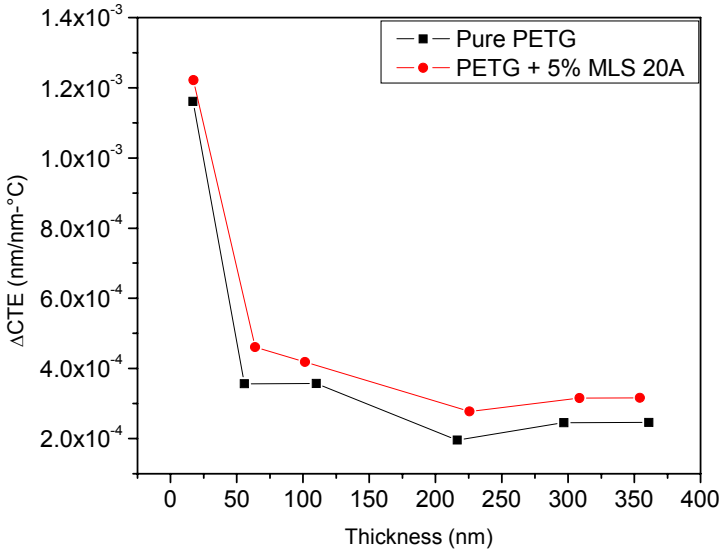

Figure 6.26: Difference of CTE as a function of thickness and MLS 20A below and above T_g in PETG and PETG nanocomposites.

6.9 Discussion

For both PETG and PET, from CTE and T_g results it is clear that lower thickness films show lower T_g and higher CTE. This explains that the substrate and the film are either not interacting or there is weak interaction. The free surface is more mobile compared to other regions of the film. The three layers model can be considered for these thin films. They are: the interface (next to substrate), the free surface which is exposed to air, and the middle layer in between them. As observed from the T_g data, with the increase in thickness, the restricted mobility of the middle layer dominated and this behavior is also reflected in the CTE data. Initially in films with lower thickness, there is weak interaction of polymer film with the substrate, hence, higher mobility of polymer chain with temperature leads to higher thermal expansion. When the thickness of the polymer film is increased, the restricted mobility region i.e. middle layer dominates. With the increase in temperature restricted mobility results in a decrease in thermal expansion. Another possible reason could be higher packing density in the middle layer. With increase in thickness there is not significant increase of liquid layer at the top surface of the film as predicted and shown in Table 6.1. This indicates packing density is a factor. Films with lower thickness show lower T_g, which clearly indicates that there is no attraction at the interface of the film at the substrate. Therefore thickness of middle layer (higher packing density layer with restricted mobility) increased with increase in thickness as illustrated in Figure 6.28. This results in lower T_g and CTE in thicker films.

CTE as a function of thickness was empirically described by Keddie et al. [23] including CTE of liquid like layer in thin films as follow

$$\alpha = \frac{\overline{\xi}}{d}(\alpha_{melt} - \alpha_{glass}^{\infty}) + \alpha_{glass}^{\infty} \qquad (6.14)$$

where $\bar{\xi}$ is average size of liquid like layer over the temperature range in which CTE is measured in the glass region. α_{glass}^{∞} is CTE of glassy region in the bulk. α_{melt} is CTE of melted liquid like region. For these data set CTE value of lowest thickness i.e. 25 nm is taken assuming that, the most of these 25 nm thick layer behaves like a liquid layer on the surface. For the CTE of glass, CTE of 600nm thickness film is taken for the calculation of ξ. From the Table 6.2 it is clear that minimum value of $\bar{\xi}$ is observed for 40 nm thickness film for all the compositions and they are in the range of 3-3.75 nm. For almost all compositions, the maximum value of $\bar{\xi}$ is obtained for 150 nm thickness. With increase in MLS 30B content, decrease in $\bar{\xi}$ was not observed for some composition as expected, however, for some other composition it has increased. For all the film composition and thickness, $\bar{\xi}$ is in the range of 3-8.5 nm. With an increase in thickness, the increase in $\bar{\xi}$ is less than 6 nm. Though this surface liquid like mobile layer increased with thickness but the increase is not much and that is the reason T_g did not decrease with increase in thickness. When equation (6.14) was fitted, best fit is got with CTE data of 1.9E-4 and 1.1E-4 nm/nm-°C for pure PET and PET+5% MLS 30B, of respectively as shown in Table 6.3. The comparison of experimental data and the fitted data is shown in Figure 6.27. It shows there is constantly decrease in CTE with increase in MLS 30B content. $\bar{\xi}$ is calculated for PETG and PETG nanocomposite and reported in Table 6.4. For 17 nm film thickness of pure PETG, it is 1.45 nm and it increased to 2.41 nm for nanocomposite film. With the increase in thickness $\bar{\xi}$ is increased and it is higher compared to semicrystalline PET film of the same thickness range. Increase in $\bar{\xi}$ with thickness does not correlate with experimentally determined T_g and CTE data. As thickness increases, T_g also increases. For films with lower thickness, lower T_g is observed. Therefore interface of polymer film with the substrate is not interacting. In this care the interface

layer is very thin as shown in Figure 6.29 (a). If the interaction between the polymer film and the substrate is interacting then a larger interface layer will form and will lead to increase in T_g. If the liquid like layer is increasing with the increase in the thickness and the polymer-silicon interface is weak (which is clear from T_g data) then it has to be the middle layer which contributes to increase in T_g and decrease in CTE with increase in thickness. Again, $\bar{\xi}$ increased from pure PETG to nanocomposite film for the film of same thickness. Addition of MLS 20A did not help in decreasing the liquid like layer at the surface. However, decrease in CTE is observed with the addition of MLS 20A in PETG like PET nanocomposites.

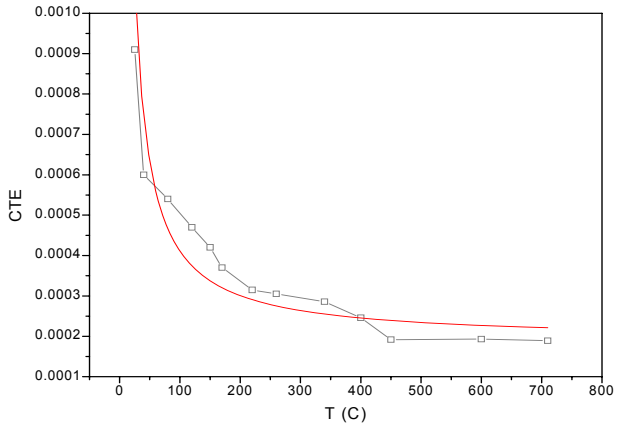

Figure 6.27: (□) are experimental CTE data for pure PET and the solid lines are fitted data using equation (6.14) in origin software.

Table 6.2: ξ values for different film thickness of different compositions, using equation (6.14).

Thickness (nm)	PET	PET+ 1 %MLS-30B	PET+ 2% MLS-30B	PET+ 3 %MLS-30B	PET+5 %MLS-30B
25	4.16	4.28	4.18	4.30	4.35
40	3.78	3.75	3.66	3.68	3.16
80	6.45	5.12	6.49	5.45	5.72
120	7.72	7.08	8.18	7.54	6.55
150	7.91	8.10	7.87	8.23	7.78
170	6.99	6.64	6.26	6.61	6.05
220	6.23	6.96	7.81	7.97	6.93
260	6.76	5.95	6.92	8.31	7.28
340	7.34	5.67	6.48	8.69	7.67
400	4.92	3.19	3.03	4.05	6.19

Table 6.3: A best fitted value of α from equation (6.14) using origin software.

Sample	α (nm/nm-°C)
Pure PET	1.90E-04
PET+1%MLS	1.70E-04
PET+2%MLS	1.60E-04
PET+3%MLS	1.40E-04
PET+5%MLS	1.10E-04

Table 6.4: ξ values for different film thickness of PETG and nanocomposite, from equation (6.14).

Thickness (nm)	PET	PET+5 %MLS-20 A
17	1.45	2.41
60	7.66	9.26
105	11.31	18.41
220	8.74	10.28

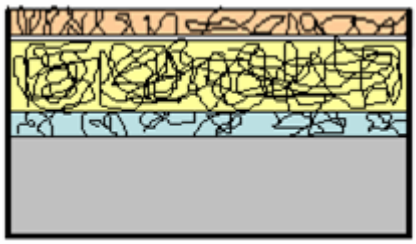

(a)

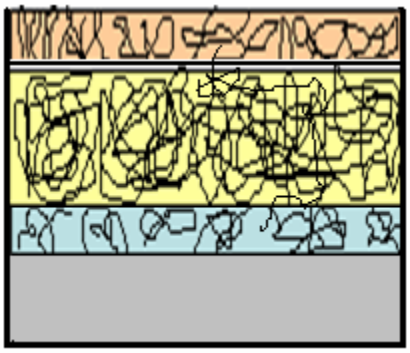

(b)

Figure 6.28: Structure of (a) thin and (b) comparatively thicker polymer film on Si.

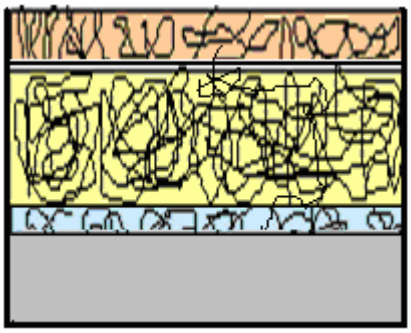

(a)

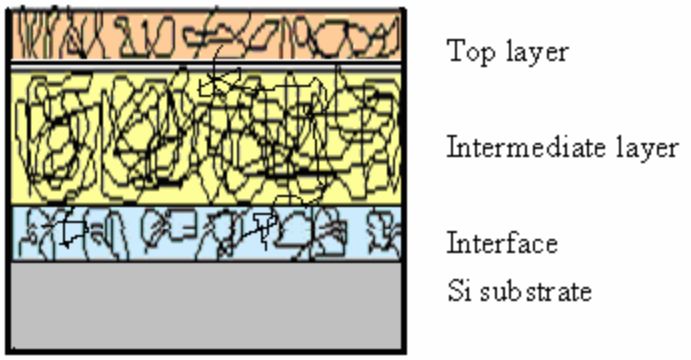

(b)

Figure 6. 29: (a) Schematic showing weak interaction (lower thickness of interface) and (b) strong interaction (comparatively larger thickness of interface) of polymer film with the substrate.

6.10 Conclusions

The effect of film thickness on T_g and CTE was studied in pure PET and nanocomposite films. An increase in 40 ºC in T_g for 220 nm film thickness compared to bulk film was observed. The addition of MLS to pure PET film did not change T_g significantly and the maximum decrease was 6 ºC. This is due to the weak interface of MLS and polymer which correlates with AFM data. The same trend is observed in the bulk film. T_g and CTE of PETG followed a similar trend to PET. A 30 ºC increase in T_g is observed for 220 nm film thickness compared to bulk film. 84% decrease in CTE for film of thickness of 360 nm is observed compared to the 17 nm film for PETG nanocomposite above T_g and 59% decrease is observed for films below T_g. By fitting the empirical equation described by Keddie et al., significant variation in σ is not observed for pure PET films to nanocomposite which correlates well with our T_g data. CTE of all films showed highly thickness dependent. The CTE of the film below T_g decreased when thickness increased from 25 nm to 710 nm for pure PET and PET+5% MLS concentration film by 79% and 86% respectively. Though any large change in T_g is not observed with the addition of MLS, CTE

decreased by 40% for films of 450 nm thickness. When the film thickness increased from 25 to 220 nm, 77% decrease in CTE above T_g is observed. Form CTE and T_g data it is clear that substrate-polymer is non-interacting or weak interacting system. Three layer models is considered for the thin film system and with increase in thickness; middle layer (possibly with higher packing density restricted mobility) has dominated. This has contributed to increase in T_g and decrease in CTE.

6.11 References

[1] http://www.polymers.tudelft.nl/wubweb/PDF/MW82-WuebbenhorstProc-ISE12-2005.pdf

[2] Mansfield, K.F.; Theodorou, D.N. Macromolecules **24** (1991) 6283.

[3] van Zanten, J. H.; Wallace, W. E.; Wu, W. Phys Rev E **53** (1996) R 2053.

[4] Zheng, X.; Rafailovich, M.H.; Sokolov, J.; Strzhemechny, Y.; Schwarz, S.A; . Sauer, B.B.; Rubinstein, M. Phys Rev Lett **79** (1997) 241.

[5] Demaggio, G. B.; Frieze, W. E.; Gidley D. W.; Zhu, M.; Hristov, H. A.; Yee, A. F., Phys Rev Lett **78** (1997) 1524.

[6] Forrest, J. A.; Dalnoki-Veress, K.; Dutcher, J. R. Phys Rev E **56** (1997) 5705.

[7] Fukao, K.; Miyamoto, Y. Europhy. Lett **46** (1999) 649.

[8] Forrest, J. A.; Dalnoki-Veress, K.; Stevens, J. R.; Dutcher, J. R. Phys Rev Lett **77** (1996**)** 2002.

[9] Arndt, M.; Stannarius, R.; Groothues, H.; Hempel, E.; Kremer, F. Phys Rev Lett. **79** (1997) 2077.

[10] Jackson, C. L.; McKenna, G.B. J Non-Cryst Solids **131-133** (1991) 221.

[11] Alcoutlabi, M.; McKenna, G. B. J Phys: Condens Matter **17** (2005) R461.

[12] McKenna, G. B. J. Phys IV, France **10** (2000) Pr7.

[13] Kawana, S.; Jones, R. A. L. Phys Rev E **63** (2001**)** 021501.

[14] Pham, J. Q.; Green, P. F. J.Chem Phys **116** (2002) 5801.

[15] Torres, A.; Nealy, P. F. J. J. de Pablo, Phys Rev Lett **85** (2001) 3221.

[16] Wu , G.; Nishida , K.; Takagi , K. ; Sano, H.; Yui, H. Polymer **45** (2004) 3085.

[17] Chow, T.S.; Wilson, J.C. J. Polym. Sci. Part B: Ploym. Phys. **16** (1978) 967.

[18] Yoon, P.J.; Fornes, T.D.; Paul, D.R. Polymer **43 (**2002) 6727.

[19] Jackson, C L; McKenna, G. B. J Non-Cryst Solids **131–133 (**1991)221.

[20] Alba-Simionesco, C.; Dosseh, G.; Dumont, E.; Frick, B.; Geil, B.; Morineau, D.; Teboul, V.; Xia, Y. Eur Phys J E **12 (**2003) 19.

[21] Morineau, D.; Xia, Y. D. Alba-Simionesco, C .J Chem Phys **117** (2002) 8966.

[22] Pissis, P.; Daoukaki, D.; Apekis, L.; Christodoulides, C. J Phys: Condens Matter **6 (**1994) L325.

[23] Keddie, J. L.; Jones, R. A. L; Cory, R. A.; Europhys Lett **27** (1994) 59.

[24] Keddie, J. L.; Jones, R. A. L; Cory, R. A. Faraday Discuss **98** (1995) 219.

[25] Prucke, O.; Christian, S.; Bock, H.; Ruhe, J.; Frnak, C. W.; Knoll, W. Macromolec Chem Phys **199** (1998) 1435.

[26] Pham, J. Q.; Green, P. F., Macromolecules **36** (2003) 1665.

[27] Pham, J. Q.; Green, P. F. J Chem. Phys **116** (2002**)** 5801.

[28] Kim, J. H.; Jang, J.; Zin, W.; Langmuir **16** (2001) 2703.

[29] Angell, C. A.; Ngai, K. L.; McKenna, G. B.; McMillan, P. F.; Martin, S. W. J Appl Phys **88 (**2000) 3113.

[30] Polymer Surface and Interface III, Edited by R. W. Richards and S. K. Peace, 1999

[31] Wollam, J. A. Reference Manual, 2006

[32] Ellison, C. J.; Torkelson, J. M. Nat Mater **2 (**2003) 695.

[33] Reiter, G., Phys. Rev. Lett. **68** (1992) 75.

[34] Reiter, G., Langmuir, **9** (1993) 1344.

[35] Stange, T. G.; Mathew, R.; Evans, D. F.; Hendrickson, W. A., Langmuir **8** (1992) 920.

[36] Sentech SE 800 spectroscopic ellipsomter, Reference manual

[37] Binder, K.; Baschnagel, J.; Bennemann, C.; Paul, W. J Phys: Condens Matter A **11** (1999) 47.

[38] Doruker, P.; Mattice, L. W. Macromolecules **32** (1999) 194.

[39] Baschnagel, J.; Binder, K. Macromolecules **28** (1995) 6808.

[40] Ash, B. J.; Siegel, R. W.; Schadler, L. S. J Polym Sci Part B: Polym Phys **42** (2004) 4371.

[41] Brandrup, J.; Immergut, E. H.; Grulke, E. A. Polymer handbook (1999).

[42] Durell, M.; MacDonald, J.E.; Trolley, D.; Wehrum, A.; Jukes, P.C.; Jones, R.A.L.; Walker, C.J.; Brown, S. Euro Phys Lett **58** (2002) 844.

CHAPTER 7

CONCLUSIONS

The bulk and interfacial phenomena in semicrystalline polymer nanocomposites was investigated. The materials selected were nylon, PET, and PEN. MLS was used to process the nanocomposites by extrusion. The different properties such as crystallization and thermal transitions, barrier, and mechanical properties of polymer were studied and compared with that of nanocomposites.

7.1 Polymer Nanocomposites Bulk Structure Property Relationships

To understand the structure of nanocomposite, dispersion of MLS was studied using either one or more of the following techniques: XRD, TEM, SEM cross section prepared by FIB. From the XRD data, exfoliated structure can be inferred in nylon nanocomposites. From both XRD data and TEM images, a combination of intercalation and exfoliation can be inferred in PET nanocomposites. PEN nanocomposites indicated an intercalated dispersion but which was well distributed in the polymer.

Mechanical properties showed improvement in nylon and PEN but decreased performance in PET nanocomposites. The yield strength and modulus of pure nylon was 23 MPa and 1.2 GPa, respectively. The yield strength increased from 23 to 28 MPa with the addition of 5% MLS. The UTS also increased from 28 to 36 MPa. The addition of MLS improved the tensile properties of nylon. The yield strength and modulus of PET are 44 MPa and 2 GPa, respectively. PET had higher yield strength compared to that of nanocomposites. The yield strength of PET decreased from 44 to 35 MPa with the addition of 3% MLS. PET nanocomposites showed an increase in modulus compared to pure PET. However, a decrease in

yield stress and UTS was observed. On the other hand, improvement in tensile results was observed for PEN nanocomposites compared to pure PEN. Yield stress, UTS, and modulus of pure PEN was 50 MPa, 68.6 MPa, and 1.98 GPa and that of PEN+2% MLS-2S nanocomposite was 62.3 MPa, 84.9 MPa, and 2.27 Gpa, respectively. 24% improvement in yield stress was observed in nanocomposite compared to pure PEN.

Crystallization in all polymers was studied by DSC. In nylon and PEN, an increase in fusion temperatures was obtained while in PET, a decreased fusion temperature was obtained. The fusion temperature of pure nylon was 167 ºC and it increased by ~20 ºC in nanocomposites. The crystallization peaks were narrower in nanocomposites compared to pure nylon explaining higher crystallization rate in nanocomposites. The T_g and T_m for pure PET is 69 and 247 ºC, respectively. Both the cold crystallization temperature and the fusion temperature were decreased by ~ 5 ºC with the addition of MLS in PET. In PEN nanocomposites, fusion temperature increased compared to pure PEN. In the first heat, crystallinity almost got doubled in nanocomposites compared to PEN. In the second heat, a doublet in the melting peak was observed, explained by the enhancement of formation of β crystal structure with the addition of MLS in nanocomposites. Percentage haze (which is measure of opaqueness) decreased with the addition of MLS. PEN+1%MLS-3S film had the lowest % haze compared to all other nanocomposites.

Permeability of these films were measured on an in-house manufactured permeability system and analyzed. The addition of MLS showed a drop in helium permeability by 63 % and 59% in PET+3% MLS and nylon +5% MLS, respectively compared to pure PET and nylon 6. For some composition of PET nanocomposites, an increase in permeability was observed instead of a decrease in permeability. Therefore, permeability of nanocomposites is predicted under

different conditions considering amorphous, crystalline, and MLS content. It was concluded that both MLS and crystallinity due to addition of MLS contribute to the barrier properties. For PET films containing lower % of MLS, effect of crystallization played a significant role and for PET with higher % of MLS film, MLS played a significant role in determining permeability. Viability of the films as flexible substrates in the end product requires examination of the influence of fatigue on the permeability. All the oxygen permeability values of PET with 50 and 10,000 fatigue cycles for 3% MLS nanocomposite showed a decrease in permeability compared to pure PET. The behavior under mechanical loads differed when comparing nylon to PET. For nylon, in low-cycle fatigue, permeability increased due to defect generation. In high-cycle fatigue, permeability decreased and the possible reason could be thermal healing and rearrangement of polymer chains. For PET nanocomposites, any mechanical force resulted in increased permeability compared to the as processed nanocomposite. Helium and oxygen permeability results showed different concentration dependent trends indicating differences in polymer solubility.

Water adsorption was also studied in nylon and PET films. Nylon films absorbed more water compared to PET films in the same time period. The maximum percentage change in weight for nylon and nylon +3% MLS films were 7% and observed at ~ 24 hr. On the other hand, it was only 0.62% and 0.42 % for pure PET and PET+3% MLS, respectively. When as-processed nylon films were annealed, annealed sample showed more permeable to the helium gas than the as processed sample. It could be that the moisture in the sample occupies the free volume and does not let the gas permeate through. Among all the PEN nanocomposites, PEN+1% MLS-3S nanocomposites sample showed the lowest permeability and it was approximately five times lower than that of pure PEN.

7.2 Local and Long Range Interfacial Dynamics in Polymer Nanocomposites

The decreased mechanical and barrier properties of the PET nanocomposites independent of an excellent dispersion were reviewed in the context of interfacial properties. Local polymer differences were probed using atomic force microscopy while longer range impact was studied by investigating glass transitions in films of varying thickness and MLS content.

Using force modulation AFM, an interesting result of weak or softer interface of polymer-MLS compared to relatively hard matrix and harder MLS phase was observed. PET nanocomposite showed softening around the MLS plate while PEN did not.

The MLS-polymer interfacial property was also studied in thin films by studying the polymer physics of confinement. The thermal properties of PET polymer thin film and their nanocomposite with varied thickness and concentration of MLS was studied. In thin nanocomposite film, optical microscopy, SEM, and GAXRD data showed the presence and dispersion of MLS in PET. The effect of film thickness on T_g and CTE was studied in pure PET and nanocomposite films. An increase in T_g by 40 ºC was observed for 220 nm film thickness compared to bulk film. The addition of MLS in PET thin film decreased T_g by 6 ºC. It is due to the weak interface of polymer-MLS which was confirmed by AFM results. By fitting empirical equation described by Keddie et al.[1] significant change of σ was not observed for pure PET films to nanocomposite which correlates well with T_g data. CTE of all the film showed highly thickness dependent. The CTE of the film (below T_g) decreased by 79% and 86%, respectively when thickness increased from 25 to 710 nm for pure PET and 5% MLS concentration film. Though a large variation in T_g with the addition of MLS is not observed, CTE decreased by 40% for films of 450 nm thickness. When the film thickness increased from 25 to 220 nm, a 77%

decrease in CTE above T_g was observed. Form CTE and T_g data, it was clear that substrate-polymer was non-interacting or weak interacting system. If three layer models is considered for these thin film systems ,with increase in thickness, higher thickness of middle dense layer and restricted mobility has dominated that has contributed to an increase in T_g and a decrease in CTE.

Concluding the work, some composition of PET nanocomposites did not show any improvement in barrier and mechanical properties due to weak polymer-MLS interface as confirmed by FM-AFM and ellipsometry data. On the other hand, improvement in properties is observed for both nylon and PEN nanocomposites. Permeability is decreased by approximately one order of magnitude in PEN+1%MLS-3S compared to pure PEN. This study clearly explains that properties can not be improved just by adding nanofiller into the matrix, rather its interaction with the matrix and their interface plays significant role in the final properties of the material. PET thin film approaches bulk property in terms of thermal expansion and T_g was increased by 40 ºC when film thickness is more than 220 nm. This increase in T_g by 40 ºC is an achievement for different applications of these thin polymer coatings where temperature limits the applications.

7.3 References

[1] Keddie, J. L.; Jones, R. A. L; Cory, R. A.; Europhys Lett **27** (1994) 59.